NUMERICAL MODELLING OF THE COMBUSTION PROCESS AND EMISSIONS FORMATION OF KEROSENE AND ITS BLENDS IN DIESEL ENGINES

TAY KUN LIN CLEMENT

(B.Eng.(Hons.), National University of Singapore, Singapore)

A THESIS SUBMITTED
FOR THE DEGREE OF DOCTOR OF PHILOSOPHY
DEPARTMENT OF MECHANICAL ENGINEERING
NATIONAL UNIVERSITY OF SINGAPORE
2017

Supervisors:
Assistant Professor Yang Wenming, Main Supervisor
Professor Chou Siaw Kiang, Co-Supervisor

Examiners:
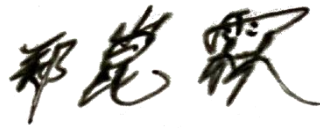Associate Professor Yap Christopher Robert
Associate Professor Palani Balaya
Professor Wang Zhi, Tsinghua University

DECLARATION

I hereby declare that the thesis is my original work and it has been written
by me in its entirety. I have duly acknowledged all the sources of information
which have been used in the thesis.

This thesis has also not been submitted for any degree in any university
previously.

_____
Tay Kun Lin Clement
5th June 2017

Dedicated to my beloved family, relatives and friends

Acknowledgements

This research work would not have been possible without the help, support, advice and encouragement from the people around me. At this moment, I would like to take this opportunity to sincerely thank all who have made my postgraduate journey possible and memorable.

First, I would like to thank my supervisor Dr. Yang Wenming who has been a great source of guidance, help, support and encouragement to me. I am privileged to have such a patient supervisor who has a great wealth of knowledge in the field of combustion. At times, when I found it difficult to proceed with my research, his constructive suggestions and advice were extremely helpful for me. Also, I would like to thank him for proofreading my work before they were submitted to journals.

Next, I would like to thank my co-supervisor Prof. Chou Siaw Kiang who has also been very gracious and kind in accepting me as his student. He has tremendous amounts of experience and it is an honor to be guided by him. Moreover, he is also very supportive of my research work.

Following which, I would like to express my gratitude to my examiners who were present during my qualifying and my final examinations. Examiners Dr. Yang Wenming, Dr. Koh Yee Kan, A/Prof. Christopher Yap, A/Prof.

Furthermore, I would like to thank my parents and sister for their unwavering support for me during this arduous period. Their encouragement and support have helped me through grueling times. I sincerely thank them for being my silent supporters.

Finally and most importantly, I thank GOD for giving me this opportunity and the wisdom to do my postgraduate studies. I sincerely thank GOD for everyone HE has placed in my life to make all things possible.

Clement

Philippians 4:13 "I can do all things through Christ which strengtheneth me."

Table of Contents

This page was intentionally left blank.

Executive Summary

The use of kerosene in direct injection compression ignition (DICI) engines is fundamentally due to the introduction of the Single Fuel Concept (SFC) as highlighted in Chapter 1. As conventional DICI diesel engines are made specifically to use diesel fuel, the usage of kerosene will have adverse effects on engine emissions and combustion characteristics. As a result, in order for kerosene to be properly and efficiently used in diesel engines, a comprehensive literature review was carried out in Chapter 2 to identify the research gaps. Through the literature review, it was noted that much experimental work was done for kerosene combustion in DICI engines. However, reliable and compact chemical reaction mechanisms for kerosene combustion under DICI diesel engine conditions are sorely lacking and, as a result, negligible numerical simulation has been carried out in this area. Hence, the primary objective of this thesis is to develop suitable kerosene reaction mechanisms which are small and yet robust enough to be used for DICI engine simulations which are capable of predicting the major emissions such as soot, carbon monoxide (CO) and nitrogen oxide (NO). The secondary objective is to investigate the potential of kerosene in reducing emissions through different injection rate-shapes and bowl geometries. The background, motivation, research gaps, objectives as well as the thesis organization are

mentioned in Chapter 1. Moreover, Chapter 3 gives an overview of the experimental setup and the numerical code used in this thesis.

A validated $C_{12}H_{24}$ kerosene reaction mechanism, containing only 122 species and 585 reactions, with embedded soot chemistry for diesel engine simulations was developed in Chapter 4. The $C_{12}H_{24}$ kerosene reaction mechanism was validated for its ignition delay times under different initial shock tube conditions. Constant volume heat-release rate as well as ignition delay validations were also carried out under different ambient conditions. Furthermore, the reaction mechanism is able to predict the combustion characteristics and soot trends of kerosene reasonably under real engine conditions.

In order to further reduce computational time, a more compact reaction mechanism was developed in Chapter 5. The new kerosene-diesel reaction mechanism consists only of 48 species and 152 reactions. Furthermore, the kerosene sub-mechanism is validated for its ignition delay times under different initial shock tube conditions and constant volume combustion conditions. The predicted and experimental constant volume heat-release rates as well as flame lift-off lengths (FLOLs) are also similar. Overall, this new kerosene-diesel reaction mechanism is proven to be robust and practical for diesel engine simulations.

In Chapter 6, parametric studies were carried out using the mechanism developed in Chapter 5. Chapter 6 Part A investigates the combustion and emissions characteristics of a DICI engine fueled with kerosene-diesel blends, using different piston bowl geometries together with varying injection rate-shapes were investigated. On the other hand, Chapter 6 Part B investigates the effects of boot injection rate-shapes on the combustion process and emissions formation of a direct injection compression ignition engine fueled with kerosene and diesel. A phenomenological soot model and the adjusted and enhanced kerosene-diesel reaction mechanism were used to study the combustion process and emissions formation. From Chapter 6, it can be seen that by using kerosene together with the appropriate injection rate-shape, one is able to reduce DICI diesel engine emissions relative to diesel fuel combustion.

Finally, Chapter 7 sums up the contributions of this thesis and recommends possible future work.

This page was intentionally left blank.

List of Tables

This page was intentionally left blank.

List of Figures

List of Symbols

Abbreviations

AHRR	Apparent heat-release rate
ALE	Arbitrary Lagrangian-Eulerian
AMP	Accumulation mode particle
ASI	After start of injection
ATDC	After top dead center
CA	Crank angle
CAD	Crank angle degrees
CA50	Crank angle at 50% of total heat-released
CCD	Charge-coupled device
CE	Combustion efficiency
CI	Compression ignition
CMOS	Complementary metal-oxide-semiconductor
CN	Cetane number
CO	Carbon monoxide
CO_2	Carbon dioxide
C(S)	Gas phase soot
CVCC	Constant volume combustion chamber
C9H12	1,2,4,5-teeramethylbenzene
DCN	Derived Cetane number
DI	Direct injection
DICI	Direct injection compression ignition
DOC	Duration of combustion
ECU	Electronic control unit
EGR	Exhaust gas recirculation
E.R.	Equivalence ratio

EVO	Exhaust valve open
Eqmt	Equipment
FIT	Fuel ignition tester
FLOL	Flame lift-off length
HACA	Hydrogen-abstraction-carbon-addition
H/C	Hydrogen-to-carbon ratio
HCCI	Homogeneous charge compression ignition
ID	Ignition delay
IVC	Intake valve close
JSR	Jet-stirred reactor
K	Coefficient of soot absorption
KERO	Pseudo kerosene C_{10} alkane
KH	Kelvin-Helmholtz
L	Line of sight path length through flame
LHV	Lower heating value
MCE	Multi-cylinder engine
MCH	Methylcyclohexane
MURI	Multi-University Research Initiative
MW	Molecular weight
NASA	National Aeronautics and Space Administration
NMP	nucleation mode particle
NO	Nitrogen monoxide
NO_2	Nitrogen dioxide
NO_x	Nitrogen oxides
n-PB	n-propylbenzene
n-PCH	n-propylcyclohexane
NTC	Negative temperature coefficient
OCC	Omega combustion chamber

P	Pressure
PAH	Polyaromatic hydrocarbon
PLII	Planar laser-induced incandescence
PM	Particulate matter
PRF	Primary reference fuel
PSD	Pseudo-surrogate decoupling
RCCI	Reactivity controlled compression ignition
RCM	Rapid compression machine
RNG	Re-Normalization group
rpm	Revolution per minute
RP-3	Chinese equivalent of Jet-A
RT	Rayleigh-Taylor
SCC	Shallow-depth combustion chamber
SCE	Single-cylinder engine
SFC	Single Fuel Concept
SOC	Start of combustion
SOI	Start of injection
SNL	Sandia National Laboratory
SRCC	Shallow-depth re-entrant combustion chamber
T	Temperature
TAB	Taylor analogy breakup
TDC	Top dead center
TKE	Turbulent kinetic energy
TRF	Toluene reference fuel
TSI	Threshold sooting index
UHC	Unburnt hydrocarbon
US	United States
V	Volume

1MN	1-methylnapthalene
1,2,4-TMB	1,2,4-trimethylbenzene
1,3,5-TMB	1,3,5-trimethylbenzene

Symbols

$\mathbf{x}$	droplet position
$\mathbf{v}$	droplet velocity
r	droplet radius
T_d	droplet temperature
t	time
y	parameter for droplet distortion
$\dot{y}$	droplet oscillation velocity
f	droplet distribution function with time/space progression
F_i	rate of change of droplet velocity
R	rate of change of droplet radius
$\dot{T}_d$	rate of change of droplet temperature
$\ddot{y}$	rate of change of droplet oscillation velocity
$\dot{f}_{coll}$	droplet collision source term
$\dot{f}_{bu}$	droplet breakup source term
r_p	parent droplet radius
r_c	child droplet radius
τ_{KH}	breakup timescale
B_{KH}	KH model constant
C_{KH}	KH model constant

Λ_{KH}	fastest growing wave wavelength
Ω_{KH}	fastest growing wave growth rate
σ	surface tension
ρ	density of droplet
Z	Ohnesorge number
T	Taylor number
We_g	gas Weber number
C_{RT}	RT model constant
Ω_{RT}	fastest growing wave growth rate
$|\mathbf{F}|$	travel direction acceleration
Λ_{RT}	wavelength
B_{RT}	size constant
ν	frequency of collision
1	"collector"
2	"droplet"
N_2^n	droplet number in one parcel
$\forall$	cell volume containing "droplets" and "collectors"
P_n	collision probability given by Poisson distribution for

one "collector" and n "droplets"

Δt	computational time step
b	collision impact parameter
θ_2	random number
$\dot{W}^s$	working rate of turbulent eddies on spray breakup source

term

Pr	Prandtl number
ρ	mass density
u	fluid velocity
D	Fick's Law coefficient of diffusion
δ	Dirac delta function
a	dimensionless number
p	pressure of fluid
$\boldsymbol{\sigma}$	stress tensor
F	momentum gain rate per unit volume
g	specific force on body, presumed constant
I	specific internal energy, without chemical input energy
J	heat flux
k	turbulent kinetic energy
ε	turbulent dissipation rate
Q	energy source term
m	mixture species
c	chemistry source term
s	spray source term
M	number of chemical species
X_m	arbitrary specie m
υ_{mi}	specie m's stoichiometric coefficient
$'$	forward
$''$	reverse
$\dot{\omega}_m$	rate of production if specie m
q_i	reaction i's variable for rate of process
$\left[X_m \right]$	specie m's molar concentration

k_{fi}	Reaction i's forward reaction rate constant
k_{ri}	Reaction i's reverse reaction rate constant
A_i	pre-exponential factor
β_i	temperature exponent
E_i	activation energy
τ	shock tube ignition delay time
U_b	exit velocity of fuel at the injector nozzle hole
P_f	common rail pressure
P_a	ambient pressure
ρ_f	density of fuel
$\dot{m}_f$	mass flow rate of fuel
C_d	coefficient of discharge
A_f	hole area of the injector nozzle
$\dfrac{dQ}{dt}$	AHRR
γ	specific heat ratio

This page was intentionally left blank.

List of Publications

Publications in peer reviewed journals during Ph.D. study:

1. **Tay, KL**; Yang, WM; Mohan, B; An, H; Zhou, DZ; Yu, WB; Development of a robust and compact kerosene-diesel reaction mechanism for diesel engines. Energy Conversion and Management 108 (2016): 446-458. [Link to this article]

2. **Tay, KL**; Yang, WM; Mohan, B; Zhou, DZ; Yu, WB; Zhao, FY; Development of a reduced kerosene-diesel reaction mechanism with embedded soot chemistry for diesel engines. Fuel 181 (2016): 926-934. [Link to this article]

3. **Tay, KL**; Yang, WM; Zhao, FY; Yu, WB; Mohan, B; Effects of triangular and ramp injection rate-shapes on the performance and emissions of a kerosene-diesel fueled direct injection compression ignition engine: A numerical study. Applied Thermal Engineering 110 (2017): 1401-1410. [Link to this article]

4. **Tay, KL**; Yang, WM; Zhao, FY; Yu, WB; Mohan, B; Numerical investigation on the combined effects of varying piston bowl geometries and ramp injection rate-shapes on the combustion characteristics of a kerosene-diesel fueled direct injection compression ignition engine. Energy Conversion and Management 136 (2017): 1-10. [Link to this article]

5. **Tay, KL**; Yang, WM; Zhao, FY; Yu, WB; Mohan, B; A numerical study on the effects of boot injection rate-shapes on the combustion and emissions of a kerosene-diesel fueled direct injection compression ignition engine. Fuel 203 (2017): 430-444. [Link to this article]

6. **Tay, KL**; Yang, WM; Li, J; Zhou, DZ; Yu, WB; Zhao, FY; Chou, SK;

Mohan, B; Numerical investigation on the combustion and emissions of a kerosene-diesel fueled compression ignition engine assisted by ammonia fumigation. Applied Energy (2017) Article in Press. [Link to this article]

Proceedings in peer reviewed conferences during Ph.D. study:

1. **Tay, KL**; Yang, WM; Chou, SK; Zhou, DZ; Li, J; Yu, WB; Zhao, FY; Mohan, B; Effects of injection timing and pilot fuel on the combustion of a kerosene-diesel/ammonia dual fuel engine: A numerical study. 8th International Conference on Applied Energy. October 8-11, 2016, Beijing, China.

****

Important Note:

Parts of this thesis have already been published in the aforementioned

journals.

****

Chapter 1 Introduction

1.1 Background and motivation

Kerosene has primarily been used for gas turbine engines [1, 2] as well as rocket engines [3, 4]. However, in recent times, kerosene has also found its use in direct injection compression ignition (DICI) engines [5, 6]. The use of kerosene in DICI engines is fundamentally due to the introduction of the Single Fuel Concept (SFC) [7-11] proposed by the North Atlantic Treaty Organization (NATO) military which includes the United States (US). This concept was proposed to eradicate the problem of fuel supply during both peacetime and wartime operations. In the past when aircraft, ground vehicles and equipment all used different fuels, it was logistically challenging to supply them with their respective fuels. Hence, with the introduction of SFC, logistical fuel supply challenges can be significantly reduced. Moreover, by supplying just one type of fuel to all military assets, it can help to enhance the operational readiness of the military [11].

Another driving factor behind the use of kerosene in DICI engines is fuel adulteration. In some parts of the world where there is corruption, the problem of adulterated diesel persists, where kerosene is illegally and unethically mixed with diesel for more profit [12-15]. Inevitably, the use of kerosene in diesel engines can result in undesired emissions [12, 13].

Presently, the use of DICI engines in the form of diesel engines is widespread for both military as well as civilian applications. This is because of the high thermal efficiency of the diesel engine as well as the huge amount of

torque it can produce relative to the gasoline engine [16]. However, the shortcoming of the diesel engine is the amount of soot, oxides of nitrogen (NO_x) and particulate matter (PM) emissions it produces [16]. These emissions are harmful to both human health [17-21] as well as the environment [22-27] and are undesirable. As a result, stringent emissions standards [28-31] were implemented over many years to regulate exhaust emissions from diesel engines. This can be seen from Figure 1-1 which shows the different Euro emissions standards for diesel engines [32].
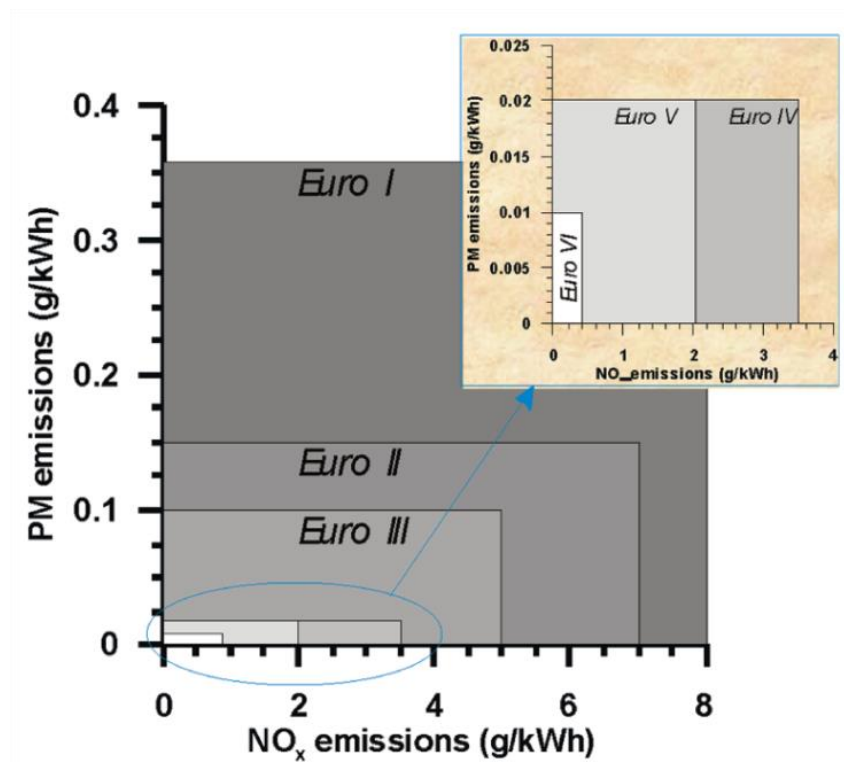
Figure 1-1 The different Euro emissions standards for diesel engines [32]. Reproduced from [32].

As conventional diesel engines are made specifically to use diesel fuel, the usage of any other alternative fuels with different fuel properties such as kerosene will have adverse effects on engine emissions [33]. Moreover, engine

performance [33] and longevity [34-36] will also be affected due to differences between the fuel properties of kerosene and diesel.

1.2 Research Gaps

To effectively and efficiently use a new alternative fuel such as kerosene in a diesel engine, huge amounts of research have to be spent studying the properties of the new fuel, its combustion characteristics as well as its emissions behavior under diesel engine conditions. Today, engine research is done using both experiments as well as simulations. Both simulations and experiments work hand-in-hand to give researchers a better and more complete understanding of the combustion process and emissions formation which are crucial in improving engine efficiency and lowering emissions. Currently, due to the advancement of computer technology, numerical simulations are widely used by engine researchers to gather more insights about engine combustion.

As kerosene is a relatively newer fuel to be used in diesel engines as compared to diesel and biodiesels, much experimental work [5, 6, 37] had already been carried out by the scientific community to study kerosene's combustion characteristics as well as emissions behavior in diesel engines. However, as seen from the literature review in Chapter 1, there is a severe lack of engine simulations for kerosene combustion in diesel engines. This is primarily due to the lack of compact and robust kerosene reaction mechanisms for 3-dimensional (3D) computational fluid dynamics (CFD) engine simulations. Nevertheless, it should be noted that engine simulations will give more insights about kerosene's combustion characteristics in diesel engines,

particularly for in-cylinder emissions evolutions and contours which are extremely difficult to acquire through engine experiments.

Furthermore, as soot emissions are detrimental to both human health [17-21] and the environment [22-27], it is essential to study the sooting behaviour of kerosene when it is used in diesel engines. Moreover, soot emissions from military diesel engines do compromise the stealth of military vehicles [38]. Due to the aforementioned reasons, it is extremely desirable to know kerosene's soot formation and oxidation behaviour during diesel engine combustion. As seen from Chapter 2, there is little study done using numerical simulations about the sooting behaviour of kerosene in diesel engines.

In addition, as kerosene was suggested by the scientific community to be an alternative fuel for diesel [7-11], it is highly desirable to study the combustion and emissions characteristics of kerosene and its blends with diesel, so as to gain more insights on the optimization of kerosene combustion in diesel engines. Furthermore, as vehicular NO_x and soot emissions are of great concern these days [32], it is necessary to find ways to mitigate them especially when kerosene is used as a new alternative in diesel engines.

1.3 Objectives

The research objectives stated here will directly address the research gaps highlighted in Section 1.2. They are as follows:

➢ To develop chemical reaction mechanisms for kerosene combustion in diesel engines. The kerosene reaction mechanisms must be small and compact, but yet reliable and robust enough to be used in diesel engine simulations.

➢ To incorporate soot formation and oxidation precursors and chemistry into the kerosene reaction mechanisms. This is to facilitate the study of kerosene's sooting behavior in diesel engine simulations.

➢ To systematically study the combustion characteristics as well as the emissions behavior of kerosene and its blends in diesel engines under various operating environments in order to know more of kerosene's advantages and limitations, so that new solutions can be discovered to minimize engine emissions. It can be seen from Chapter 2 that although the combustion of kerosene under high engine load produces more NO_x emissions as compared to diesel, using the appropriate injection rate-shape can mitigate this problem.

1.4 Thesis organization

This thesis is divided into several chapters. A short description of each chapter is given below:

✓ Chapter 1 gives the background and the motivation behind the research work carried out in this thesis. It also highlights the research gaps and the research objectives.

✓ Chapter 2 is a comprehensive literature review which covers kerosene's fuel properties, its autoignition characteristics, its spray and combustion in constant volume combustion chambers (CVCCs), its combustion and emissions behavior in optical and non-optical engines as well as its surrogates and reaction mechanisms developed to date. Available literature regarding the numerical simulation of kerosene combustion in diesel engines is also covered. Research gaps are highlighted here.

- ✓ Chapter 3 states the methodology used in this research work. It includes a comprehensive overview of the experimental engine testbed and the important models that are used in the KIVA4-CHEMKIN [39, 40] code.
- ✓ Chapter 4 shows the development of a reduced kerosene reaction mechanism with embedded soot chemistry for diesel engines, whereby soot is represented simply by gas phase C(S).
- ✓ Chapter 5 talks about the development of a robust and compact kerosene-diesel reaction mechanism for diesel engines. The kerosene reaction mechanism developed in this chapter is much smaller than the previously developed mechanism.
- ✓ Chapter 6 investigates the effects of injection rate-shapes and bowl geometries on the combustion characteristics and emissions formation of a kerosene-diesel fueled diesel engine. This chapter also highlights the potential of kerosene in reducing emissions when it is used with the appropriate injection strategy. It can be seen in this chapter that the enhanced kerosene-diesel reaction mechanism developed in Chapter 5 can be used in conjunction with a phenomenological soot model to study soot trends such as soot particle mass, size and number under different operating parameters.
- ✓ Chapter 7 concludes the work accomplished in this thesis and suggests recommendations for potential future research works to be done for more improvement of kerosene combustion in diesel engines.

Chapter 2 Literature review

2.1 Introduction

Figure 2-1 shows a typical quasi-steady conventional diesel spray combustion [41-43] and its effect on heat-release [16, 44], NO_x and soot emissions [42, 45-48]. The conventional diesel spray combustion schematic and the equivalence ratio-temperature (φ-T) map are primarily taken from the original works of Dec [41] and Kamimoto and Bae [45] respectively.
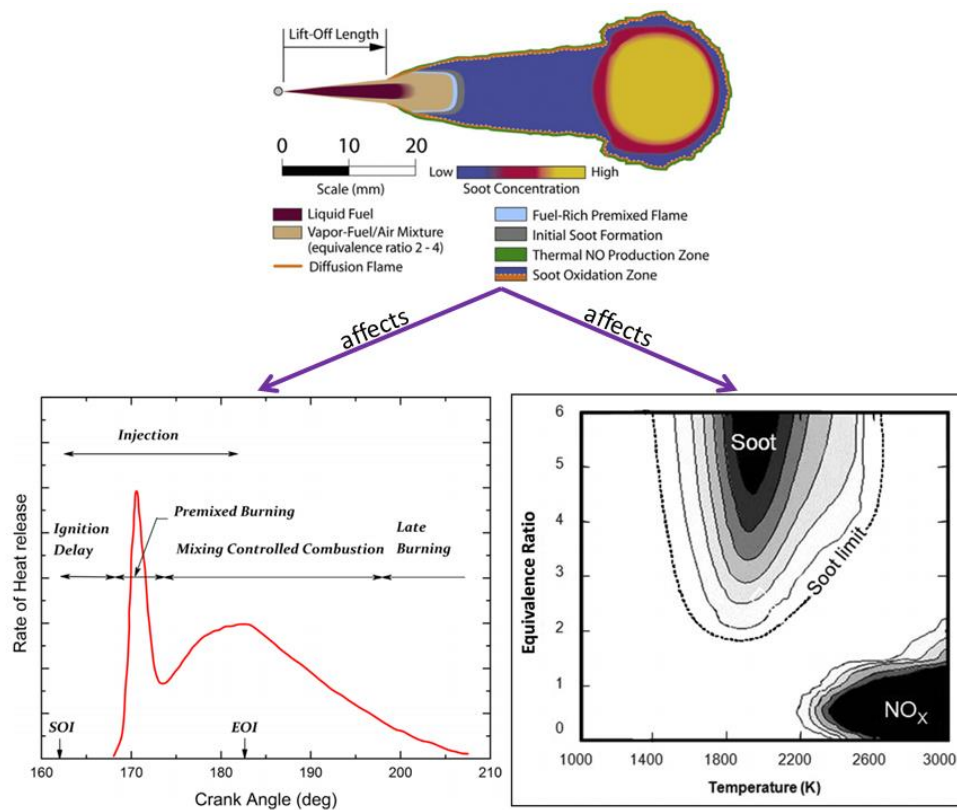
Figure 2-1 A typical quasi-steady conventional diesel spray combustion [41-43] and its effect on heat-release [16, 44], NO_x and soot emissions [42, 45-48]. The conventional diesel spray combustion schematic and the equivalence ratio-temperature (φ-T) map are primarily taken from the original works of Dec [41] and Kamimoto and Bae [45] respectively. Reproduced from [43, 44, 47].

The aforementioned proposed diesel spray combustion concept and φ-T map are well established in the engine community [49]. For the ease of

understanding subsequent sections in this work, the conventional diesel spray combustion process [16, 41-43] will be highlighted here. Concisely, high pressure diesel fuel from the common rail is injected into the combustion chamber through either a solenoid or piezoelectric injector [50, 51] when the piston is near top dead center (TDC). The liquid fuel then enters into the combustion chamber at a high velocity and spreads out in a conical shape as it experiences breakup and atomization due to turbulence, aerodynamic drag and instabilities. Due to the aerodynamic drag as a result of high ambient density, the fuel jet experiences a decrease in velocity once it exits the nozzle. It should be noted that the spreading angle of a spray is also known as the cone angle. Consequently, as the liquid fuel jet travels downstream, hot air entrainment of the fuel takes place. At a certain point further downstream, fuel droplets absorb sufficient heat energy from the surroundings and they vaporize. The vaporized fuel then mixes with the hot ambient air to form a combustible fuel-air premixed charge. The distance from the nozzle to the liquid tip of the fuel jet just before vaporization is known as the liquid penetration while the distance from the nozzle to the vapor tip is called the vapor penetration. The time delay from the start of injection (SOI) to just before the start of combustion (SOC) is known as the ignition delay period. Following which, the premixed charge at the tip of the still-developing spray undergoes autoignition due to the high ambient temperature. This is known as premixed combustion which occurs at about $\varphi=4$ [42, 43] and it happens via a two-stage ignition, with the second stage combustion being highly exothermic which results in an initial rapid heat-release rate. Due to the locally high equivalence ratios near the axial location of the jet, polyaromatic hydrocarbon (PAH) and soot

formation occurs near the jet axis. Subsequently, as more fuel is being injected after SOC, diffusion combustion occurs. This phase is also known as the mixing-controlled combustion phase whereby the combustion process is very much dependent on the fuel spray. NO_x is seen to be formed radially away from the spray axis, near the spray periphery, where $\varphi=1$ [42, 43] as combustion proceeds towards completion. It is interesting to note that the diffusion flame is seen to be located at a distance away from the nozzle and this distance is termed as the flame lift-off length (FLOL) [43]. FLOL is affected by factors such as ambient density, oxygen concentration, temperature, nozzle diameter, injection pressure as well as fuel composition [43]. The final phase of combustion is known as the late combustion phase whereby residual hydrocarbons burnout. From the φ-T map in Figure 2-1, in-cylinder local equivalence ratios and temperatures should be kept below 2 and 2200K respectively in order to avoid both the soot and NO_x peninsulas [45, 47].

From the previous paragraph, it can be seen that fuel spray considerably influences the combustion process and emissions formation in a DICI engine. Therefore, any changes in fuel properties will affect the spray, atomization, evaporation, mixing, autoignition and combustion in an engine [16]. As a result, in order for kerosene to be more effectively and efficiently used in diesel engines with lower emissions, it is needful to know the progress made thus far in this area of research so that research gaps can be identified for further improvement. Moreover, this chapter not only serves to identify the research gaps, it also gives a proper understanding of kerosene's autoignition and combustion characteristics together with its emissions formation

behaviour under various diesel engine operating conditions. Having a good understanding of kerosene's combustion and emissions behaviour will aid in the explanation of some simulation results in this thesis. It should be noted that the scope of this review work will only be limited to the conventional kerosene distillate.

Therefore, in this chapter, a comprehensive review will be carried out systematically to better understand the characteristics and behaviour of kerosene in a DICI environment as well as to identify the research gaps. The subsequent sections of this review work are listed as follows:

(a) Fuel properties of kerosene.

(b) Fundamental autoignition studies of kerosene in shock tube, rapid compression machine (RCM), fuel ignition tester (FIT), ignition quality tester (IQT), constant volume combustion chamber (CVCC) and engine.

(c) Experimental studies of kerosene spray and combustion in CVCCs.

(d) Experimental investigations of kerosene combustion and emissions in DICI engines.

(e) Development of kerosene surrogates, their chemical reaction mechanisms and the modelling of kerosene combustion in DICI engines.

(f) Research gaps to be addressed in this thesis.

2.2 Kerosene fuel properties

The three most common conventional kerosene distillate fuels are Jet-A, Jet A-1 and JP-8 [52]. Jet A and Jet A-1 are used in civilian aircrafts, with Jet A being used only in the US while Jet A-1 is used throughout the rest of the

world [7]. The freezing point of Jet A is at -40 ℃ while that of Jet A-1 is at -47 ℃ [7]. On the other hand, JP-8 is the military version of Jet A-1 and is used in military aircrafts of the NATO and the US [7]. JP-8 is essentially Jet A-1 with additional additives for anti-icing, anti-corrosion and anti-static purposes [7]. It can be observed from [52] that Jet-A, Jet A-1 and JP-8 are almost identical in terms of their physical properties such as density, viscosity, surface tension and vapour pressure. Moreover, it should be noted that Jet-A, Jet A-1 and JP-8 are chemically very similar except for the additives that are used in them [53].

Table 2-1 Kerosene and diesel fuel properties [49, 54-60].

Fuel property	Kerosene (Jet-A/JP-8/Jet A-1)	Diesel (D2)
Density @ 15 ℃ (kg/m^3)	806	843
Kinematic viscosity @ 40 ℃ (mm^2/s)	~1.4	2.35
Surface tension (dyn/cm)	27.7	29.8
Boiling point @ T_{10} (℃)	180	211
Boiling point @ T_{90} (℃)	251	315
Boiling point @ T_{100} (℃)	274	350
Cetane number (CN)	46	51
Autoignition temperature (℃)	210	235
Flash point (℃)	51	73
Lower heating value (LHV; MJ/kg)	43.2	42.975
Aromatic content (by volume fraction)	0.19	0.27
Threshold sooting index (TSI)	21.4	~28

Table 2-1 shows the fuel properties of kerosene and diesel [49, 54-60]. It is observed that kerosene has got lower viscosity, density, Cetane number (CN), aromatic content and threshold sooting index (TSI) as compared to diesel. On the other hand, the volatility of kerosene is higher than diesel and this can be inferred from the range of boiling point temperatures [61] for kerosene and diesel. This can also be seen from Figure 2-2 which shows the distillation curves of JP-8 and diesel [5].
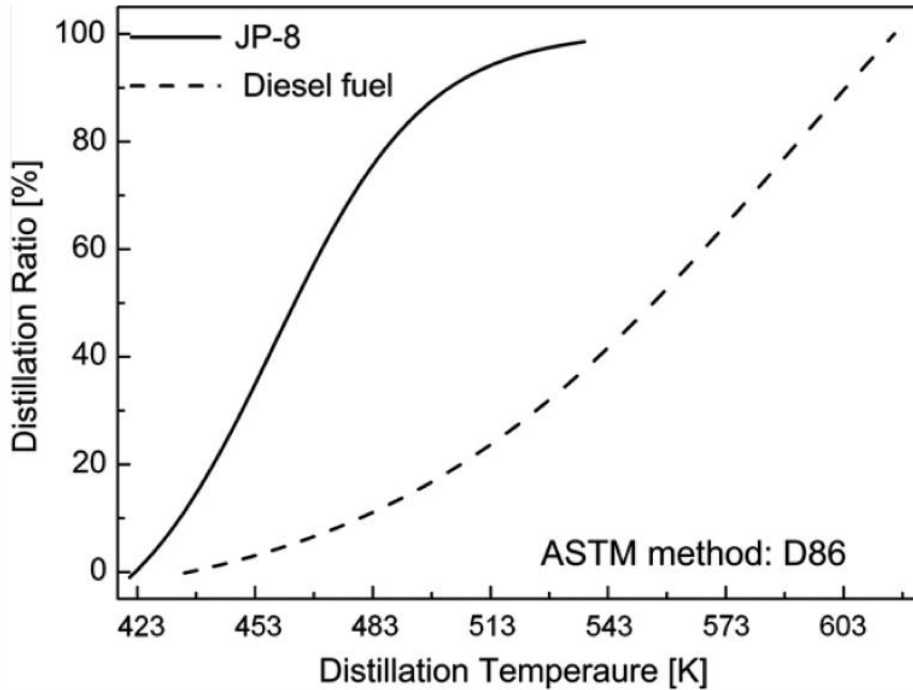
Figure 2-2 The distillation curves of JP-8 and diesel [5]. Reproduced from [5].

A fuel that has a lower viscosity is able to undergo atomization more easily as compared to a higher viscosity fuel [62, 63]. In addition, the density of a fuel directly affects fuel volatility as a lower density fuel will contain smaller molecules that can vaporize more easily which results in its higher volatility [64]. Consequently, a low density, low viscosity and high volatility fuel contributes to better fuel atomization and fuel-air mixing in a conventional diesel engine which is beneficial for a more complete combustion. Furthermore, a fuel with a lower aromatic content, and hence a lower TSI value, will give lower soot emissions during combustion as PAH plays a crucial role in the formation of soot [57, 65, 66]. Another important property is the CN of a fuel, which is a measure of fuel ignition quality [49]. A lower CN fuel will give a longer ignition delay period [16]. Despite the many differences between kerosene and diesel, their lower heating values (LHVs) are rather similar. Finally, it is interesting to note that kerosene has a lower lubricity as

12

compared to diesel which contributes to the greater wear of the fuel injection system when kerosene is used [35, 36]. This shortcoming, however, can be circumvented by the addition of lubricity additives such as esters [67, 68].

A comprehensive knowledge of the differences between kerosene's and diesel's fuel properties is important for understanding the combustion process and emissions formation in a kerosene fueled diesel engine. Beyond that, a good understanding of kerosene fuel properties will help in the development of suitable kerosene surrogates for DICI engine applications [69]. The effects of kerosene fuel properties on combustion and emissions under diesel-like operating conditions and in actual diesel engines will be further discussed in the following sections.

2.3 Fundamental autoignition studies of kerosene

A deep understanding of the autoignition characteristics of kerosene is important [70] for the successful and efficient usage of kerosene in DICI engines. This is because the combustion process and emissions formation that occur in a conventional diesel engine are very much affected by the autoignition characteristics of a fuel [16]. As discussed previously, the CN of a fuel dictates the period of ignition delay after fuel injection [16]. The larger the CN, the shorter will be the period of ignition delay. It should be noted that the overall ignition delay period comprises of the physical and the chemical delays [16, 71]. The physical properties of a fuel such as the viscosity, volatility and density will affect the spray breakup, atomization, evaporation and fuel-air mixing in a DICI engine. Hence, as fuel is directly injected into the combustion chamber for the case of a DICI engine, the physical fuel

properties will affect the physical delay [16, 71] unlike a traditional gasoline engine whereby fuel is already premixed with air before it enters the combustion chamber. On the other hand, the chemical delay is very much affected by the fuel structure and composition [71, 72].

In addition to having a better understanding of kerosene's autoignition characteristics, data gathered from autoignition studies is crucial in aiding the development of kerosene surrogates and their reaction mechanisms [73, 74]. Autoignition studies from literature [53, 61, 70-89] mainly investigate the ignition delay times of kerosene using different equipment such as shock tube, rapid compression machine (RCM), fuel ignition tester (FIT), ignition quality tester (IQT), constant volume combustion chamber (CVCC) and even single- and multi-cylinder engines. Of all the aforementioned equipment, the shock tube and RCM are meant to test only the chemical ignition delay as the investigated fuel is fully vaporized prior to ignition. On the contrary, the IQT, FIT, CVCC and engine take into consideration both the chemical as well as the physical delays because fuel spray is involved. Table 2-2 shows a compilation of the different kerosene autoignition studies [53, 61, 70-89] carried out under different conditions with varying temperatures (T), pressures (P), equivalence ratios (φ), ambient densities and levels of oxidizer. From [53, 61, 70-89], it can be seen that all of the studies investigated the autoignition characteristics of Jet-A, Jet A-1 and JP-8 except for one study done by Zhang et al. [73] which focused on RP-3. From their study, RP-3, which is the Chinese equivalent of Jet-A, was observed to have very similar ignition delay times as Jet-A when tested in a shock tube [73].

Table 2-2 Compilation of the different kerosene autoignition studies [53, 61, 70-89] carried out under different conditions with varying temperatures (T), pressures (P), equivalence ratios (φ), ambient densities and levels of oxidizer.

Reference	Eqmt.	Fuel(s)	P (atm)	T (K)	E.R., φ	Oxidizer	Ambient Density (kg/m^3)
Dean et al. [75]	ST	Jet-A	8.5 $\pm$ 1	1000-1700	0.5, 1, 2	Air (21% O_2)	-
Vasu et al. [76]	ST	Jet-A, JP-8	17-51	715-1229	0.5, 1	Air (10%, 21% O_2)	-
Dooley et al. [77]	ST	Jet-A	16.3-24.8	674-1222	1	Air (21% O_2)	-
Balagurunathan [78]	ST	JP-8	14.87-17.94	1021.2-1546.6	0.5, 1, 3	7% O_2, 93% Ar	-
Wang and Oehlschlaeger [53]	ST	Jet-A, Jet-A with JP-8 additives	8, 11, 20, 39	662-1381	0.25, 0.5, 1, 1.5	Air (21% O_2)	-
Mzé-Ahmed et al. [79]	ST	Jet A-1	16	909-1429	0.5, 1	Air (20% O_2) diluted in extra N_2	-
Zhukov et al. [80]	ST	Jet-A	10, 20	1040-1380	0.5, 1, 2	Air (21% O_2)	-
Zhang et al. [73]	ST	RP-3	1-20	650-1500	0.2, 1, 2	Air (21% O_2)	-
Zhu et al. [74]	ST	JP-8	2.07-6.37	1103-1341	0.48-1.42	Air (21% O_2)	-
Valco et al. [72]	ST	JP-8	17-23	667-1111	1	Air (21% O_2)	-
De Toni et al. [81]	ST	Jet A-1	15, 30	714-1250	0.3, 1	Air (21% O_2)	-
Davidson et al. [82]	ST	Jet-A, JP-8	9.51-53.8	1008-1411	0.37-2.14	Air (21% O_2), 4% O_2 with Ar, 21% O_2 with Ar	-
Kumar and Sung [83]	RCM	Jet-A, JP-8	7, 15, 30	650-1100	0.42-2.26	Air (10%, 21%, 32% O_2), including 50% Ar for some cases	-
Dooley et al. [77]	RCM	Jet-A	22.3	653.3-709.6	1	Air (21% O_2)	-
Hui et al. [70]	RCM	Jet-A	22	642, 654, 661	1.13	Air (21% O_2)	-
Allen et al. [84]	RCM	JP-8	7, 10	670-750	-	Oxidizer-to-fuel mass ratio =	-

	Eqmt.	Fuel	P	T	E.R.	Oxidizer	
							14.6, 48.6
Allen et al. [85]	RCM	JP-8	5, 10, 20	625-730	0.25, 0.5, 1	Air (21% O_2)	-
Valco et al. [72]	RCM	JP-8 and its blends with alternative jet fuels	20	625-714	0.25, 0.5, 1	Air (21% O_2)	-
De Toni et al. [81]	RCM	Jet A-1	7, 15	645-909	0.3, 0.7, 1, 1.3	Air (21% O_2)	-
Hui et al. [70]	FIT	Jet-A and its blends with alternative jet fuels	22	850	-	Air (21% O_2)	-
Pickett and Hoogterp [86]	CVCC	JP-8	-	750-1250	-	Air (21% O_2)	7.27, 14.8, 30
Kang et al. [71]	CVCC	Jet-A	20	813-913	-	Air (21% O_2) with varying EGR from 0-55%	-
Zheng et al. [87]	IQT	JP-8	21.37	778-848	-	Air (21% O_2)	-
Shrestha et al. [61]	IQT	JP-8	21.37	808, 858, 878 @ skin	-	Air (21% O_2)	-
Schihl and Hoogterp-Decker [88]	SCE, MCE	JP-8	-	850-1200	-	Air (21% O_2)	18, 24, 30
Rothamer and Murphy [89]	SCE	Jet-A and its blends with alternative jet fuels	40-125	900-1100	-	Air (21% O_2)	15-40

Eqmt.: Equipment	P: Pressure	T: Temperature	E.R.: Equivalence Ratio	ST: Shock Tube
Skin: Refers to the skin temperature of the combustion chamber	RCM: Rapid Compression Machine	CVCC: Constant Volume Combustion Chamber	FIT: Fuel Ignition Tester	RP-3: Chinese equivalent of Jet-A
IQT: Ignition Quality Tester	SCE: Single Cylinder Engine	MCE: Multi-Cylinder Engine	EGR: Exhaust Gas Recirculation	

Shock tube experiments were done by Dean et al. [75], Vasu et al. [76], Dooley et al. [77], Balagurunathan [78], Wang and Oehlschlaeger [53], Mzé-Ahmed et al. [79], Zhukov et al. [80], Zhang et al. [73], Zhu et al. [74], Valco et al. [72], De Toni et al. [81] and Davidson et al. [82] under a wide range of conditions as seen from Table 2-2. For the sake of completeness, Figure 2-3a shows a typical shock tube experimental setup [80]. From the work of Wang and Oehlschlaeger [53], as seen from Figure 2-3b, they compared the experimental shock tube ignition delay times of Jet-A and Jet-A with JP-8 additives.
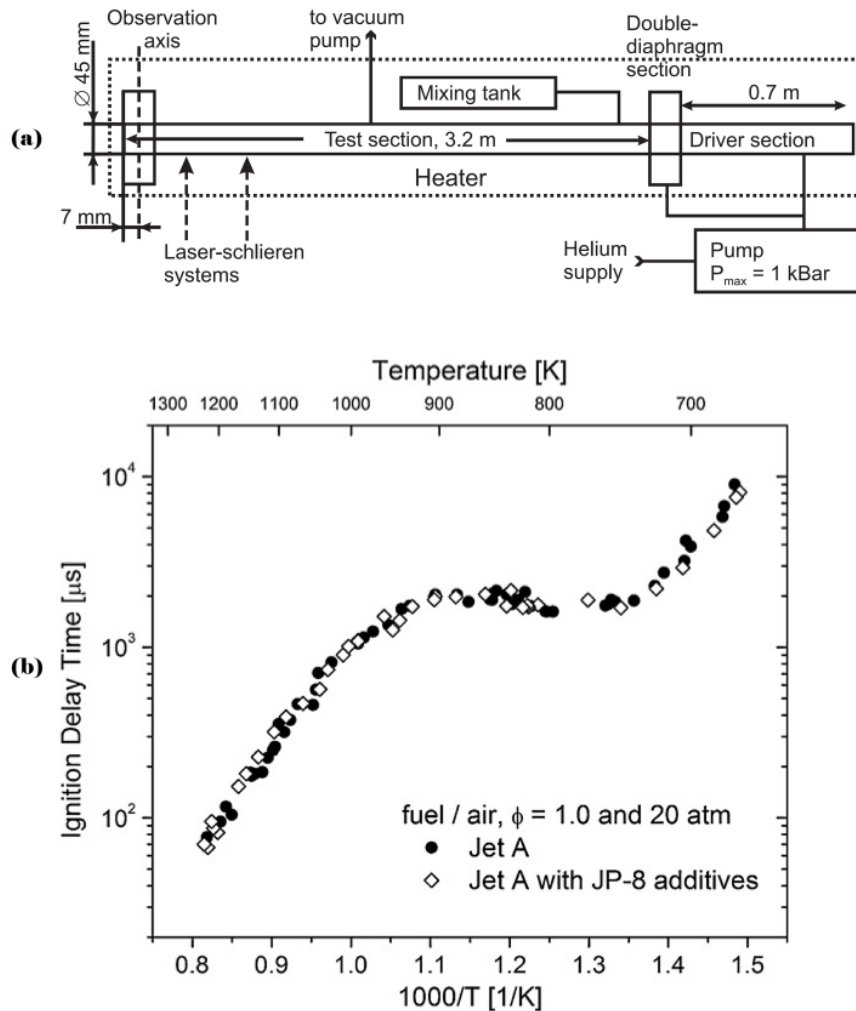
Figure 2-3 (a) A typical shock tube experimental setup [80] and (b) comparison of experimental shock tube ignition delay times of Jet-A and Jet-A with JP-8 additives [53]. Reproduced from [53, 80].

17

JP-8 additives were seen to have negligible effect on the ignition delay times of Jet-A. The slight differences between their ignition delay times were likely due to variations in their fuel compositions. Consequently, they concluded that the effects of JP-8 additives on autoignition could be ignored when developing kerosene surrogates and their reaction mechanisms. In addition, Vasu et al. [76] established $\tau \propto 1/P$ to be valid for pressures of 20-50 atm and temperatures of 950-1250K from shock tube experiments, where τ is the ignition delay time and P is the initial pressure. This equation is important for pressure scaling the ignition delay times of kerosene. Not surprisingly, other researchers such as Kim et al. [90] and Rothamer and Murphy [89] used it to scale shock tube and RCM data for the ease of comparison. However, Schihl and Hoogterp-Decker [88] cautioned that $\tau \propto 1/P$ cannot be used for pressure scaling ignition delay times that are derived from spray combustion experiments, including those from engine experiments, as both physical and chemical ignition delays are involved. Interestingly, Balagurunathan [78] and Davidson et al. [82] discovered from their shock tube experiments that under high temperature conditions, the ignition delay times of the tested kerosene fuels were shorter with leaner mixtures and longer with richer mixtures, which were contrary to those of lower temperature conditions. Moreover, Davidson et al. [82] found that changes in equivalence ratio had little effect on kerosene ignition delay under high temperature conditions. Furthermore, it can be seen that RP-3 [73], Jet-A [53], Jet A-1 [81] and JP-8 [76, 83] have three distinct ignition delay regions which can be classified into the low (T<750K), negative temperature

coefficient (NTC) (750K≤T≤900K) and high (T>900K) temperature regions [53].

On the other hand, RCM experiments were carried out by Kumar and Sung [83], Dooley et al. [77], Hui et al. [70], Allen et al. [84, 85], Valco et al. [72] and De Toni et al. [81] under a wide range of conditions as seen from Table 2-2. From the RCM experiments, kerosene was seen to exhibit a two-stage ignition behavior, first with a low temperature heat-release and then followed by a high temperature heat-release [70, 81, 83, 84]. Interestingly, from the work of De Toni et al. [81] in a RCM, the first and second stage ignition delay times of kerosene were very similar when initial temperatures were below 700K. Moreover, Kumar and Sung [83] found from RCM experiments that the first stage ignition delay times of kerosene were very much affected by temperature changes but variations in equivalence ratio had minimal effect. Furthermore, they highlighted that low compression pressures resulted in a more distinct ignition delay NTC region. Also, it can be observed from literature that fuel composition significantly affects the chemical ignition delay of kerosene [70, 72]. Straight hydrocarbon chains have higher reactivity as compared to branched and cyclic hydrocarbons including aromatics.

IQT, FIT, CVCC and engine experiments [61, 70, 71, 86-89] complement the shock tube and RCM experiments as the effects of kerosene's physical properties on autoignition are taken into consideration. It should be noted that the IQT and FIT experiments were done in accordance to ASTM D6890 and ASTM D7170 standards respectively [61, 70, 87, 91]. From the IQT and FIT experiments, the derived Cetane number (DCN) of kerosene can be established. Also, CVCC experiments done by Pickett and Hoogterp [86] of

Sandia National Laboratory (SNL) showed that JP-8 kerosene exhibited a longer ignition delay than diesel under different ambient densities and temperatures due to the lower CN of kerosene as shown in Table 2-1. Furthermore, Kang et al. [71] found from CVCC experiments that exhaust gas recirculation (EGR) significantly affected the chemical ignition delay of kerosene but effects on the physical delay was negligible. Interestingly, from engine experiments, Rothamer and Murphy [89] discovered that the ignition delay times of kerosene was dominated by its chemical delay at lower temperatures (800K≤T≤1000K) and its physical delay at higher temperatures (T>1000K).

2.4 Experimental studies of kerosene spray and combustion in CVCCs

The study of kerosene spray and combustion in a CVCC will enable researchers to have a deeper understanding of the effects of kerosene fuel properties on spray characteristics and combustion behavior. As a CVCC eliminates much of the engine parameters that can affect the spray and combustion process, such as swirl, intake and exhaust valve opening and closing timing, piston bowl geometry and injection timing [16], one can have a more in-depth look into the effects of fuel thermo-physical properties on spray and combustion. There were various research groups that had done significant work on the constant volume spray and combustion of kerosene. The pioneering work was done by the group from SNL which consisted of Pickett and Hoogterp [86] as well as Kook and Pickett [54, 92, 93]. Following their lead, others that had contributed to this area were Lee and Bae [5], Park et al. [58], Jing et al. [94], Yu et al. [95, 96], Kang et al. [71] and Song et al. [97].
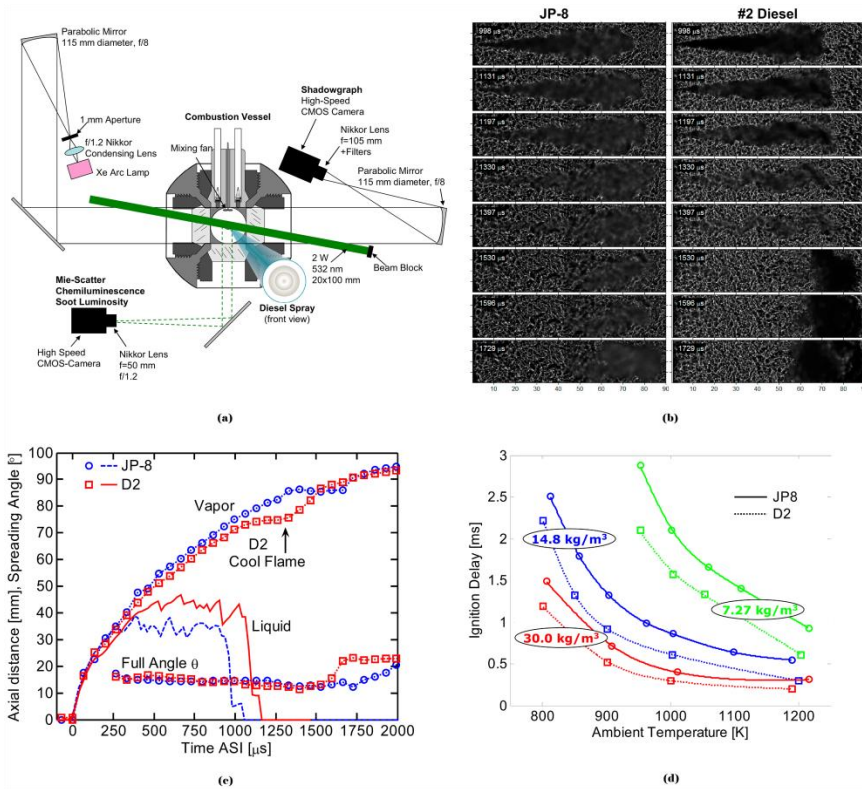
Figure 2-4 (a) A schematic of SNL's CVCC [86], (b) the comparisons of the shadowgraph images of JP-8 and diesel sprays [86], (c) the liquid and vapor penetrations together with the spreading angles of JP-8 and diesel sprays in a reacting environment [86] and (d) the ignition delay plots of JP-8 and diesel under different ambient densities and temperatures [86]. Reproduced from [86].

Figure 2-4 shows (a) a schematic of SNL's CVCC [86], (b) the comparisons of the shadowgraph images of JP-8 and diesel sprays [86], (c) the liquid and vapor penetrations together with the spreading angles of JP-8 and diesel sprays in a reacting environment [86] and (d) the ignition delay plots of JP-8 and diesel under different ambient densities and temperatures [86]. Briefly, the CVCC of SNL [54, 86, 92] is a cubic fixed-volume spray combustion chamber. This chamber is designed to withstand high ambient temperatures and pressures, and so it is capable of mimicking the extreme in-cylinder conditions in a typical DICI engine. Also, it is equipped with a high pressure diesel injector that is able to inject fuel into the chamber at various injection pressures. Moreover, the chamber is made optically

accessible by the use of Sapphire glass. This feature is important in the design of the chamber as it allows optical sensors to monitor the entire spray and combustion process. Shadowgraph, chemiluminescence, Mie-scattering, soot luminosity, planar laser-induced incandescence (PLII) and Schlieren imaging are some ways used to investigate the entire spray and combustion process. From Figure 2-4c, it was observed that the cool-flame of JP-8 occurred later than that of diesel [86]. This was not surprising as JP-8 has a lower CN than diesel. Consequently, from Figure 2-4d, the main ignition of JP-8 was also seen to be retarded when compared to that of diesel under different ambient conditions [86]. Notably, from the work of Kang et al. [71] that was done in a CVCC, it was observed for Jet-A that there was less low temperature heat-release and more high temperature heat-release with increasing ambient temperatures.
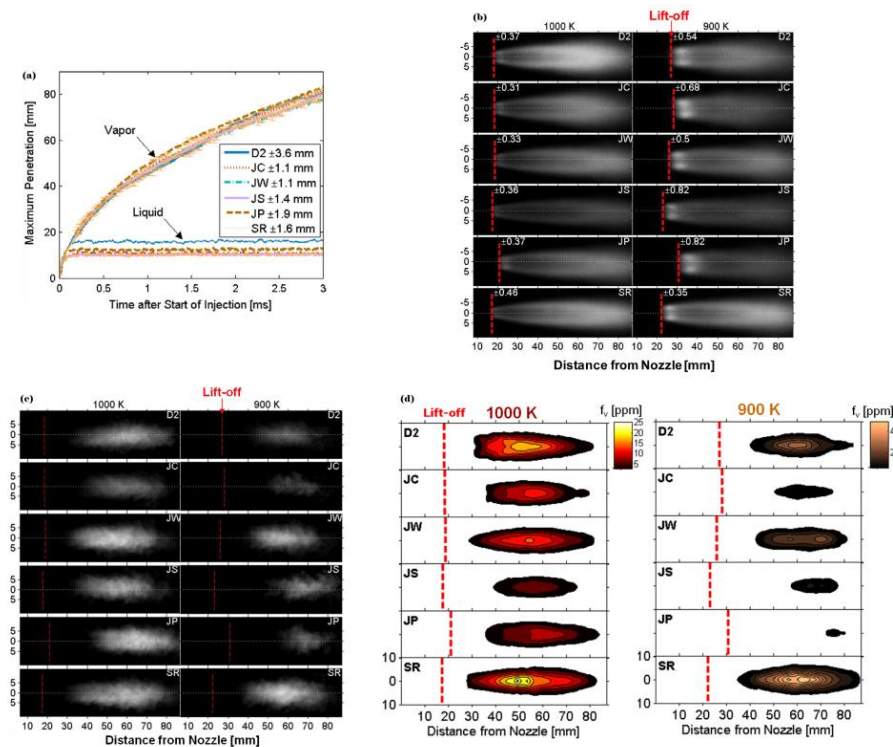
Figure 2-5 (a) The liquid and vapor penetrations in a non-reacting environment [54] and (b) the OH chemiluminescence [93], (c) soot PLII [93] and (d) soot volume fraction [93] images in a reacting environment. Reproduced from [54, 93].

22

Figure 2-5 shows (a) the liquid and vapor penetrations in a non-reacting environment [54] and (b) the OH chemiluminescence [93], (c) soot PLII [93] and (d) soot volume fraction [93] images in a reacting environment. The fuels investigated were Jet-A (JW), JP-8 (JC), diesel (D2), Fischer-Tropsch (JS), kerosene surrogate (SR) and coal-derived (JP) fuels [54, 93]. It was seen from the work of Kook and Pickett [93] that fuels which has a lower CN not only had a longer ignition delay but also a longer FLOL. It should be noted that FLOL generally increases with a decrease in CN. Moreover, it was observed from Figure 2-5b, c and d that the FLOL and the first-soot length both affect soot formation and oxidation [93]. With a longer FLOL, entrainment of air in the fuel spray increases before combustion begins and this reduces the fuel-air equivalence ratio [93]. As a result, there will be less soot volume fraction. Furthermore, with a longer first-soot length, soot volume fraction was also seen to decrease [93]. Interestingly, a greater difference between FLOL and first-soot length resulted in decreased soot emissions [93]. In addition, soot emissions resulting from spray combustion did not solely depend on FLOL and first-soot length but also depended vitally on fuel composition. It was seen that fuels containing more aromatics had a higher sooting tendency [92, 93]. As Jet-A and JP-8 kerosene had less aromatics as compared to diesel, their soot volume fraction were consequently lesser than diesel [93]. This trend can also be seen from [65, 66]. Moreover, it was observed that the soot structure of higher sooting fuels was agglomerated and clustered together while that of lower sooting fuels were chain-like [65, 66].
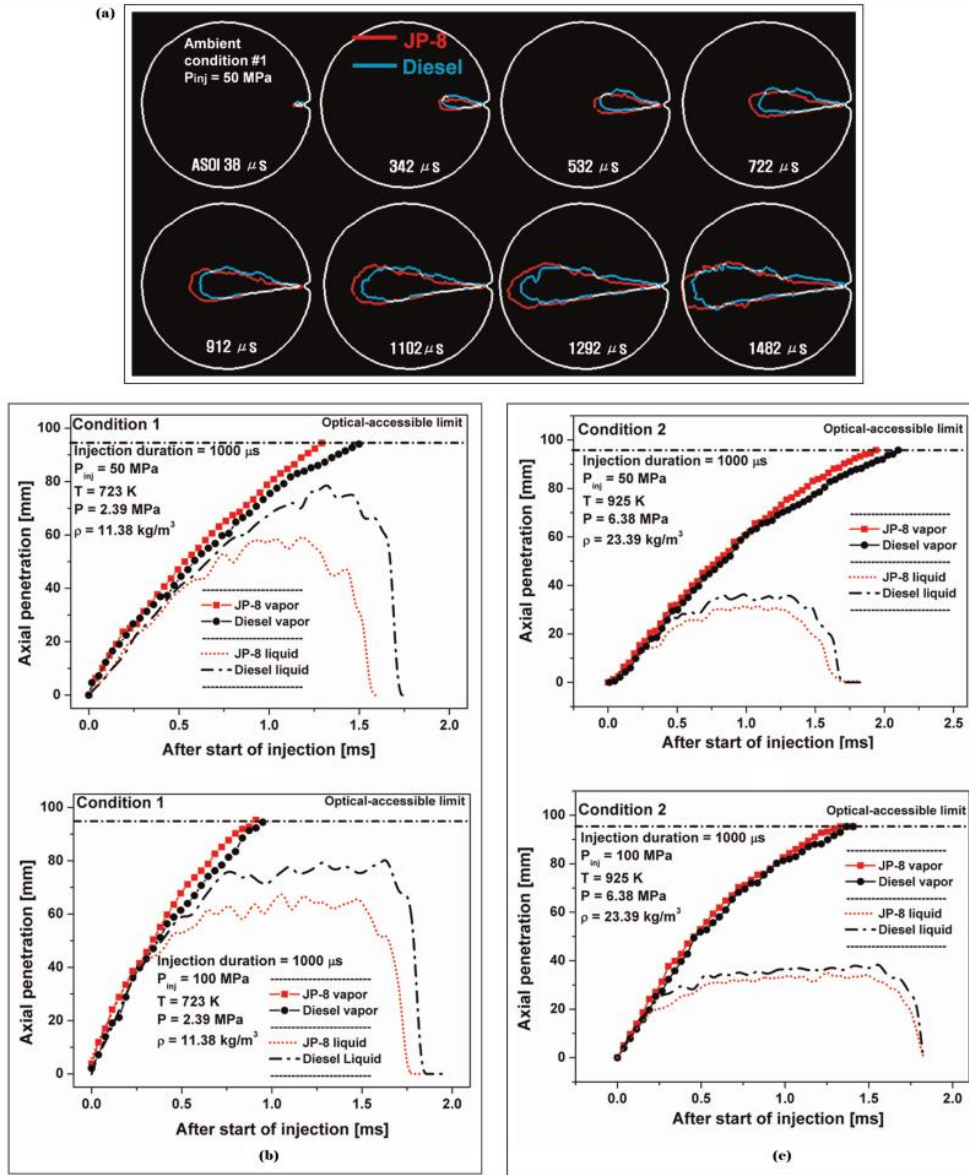
Figure 2-6 This figure shows the non-reacting vaporizing sprays of kerosene and diesel under different ambient conditions and injection pressures [58]. Figure 2-6a shows the sprays of kerosene and diesel at an ambient condition of 723K and 11.38 kg/m^3 and an injection pressure of 50MPa [58]. Figure 2-6b and c show the vapor and liquid penetrations at different ambient conditions of 723K/11.38 kg/m^3 and 925K/23.39 kg/m^3 respectively, with two different injection pressures [58]. Reproduced from [58].

Figure 2-6 shows the non-reacting vaporizing sprays of kerosene and diesel under different ambient conditions and injection pressures [58]. Figure 2-6a shows the sprays of kerosene and diesel at an ambient condition of 723K and 11.38 kg/m^3 and an injection pressure of 50MPa [58]. On the other hand,

Figure 2-6b and c show the vapor and liquid penetrations at different ambient conditions of 723K/11.38 kg/m^3 and 925K/23.39 kg/m^3 respectively, with two different injection pressures [58]. From Figure 2-6, Figure 2-4c and Figure 2-5a, it can be observed that kerosene and diesel sprays are generally quite similar except for some minor differences [54, 58, 86]. Due to kerosene's lower density and higher volatility as compared to diesel, kerosene's liquid penetration was seen to be shorter than diesel [58, 86]. However, this difference was less obvious when the ambient density was higher as spray behavior became dominated by ambient condition [58]. On the contrary, the vapor penetrations of both kerosene and diesel were almost identical, especially under conditions of high ambient density [54, 58, 86]. Furthermore, there was no known effect of fuel density and volatility on vapor penetration [54]. This implied that under high temperature vaporizing conditions, air entrainment of kerosene and diesel sprays were very similar [86]. From other kerosene spray experiments [5, 95, 96] conducted under non-vaporizing and non-reacting conditions, kerosene was seen to give a shorter spray penetration as compared to diesel. This was attributed to the lower viscosity of kerosene which contributed to better spray breakup to form smaller droplets with lower momentum that resulted in a shorter penetration. Furthermore, wider spray angles were also observed for kerosene sprays [5, 95, 96]. Interestingly, at higher injection pressures, the difference in kerosene's and diesel's spray angles became insignificant as injection pressure dominated the spray behavior [5].

(a) Spray penetration

(b) Spray velocity

(c) Spray angle

(d) Spray evolution (ASOI: 0.55ms)
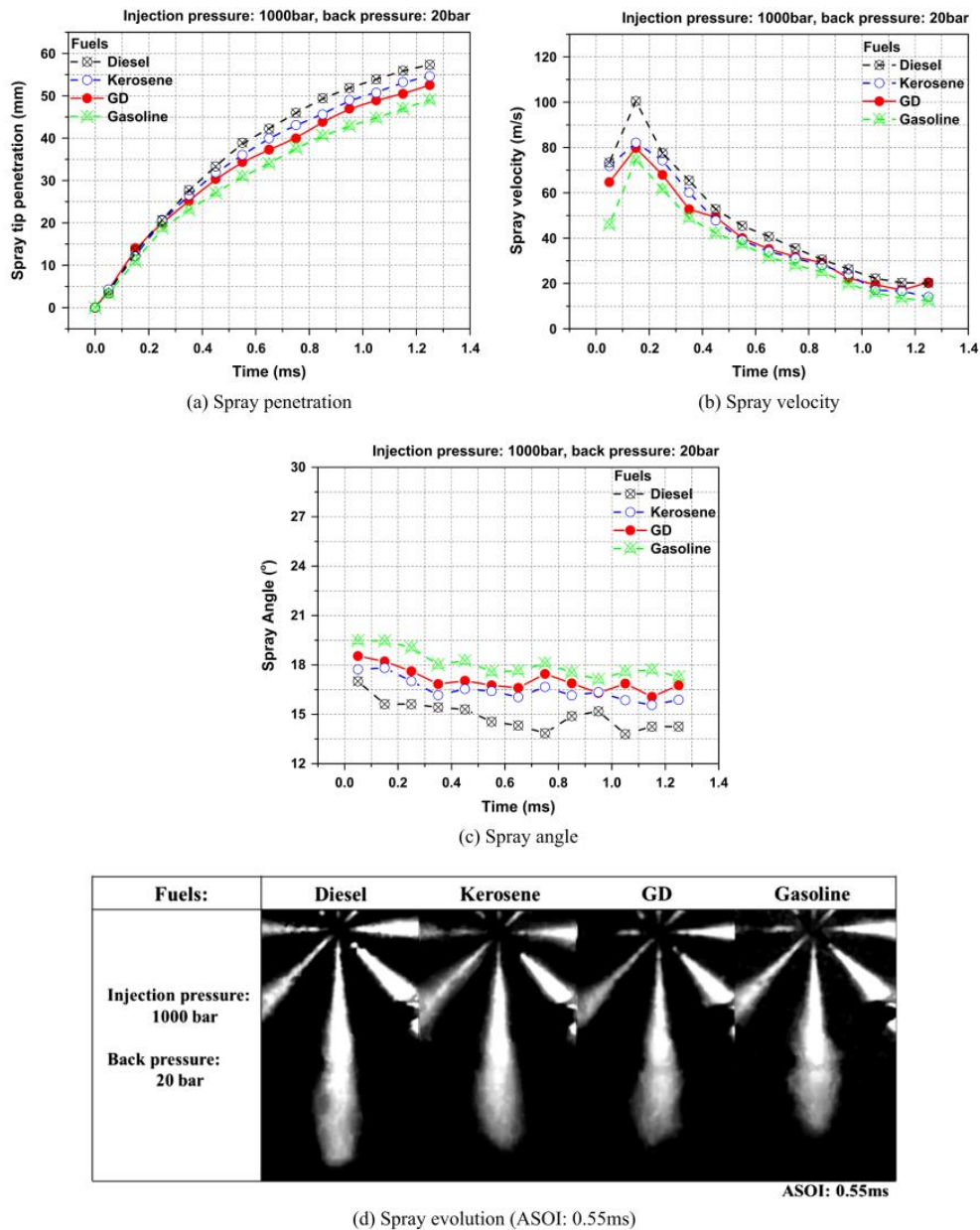
Figure 2-7 Comparisons between kerosene's, diesel's, gasoline's and gasoline/diesel blend's (a) spray penetrations, (b) spray velocities and (c) spray angles [96]. (d) The spray images of the four fuels [96]. Reproduced from [96].

Figure 2-7 shows the comparisons between kerosene's, diesel's, gasoline's and gasoline/diesel blend's (a) spray penetrations, (b) spray velocities and (c) spray angles [96]. In addition, Figure 2-7d shows the spray images of the four fuels [96]. From Figure 2-7, it was observed that kerosene which has a lower viscosity than diesel underwent atomization more easily. As a result, kerosene spray experienced a lower velocity and penetration, but had a wider spray

26

angle, as compared to those of diesel due to smaller droplet sizes that contributed to a lower spray momentum and increased spray resistance [96]. Similar spray behaviors were seen from the work of Song et al. [97] when they mixed lower viscosity, lower density and higher volatility ethanol with JP-8 in their spray experiments.

2.5 Experimental investigations of kerosene combustion and emissions in DICI engines

The properties of kerosene as well as its autoignition, combustion and sooting characteristics in different equipment such as shock tube, RCM, IQT, FIT and CVCC have been discussed in detail in the previous sections. In this section, the combustion of kerosene in DICI engines will be looked into. This will enable researchers to have a good understanding of the effects of kerosene on the combustion process and emissions formation under real engine conditions.

2.5.1 Kerosene combustion in optical engines

Optical engines [98] allow visual access into the combustion chamber during the entire combustion process. This is especially needful to better understand the combustion and emissions characteristics of a particular fuel under a certain engine operating condition. Primarily, researchers such as Zha et al. [98] had used the high-speed complementary metal-oxide-semiconductor (CMOS) color camera and the charge-coupled device (CCD) camera in addition to the in-cylinder pressure transducer and exhaust gas analyzer to study the effects of kerosene combustion in optical DICI engines. Various other researchers such as Lee et al. [5, 37], Jansons and company [99-102] as

well as Lee [103] also contributed significantly to the study of the behavior and characteristics of kerosene combustion in optical engines.

Lee et al. [5, 37] investigated the combustion characteristics and emissions of JP-8 and diesel in an heavy-duty optical engine. Figure 2-8 shows the natural and normalized flame luminosities of JP-8 and diesel under injection pressures of (a) 30MPa and (b) 140MPa, the respective (c) flame temperature, KL factor distribution, (d) in-cylinder pressures and heat-release rates [5, 37]. It should be noted that K is the coefficient of soot absorption and L is the "line of sight path length through flame" [37].
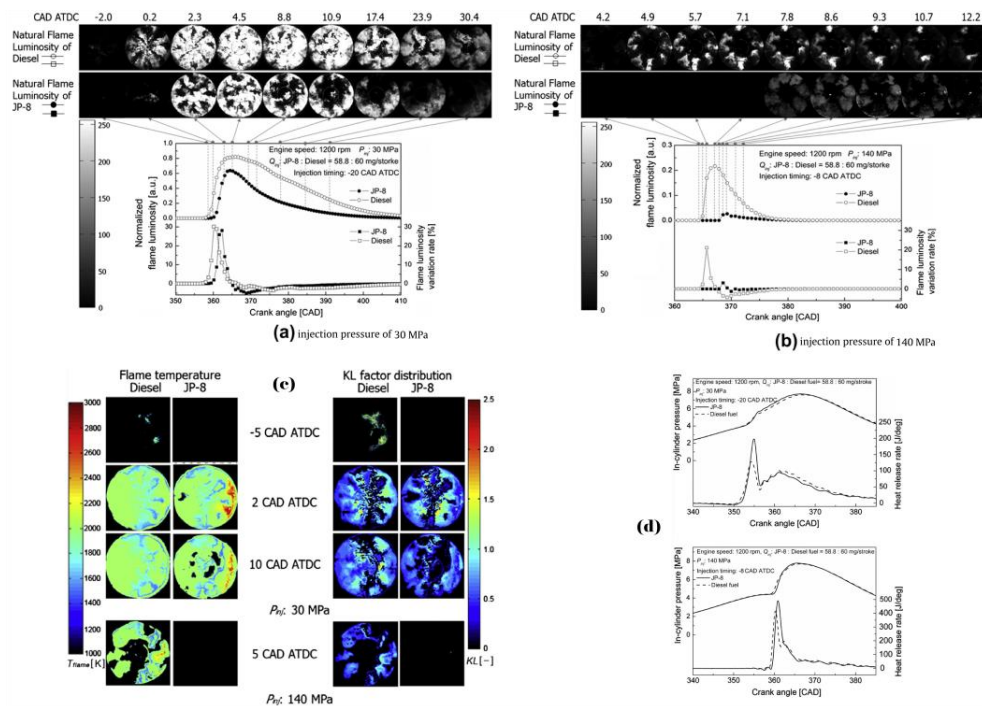
Figure 2-8 The natural and normalized flame luminosities of JP-8 and diesel under injection pressures of (a) 30MPa and (b) 140MPa, the respective (c) flame temperature, KL factor distribution, (d) in-cylinder pressures and heat-release rates [5, 37]. Reproduced from [5, 37].

From their works as seen from Figure 2-8d, it was observed that JP-8 had a longer ignition delay than diesel which was primarily due to the lower CN of JP-8 [5, 37]. Moreover, the heat-release during the premixed combustion

phase of JP-8 was substantially higher than that of diesel because of the longer ignition delay of JP-8 and its superior vaporization characteristic [5, 37]. With a longer ignition delay, more JP-8 was accumulated in the combustion chamber and more time was available for fuel-air mixing prior to the start of combustion (SOC). As a result, premixed heat-release of JP-8 was higher than that of diesel. Consequently, the heat-release of JP-8 during the diffusion combustion period was lower than diesel's. Furthermore, from the natural and normalized flame luminosities of JP-8 and diesel as seen from Figure 2-8a and b, the flame luminosities of JP-8 were generally lower than those of diesel [5, 37]. This implied that JP-8 experienced more premixed combustion and less diffusion combustion as compared to diesel. Moreover, it was seen from the flame luminosities that the duration of combustion (DOC) for JP-8 was shorter than diesel's because of the superior vaporization property of JP-8 which caused rapid fuel oxidation during the late-stage combustion [5, 37]. Interestingly, the longer ignition delay of JP-8 was also reflected in the flame luminosities. Moreover, JP-8 combustion resulted in more NO_x and less smoke as compared to diesel. This was because of the superior vaporization characteristic of JP-8 which allowed for a near-stoichiometric fuel-air mixture that gave high flame temperatures that resulted in more NO_x and less smoke [5, 37].
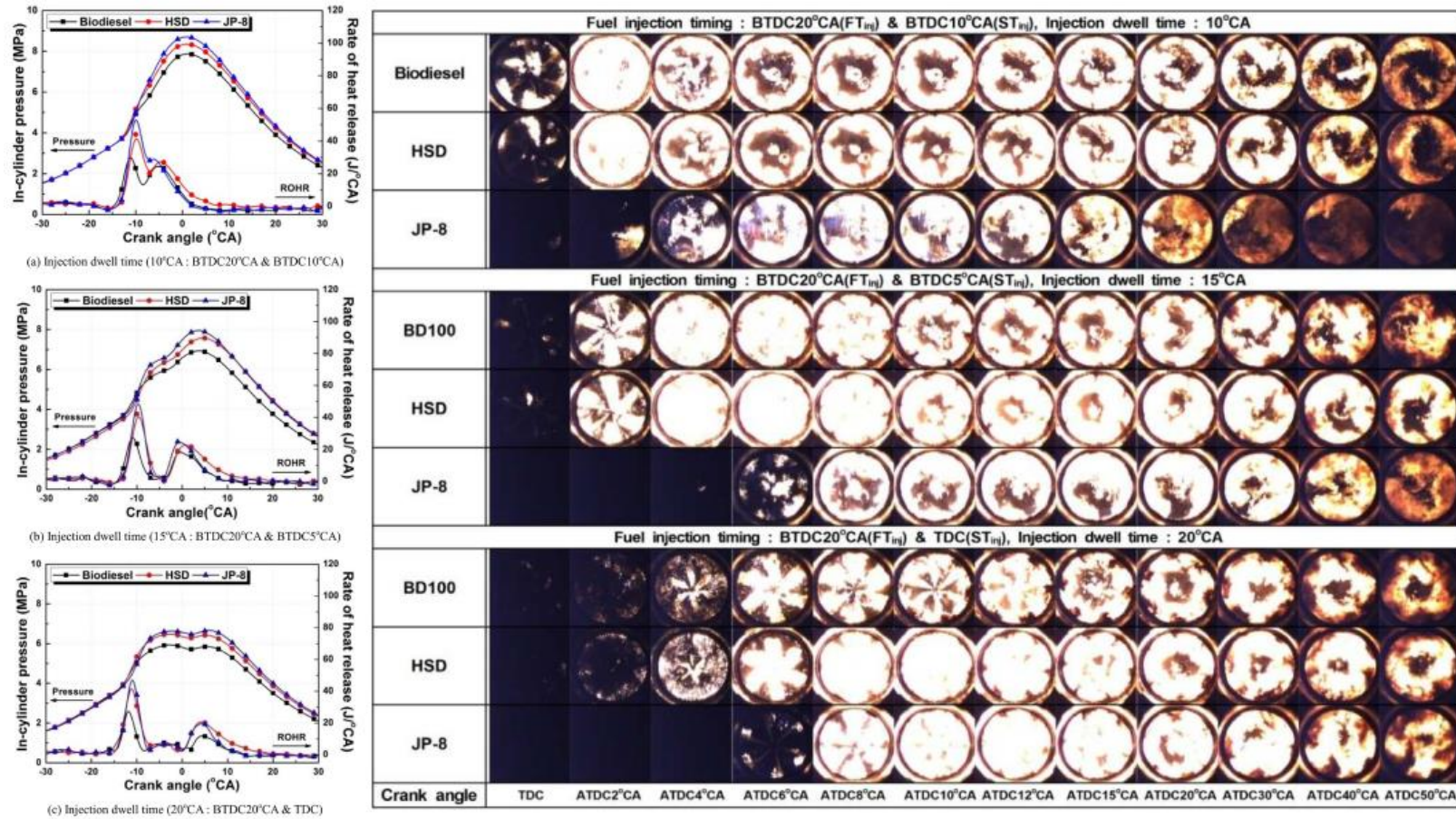
Figure 2-9 The in-cylinder pressures and heat-release rates together with the natural flame luminosities of biodiesel, HSD and JP-8 for different split injection dwell times of (a) 10 °CA, (b) 15 °CA and (c) 20 °CA, where CA stands for crank angle [103]. Reproduced from [103].

Another similar work was done by Lee [103] who investigated the effects of split injection dwell time on the combustion of biodiesel, high sulfur diesel (HSD) and JP-8 in an optical engine. Not surprisingly, the findings of Lee [103] concurred with those of Lee et al. [5, 37]. Figure 2-9 shows the in-cylinder pressures and heat-release rates together with the natural flame luminosities of biodiesel, HSD and JP-8 for different split injection dwell times of (a) 10 °CA, (b) 15 °CA and (c) 20 °CA, where CA stands for crank angle [103]. From their work, Lee [103] found through the flame luminosities that the combustion of biodiesel and HSD were more dominated by diffusion combustion but the opposite was true for JP-8. Moreover, JP-8's oxidation was also found to be the quickest due to its superior evaporation characteristic [103]. Consequently, NO_x emissions and peak in-cylinder pressures were the highest for JP-8 combustion.

Also, Jansons and co-workers [99-102] did some interesting work regarding JP-8 combustion in an optical engine. Firstly, they found that JP-8 had a lower sooting tendency than diesel [99]. This was due to the lower aromatic content of JP-8 as well as its higher volatility that enabled it to evaporate and mix with ambient in-cylinder air more easily. Next, they investigated the effects of formaldehyde and ethylene on JP-8 combustion [100, 101] and found that formaldehyde retarded low temperature heat-release, lengthened DOC, decreased the magnitude of heat-release and enhanced soot formation. On the other hand, ethylene did not have any impact on ignition delay but did contribute to some soot formation. Apart from using conventional JP-8, they also used low CN Sasol JP-8 which gave poorer performance and higher emissions as compared to conventional JP-8 [102].

2.5.2 Kerosene combustion in non-optical engines

The use of optical engines to study the combustion and emissions of kerosene has been discussed in the previous section. The advantage of using optical engines is that it allows for the visualization of the entire combustion process. However, since the piston bowls of optical engines are made of glass, the combustion bowl geometries are all basically flat [104] and do not take into consideration the in-cylinder turbulence caused by the different bowl geometries like in real engines. Moreover, optical engines are operated under skip-fire mode [102] to avoid excessive thermal loading on the glass. Furthermore, optical engines also suffer from high blow-by losses [99]. Therefore, it is also desirable to study the combustion process and emissions formation of kerosene in real engines. The following paragraphs in this section will summarize the combustion characteristics and the emissions behavior of kerosene in non-optical DICI engines.

From literature, it can be seen that much research had been done regarding the use of kerosene in compression ignition (CI) engines. Some researchers modified and improved commercial diesel engines to run on kerosene [105, 106]. Others studied the effects of high Sulphur kerosene on engine combustion and emissions [107-109]. Also, the effects of using kerosene during engine cold-starting was investigated [110]. Furthermore, some works were done using kerosene under part-homogeneous or homogeneous engine operating conditions [111-116] while others investigated the use of kerosene in indirect injection (IDI) engines [117-123]. It should be noted that studies done recently on kerosene combustion were predominantly done using DICI engines [6, 49, 58, 59, 124-133]. From DICI engine experiments, it was

observed that kerosene had a longer ignition delay period than diesel even though kerosene had a lower viscosity and better vaporization characteristic [6, 58, 59]. Under high EGR rates, the difference between diesel's and kerosene's ignition delay became much more obvious [6]. This was attributed to kerosene's lower CN. However, the difference in kerosene's and diesel's ignition delays could be minimized by using pilot injections which negated the CN effect by raising the in-cylinder temperature prior to the main injection and combustion [6]. On the other hand, for kerosene that had a similar CN as diesel, it was observed that combustion started earlier than diesel due to the higher volatility and evaporation rate of kerosene [49, 130, 131, 133]. It is interesting to note from experiments that even though kerosene and diesel had different densities, volatilities and viscosities, their combustion characteristics in terms of heat-release and pressure rise were very similar owing to the fact that they had similar CNs and air entrainment characteristics [130, 132, 133]. Moreover, it was observed that under high boost pressures, combustion was significantly affected for fuels with low CN and high volatility such as kerosene. On this note, it was concluded that fuel volatility affected the physical delay while CN affected the chemical delay [131]. Generally, in most cases, kerosene was seen to have a lower CN than diesel [6, 58, 59]. As the CN of kerosene was lower than diesel, combustion was retarded under both low and high load conditions [6, 49, 58, 59]. Under low load conditions, the magnitude of heat-release of kerosene was lower than that of diesel due to the superior evaporation characteristic of kerosene which caused a leaner fuel-air mixture to be formed prior to combustion [58]. Also, coupled with the fact that kerosene had a lower aromatic content than diesel, NO_x emissions decreased

[49, 58, 59, 126]. On the other hand, under high load conditions, the magnitude of heat-release of kerosene was seen to be higher than that of diesel due to the longer ignition delay and better evaporation characteristic of kerosene which resulted in a more intense premixed burn [58, 59]. Lower CN fuels generally gave a larger fraction of premixed burn [133]. Due to the higher volatility of kerosene, a near-stoichiometric fuel-air mixture was formed and NO_x emissions increased significantly [49, 58]. However, by using EGR and optimized injection strategies, NO_x and soot trade-off was proven to be possible with minimal loss in efficiency [6, 58, 59]. In general, smoke and PM emissions decreased with the use of kerosene due to its higher volatility and lower aromatic content [6, 49, 58, 59, 126]. From experiments, it was seen that nucleation mode particles (NMPs) were more and accumulation mode particles (AMPs) were less when kerosene was used in place of diesel [126]. This could be attributed to kerosene's lower aromatic content, lower viscosity, higher volatility, lower density, lower surface tension and smaller carbon molecules [6, 49, 58-60, 126, 128]. Under higher swirl intensity, AMPs were seen to decrease with the increase of NMPs [125]. In essence, the use of kerosene with EGR and/or the right injection strategy can reduce emissions and/or lower power loss [6, 58, 59, 124, 126, 127, 129].

Interestingly, some other engine experiments had been done using kerosene, diesel and biodiesel [134-136]. As compared to kerosene and diesel, the in-cylinder combustion of biodiesel gave a shorter ignition delay period due to its higher CN. Consequently, the combustion of biodiesel gave less premixed combustion and more diffusion combustion when compared to both kerosene and diesel due to biodiesel's short ignition delay and low volatility

[136]. Moreover, as compared to kerosene and diesel, the combustion of biodiesel gave the highest NMPs due to better oxidation of soot as biodiesel fuel molecules contained oxygen and also due to the fact that biodiesel had no aromatic content [135, 136]. On the other hand, as compared to kerosene and biodiesel, diesel gave more AMPs due to lower amounts of NMPs as well as the presence of higher amounts of aromatics in diesel fuel [136]. Furthermore, when using kerosene for power generation in an engine, it was found that the stability of both power and frequency were slightly lower as compared to using diesel and biodiesel [134]. Finally, as the popularity of biodiesels had increased over the years [137], the use of kerosene and biodiesel blends in DICI engines [138-149] had also been tested and proven feasible under different engine operating conditions.

Therefore, from this section, it can be seen that comprehensive experimental studies in both optical and non-optical DICI engines gave valuable insights on the combustion process and emissions formation of kerosene. The knowledge of kerosene's combustion characteristics and emissions behavior in DICI engines will enable researchers to better utilize kerosene under different operating conditions.

2.6 Development of kerosene surrogates, their chemical reaction mechanisms and the modelling of kerosene combustion in DICI engines

Previously, the combustion characteristics and emissions behavior of kerosene in DICI engines have been discussed in much detail. Through those experimental studies, researchers and engineers were able to optimize the combustion and emissions of kerosene in DICI engines. However, a deeper

understanding of kerosene combustion and the optimization of its combustion process can also be achieved through numerical simulations [38]. Today, numerical simulations and experiments are coupled together [38] to give a more comprehensive analysis of a combustion system. Therefore, in this section, a comprehensive review of existing kerosene surrogates and their respective chemical reaction mechanisms will be given.

As distillate fuels such as kerosene contain thousands of chemical compounds [38], it is impossible to include every chemical component into a chemical reaction mechanism. As a result, in all instances, a surrogate had to be used to represent a complex class of hydrocarbons [38, 56, 77, 90, 150, 151]. This had to be done to reduce the number of species and reactions in a reaction mechanism in order to cut down on the computational time required for numerical simulations. From literature, it was seen that kerosene surrogates could be split into two classes. The first class of surrogate was the chemical surrogate which only emulated the chemical properties of kerosene such as the lower heating value (LHV), threshold sooting index (TSI), hydrogen-to-carbon (H/C) ratio, derived Cetane number (DCN) and molecular weight (MW) [56, 77, 90, 150]. The second class of surrogate was a surrogate that could emulate both the chemical as well as the physical properties of kerosene [87, 90, 152]. Time dependent physical properties include volatility, density, viscosity and surface tension [90, 152].

From the review work of Dagaut and Cathonnet [38], it was seen that kerosene surrogates could have one or more components. Kerosene was seen to be represented purely by an alkane such as n-decane. On the other hand, different combinations and fractions of hydrocarbon classes like alkanes,

cycloalkanes and aromatics could also be used to represent kerosene. From their review work which was published in 2006 [38], it was observed that only chemical surrogates existed for kerosene. Furthermore, most kerosene surrogates at that time were only validated for their speciation data in jet-stirred reactors (JSRs) and premixed flat flame burners. Experimental validations for the autoignition characteristics of kerosene surrogates were very few and even if there were validations done, the range of experimental conditions under which validations were carried out was narrow. In addition, it was observed from their review work [38] that many of the surrogate reaction mechanisms contained more than a hundred species and a thousand reactions. Reasonable agreements for speciation data were seen between experiments and simulations. Refer to [38] for more details.
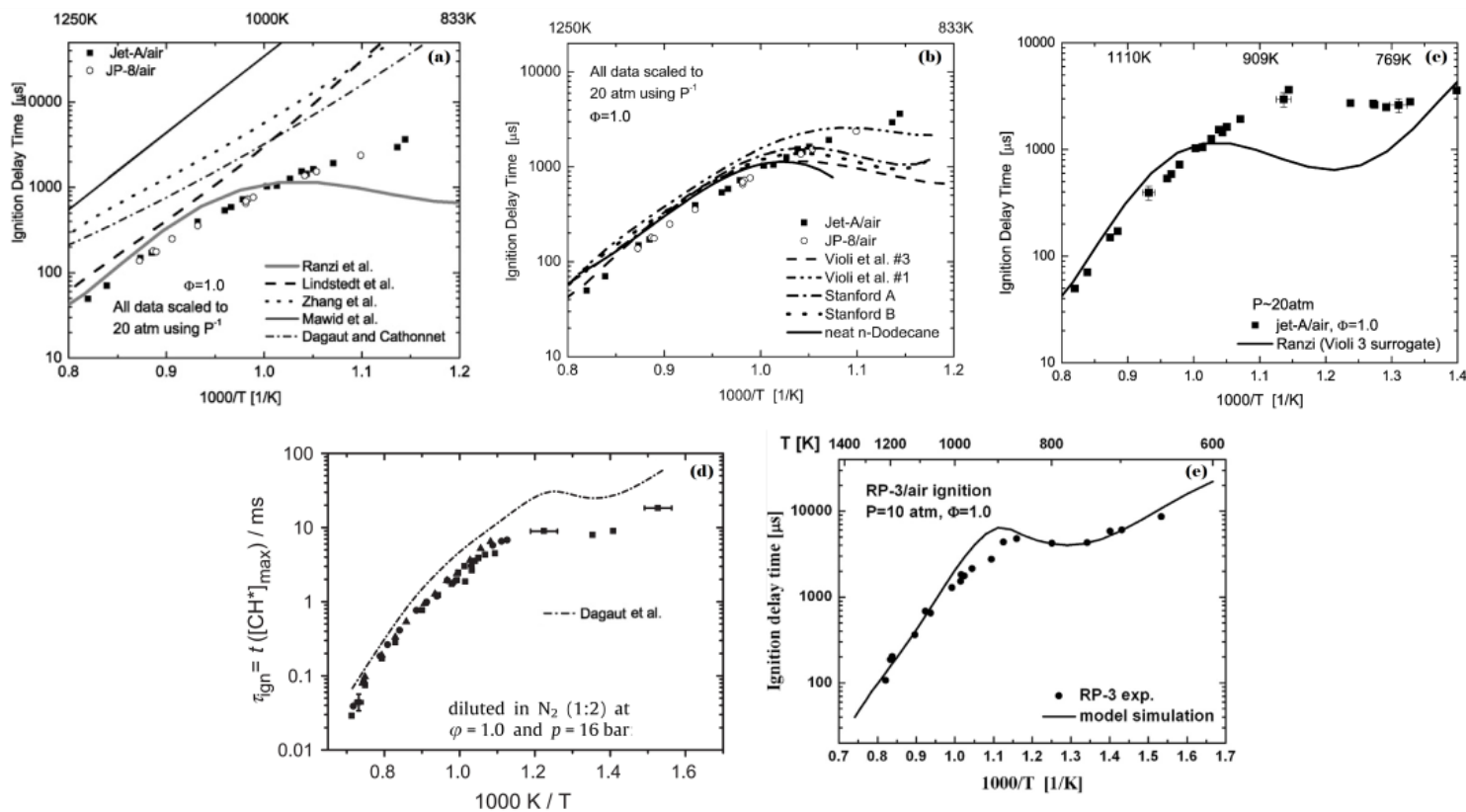
Figure 2-10 The experimental [73, 76, 153] shock tube ignition delay times of kerosene (symbols) together with the simulated [38, 73, 76, 153-159] ignition delay times (lines) using different kerosene surrogate models and reaction mechanisms from literature. Figure 2-10a, b and c are from the work of Vasu et al. [76] while Figure 2-10d and e are from Dagaut et al. [153] and Zhang et al. [73] respectively. Notable chemical surrogates for kerosene were proposed by researchers like Lindstedt and Maurice [158], Mawid and Sekar [157], Violi et al. [156], Vasu et al. [76], Zhang et al. [73] as well as Daguat and company [38, 153, 155]. Reproduced from [38, 73, 76, 153-159].

Next, Figure 2-10 shows the experimental [73, 76, 153] shock tube ignition delay times of kerosene (symbols) together with the simulated [38, 73, 76, 153-159] ignition delay times (lines) using different kerosene surrogate models and reaction mechanisms from literature. Figure 2-10a, b and c are from the work of Vasu et al. [76] while Figure 2-10d and e are from Dagaut et al. [153] and Zhang et al. [73] respectively. Notable chemical surrogates for kerosene as seen in Figure 2-10 were proposed by researchers like Lindstedt and Maurice [158], Mawid and Sekar [157], Violi et al. [156], Vasu et al. [76], Zhang et al. [73] as well as Daguat and company [38, 153, 155]. Generally, it can be observed from Figure 2-10 that most of the predicted ignition delay times were in reasonable agreement with experiments conducted under high initial temperatures above 1000K. However, at lower initial temperatures below 1000K, many of the predicted ignition delay times were far from experiments especially in the negative temperature coefficient (NTC) and low temperature regions except for the work of Zhang et al. [73]. Moreover, from Figure 2-10 and from literature [56, 77, 90, 150, 160], the majority of ignition delay validations between simulations and experiments for kerosene were done for initial shock tube conditions of about 10-20atm and 1.0 equivalence ratio.

Table 2-3 shows a compilation of the latest as well as significant kerosene surrogates from literature, the number of species and reactions in their respective reaction mechanisms as well as the target properties that each surrogate was made to emulate [38, 54, 56, 61, 71, 73, 75-77, 87, 90, 92, 93, 150-176].

Table 2-3 A compilation of the latest as well as significant kerosene surrogates from literature, the number of species and reactions in their respective reaction mechanisms as well as the target properties that each surrogate was made to emulate [38, 54, 56, 61, 71, 73, 75-77, 87, 90, 92, 93, 150-176].

Components	Species/Reactions	To Emulate
n-dodecane/iso-cetane/MCH/toluene 0.3844/0.1484/0.2336/0.2336 (mole fraction) [90]	Detailed reaction mechanism library	Density, viscosity, surface tension, volatility, MW, LHV, CN, H/C, gas phase ignition delays of Jet-A [90] and its autoignition behaviors in a CVCC and an engine [71]
n-dodecane/iso-cetane /decalin/toluene 0.2897/0.1424/0.3188/0.2491 (mole fraction) [90]	4014/ 16936 [90]	
n-dodecane/iso-cetane /decalin/toluene 0.456/0.145/0.2632/0.1358 (volume fraction) [152]	-	Density, viscosity, surface tension, volatility, MW, LHV, DCN, H/C, engine in-cylinder spray, combustion and emissions of Jet-A [152]
n-dodecane/isocetane/transdecalin/toluene 0.3/0.36/0.246/0.094 (mole fraction) [160]	231/5591 [160]	Autoignition, volatility, laminar flame speeds and evaporation characteristics of Jet-A [160]
n-dodecane/1,2,4-TMB 0.6/0.4 (volume fraction) [87]	-	Volatility, TSI, H/C, LHV, MW, density, DCN, spray, autoignition and combustion characteristics of JP-8 [87]
n-hexadecane/ n-dodecane/iso-cetane/decalin/1,2,4-TMB/m-xylene 0.01/0.49/0.16/0.19/0.11/0.04 (volume fraction) [87]		
n-dodecane/1,2,4-TMB 0.6/0.4 (volume fraction) [61]	120/1471 [161]	Volatility, TSI, H/C, LHV, MW, density, DCN, autoignition and combustion characteristics of JP-8 [61] and its combustion and emissions in an engine [161]
n-decane/iso-octane/toluene 0.4267/0.3302/0.2431 (mole fraction) [77]	1599/6633 [77]	DCN, H/C of Jet-A and its chemical reactivity, gas phase ignition delays and extinction strain rates [77]
n-dodecane/iso-octane/1,3,5-TMB/n-PB 0.404/0.295/0.073/0.228 (mole fraction) [56]	2080/8310 [150]	TSI, DCN, MW, H/C of Jet-A and its gas phase ignition delays, speciation data, extinction strain rates, laminar flame speeds and chemical reactivity [56, 150]
n-dodecane/m-xylene 0.77/0.23 (volume fraction) [162]	243/3384 [162]	PAH, soot and flame dynamics, autoignition and combustion characteristics, speciation data of JP-8

		[162] and its spray, combustion and soot behavior in a CVCC [54, 92, 93]
n-decane/MCH/toluene 0.821/0.079/0.1 (mole fraction) [163] n-decane/toluene 0.596/0.404 (mole fraction) [163]	348/2163 [163]	H/C and flame speed of kerosene [163]
n-decane/1,2,4-TMB 0.8/0.2 (mass fraction) [154]	122/900 [154]	Soot evolution and extinction strain rate of kerosene in a counter flow flame [154]
n-decane/1,2,4-TMB 0.887/0.113 (mole fraction) [73]	122/900 [73, 154]	Gas phase ignition delays of RP-3 [73]
n-decane/n-PCH/n-PB/decene Varying depending on fuel composition [164]	550/1400 [164]	Speciation data and autoignition behavior of Jet-A/Jet A-1/JP-8 [164]
hexane/decane 0.2/0.8* [75] benzene/decane 0.2/0.8* [75] benzene/hexane/decane 0.182/0.091/0.727* [75] (*All in mass fraction) [165]	-	Gas phase ignition velocities and delays of Jet-A [75]
n-dodecane/n-tetradecane/iso-octane/MCH/tetralin/m-xylene 0.3/0.2/0.1/0.2/0.05/0.15 (volume fraction) [157] n-decane/n-dodecane/n-tetradecane/iso-octane/MCH/toluene 0.25/0.25/0.2/0.05/0.05/0.2 (volume fraction) [157]	234/1592 [157]	Autoignition behavior of Jet-A/JP-8 [157]
m-xylene/iso-octane/MCH/n-dodecane/n-tetradecane/tetralin 0.15/0.1/0.2/0.3/0.2/0.05* [156] n-octane/n-dodecane/n-hexadecane/xylenes/decalin/tetralin 0.035/0.4/0.05/0.085/0.35/0.08* [38, 156] MCH/toluene/benzene/iso-octane/n-dodecane 0.1/0.1/0.01/0.055/0.735* [156]	280/7800 [76] 208/1087 [76, 159] 221/5032 [166]	TSI, volatility, reactivity, LHV, regression rate, speciation data and flammability of JP-8 [156] and its gas phase ignition delays [76], extinction limits and temperature profiles [166]

MCH/toluene/benzene/iso-octane/n-dodecane 0.1/0.1/0.01/0.25/0.54* [76]		
MCH/toluene/benzene/iso-octane/n-dodecane 0.1/0.295/0.01/0.055/0.54* [76] (*All in volume fraction)		
n-decane/n-dodecane/n-tetradecane/n-hexadecane/iso-octane/MCH/ cyclo-octane/m-xylene/butylbenzene/C9H12/tetralin/1MN 0.15/0.20/0.15/0.1/0.05/0.05/0.05/0.05/0.05/0.05/0.05/0.05 (mass fraction) [167]	221/1483 [167]	Gas phase ignition delay times of JP-8 [167]
n-dodecane/n-decane/butylbenzene/MCH 0.45/0.2/0.25/0.1 (mass fraction) [167]		
n-dodecane/n-decane/butylbenzene/MCH 0.347/0.326/0.16/0.167 (mole fraction) [168]	164/1162 [168]	Speciation data and ignition delay times of JP-8 [168]
n-dodecane/iso-cetane/MCH/decalin/α-methylnaphthalene 0.26/0.36/0.14/0.06/0.18 (volume fraction) [169]	-	Oxidative and reactivity characteristics of JP-8 [169]
n-undecane/n-PCH/1,2,4-TMB 0.79/0.1/0.11 (mass fraction) [38, 170]	Quasi-global [38, 170]	Speciation data of Jet A-1 in a JSR [38, 170]
n-decane/toluene 0.9/0.1 (volume fraction) [38, 171]	39/207 [38, 171]	Speciation data of kerosene in a flat flame burner [38, 171]
n-decane/n-PB/n-PCH 0.74/0.15/0.11 (volume fraction) [38, 172]	207/1592 [38, 172]	Speciation data of Jet A-1 in a JSR [38, 172]
n-decane/n-PB/n-PCH 0.74/0.15/0.11 (mole fraction) [38, 173, 174]	209/1673 [38, 173, 174]	Speciation data of Jet A-1 in a premixed flame and JSR as well as its autoignition behavior [38, 173, 174]
n-decane/n-PB/n-PCH 0.69/0.2/0.11 (mole fraction) [153, 155]	263/2027 [153, 155]	Speciation data of Jet A-1 in a premixed flame and JSR as well as its autoignition behavior [153, 155]
n-decane/aromatic 0.89/0.11 (mole fraction) [158]; Aromatics can be benzene, toluene, ethylbenzene,	193/1085 [158]	Speciation data of kerosene in premixed flames [158]

ethylbenzene/napthalene		
Fuel/alkenic species, F (one component) [151]	8/7 [151]	Heat-release, autoignition and speciation data of kerosene [151]
$C_{12}H_{23}$ (one component) [175]	15/13 [175]	Reflected wave speeds and ignition delay characteristic of Jet-A in a shock tube [175]
$C_{12}H_{24}$ (one component) [176]	10/17 [176]	Soot, LHV, H/C, MW of kerosene [176]

MCH: Methylcyclohexane   1,3,5-TMB: 1,3,5-trimethylbenzene   1,2,4-TMB: 1,2,4-trimethylbenzene   n-PCH: n-propylcyclohexane

n-PB: n-propylbenzene   C9H12: 1,2,4,5-teeramethylbenzene   1MN: 1-methylnapthalene   PAH: Polyaromatic Hydrocarbon

MW: Molecular Weight   LHV: Lower Heating Value   H/C: Hydrogen-to-Carbon ratio   CN: Cetane Number

DCN: Derived Cetane Number   TSI: Threshold Sooting Index   CVCC: Constant Volume Combustion Chamber   JSR: Jet-stirred reactor

Recent notable chemical surrogates for kerosene (Jet-A) were developed by a consortium of universities under the Multi-University Research Initiative (MURI) [56, 77, 150]. Their goal was to mimic the gas phase combustion phenomena of kerosene using suitable surrogates [56]. Their first generation chemical surrogate (MURI1) consisted of 0.4267 n-decane/0.3302 iso-octane/0.2431 toluene by mole fraction [77]. MURI1 was made to emulate the DCN and the H/C ratio of kerosene. As compared to kerosene, it was seen that MURI1 gave similar low temperature reactivity in a flow reactor, similar autoignition characteristics in a shock tube and RCM as well as similar extinction strain rates in a counter flow diffusion flame. However, MURI1 was not able to mimic the TSI and MW of kerosene as it only consisted of three components. Modelling of MURI1 was done using a detailed reaction mechanism that consisted of 1599 species and 6633 reactions [77]. Generally, reasonable agreements were seen between the simulation results and the experimental results of the counter flow diffusion flame, flow reactor, shock tube and RCM. Interestingly, MURI1 was used by Cung et al. [177] for CVCC and closed reactor simulations. Subsequently, their second generation surrogate (MURI2) was developed to meet four target properties of kerosene which were the H/C ratio, MW, DCN and TSI [56]. MURI2 consisted of 0.404 n-dodecane/0.295 iso-octane/0.073 1,3,5-trimethylbenzene/0.228 n-propylbenzene by mole fraction. With the inclusion of two aromatic

compounds, MURI2 was able to match not only the TSI but also the DCN, MW and H/C ratio of kerosene simultaneously. From experiments, reasonable agreements were seen between MURI2 and kerosene for both low and high temperature reactivity, autoignition characteristics, laminar flame speeds, shock tube speciation data as well as sooting propensity. A detailed chemical reaction mechanism was also developed for MURI2 from the mechanism of MURI1 and it had 2080 species amongst 8310 reactions [150]. Simulation results for MURI2 were seen to match those of experiments in a flow reactor, shock tube and RCM fairly well. Figure 2-11 shows the RCM and shock tube experimental and simulated ignition delay times of kerosene, MURI1 and MURI2 at initial conditions of around 20atm and 1.0 equivalence ratio [56, 77, 150]. From Figure 2-11, the reaction mechanisms of both MURI1 and 2 predicted the autoignition trends reasonably. It should be noted that both MURI1 and 2 were not designed to emulate the physical characteristics of kerosene [56].
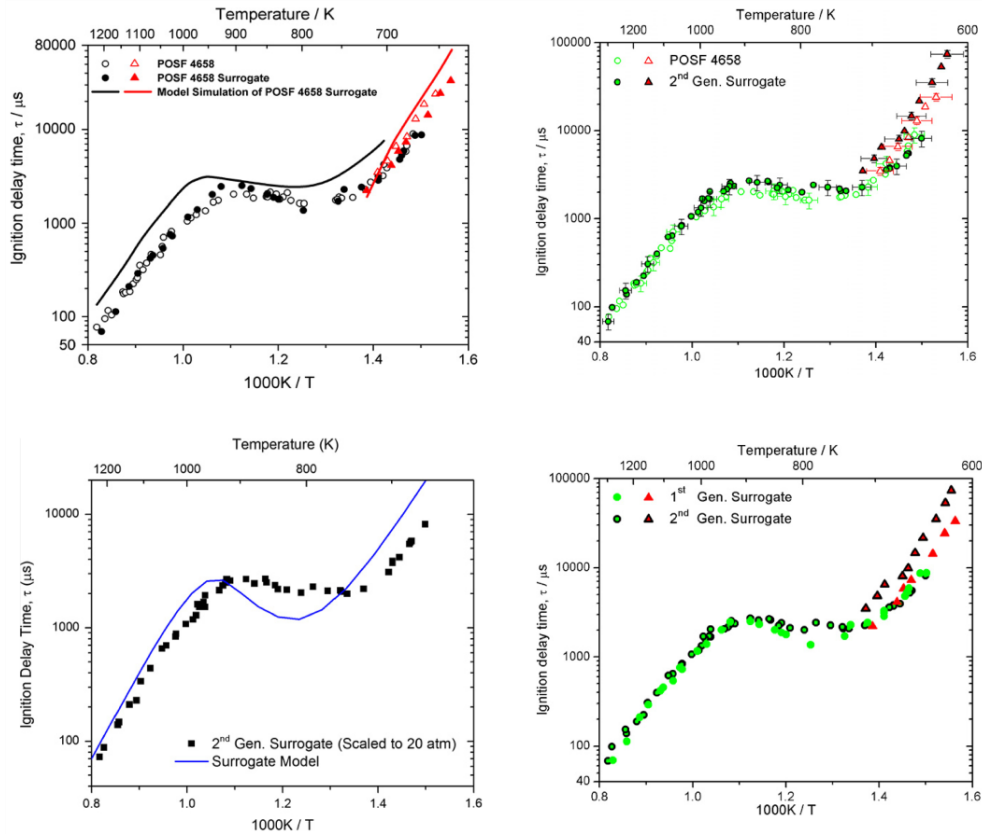
Figure 2-11 The RCM and shock tube experimental and simulated ignition delay times of kerosene, MURI1 and MURI2 at initial conditions of around 20atm and 1.0 equivalence ratio [56, 77, 150]. Reproduced from [56, 77, 150].

Other noteworthy surrogates were developed by the University of Michigan [71, 90, 152] in conjunction with other universities to emulate both the chemical as well as the physical characteristics of kerosene (Jet-A). Two surrogates, namely UM1 and UM2 [71, 90], both containing four components, were developed by them to meet eight target properties of kerosene. The target properties were volatility, density, viscosity, surface tension, MW, LHV, CN and H/C ratio [71, 90, 152]. The UM1 surrogate consisted of 0.3844 n-dodecane/0.1484 iso-cetane/0.2336 methylcyclohexane/0.2336 toluene while the UM2 surrogate consisted of 0.2897 n-dodecane/0.1424

46

iso-cetane/0.3188 decalin/0.2491 toluene by mole fraction. Simulations for UM1 and 2 were done using a detailed reaction mechanism containing 4014 species with 16936 reactions [90].
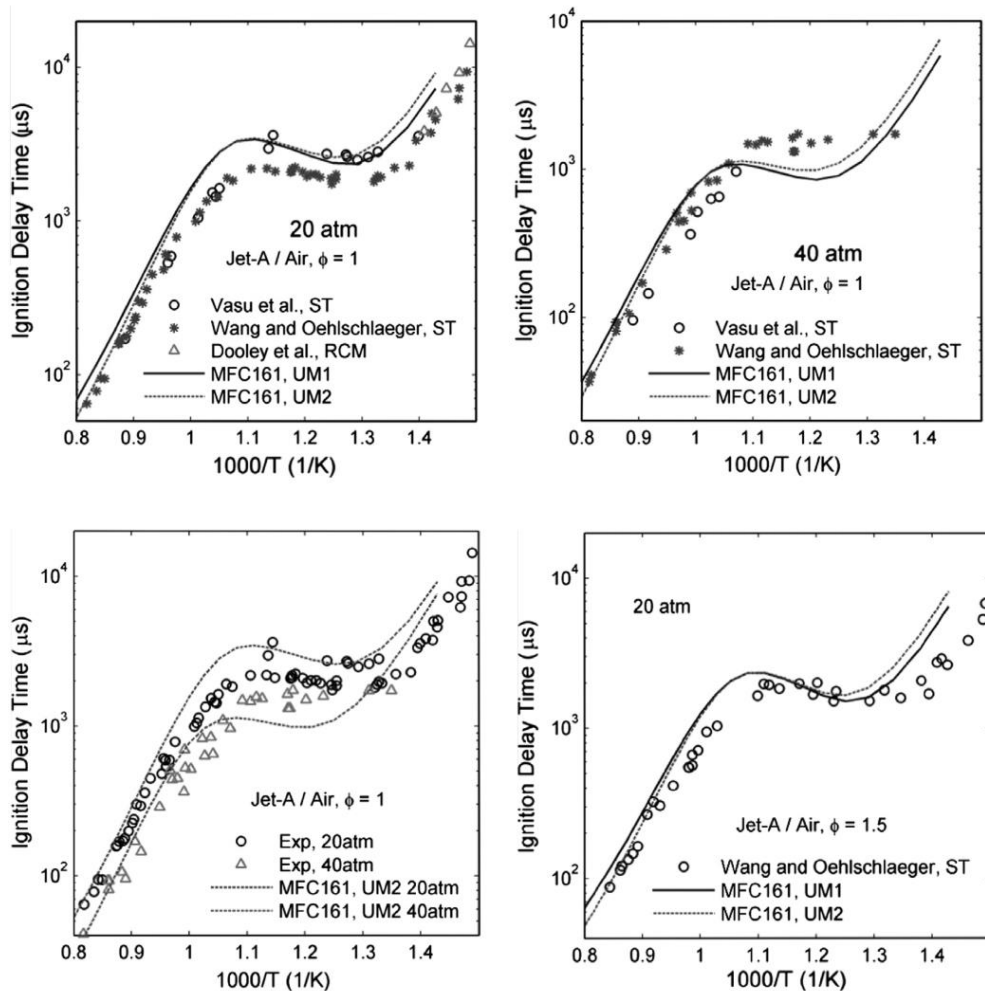
Figure 2-12 The ignition delay comparisons between simulations (UM1 and 2) [90] and experiments (Jet-A) [53, 76, 77] at initial pressures of 20atm and 40atm. Reproduced from [90].

Figure 2-12 shows the ignition delay comparisons between simulations (UM1 and 2) [90] and experiments (Jet-A) [53, 76, 77] at initial pressures of 20atm and 40atm. It can be seen from Figure 2-12 that at temperatures above 1000K, the predicted and the experimental results were rather close but poorer

agreements were seen for temperatures below 1000K. Figure 2-13 shows the

(a) density, (b) viscosity, (c) surface tension and (d) volatility comparisons of

UM1, UM2, kerosene [90] and other kerosene surrogates [56, 154, 178, 179]

from literature. Overall, it can be seen from Figure 2-13 that on the whole

UM2 gave quite a good emulation of kerosene's physical properties especially

for density and viscosity which are important for accurately predicting sprays

in DICI engines [16].
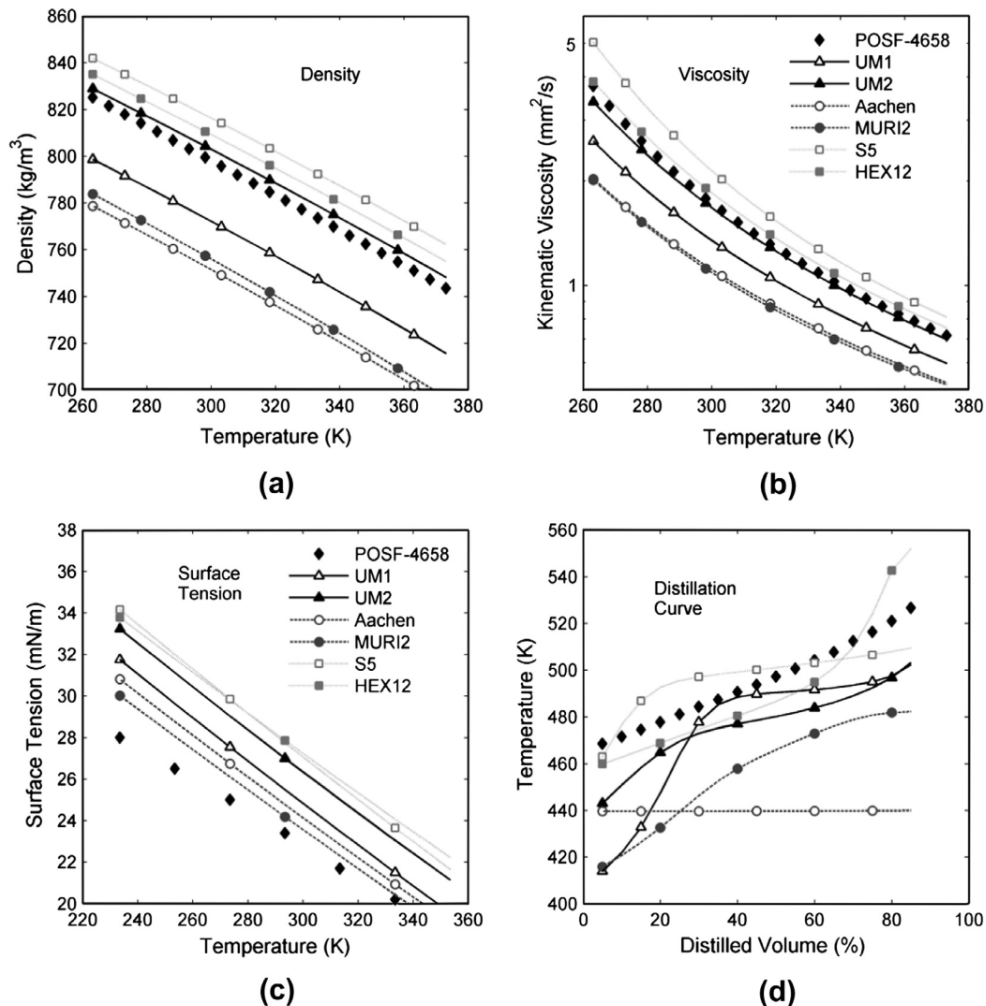
Figure 2-13 The (a) density, (b) viscosity, (c) surface tension and (d) volatility
comparisons of UM1, UM2, kerosene [90] and other kerosene surrogates [56, 154,
178, 179] from literature. Reproduced from [90].

Not surprisingly, UM2 gave a better agreement than UM1 in predicting both the physical and chemical ignition delays of kerosene because UM2 contained decalin instead of methylcyclohexane [71]. Moreover, it was seen that both UM1 and 2 gave a two-stage combustion behavior which was similar to that of kerosene. Using the same methodology, Yu et al. [152] developed a similar kerosene surrogate and tested it in an optical diesel engine. Figure 2-14 shows the in-cylinder (a) broadband and (b) OH chemiluminescence for two different engine operating conditions [152]. From the work of Yu et al. [152] and as seen from Figure 2-14, the kerosene surrogate gave similar spray behavior, premixed combustion duration, high temperature ignition delay and radical distribution as kerosene. Furthermore, low temperature radical distribution and ignition delay, when compared to kerosene, were fairly similar. Overall, the developed surrogate was able to give similar combustion and emissions behavior as kerosene under different engine operating conditions. The methodology proposed by the University of Michigan was proven by others [61, 87, 161] to be reliable for kerosene surrogate development for DICI engine applications.
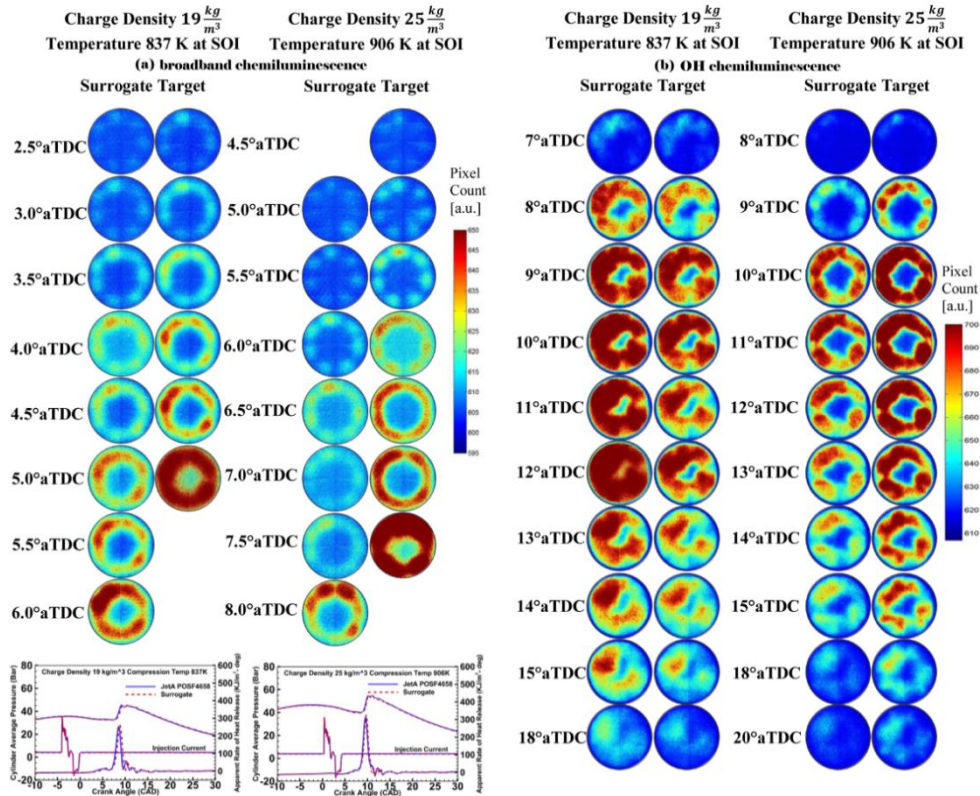
Figure 2-14 The in-cylinder (a) broadband and (b) OH chemiluminescence for two different engine operating conditions [152]. Reproduced from [152]. Reprinted with permission Copyright © 2015 SAE International. Further distribution of this material is not permitted without prior permission from SAE.

Similar to the review done by Dagaut and Cathonnet [38], most of the kerosene reaction mechanisms in literature as seen from Table 2-3 and from Vasu et al. [76] contained more than a hundred species and a thousand reactions. However, some researchers [151, 175, 176] had also developed single component reaction mechanisms with very few reaction steps for kerosene combustion. Zaev et al. [175] and Wang [176] developed single component reaction mechanisms for pulsed detonation (15 species and 13 reactions) and rocket (10 species and 17 reactions) engines respectively. On the other hand, Vandersickel et al. [151] developed a single component

reaction mechanism for homogeneous or semi-homogeneous engine combustion which consisted of 8 species and 7 reactions. Vandersickel et al.'s [151] mechanism was able to mimic the species concentration, two-stage combustion, heat-release as well as the low and high temperature ignition delays of a single class of distillate fuel such as kerosene. It should be noted that the aforementioned single component surrogates for kerosene were only validated for a limited range of conditions and were not built for 3D DICI engine simulations. Refer to Table 2-3 for more details on other prominent kerosene surrogates and their reaction mechanisms.

2.7 Research gaps

At present, the modelling of kerosene combustion in DICI engines is sorely lacking. As seen from above, although there were many reaction mechanisms proposed in literature, most of the reaction mechanisms were rather large in size which made them impractical to be used for 3-dimensional (3D) engine simulations [151]. This may be one of the possible reasons why very few 3D engine simulations were performed using kerosene as compared to other fuels like diesel [180], gasoline [181] and biofuels [182]. The simulation of in-cylinder kerosene combustion in DICI engines had only been done by Kavuri et al. [183] and Shrestha et al. [161]. Kavuri et al. [183] used a primary reference fuel (PRF) mechanism to simulate the combustion of gasoline,

kerosene and diesel by varying the proportion of iso-octane and n-heptane depending on the CN of each fuel used. On the other hand, Shrestha et al. [161] used a two component surrogate consisting of 0.6 n-dodecane/0.4 1,2,4-trimethylbenzene by volume fraction. Although the two component reaction mechanism used for 3D engine simulations reasonably predicted the in-cylinder combustion characteristics, it had 120 species amongst 1471 reactions [161]. Moreover, as seen from Table 2-3, most kerosene surrogate reaction mechanisms were validated only for their species concentration in premixed flat flame burners and in JSRs, with negligible focus on the autoignition behaviour which is important for accurately predicting the ignition delay in DICI engines as it will affect the subsequent in-cylinder combustion process and emissions formation [16]. Therefore, much work can still be done in order to develop more compact, robust and reliable reaction mechanisms for the simulation of kerosene combustion in DICI engines which will drastically cut down the computational time required for simulations [151].

Furthermore, as soot emissions are detrimental to both human health [17-21] and the environment [22-27], it is essential to study the sooting behaviour of kerosene when it is used in diesel engines. Moreover, soot emissions from military diesel engines do compromise the stealth of military vehicles [38]. Due to the aforementioned reasons, it is extremely desirable to

know kerosene's soot formation and oxidation behaviour during diesel engine combustion. As seen from this chapter, there is little study done using numerical simulations about the in-cylinder sooting behaviour and soot particle evolution of kerosene in diesel engines. Therefore, more work ought to be done regarding the simulation of kerosene's soot formation and oxidation trends as well as kerosene's soot particle dynamics such as soot mass, number and size. This will enable researchers to find better ways to reduce soot emissions when kerosene is used in diesel engines.

In addition, as vehicular NO_x and soot emissions are of great concern these days [32], it is necessary to find ways to mitigate them especially when kerosene is used as a new alternative in diesel engines. From the above literature review, it can be seen that NO_x emissions for kerosene combustion were generally higher than that of diesel [5, 37]. Moreover, even though kerosene combustion produced less soot as compared to diesel combustion [5, 37], more can be done to further mitigate soot emissions. Hence, more work can still be done to find solutions to mitigate the shortcomings and to enhance the strengths of kerosene combustion.

2.8 Summary

A comprehensive review was carried out systematically in this chapter to better understand the characteristics and behaviour of kerosene in DICI

engines. The areas that were reviewed include the fuel properties of kerosene as well as the fundamental autoignition studies of kerosene in shock tube, RCM, FIT, IQT, CVCC and engine. Moreover, experimental studies of kerosene spray and combustion in CVCCs and experimental investigations of kerosene combustion and emissions in DICI engines were reviewed. Also, the development of kerosene surrogates, their chemical reaction mechanisms and the modelling of kerosene combustion in DICI engines were evaluated. Most importantly, the research gaps were highlighted for further improvement in this thesis.

Chapter 3 Methodology

3.1 Numerical modelling

In order to successfully model the combustion process and emissions formation in a DICI engine, one has to consider both the physical and the chemical processes [16] that take place within the engine cylinder. In this work, the established KIVA4-CHEMKIN [39, 40, 184-186] computational fluid dynamics (CFD) code which was developed by Los Alamos National Laboratory was used to simulate diesel engine combustion.
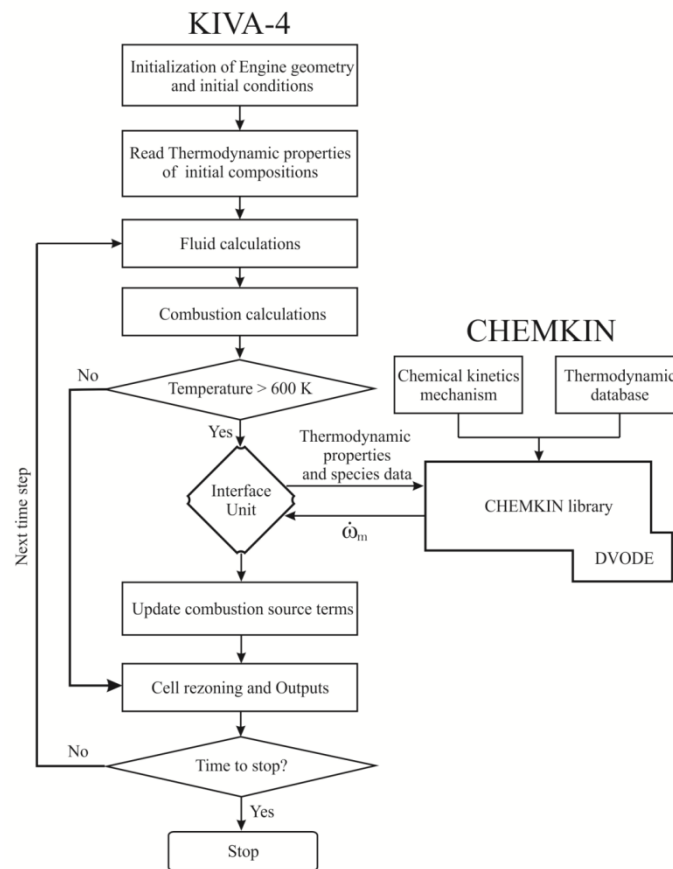
Figure 3-1 An overview of the operating sequence of the KIVA4-CHEMKIN [39, 40, 184-187] code. Reproduced from [187].

It should be noted that both KIVA4 [39] and CHEMKIN II [40] are written in FORTRAN. KIVA4 [39] deals with the physical in-cylinder processes while CHEMKIN II [40] takes care of the chemical reactions and combustion. Moreover, by utilizing the KIVA3V [184] pre-processor, one is able to generate meshes for different bowl geometries. On the other hand, the ICEMCFD [188, 189] software is another alternative for mesh generation. Figure 3-1 shows an overview of the operating sequence of the KIVA4-CHEMKIN [39, 40, 184-187] code. For a closed-cycle diesel simulation, initialization of the KIVA4-CHEMKIN [39, 40, 184-186] code begins at the crank angle when the intake valve closes. At every crank angle where the temperature of any computational cell is below the user specified cut-off temperature, the KIVA4 [39] code will only compute the temperature, pressure and fluid flow evolution. However, once the temperature of any computational cell exceeds the cut-off temperature, KIVA4 [39] will engage CHEMKIN II [40] to calculate the species evolution and the heat-release based on the reaction mechanism that is used. At every time step above the cut-off temperature, KIVA4 [39] will pass the temperature and pressure in each respective cell to CHEMKIN II [40] which will calculate the change in species concentration and heat-release according to the in-cylinder ambient conditions. Following which, CHEMKIN II [40] will return the heat-release and the species concentration back to KIVA4 [39] which will calculate the

subsequent rise or drop in in-cylinder temperature and pressure. This process repeats itself till the end of the simulation. It should be noted that the KIVA4 [39] code includes a multi-component evaporation model [190] which enables a multi-component fuel to be used in simulations.

Table 3-1 shows the important numerical models and equations used in the KIVA4-CHEMKIN [39, 40, 184-186] code. As DICI engine simulations involve fuel spray, the discrete droplet model (DDM) [191], which is based on the Monte-Carlo approach, is used to solve the droplet distribution function at each time step. Subsequently, the Kelvin-Helmholtz and Rayleigh-Taylor (KH-RT) spray breakup model [192] is used to describe spray atomization and breakup which is caused by aerodynamic instabilities. This model is proven to be accurate in predicting spay penetration for DICI engine simulations and it is superior [193] as compared to the Taylor Analogy Breakup (TAB) [194] model. The KH component of the model takes care of the primary fuel atomization process within the spray breakup length while the RT component of the model deals with the secondary spray breakup beyond the breakup length. Moreover, droplet collision is dealt with by the O'Rourke model [186, 195]. In the O'Rourke model [186, 195], probability is used in the simulation of droplet collision. A random number between 0 and 1 is first generated and compared to the collision probability P_n. If that random number is equal to or more than the collision probability, collision occurs between a larger

"collector" droplet and smaller "droplets". Subsequently, a second random

number between 0 and 1 is generated for the calculation of collision impact

parameter b. If the calculated collision impact parameter is lesser than the

critical impact parameter, coalescence between droplets will occur.

Furthermore, the KIVA4 [39] code also includes the Re-Normalized Group

(RNG) $k-\varepsilon$ turbulence model [186, 196, 197] to account for the changes in

in-cylinder fluid flow field caused by fuel spray and piston movement. It

should be noted that the conservation of energy, mass and momentum are all

accounted for by the KIVA4 [39] code and the calculation of gas phase

solution is through the arbitrary Lagrangian-Eulerian (ALE) approach. In

addition, CHEMKIN II [40], which is coupled to KIVA4 [39], accounts for

the elementary chemical reactions that occur during combustion. The speeds

of forward and reverse reactions depend on the respective Arrhenius rates.

Based on the initial in-cylinder ambient conditions like temperature, pressure

and oxygen concentration, CHEMKIN II [40] calculates the resultant

heat-released and species density for the next time step. Refer to Table 3-1 for

details on the mathematical equations and models used in the

KIVA4-CHEMKIN [39, 40, 184-186] code.

Moreover, in this work, the FORTRAN SENKIN [198] code was used to

do sensitivity analysis and ignition delay calculations in a homogeneous

closed reactor for the development of chemical reaction mechanisms. The

ignition delay period calculated by SENKIN [198] is defined as the time taken

for a 400K rise in temperature from the initial reactor temperature.

Table 3-1 Numerical models and equations in the KIVA4-CHEMKIN [39, 40, 184-186] code.

Equations	Remarks
Spray equations [191]	$\mathbf{x}$ droplet position
	$\mathbf{v}$ droplet velocity
	r droplet radius
	T_d droplet temperature
	t time
Droplet distribution function:	y parameter for droplet distortion
$\dfrac{probable\_number\_of\_droplets}{unit\_volume} = f(\mathbf{x},\mathbf{v},r,T_d,y,\dot{y},t)d\mathbf{v}drdT_ddyd\dot{y}$	$\dot{y}$ droplet oscillation velocity
	f droplet distribution function with time/space progression
Droplet distribution function with time/space progression (discrete droplet model [191]):	F_i rate of change of droplet velocity
$\dfrac{\partial f}{\partial t} = -\dfrac{\partial}{\partial x_i}(fv_i) - \dfrac{\partial}{\partial v_i}(fF_i) - \dfrac{\partial}{\partial r}(fR)$	R rate of change of droplet radius
$-\dfrac{\partial}{\partial T_d}(f\dot{T}_d) - \dfrac{\partial}{\partial y}(f\dot{y}) - \dfrac{\partial}{\partial \dot{y}}(f\ddot{y}) + \dot{f}_{coll} + \dot{f}_{bu}$	$\dot{T}_d$ rate of change of droplet temperature
	$\ddot{y}$ rate of change of droplet oscillation velocity
	$\dot{f}_{coll}$ droplet collision source term

$\dot{f}_{bu}$ droplet breakup source term

Spray breakup equations (KH-RT model [192])

r_p parent droplet radius

r_c child droplet radius

Before spray breakup:

τ_{KH} breakup timescale

B_{KH} KH model constant

$$\dot{r}_p = \frac{r_p - r_c}{\tau_{KH}}$$

C_{KH} KH model constant

$$\tau_{KH} = \frac{3.726 C_{KH} \tau_p}{\Lambda_{KH} \Omega_{KH}}$$

Λ_{KH} fastest growing wave wavelength

Ω_{KH} fastest growing wave growth rate

$$\frac{\Lambda_{KH}}{r_p} = 9.02 \frac{\left(1 + 0.45 Z^{0.5}\right)\left(1 + 0.4 T^{0.7}\right)}{\left(1 + 0.87 We_g^{1.67}\right)^{0.6}}$$

σ surface tension

ρ density of droplet

Z Ohnesorge number

T Taylor number

$$\Omega_{KH}\left[\frac{\rho r_p^3}{\sigma}\right] = \frac{\left(0.34 + 0.385 We_g^{1.5}\right)}{\left(1 + Z\right)\left(1 + 1.4 T^{0.6}\right)}$$

We_g gas Weber number

After spray breakup:

$$\dot{r}_p = \frac{r_p - r_c}{\tau_{RT}}$$

$$\tau_{RT} = \frac{C_{RT}}{\Omega_{RT}}$$

$$\Omega_{RT} = \sqrt{\frac{2}{3\sqrt{3\sigma}} \frac{\left[|\mathbf{F}|(\rho_l - \rho_g)\right]^{1.5}}{\rho_l + \rho_g}}$$

$$r_C = B_{RT}\Lambda_{RT}$$

$$\Lambda_{RT} = 2\pi \sqrt{\frac{3\sigma}{|\mathbf{F}|(\rho_l - \rho_g)}}$$

C_{RT} RT model constant

Ω_{RT} fastest growing wave growth rate

$|\mathbf{F}|$ travel direction acceleration

Λ_{RT} wavelength

B_{RT} size constant

Droplet collision equations (O'Rourke model [186, 195])

$$\nu = \frac{N_2^n}{\forall} \pi \left(r_1^n + r_2^n \right)^2 \left| \mathbf{v}_1 - \mathbf{v}_2 \right|$$

$$P_n = e^{-\bar{n}} \frac{\bar{n}^n}{n!}$$

$$\bar{n} = \nu \Delta t$$

$$b = \sqrt{\theta_2} \left(r_1 + r_2 \right)$$

ν frequency of collision

1 "collector"

2 "droplet"

N_2^n droplet number in one parcel

$\forall$ cell volume containing "droplets" and "collectors"

P_n collision probability given by Poisson distribution for one "collector"

and n "droplets"

Δt computational time step

b collision impact parameter

θ_2 random number

Turbulence equations (RNG $k - \varepsilon$ model [186, 196])

$$\frac{\partial (\rho k)}{\partial t} + \nabla \cdot (\rho \mathbf{u} k) = -\frac{2}{3} \rho k \nabla \cdot \mathbf{u} + \sigma : \nabla \mathrm{u} + \nabla \cdot \left[\left(\frac{\mu}{Pr_k} \right) \nabla k \right] - \rho \varepsilon + \dot{W}^s$$

$\dot{W}^s$ working rate of turbulent eddies on spray breakup source term

Pr Prandtl number

C_{ε_1} 1.42

C_{ε_2} 1.68

C_{ε_3} $\quad C_{\varepsilon_3} = \dfrac{-1 + 2C_{\varepsilon_1} - 3m(n-1) + (-1)^{\delta} \sqrt{6} C_{\mu} C_{\eta} \eta}{3}$;

$$\frac{\partial(\rho\varepsilon)}{\partial t}+\nabla\cdot(\rho\mathbf{u}\varepsilon)=-\left(\frac{2}{3}C_{\varepsilon_1}-C_{\varepsilon_3}\right)\rho\varepsilon\nabla\cdot\mathbf{u}+\nabla\cdot\left[\left(\frac{\mu}{Pr_\varepsilon}\right)\nabla\varepsilon\right]$$

$$+\frac{\varepsilon}{k}\left[C_{\varepsilon_1}\sigma:\nabla\mathbf{u}-C_{\varepsilon_2}\rho\varepsilon+c_s\rho\varepsilon+c_s\dot{W}^s\right]-\rho R$$

$$C_\eta=\frac{\eta(1-\eta/\eta_0)}{1+\beta\eta^3}$$

$m=0.5\,,n=1.4$ (adiabatic process)

$$\delta=\begin{cases}1, & \nabla\cdot\mathbf{u}\le 0.0\\0, & \nabla\cdot\mathbf{u}>0.0\end{cases}$$

RNG $k-\varepsilon$ model rate-of-strain term:

$$R=\frac{C_\mu\eta^3\left(1-\eta/\eta_0\right)}{1+\beta\eta^3}\frac{\varepsilon^2}{k}$$

$$\eta=\frac{k}{\varepsilon}S$$

$$\eta_0=\sqrt{\frac{C_{\varepsilon_1}-1}{C_\mu\left(C_{\varepsilon_1}-1\right)}}$$

$$S_{ij}=\frac{1}{2}\left(\frac{\partial\bar{u}_i}{\partial x_j}+\frac{\partial\bar{u}_j}{\partial x_i}\right)$$

$$S=\sqrt{2S_{ij}S_{ij}}$$

$$\beta=0.012$$

Conservation equations

Continuity:

$$\frac{\partial\rho_m}{\partial t}+\nabla\cdot(\rho_m\mathbf{u})=\nabla\cdot(\rho D\nabla(\frac{\rho_m}{\rho}))+\dot{\rho}_m^C+\dot{\rho}^S\delta_{m1}$$

ρ mass density

t time

$\mathbf{u}$ fluid velocity

D Fick's Law coefficient of diffusion

δ Dirac delta function

a dimensionless number

p pressure of fluid

Momentum:	$\boldsymbol{\sigma}$ stress tensor

Momentum:

$$\frac{\partial(\rho\mathbf{u})}{\partial t} + \nabla\cdot(\rho\mathbf{u}\mathbf{u}) = -\frac{1}{a^2}\nabla p - \nabla(\frac{2}{3}\rho k) + \nabla\cdot\boldsymbol{\sigma} + \mathbf{F^S} + \rho\mathbf{g}$$

Energy:

$$\frac{\partial(\rho I)}{\partial t} + \nabla\cdot(\rho\mathbf{u}I) = -p\nabla\cdot\mathbf{u} - \nabla\cdot\mathbf{J} + \rho\varepsilon + \dot{Q}^C + \dot{Q}^S$$

$\boldsymbol{\sigma}$ stress tensor

$\mathbf{F}$ momentum gain rate per unit volume

$\mathbf{g}$ specific force on body, presumed constant

I specific internal energy, without chemical input energy

J heat flux

k turbulent kinetic energy

ε turbulent dissipation rate

Q energy source term

m mixture species

c chemistry source term

s spray source term

Combustion equations (CHEMKIN II [40])

Elementary reactions: $\displaystyle\sum_{m=1}^{M}\upsilon'_{mi}X_m \Leftrightarrow \sum_{m=1}^{M}\upsilon''_{mi}X_m \quad (i=1,...,I)$
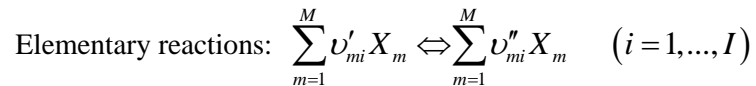
$$\dot{\omega}_m = \sum_{i=1}^{I}\upsilon_{mi}q_i \quad (m=1,..,\mathrm{M})$$

M number of chemical species

X_m arbitrary specie m

υ_{mi} specie m's stoichiometric coefficient

$'$ forward

$''$ reverse

$\dot{\omega}_m$ rate of production if specie m

q_i reaction i's variable for rate of process

$$\upsilon_{mi} = \upsilon''_{mi} - \upsilon'_{mi}$$

$$q_i = k_{fi} \prod_{m=1}^{M} [X_m]^{\upsilon'_{mi}} - k_{ri} \prod_{m=1}^{M} [X_m]^{\upsilon''_{mi}}$$

$$k_{fi} = A_i T^{\beta_i} \exp\left(\frac{-E_i}{R_c T}\right)$$

Specie m's density change: $\dot{\rho}_m^C = W_m \dot{\omega}_m$

Heat-release during combustion: $\dot{Q}^C = -\sum_{m=1}^{M} \dot{\omega}_m \left(\Delta h_f^\circ\right)_m$

$[X_m]$ specie m's molar concentration

k_{fi} Reaction i's forward reaction rate constant

k_{ri} Reaction i's reverse reaction rate constant

A_i pre-exponential factor

β_i temperature exponent

E_i activation energy

3.2 Experimental engine testbed

Figure 3-2 Picture of the engine testbed at the National University of Singapore.

Table 3-2 Engine specifications.

Engine characteristics	
Bore	9.2cm
Stroke	9.38cm
Compression ratio	18.5
Number of cylinders	4
Engine displacement	2494cm3
Connecting rod length	15.85cm
Piston bowl geometry	Omega-shaped
Aspiration type	Turbocharged
Fuel supply system	Common rail direct injection
Injector	Denso 6-hole injector
Rated engine power	75kW @ 3600rpm

Figure 3-2 shows a picture of the engine testbed, done entirely by AVL, at the National University of Singapore and Table 3-2 shows the engine specifications. The details of the engine testbed's instruments and sensors are given in Table 3-3. Concisely, the engine is a 4-cylinder engine with a

displacement of about 2.5 litres and it has a compression ratio of 18.5. This engine is a common rail direct injection compression ignition engine with turbocharging and it has a rated power of 75kW at 3600rpm. Many instruments and sensors are hooked up to the engine. A water-cooled passive dynamometer is used to measure the engine's torque and power while the crank angle encoder measures its speed. Moreover, an air flow meter is used to measure the flow rate of air into the engine and a pressure transducer is used to measure the in-cylinder pressure fluctuations. Also, exhaust gas sensors collect data on the emissions such as CO, NO and UHC. In this work, the purpose of the experimental results derived from the engine experiments is for the validation of simulation results in subsequent chapters.

Table 3-3 Engine testbed's instruments and sensors.

Instrument	Remarks
AVL Sensyflow P air flow meter	To measure air flow rate
AVL 733S.18 fuel balance	To measure fuel consumption ($\pm1\%$)
AVL GH13P water-cooled pressure transducer	To measure instantaneous in-cylinder pressure (±0.3bar)
AVL DP 160 water-cooled passive dynamometer	To measure engine torque ($\pm0.3\%$) and engine power
E instrument 4400 N emissions sensor	To measure exhaust emissions like CO (±10ppm for 0-200ppm and $\pm5\%$ for 201-2000ppm) and NO (±5ppm for 1-100ppm and $\pm5\%$ for 101-5000ppm)
AVL Digas 2200 emission sensor	To measure UHC (±10ppm) and calculate λ
AVL Indicom user interface	To compile all data from the sensors such as engine coolant temperature, engine speed, engine torque, air flow rate, in-cylinder pressure, rate of fuel consumption etc

3.3 Summary

In this chapter, an overview of the numerical and the experimental approaches are presented. The KIVA4-CHEMKIN [39, 40, 184-186] code will be used to simulate the in-cylinder spray, atomization, evaporation, mixing, combustion and emissions during DICI engine simulations. Furthermore, an in-house experimental engine testbed is used to carry out engine experiments to collect essential experimental data for simulation validation purposes.

This page was intentionally left blank.

Chapter 4 Development of a reduced kerosene reaction mechanism with embedded soot chemistry for diesel engines

4.1 Introduction

From Chapter 2, it can be seen that most kerosene surrogate mechanisms' ignition delay times were not extensively validated against that of kerosene shock tube as well as constant volume combustion experiments. It should be noted that a fuel's ignition delay will affect both the performance and emissions of diesel engines [16] and so extensive validation of ignition delay times under different conditions is important. Furthermore, as some mechanisms are rather huge in size as seen from Chapter 2, it is not practical for them to be used in engine simulations as it will consume much computational time. More importantly, it is extremely desirable to have a mechanism that can predict soot trends of kerosene in diesel engines as highlighted in Chapter 2. Although some mechanisms such as those from [150] and [154] have PAH formation reactions, the total number of reactions is just too big to be used for engine simulations.

Therefore, the objective of this chapter is to develop a relatively smaller but comprehensive kerosene reaction mechanism for diesel engine simulations. The developed mechanism must be able to reasonably predict soot trends

during kerosene combustion. Furthermore, to keep the mechanism size small,

kerosene will be represented by a single fuel component like in [175, 176].

Moreover, to ensure the reliability and robustness of the mechanism, a series

of vigorous validations will be carried out and they are (a) shock tube ignition

delay validation, (b) heat-release and ignition delay validation in a constant

volume combustion chamber and (c) optical engine validation.

4.2 Modelling methodology

It should be noted that distillate fuels such as kerosene contain aromatic

compounds [93] which contribute to the formation of soot. To construct a

mechanism with soot chemistry, PAH reactions are important as PAH

formation will eventually lead to the development of soot like in [199] and

[180]. Thus, the starting mechanism chosen for the development of the

kerosene reaction mechanism is a toluene reference fuels (TRFs) mechanism

developed by Wang et al. [200], containing 109 species amongst 543

reactions. Briefly, this mechanism comprises three fuel components, namely

n-heptane, iso-octane and toluene. It is validated against experiments for its

ignition delay times, laminar flame speeds, speciation data as well as engine

in-cylinder pressures and heat-release rates. Moreover, it contains PAH

formation reactions up to four aromatic rings (A_4) which is crucial for soot

formation. Considering the number of fuel components, PAH formation

reactions as well as the robustness of the mechanism, the mechanism is notably compact and reasonable in size. Refer to [200] for more details.

Keeping in mind the objective of this chapter, which is to represent kerosene fuel using a single component, and the fact that kerosene contains aromatic compounds which contribute to the formation of soot during combustion [201], a global reaction step was selected wherein $C_{12}H_{24}$ (kerosene) oxidizes to give an alkane and toluene like in [199]. The role of alkane is to replicate the negative temperature coefficient (NTC) characteristic of distillate fuels such as kerosene [53] while that of toluene is to contribute to PAH and soot formation during combustion [199]. Moreover, using a single fuel component to represent kerosene allows for $C_{12}H_{24}$ to take on kerosene thermo-physical properties in the KIVA4 fuel library [39] which is of great advantage when modelling kerosene spray combustion. Hence, a global reaction step was selected for the oxidation of $C_{12}H_{24}$.

Beginning from the base TRF mechanism, kerosene's species and their reactions are added to the base mechanism. Using diesel as an example, $C_{14}H_{28}$ was assumed to be oxidized by oxygen via a global reaction step to form n-heptane (NC_7H_{16}) and toluene (C_7H_8) in the ratio of 7:3 [199] (by considering carbon atoms) and this is as shown in Equation (4.1) below.

$$5C_{14}H_{28} + O_2 => 3C_7H_8 + 7NC_7H_{16} + 2H_2O \qquad (4.1)$$
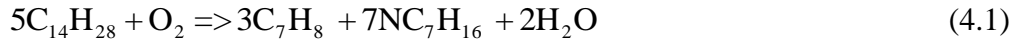
Similar to the case of diesel, the chemical formula of kerosene is assumed to be $C_{12}H_{24}$, with the same ignition delay times as that of real kerosene (Jet-A/JP-8). The employment of $C_{12}H_{24}$ is not foreign as Wang [176] from the National Aeronautics and Space Administration (NASA) also used it to represent kerosene. Similar to [199], a global reaction step is considered for the oxidation of $C_{12}H_{24}$ and it is shown in Equation (4.2) below.

$$7C_{12}H_{24} + O_2 => 3C_7H_8 + 7NC_9H_{20} + 2H_2O \qquad (4.2)$$
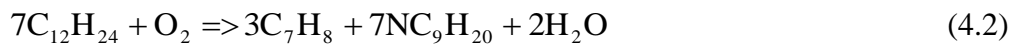
From Equation (4.2), $C_{12}H_{24}$ is oxidized to give a pseudo C_9 alkane and toluene in the ratio of 7.5:2.5[1]. This ratio is used since kerosene has a slightly lower aromatic content as compared to diesel [93]. Also, this strategy of using a pseudo C_9 alkane is partially similar to the approach used by Vandersickel et al. [151]. This approach is used so as to reduce the complexity and size of the kerosene mechanism since it is difficult and impractical to use a few components to match the ignition delay of kerosene as seen from [77], [150] and [90]. The major reactions for the pseudo C_9 alkane, which were identified through the work of Chang et al. [202], are initially adapted from the work of

---

[1] As seen from Equation (4.2), 7 moles of $C_{12}H_{24}$ oxidize to give 3 moles of toluene and 7 moles of pseudo C_9 alkane. On the left hand side of the equation, there are a total of 84 carbon atoms while on the right hand side there are 21 carbon atoms that belong to toluene and 63 carbon atoms that belong to the C_9 alkane. Hence, in terms of carbon atoms, there is 21/84 toluene: 63/84 C_9 alkane which gives the ratio 2.5:7.5.

Westbrook et al. [203] and added to the base mechanism. Following which, the reaction rates concerning their oxidation and that of Equation (4.2) are adjusted such that the ignition delay times of $C_{12}H_{24}$ match that of Jet-A/JP-8 shock tube experiments. It should be noted that the reaction rates of toluene reactions remained unchanged.

Subsequently, soot formation and oxidation reactions are added into the mechanism. The soot formation and oxidation reactions used in this work are adapted from [180, 199, 204] and modified to give the correct soot trends for kerosene combustion in diesel engines. Soot, C(S), is assumed to be formed from two species, C_4H_2 and A_4, through "graphitization processes" [205]. Refer to [205] for more detailed explanation. From the work of Vishwanathan and Reitz [206], they also assumed that the formation of C(S) comes from A_4. The soot formation reactions are shown in Equations (4.3) and (4.4) below.

$$C_4H_2 = 4C(S) + H_2 \tag{4.3}$$

$$A_4 = 16C(S) + 5H_2 \tag{4.4}$$

Moreover, oxidation of soot is assumed to occur by reacting with hydroxyl radicals (OH), oxygen (O_2) and water (H_2O) molecules [199, 204, 205]. The soot oxidation reactions are shown in Equations (4.5), (4.6) and (4.7) below.

$$C(S) + OH = CO + H \tag{4.5}$$

$$C(S) + O_2 = O + CO \tag{4.6}$$

$$C(S) + H_2O = CO + H_2 \tag{4.7}$$

In this chapter, C(S) is treated as a gas phase specie like in [199] and its formation and oxidation are purely governed by chemical kinetics.

The finalized mechanism in this work contains 122 species amongst 585 reactions, with major fuel components for kerosene ($C_{12}H_{24}$), n-heptane, iso-octane and toluene. The thermodynamic data for the mechanism are taken from [200, 203, 204]. It should be noted that the lower heating value (LHV) of $C_{12}H_{24}$ is approximately 44MJ/kg [207] which is quite close to the actual LHV of kerosene which has a value of about 43MJ/kg [93]. Table 4-1 shows the adjusted reaction rates for the global $C_{12}H_{24}$ reaction, the pseudo C9 reactions as well as the soot reactions. For the sake of completeness, the $C_{12}H_{24}$ kerosene reaction mechanism is made available under Appendix A.

Table 4-1 Initial and adjusted reaction rates for the global $C_{12}H_{24}$ reaction, the pseudo C9 reactions as well as the soot reactions.

Reactions	Ref.	Initial A factor	Adjusted A factor
$7C_{12}H_{24} + O_2 => 3C_7H_8 + 7NC_9H_{20} + 2H_2O$	[180, 199, 204]	1.00E+39	1.00E+51
$NC_9H_{20} + OH = C_9H_{19}\text{-}4 + H_2O$	[203]	9.400E+07	1.500E+08
$NC_9H_{20} + O_2 = C_9H_{19}\text{-}4 + HO_2$	[203]	4.000E+13	8.000E+15
$C_9H_{19}O_2\text{-}4 = C_9OOH4\text{-}5$	[203]	2.000E+11	1.500E+12
$C_9OOH4\text{-}5O_2 = C_9OOH4\text{-}5 + O_2$	[203]	1.367E+23	4.367E+23
$C_9KET4\text{-}5 = OH + NC_3H_7CO + NC_4H_9CHO$	[203]	1.050E+16	1.050E+17
$C_4H_2 = 4C(S) + H_2$	[180, 199, 204]	1.000E+04	1.000E+04
$A_4 = 16C(S) + 5H_2$	[180, 199, 204]	2.000E+03	2.000E+03
$C(S) + O_2 = O + CO$	[180, 199, 204]	3.000E+11	1.6875E+09
$C(S) + H_2O = CO + H_2$	[180, 199, 204]	3.000E+11	4.00E+10
$C(S) + OH = CO + H$	[180, 199, 204]	3.000E+12	3.00E+10

4.3 Shock tube 0-D ignition delay validation

As highlighted previously, the ignition delay of a fuel affects the performance and emissions of a diesel engine [16]. Hence, it is important to first validate the chemical delay of the $C_{12}H_{24}$ mechanism. Ignition delay times are determined using a code from [198, 208-210].

As there are sufficient shock tube data on Jet-A/JP-8 in literature, the chemical ignition delay times of $C_{12}H_{24}$ are validated against those Jet-A/JP-8 shock tube experiments. It should be noted that Jet-A and JP-8 are extremely similar chemically [38, 53]. The experimental shock tube results of Dooley et al. [77], Wang and Oehlschlaeger [53], Zhukov et al. [80], Davidson and Hanson [211] as well as those of Vasu et al. [76] are utilized. The expression $\tau \propto P^{-1}$ [76] is used to scale all shock tube data in this work for ease of comparison, where τ is the shock tube ignition delay time and P is the corresponding initial pressure. This expression was also used by Kim et al. [90] and Vasu et al. [76] for scaling purposes. Moreover, due to lack of experimental data for pressures above 30atm, a formula from the work of Zhukov et al. [80] is used to calculate the ignition delay times of Jet-A at 30atm, 40atm and 50atm between 1000-1400K.
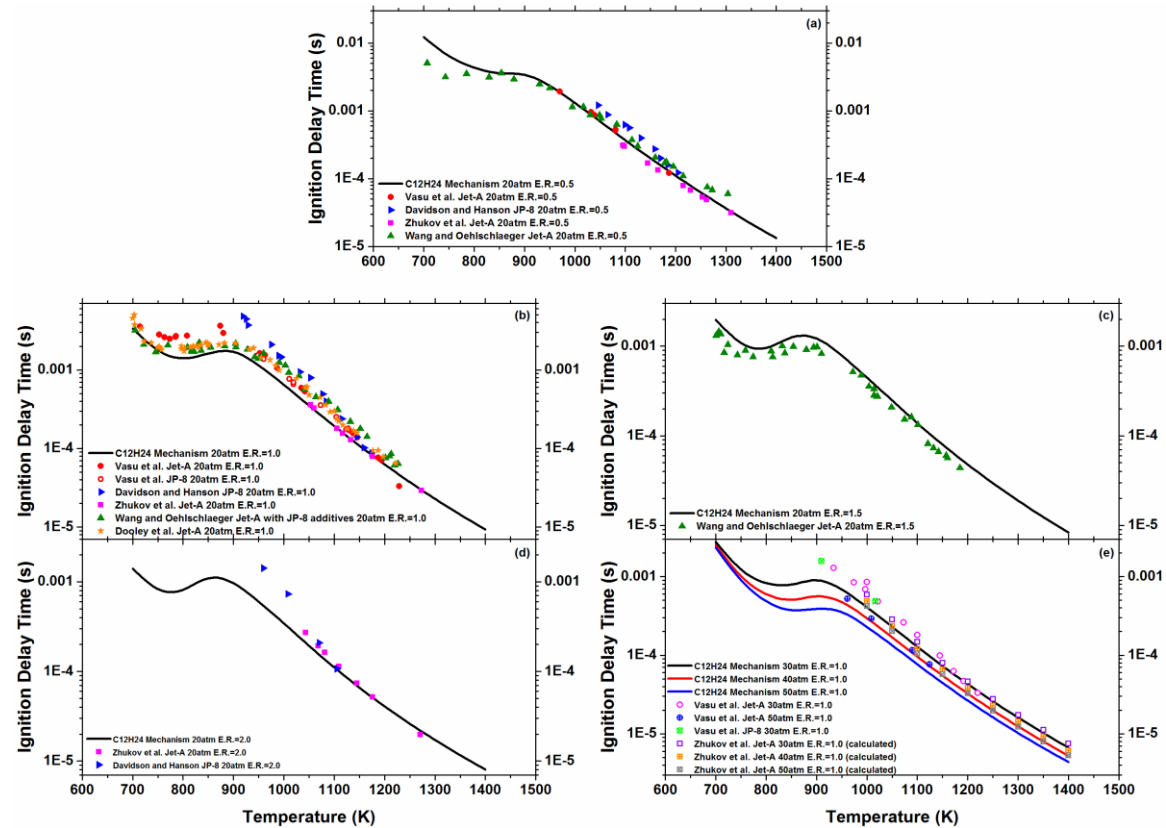
Figure 4-1 Comparisons between predicted and experimental shock tube ignition delay times are shown for initial conditions of 20atm and equivalence ratios of (a) 0.5, (b) 1.0, (c) 1.5 and (d) 2.0. Comparisons between predicted and experimental shock tube ignition delay times for initial conditions of 1.0 equivalence ratio and pressures of 30, 40 and 50atm are shown in (e). The experimental shock tube data are taken from the works of Dooley et al. [77], Wang and Oehlschlaeger [53], Zhukov et al. [80], Davidson and Hanson [211] as well as those of Vasu et al. [76].

Figure 4-1 shows the shock tube validation of the newly developed $C_{12}H_{24}$ kerosene mechanism under a wide range of temperatures, pressures and equivalence ratios. It is observed that the $C_{12}H_{24}$ kerosene mechanism performs well in predicting ignition delay times at an initial pressure of 20atm and at equivalence ratios of 0.5, 1.0, 1.5 and 2.0. The discrepancies between predicted and experimental ignition delay times are within an acceptable margin. Similar observation is made for an initial equivalence ratio of 1.0 and initial pressures of 30, 40 and 50atm. Therefore, the newly developed $C_{12}H_{24}$ kerosene mechanism has been validated for its chemical ignition delay.

4.4 Constant volume spray and combustion validation

In addition to 0-D ignition delay validation, constant volume combustion [93] is the next step to validate the fidelity of the new $C_{12}H_{24}$ kerosene mechanism under diesel engine conditions. Under real diesel engine conditions, apart from the chemical delay of the fuel, there is also the physical delay whereby the fuel that is sprayed into the combustion chamber undergoes the physical process of mixing and evaporation before combustion can occur [16]. In diesel engines, spray governs the atomization of the injected fuel, which in turn affects the engine's performance and emissions [44]. Factors such as injection pressures, injection rates as well as the number of injections per engine cycle will affect spray and the subsequent combustion process in

engines [44]. Hence, this step serves to take into consideration both the physical as well as chemical processes during the whole combustion period of kerosene under diesel engine conditions. The subsequent constant volume spray and combustion simulations are partially adapted from the work of Mohan et al. [193] and validated against the experiments of Sandia National Laboratory's (SNL's) constant volume combustion chamber (CVCC) [93]. Briefly, SNL's CVCC is shaped as a cube with its sides measuring 108mm each. It is able to replicate diesel engine conditions by allowing for very high ambient temperatures and densities. Furthermore, it is made optically accessible by Sapphire glass, thus allowing advance optical diagnostics to probe and monitor the whole combustion process. Refer to [93] for more information on SNL's CVCC.

To perform constant volume spray and combustion simulations, the KIVA4-CHEMKIN [39, 40] code is employed.

4.4.1 Constant volume spray validation

Prior to carrying out constant volume combustion simulations, it is needful to first validate both the simulated liquid and vapor penetrations because, as mentioned earlier, spray and the subsequent atomization of the fuel will affect the combustion process [44]. The purpose of this spray validation is to ensure that the grid size of the mesh as well as the number of parcels per gram of fuel

injected are optimized to ensure that the spray penetration is accurate, as seen from [193].

In this constant volume spray validation, the work of Pickett and Hoogterp [86] on JP-8 combustion is employed. In view of reducing computational time, half-cylindrical Cartesian meshes with solid sides are used instead of full-cylindrical Cartesian meshes. The use of half-cylindrical meshes for simulations is acceptable as seen from the work of Zhang et al. [212]. Three half-cylindrical meshes of different mesh sizes were created using the KIVA3V pre-processor [184]. This is better illustrated in Figure 4-2 which shows the coarse, medium and fine meshes. The fine mesh has a grid size of just slightly over 2mm in both the radial and axial directions, which is partially similar to the mesh used in [213] which has a grid size of 2mm in the axial direction.
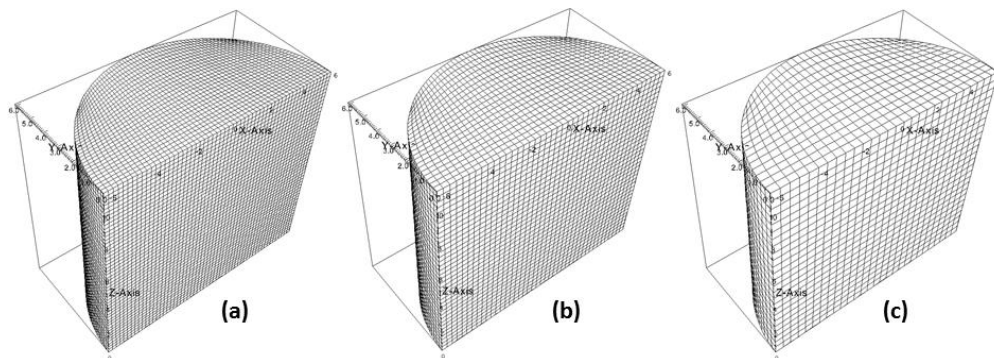
Figure 4-2 CVCC half-cylindrical Cartesian meshes with mesh sizes of (a) fine, (b) medium and (c) coarse.

Prior to the constant volume spray simulations using all three meshes, important information about the injector and experimental conditions are

acquired from the work of Pickett and Hoogterp [86]. The ambient condition

for their spray experiment is at a temperature of 850K and an ambient density

of 14.8kg/m^3 [86]. As the injected fuel mass is unavailable, an accurate

estimation had to be made. This is done through calculations using the

governing equations for fuel injection from the works of Naber as well as

Siebers [214]. The equations are

$$U_b = \sqrt{\frac{2(P_f - P_a)}{\rho_f}} \qquad (4.8)$$

$$\dot{m}_f = C_d A_f \rho_f U_b \qquad (4.9)$$

where, U_b is the exit velocity of fuel at the injector nozzle hole, P_f is the

common rail pressure, P_a is the ambient pressure, ρ_f is the density of fuel,

$\dot{m}_f$ is the mass flow rate of fuel, C_d is the coefficient of discharge and A_f

is the hole area of the injector nozzle. It should be noted that the fuel used by

Pickett and Hoogterp [86] is JP-8 and the experiment is performed under 21%

O$_2$ ambient condition [86]. However, due to the lack of thermo-physical

properties of JP-8, Jet-A thermo-physical properties in the KIVA4 fuel

library [39] are used instead because the properties of JP-8 and Jet-A are

identical [52]. It is assumed for the spray simulations that C_d is 0.93 [86] and

the density of JP-8 is also assumed to be the same as that of Jet-A at 808kg/m^3

from the KIVA4 fuel library [39]. Next, the ambient pressure and air

composition are taken from [215]. Furthermore, the spray angle is assumed

from [86] to be 15 degrees. All other important information for the spray

simulations are taken from [86]. It should be noted that the simulations are carried out only for spray without taking combustion into consideration as spray validation is the main focus in this section.

The results of the spray penetration simulations are post-processed using VisIt [216] software and subsequently measured using ImageJ [217] software. It should be noted that all simulation contours are processed using the VisIt [216] software in this thesis. The length of the vapor penetration is measured from the injector nozzle hole to the point where the mass fraction of the vapor is 0.001 [213]. From the results in Figure 4-3, it is observed that the fine mesh is the best for simulating the spray of JP-8 accurately as both the simulated liquid and vapor penetrations are closely matching with the experimental results [86].
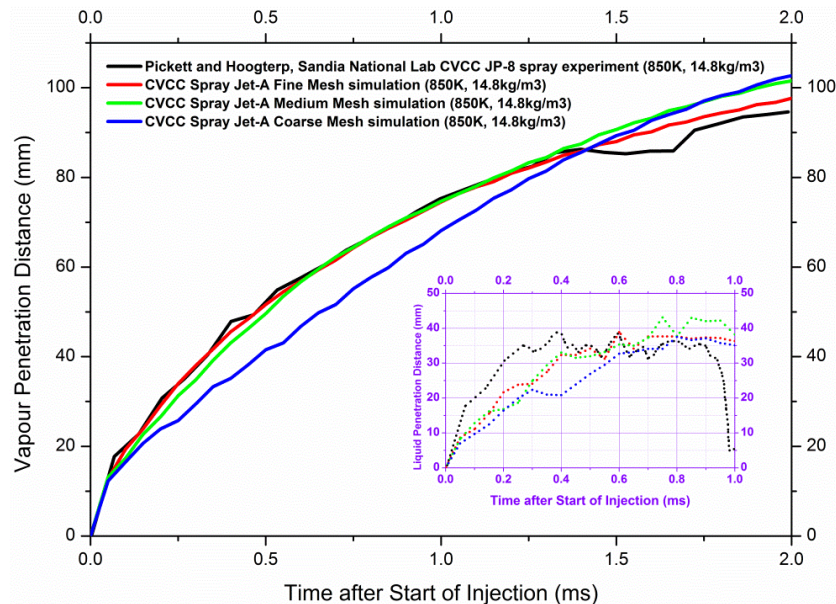
Figure 4-3 Constant volume spray validation under experimental ambient conditions of 850K, 14.8kg/m^3 and 21% O_2 and an injection duration of 1.0ms [86]. Comparison of simulated liquid and vapour penetrations (for coarse, medium and fine meshes) with experiment [86].

83

This reinforces the fact that Jet-A thermo-physical properties are identical to that of JP-8 [52]. From Figure 4-3, it is observed that the simulated vapor penetration matches that of experiment up to about 1.4ms after start of injection (ASI). After 1.4ms ASI, it is observed that the simulated vapor penetration is slightly over predicting as compared to experiment. This is not surprising as Pickett and Hoogterp [86] highlighted that the cool flame at about 1.5ms to 1.6ms actually "erodes" [86] the vapor tip. Furthermore, as the spray simulation was carried out without combustion taking place, it is logical that the vapor penetration predicted after 1.4ms ASI is longer than that of the experimental result. Moreover, the simulated liquid penetration for the fine mesh is also matching fairly well with experiment as the mean simulated liquid penetration for the fine mesh during steady state is very close to the experimental result. Therefore, it can be said that the fine mesh is the best in predicting spray penetration. More importantly, approximately the same number of parcels per gram of fuel injected in the spray simulations will also be used in the following constant volume combustion simulations to ensure that accurate results can be achieved.

4.4.2 Constant volume ignition delay validation

The work of Pickett and Hoogterp [86] is used for the constant volume ignition delay validation of the $C_{12}H_{24}$ kerosene mechanism. In the

experiments of Pickett and Hoogterp [86], JP-8 was used in the CVCC under a wide range of pressures and temperatures. Due to the lack of thermo-physical properties for JP-8, Jet-A thermo-physical properties from the KIVA4 fuel library [39] are used instead. This is acceptable as JP-8 and Jet-A have identical thermo-physical properties [52]. For more information on the input parameters for the simulations, refer to [86].
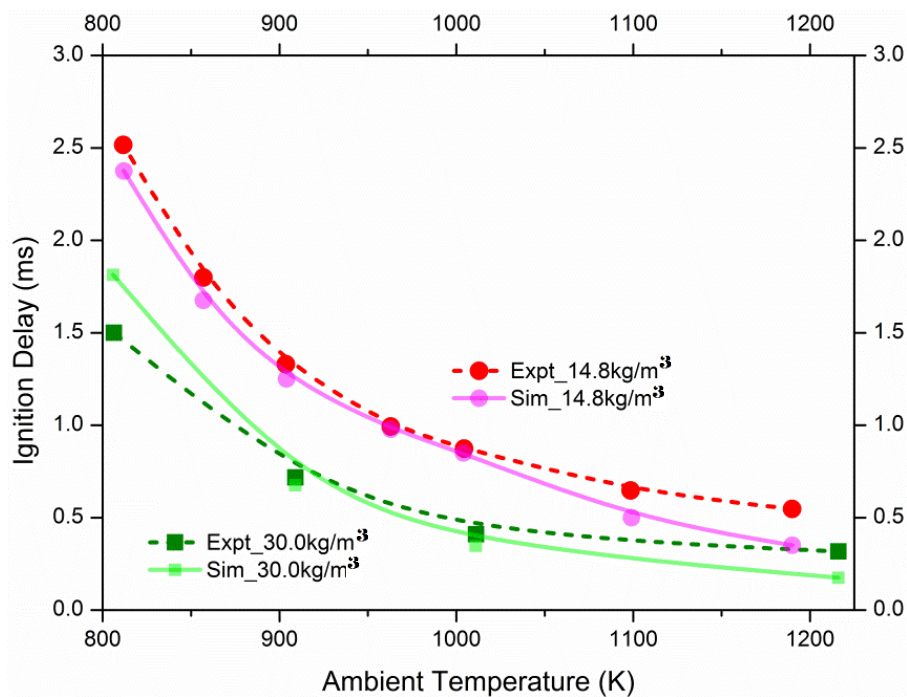
Figure 4-4 Comparisons between simulated and experimental ignition delay times of JP-8 for a wide range of temperatures with two different ambient densities of 14.8kg/m^3 and 30kg/m^3 at 21% ambient oxygen. Experimental results are from [86].

Figure 4-4 shows the simulated and experimental ignition delay times of JP-8. A wide range of temperatures with two different ambient densities of 14.8kg/m^3 and 30kg/m^3 at 21% ambient oxygen were used for the experiments [86]. It can be seen for both ambient densities that the predicted and experimental results are closely matching which means that the $C_{12}H_{24}$

kerosene mechanism together with the thermo-physical properties from the

KIVA4 fuel library [39] are performing well under diesel engine conditions.

4.4.3 Constant volume heat-release rate validation
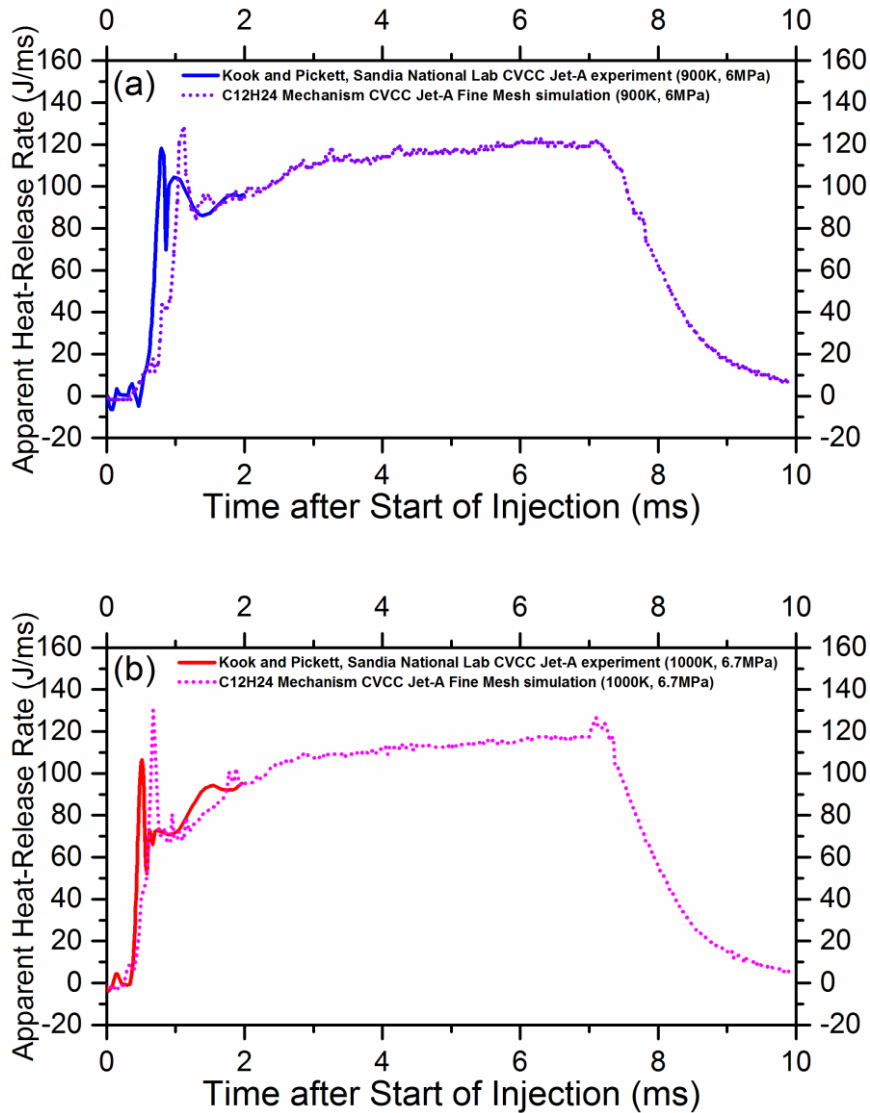
Figure 4-5 Comparisons between simulated and experimental AHRRs for ambient conditions of (a) 900K/6.0MPa and (b) 1000K/6.7MPa. Experimental results are from [93].

In addition to the constant volume ignition delay validations, comparisons

will be made for the predicted and experimental apparent heat-release rates

(AHRRs) for Jet-A fuel in a CVCC. The experimental results used is taken

from the work of Kook and Pickett [93] where Jet-A fuel is sprayed into

SNL's CVCC at two different ambient conditions of 900K/6.0MPa and

1000K/6.7MPa. Similar to previous constant volume ignition delay

simulations, constant injection rates are used. Input parameters for the

simulations are taken from [93] and [215].

Figure 4-5 shows the AHRRs of the simulations and the experiments for

the two ambient conditions. To compute the simulated AHRRs, the following

equation from [218] is used and it is

$$\frac{dQ}{dt} = \frac{\gamma}{\gamma - 1} P \frac{dV}{dt} + \frac{1}{\gamma - 1} V \frac{dP}{dt} \qquad (4.10)$$

where $\dfrac{dQ}{dt}$ is the AHRR, P is the pressure, V is the volume and γ is the

specific heat ratio. γ values for the 900K/6.0MPa and 1000K/6.7MPa cases

are assumed to be 1.3, similar to the value used in [218]. It is observed that the

times of initial peaks for both the simulated AHRRs are very close to that of

their respective experiments, with a small time difference between simulated

and experimental peaks. This confirms that the $C_{12}H_{24}$ kerosene mechanism is

reliable for predicting kerosene heat-release under diesel engine conditions.

From the constant volume combustion simulations, it is clearly seen that

the $C_{12}H_{24}$ kerosene mechanism is robust and reliable to be used for diesel

engine simulations.

4.5 Optical engine validation

The KIVA4-CHEMKIN code [39, 40] is used for engine simulations. The work of Yu et al. [99] on JP-8 combustion in an optical engine is used for the validation of the $C_{12}H_{24}$ kerosene mechanism. To the best of the authors' knowledge, Yu et al.'s [99] work provided the most comprehensive set of engine soot data for kerosene combustion as compared to other works in literature. Moreover, sufficient engine information is given by Yu et al. [99] in order for engine simulation to be carried out. Due to lack of JP-8 thermo-physical properties, Jet-A properties from the KIVA4 fuel library [39] is used instead. Also, an injection quantity of 8.3mg was assumed with a constant injection rate. As Yu et al. [99] highlighted that this particular optical engine suffers from high "blow-by losses", a lower initial pressure was used so that the simulated motoring pressure at top dead center (TDC) will be similar to experiment. This is done as the KIVA4-CHEMKIN code [39, 40] does not contain any blow-by models to account for the "blow-by losses" [99].
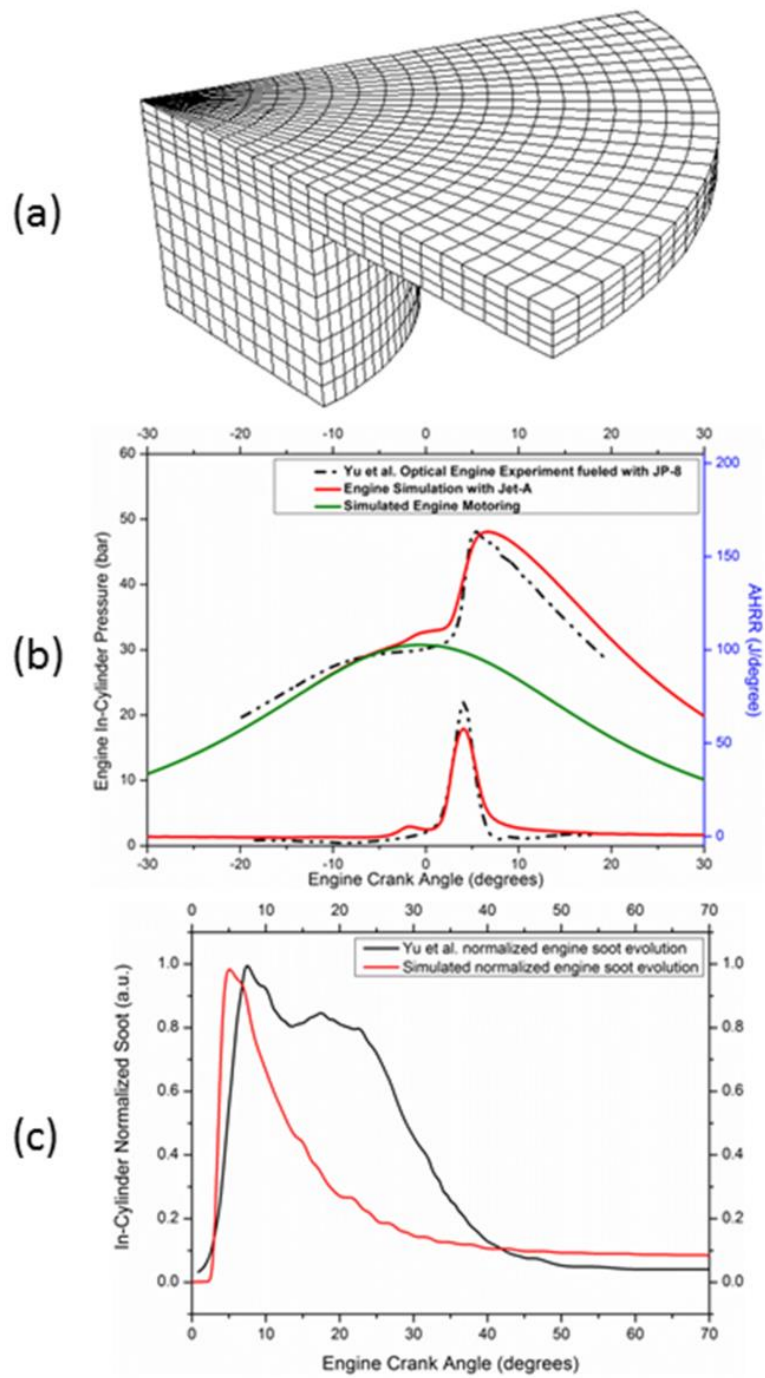
Figure 4-6 (a) Engine mesh with dimensions from [218] and comparisons between simulated and experimental in-cylinder (b) pressures, AHRRs and (c) normalized soot evolutions. Engine experiments are from [99].

Figure 4-6 shows the engine mesh with dimensions from [218] as well as the comparisons between simulated and experimental in-cylinder pressures, AHRRs and normalized soot evolutions. From the comparisons, it is seen that

there are some differences between simulated and experimental in-cylinder pressures. The differences, which are within acceptable limits, are primarily due to the "blow-by losses" [99] of the optical engine. From Figure 4-6c, which shows the normalized soot trends for both simulation and experiment, it is observed that the simulated soot formation and oxidation follow the same trends as that of the experiment. The only noteworthy difference between simulated and experimental soot trends is the "bump" [104] observed in the experiment, which may be caused by the circulation of soot rising from the squish section of the cylinder [104]. Apart from this difference, it is seen that the kerosene soot trend is reasonably predicted by the newly developed $C_{12}H_{24}$ kerosene reaction mechanism.

Therefore, from the optical engine validations for kerosene, it can be seen that the newly developed $C_{12}H_{24}$ kerosene reaction mechanism is able to predict the soot formation and oxidation trends of kerosene. It should be noted that by adjusting the reaction rates of the soot formation and oxidation reactions, the desired soot formation and oxidation trends can be achieved in different DICI engines and this implies that the $C_{12}H_{24}$ kerosene reaction mechanism can be used in any DICI engines to study kerosene's soot trends.

4.6 Summary

In conclusion, aligned with the fact that the use of kerosene in diesel engines is getting more prevalent, a reliable $C_{12}H_{24}$ kerosene reaction mechanism is developed. The ignition delay times of the $C_{12}H_{24}$ kerosene mechanism are validated with that of Jet-A/JP-8 shock tube experiments and reasonable agreements are seen between experiments and predictions. In addition to shock tube ignition delay validations, constant volume combustion validations are also carried out. The $C_{12}H_{24}$ kerosene mechanism is able to predict the ignition delay times of JP-8 in a CVCC reasonably for a wide range of engine-like conditions. Moreover, heat-release peaks of simulated and experimental Jet-A combustion in a CVCC are extremely close. Furthermore, the reaction mechanism is able to predict the combustion characteristics as well as soot formation and oxidation trends of kerosene under real engine conditions. In essence, the newly developed mechanism, containing 122 species amongst 585 reactions, is suitable for modelling kerosene combustion in diesel engines. This $C_{12}H_{24}$ kerosene reaction mechanism is smaller than the 2-component mechanism of Shrestha et al. [161] which has about 2.5 times the number of reactions. The developed $C_{12}H_{24}$ mechanism in this chapter will be useful to academic and industrial researchers and engineers.

This page was intentionally left blank.

Chapter 5 Development of a robust and compact kerosene-diesel reaction mechanism for diesel engines

5.1 Introduction

Previously in Chapter 4, a $C_{12}H_{24}$ kerosene reaction mechanism was developed for DICI engine simulations and it contained 122 species amongst 585 reactions. However, an even smaller and more compact reaction mechanism for kerosene can still be developed in order to further reduce computational time. This is especially important if a huge mesh with high cell density is used for simulations. Furthermore, it is highly desirable to develop a kerosene-diesel reaction mechanism for DICI engine simulations in order for researchers and engineers to have an alternative tool to study kerosene-diesel blends in diesel engines.

Therefore, the objective of this chapter is to develop a reliable and compact reaction mechanism for kerosene-diesel combustion under diesel engine conditions, with an extra focus on the kerosene sub-mechanism. Kerosene will only be represented by a single component, similar to the method used in Chapter 4, to allow for a more compact kerosene-diesel mechanism. The newly developed kerosene sub-mechanism must be able to imitate the heat-release characteristic and ignition delay times of real kerosene. As this chapter only focuses on replicating the heat-release and ignition delay times of

real kerosene, the simulation of kerosene's soot formation and oxidation trends will be included in Chapter 6. To ensure the fidelity of this new mechanism, especially for the kerosene sub-mechanism, a systematic validation will be performed: (a) 0-D shock tube ignition delay validation and (b) 3-D constant volume heat-release rate, OH profile and ignition delay validation.

5.2 Chemical modelling

In order to develop a kerosene-diesel reaction mechanism, a suitable reaction mechanism representing diesel has to be first selected. The diesel chemistry is usually represented simply by n-heptane and there are numerous reaction mechanisms available in literature for n-heptane, both skeletal [219] and detailed [220]. However, the diesel chemistry can also be represented by other alkanes. Recently, a highly reduced n-decane reaction mechanism developed by Chang et al. [202] was used to represent diesel. This particular n-decane reaction mechanism was chosen over other mechanisms to represent diesel because of a few reasons. Firstly, this n-decane reaction mechanism is reasonably compact, with only 40 species amongst 141 reactions [202]. Secondly, this mechanism contains a detailed $C_1/H_2/CO$ chemistry with a skeletal C_2-C_3 mechanism [202]. As highlighted by Chang et al. [202], the detailed $C_1/H_2/CO$ chemistry is important in allowing the n-decane mechanism

to accurately reproduce heat-release, laminar flame speeds, small species concentrations as well as ignition delay, while the skeletal C_2-C_3 mechanism allows for a more compact mechanism. This strategy of including a detailed C_1/H_2/CO chemistry with a skeletal C_2-C_3 mechanism, coupled to a few C_{10} reactions, allows the mechanism to replicate accurately the chemical characteristics of n-decane while simultaneously reducing the overall mechanism size [202]. The balance between mechanism size and accuracy is rather distinctive to Chang et al.'s [202] n-decane mechanism. Thirdly, from the works of Westbrook et al. [203] and Shen et al. [221], it was observed that the ignition delay times as well as reactivity of n-heptane right up to n-hexadecane are very similar. Since n-decane's chemical ignition delay times are also extremely similar to that of n-heptane, n-decane can be used as a substitute for diesel. Lastly, as highlighted by Chang et al [202], this n-decane mechanism was developed using the decoupling methodology which allows for a just few C_{10}-related reactions to dictate its ignition delay, but without having to adjust any reaction rates in the detailed C_1/H_2/CO chemistry. This is a major advantage as additional sub-mechanisms can easily be added to this n-decane base mechanism using the same decoupling methodology of Chang et al. [202] while maintaining the same reaction rates in the detailed C_1/H_2/CO chemistry.

After the selection of a suitable base mechanism for diesel, Chang et al.'s [202] decoupling methodology was applied to incorporate the kerosene sub-mechanism. From the work of Dooley et al. [56], they used four constrains to choose the right chemical components for Jet-A surrogate, which are the average molecular weight (MW), hydrogen-to-carbon (H/C) ratio, derived cetane number (DCN) and threshold sooting index (TSI). DCN was included to ensure that the Jet-A surrogate and real Jet-A have similar ignition delay times. More recently, Kim et al. [90] also developed Jet-A surrogates using eight constrains. Three of the eight constraints are chemical in nature and they are CN, H/C ratio and lower heating value (LHV). At this juncture, it is interesting to note that the constraints chosen by Dooley et al. [56] and Kim et al. [90] to imitate gaseous Jet-A combustion are similar. Like those constraints proposed by Dooley et al. [56] and Kim et al. [90] for kerosene fuels, two of their constraints are used for the formulation of the current kerosene sub-mechanism. The first constraint is that the LHV of the surrogate fuel must be similar to that of real kerosene and the second is that the ignition delay times of real kerosene fuel must be successfully reproduced by using the surrogate fuel as the performance and emissions of diesel engines are very sensitive to the ignition delay times of the fuel being used [16].

In order to overcome many of the aforementioned difficulties in developing a reliable and compact kerosene sub-mechanism for diesel engine simulations,

a single pseudo fuel component was introduced to represent kerosene in the sub-mechanism. Employing this approach is of great advantage as it will allow a single representative fuel component to mimic both the ignition delay times as well as heat release characteristics of a complex class of fuel while simultaneously allowing for a small sub-mechanism size. This approach is somewhat similar to the global reaction mechanism strategy used by Vandesickel et al. [151], in which one representative fuel component was also used to represent a class of fuel such as kerosene. The major advantage of this approach is the small mechanism size, with only 7 reactions and 8 species [151]. Chen et al.'s [199] approach is also similar to that of Vandersickel et al. [151], in which one fuel component was assumed to represent diesel in the reaction mechanism. Thus, the approach being employed in this current work calls for both the decoupling approach proposed by Chang et al. [202] as well as the single representative fuel component strategy by Vandesickel et al. [151] and Chen et al. [199]. This new hybrid approach has its advantages because the decoupling methodology enables the kerosene sub-mechanism to be small, yet being able to preserve a detailed $C_1/H_2/CO$ chemistry and simultaneously allows the sub-mechanism to mimic the combustion of a complex class of fuel. This new approach will now be termed as the pseudo-surrogate decoupling (PSD) approach.

Using the PSD approach, the representative component for kerosene in the sub-mechanism is assumed to be a pseudo C_{10} compound. A pseudo C_{10} alkane was assumed as a kerosene surrogate because an average kerosene molecule has about 10 to 12 carbon atoms [38]. Representing kerosene using an alkane is acceptable, just as how diesel combustion is represented simply by n-heptane chemistry such as in [222]. Since a pseudo C_{10} alkane was chosen as a representative for kerosene, it is assumed in this work that it has the same LHV, but different ignition delay times, as n-decane. It is noted that n-decane has a LHV of approximately 44.24 MJ/kg [223] while kerosene Jet-A has an approximate LHV of 43.2 MJ/kg [93]. This is a reasonable assumption as the difference in their LHVs is small. All thermodynamic properties and reactions for the kerosene sub-mechanism are adapted from the work of Chang et al. [202]. It should be noted that kerosene Jet-A/JP-8 will be primarily used for subsequent validations of the kerosene sub-mechanism due to the abundant availability of Jet-A/JP-8 data. For easier understanding of subsequent sections, Figure 5-1 shows the major reaction pathways of the n-decane and kerosene sub-mechanisms, together with their species and reactions. It should be noted that the reactions, species and their names, as shown in Figure 5-1, are adapted from [202, 203, 224].

Figure 5-1 Major reaction pathways for the newly developed kerosene-diesel reaction mechanism. [202, 203, 224] are acknowledged.
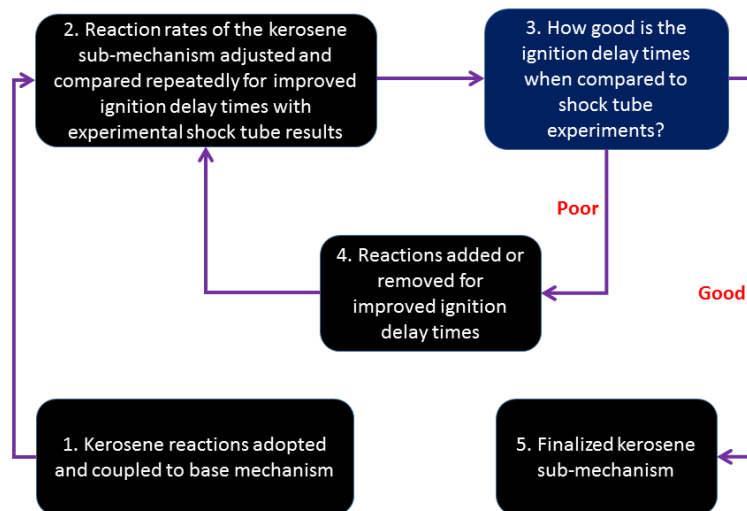
Figure 5-2 Strategy for the formulation of the kerosene sub-mechanism.

A sequence of steps is used for the formulation of the kerosene sub-mechanism as illustrated in Figure 5-2. Reactions and species describing kerosene oxidation were first added to the base mechanism. It is assumed that the representative pseudo kerosene C_{10} alkane (termed "KERO" from here on) undergoes similar high and low temperature oxidation, isomerization as well as decomposition processes [203] as that of actual n-decane and hence, the reactions and their rates for the kerosene sub-mechanism was first adapted from [202]. As real kerosene contains hundreds of compounds [77], it is not practical to include all of them and their reactions in the reaction mechanism due to size constraint. Certain chemical components, which are present in real kerosene, such as aromatics and cycloalkanes [56] and their respective reactions, are excluded from the mechanism. To allow the kerosene sub-mechanism to replicate kerosene combustion, only essential species and reactions are incorporated. At first, the pre-exponential (A) factor of the kerosene reactions were adjusted to match the ignition delay times of Jet-A/JP-8 shock tube experiments. However, to better match the ignition delay times under such a wide range of conditions for Jet-A/JP-8, especially in the region of high equivalence ratios and high temperatures, one of the existing reactions in the kerosene sub-mechanism was replaced by KR4 ($KERO \rightarrow KERO * + H$). This reaction was adapted from the work of Westbrook et al. [203] as it was classified as a high temperature single

100

molecular decomposition reaction. This means that the reaction governs the decomposition of alkanes under high temperatures and equivalence ratios. Subsequently, the reaction rates for the kerosene sub-mechanism were again readjusted as the addition of KR4 affects the overall ignition delay times. It was confirmed that KR4 is crucial in improving the ignition delay times at regions of high equivalence ratios and temperatures. The reaction rate adjustments for the kerosene sub-mechanism are shown in Table 5-1.

Table 5-1 Adjusted A factors for kerosene sub-mechanism.

Reaction	Kerosene Reactions	Ref.	Original A factor	Adjusted A factor
KR1	$KERO + O_2 \leftrightarrow$ $KERO * + HO_2$	[202]	7.00E+12	**2.90E+12**
KR2	$KERO + OH \leftrightarrow$ $KERO * + H_2O$	[202]	5.00E+07	**7.70E+06**
KR3	$KERO + H \rightarrow$ $KERO * + H_2$	[202]	1.00E+08	**1.00E+11**
KR4	$KERO \leftrightarrow$ $KERO * + H$	[203]	1.00E+14	**7.00E+17**
KR5	$KERO * + O_2 \leftrightarrow$ $KERO - OO$	[202]	3.00E+12	**4.30E+12**
KR6	$KERO - OO \leftrightarrow$ $KERO - OOH$	[202]	1.51E+11	**1.51E+11**
KR7	$KERO - OOH + O_2 \leftrightarrow$ $OO - KERO - OOH$	[202]	5.56E+10	**7.56E+12**
KR8	$OO - KERO - OOH \leftrightarrow$ $KEROket + OH$	[202]	8.91E+10	**7.31E+08**

KR9	$KEROket \rightarrow$ $CH_2O + C_5H_{11}CO + C_3H_6 + OH$	[202]	3.98E+15	**9.98E+16**
KR10	$KERO* + O_2 \leftrightarrow$ $KERO\# + HO_2$	[202]	3.16E+11	**2.16E+12**
KR11	$KERO\# + O_2 \leftrightarrow$ $2C_3H_6 + C_2H_5 + CH_2O + HCO$	[202]	3.16E+13	**5.16E+11**

It should be noted that the high A factors are a result of reaction rate adjustments. Due to using Chang et al.'s [202] decoupling methodology, the reaction rates of the kerosene sub-mechanism have been adjusted substantially in order to match the experimental Jet-A/JP-8 shock tube results. In Chang et al.'s [202] work on the n-decane mechanism, they have also highlighted that the adjusted reaction rates are quite different from original reaction rates because of the need to match n-decane experimental shock tube data. However, it is worthy to note that the decoupling methodology has produced reliable results as seen in [202, 225].

The robustness of the final kerosene-diesel mechanism which contains only 48 species amongst 152 reactions, inclusive of an oxides of nitrogen (NO_x) mechanism originally from Chang et al. [202], will be established in the coming sections through a series of vigorous validations. These validations will ensure that the kerosene sub-mechanism is reliable in reproducing the heat-release characteristics and ignition delay times of real kerosene.

5.3 0-D Ignition delay validation

0-D ignition delay validations from 700K to 1400K will be carried out for the newly developed kerosene-diesel reaction mechanism.

5.3.1 0-D Ignition delay validation for kerosene sub-mechanism

The kerosene sub-mechanism is validated extensively with shock tube experimental results available from the literature. A substantial amount of shock tube experiments were carried out for both Jet-A as well as JP-8 by many researchers such as Vasu et al. [76], Davidson and Hanson [211], Zhukov et al. [80], Wang and Oehlschlaeger [53] and Dooley et al. [77]. The ignition delay times of the kerosene sub-mechanism are validated against these shock tube results of Jet-A and JP-8. Wang and Oehlschlaeger [53] have shown in their work that the ignition delay times of Jet-A doped with JP-8 additives are indeed almost identical with that of pure Jet-A. Because of the extreme similarity in ignition delay times between Jet-A with and without JP-8 additives, it is reasonable to compare the kerosene sub-mechanism's ignition delay times to that of Jet-A as well as JP-8. The correlation $\tau \propto P^{-1}$, where τ and P are the ignition delay time and the initial pressure respectively, which was also used by Vasu et al. [76] and Kim et al. [90], is used here to scale all experimental shock tube results in Figure 5-3 and Figure 5-4 for ease of comparison.
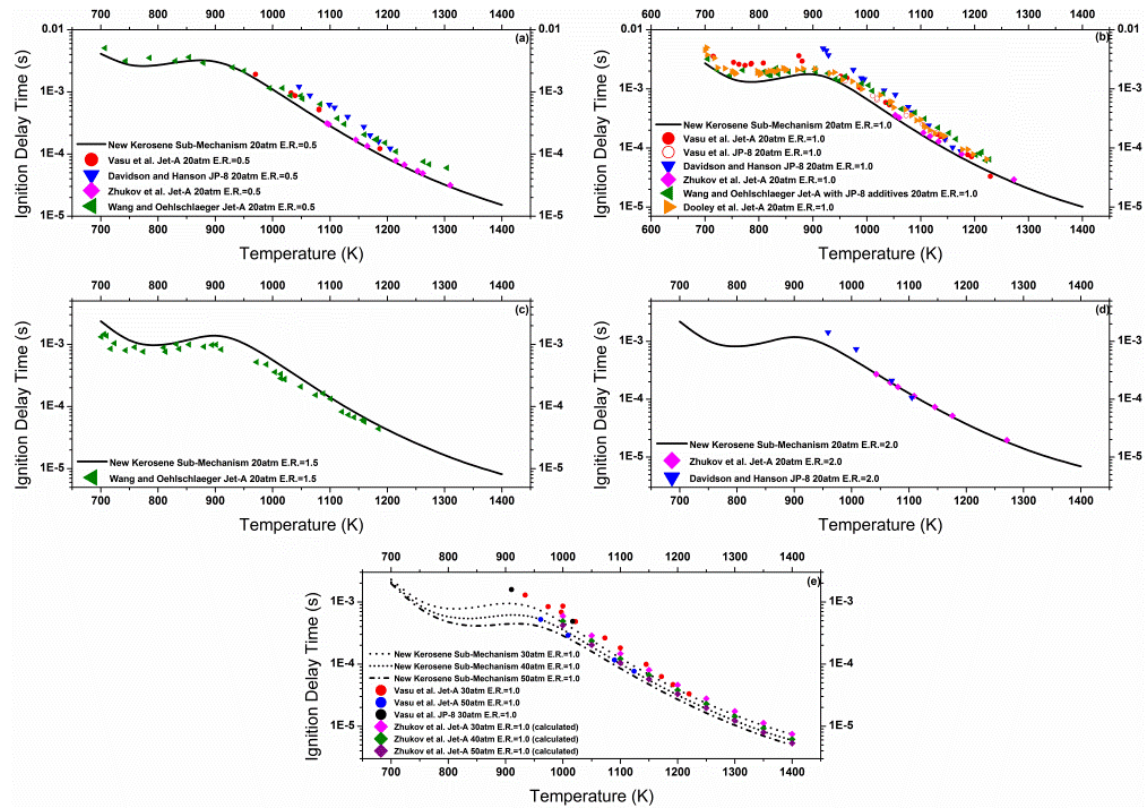
Figure 5-3 Ignition delay times validation for the new kerosene sub-mechanism with Jet-A/JP-8 experimental shock tube results (from Vasu et al. [76], Davidson and Hanson [211], Zhukov et al. [80], Wang and Oehlschlaeger [53] and Dooley et al. [77]) for initial shock tube conditions of (a) 20atm/0.5 equivalence ratio, (b) 20atm/1.0 equivalence ratio, (c) 20atm/1.5 equivalence ratio, (d) 20atm/2.0 equivalence ratio and (e) 1.0 equivalence ratio and 30/40/50atm.

Validation of ignition delay times are done starting with initial shock tube conditions of 20atm and 1.0 equivalence ratio. As observed from Figure 5-3b, the predicted ignition delay times of the kerosene sub-mechanism at initial shock tube conditions of 20atm and 1.0 equivalence ratio generally agree well with experimental results. The validation of ignition delay times is also extended to other conditions. It is done for initial shock tube conditions of 20atm and at equivalence ratios of 0.5, 1.5 and 2.0. As seen from Figure 5-3a, c and d, the predicted and experimental results are closely matching in general. Moreover, validation is also done for initial shock tube conditions of 1.0 equivalence ratio and at pressures of 30atm, 40atm and 50atm. For this validation, Zhukov et al.'s [80] experimentally determined equation is used to calculate the ignition delay times for a temperature range of 1000K to 1400K and for pressures of 30atm, 40atm and 50atm due to a lack of experimental data at these elevated pressures and temperatures. Refer to [80] for more details. In general, from Figure 5-3e, the kerosene sub-mechanism's predicted ignition delay times were reasonably validated at these elevated pressures and temperatures. Furthermore, at these elevated pressures and temperatures, the predicted ignition delay times of the kerosene sub-mechanism are fairly close to the results of Vasu et al. [76].

Hence, it can be seen that the predicted ignition delay times of the kerosene sub-mechanism have been reasonably validated under an extensive range of

conditions. This has proven that the PSD approach, using only one pseudo fuel

component, is sufficient in reproducing the ignition delay of distillate fuels.

5.3.2 0-D Ignition delay comparison for different kerosene mechanisms

This new kerosene sub-mechanism's predicted ignition delay times are

compared with those of other existing mechanisms. From Figure 5-4, under

initial shock tube conditions of 20atm and 1.0 equivalence ratio, it can be seen

that the new sub-mechanism's predicted ignition delay times have an overall

reasonable agreement with experimental results.
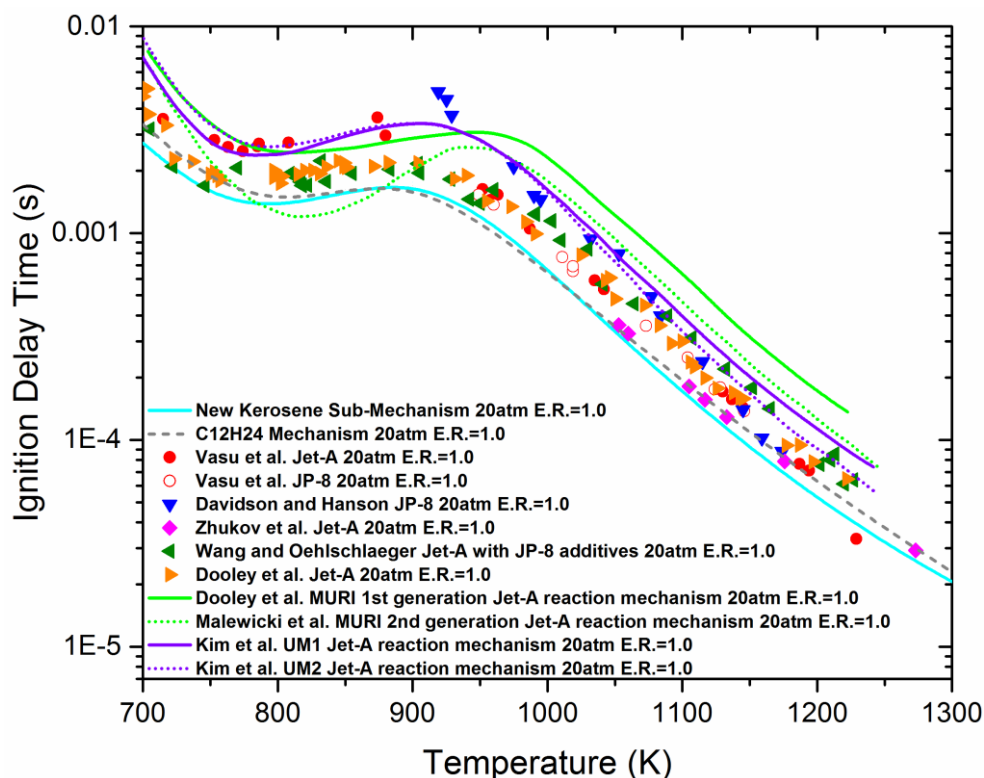
Figure 5-4 Comparison of ignition delay times of Jet-A/JP-8 experimental shock tube results (from Vasu et al. [76], Davidson and Hanson [211], Zhukov et al. [80], Wang and Oehlschlaeger [53] and Dooley et al. [77]) and that of available Jet-A surrogate mechanisms (from and Dooley et al. [77], Malewicki et al. [150] and Kim et al. [90]) together with the new kerosene sub-mechanism and the previously developed $C_{12}H_{24}$ kerosene mechanism for initial shock tube conditions of 20atm and 1.0 equivalence ratio.

5.3.3 0-D Ignition delay validation for n-decane sub-mechanism
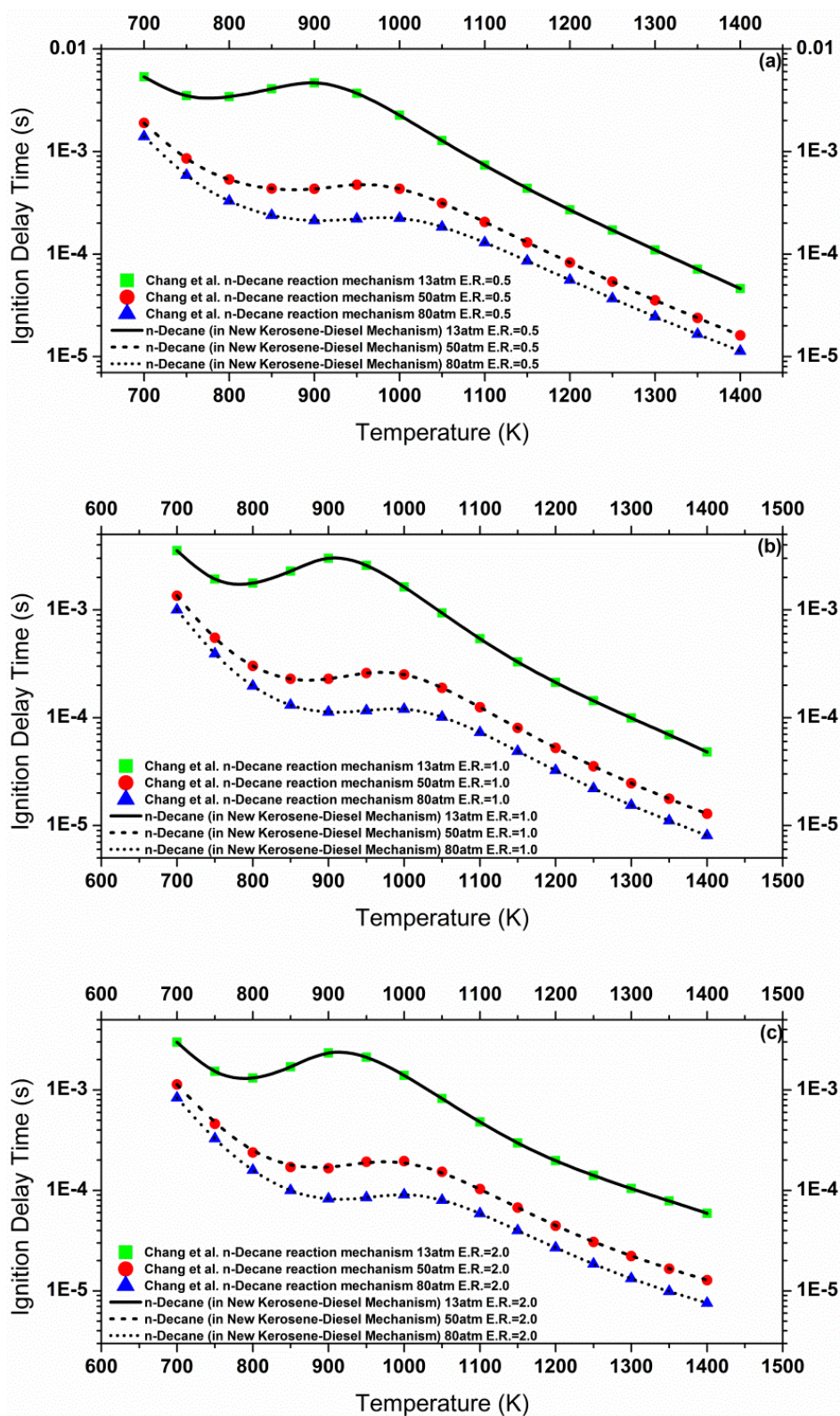
Figure 5-5 Ignition delay times validation for n-decane sub-mechanism in the new
kerosene-diesel mechanism with Chang et al.'s [202] n-decane mechanism for initial
shock tube conditions of 13/50/80atm and equivalence ratios of 0.5/1.0/2.0 [202].

The n-decane sub-mechanism's predicted ignition delay times are validated for three equivalence ratios of 0.5, 1.0 and 2.0 and at elevated pressures of 13atm, 50atm and 80atm [202] by comparing it to that of the original n-decane mechanism of Chang et al. [202]. This is sufficient because Chang et al.'s [202] original n-decane mechanism's predicted ignition delay times had already been extensively validated against a wide range of shock tube experiments. Not surprisingly, as observed from Figure 5-5, there is no difference between the predicted ignition delay times of the n-decane sub-mechanism and Chang et al.'s [202] original n-decane mechanism.

5.4 Constant volume combustion validation

The experimental results used in this section for the constant volume combustion validations are taken from SNL's CVCC experiments [93]. Prior to the constant volume combustion simulations, important information such as the injector specifications and experimental conditions are taken from the studies of Kook and Pickett [93] and SNL's website [215]. As the injected fuel mass amounts are unavailable, accurate estimations had to be made. This is done by using Equations (4.8) and (4.9) as shown in Chapter 4. By assuming the same coefficient of discharge of 0.89 [215] for the nozzle used in [93], for both Jet-A and another jet fuel surrogate from [93], under similar injection pressures of 150MPa [93], the injected mass of fuel are calculated. The density

of Jet-A used in the calculations is assumed to be 808kg/m^3, which is the same value used in the KIVA4 fuel library [39]. CVCC validations for Jet-A are done for two ambient conditions which are at 900K and 1000K, with pressures of 6.0MPa and 6.7MPa respectively [93]. In the simulations, a square injection profile is assumed [214]. Next, the thermo-physical properties of Jet-A from the KIVA4 fuel library [39] are used in the simulations. Furthermore, a spray angle of 21 degrees is used [54].

Hence, the AHRRs obtained using the fine mesh are compared to that of the experimental results, which are taken from the works of Kook and Pickett [93], for both conditions. Figure 5-6 shows the comparison between the experimental [93] and the simulated AHRRs. It can be seen that the simulated results are rather close to that of the experimental results for both conditions as their first AHRR peaks are quite close, with just a difference of about 0.407ms and 0.411ms for the 900K and 1000K conditions respectively. Moreover, the starting trends for both experiments and simulations are similar in that their AHRRs increase to a maximum value and then decrease to a stabilized value.
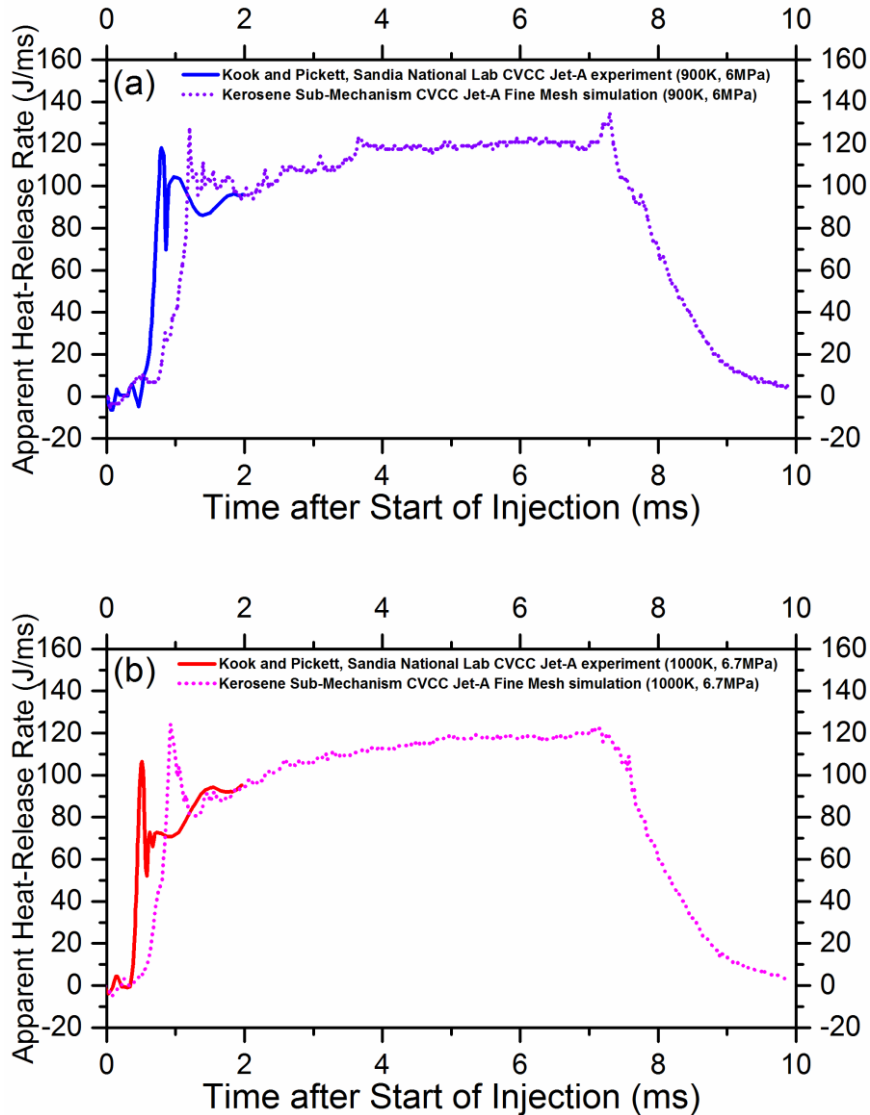
Figure 5-6 Comparison of simulated AHRRs using fine mesh with that of SNL's CVCC experiments [93] at (a) 900K/6.0MPa and (b) 1000K/6.7MPa.

Furthermore, from Figure 5-7, it can be seen that under both ambient conditions, the simulated results are comparable to the experimental [93] results. It should be noted, at this point, that the VisIt [216] software is used to generate the simulated images in Figure 5-7. Also, the simulated images in Figure 5-7 are taken from the mid-plane of the fine mesh. It can be observed that the OH profiles for both the simulation and experimental results are quite similar. More importantly, it is observed that the simulated flame lift-off

lengths (FLOLs) are also reasonably matching with that of the experimental FLOLs under both ambient conditions. It should be noted that the time frames chosen in Figure 5-7 are similar to those used in [92]. Next, from the work of Pickett et al. [226], it can be seen that FLOL is also affected by the chemistry of the fuel itself because FLOL generally lengthens with an increase in ignition delay times of a fuel. Another work by Kook and Pickett [93] also spots the same general trend. Moreover, Donkerbroek et al. [227] have highlighted that FLOL is very much dictated by the fuel chemistry. Therefore, it can be established that under the 900K/6.0MPa and 1000K/6.7MPa ambient conditions for both experiments and simulations, the fuel chemistry is crucial in governing the FLOL. It can be clearly seen from the simulation results that the chemistry of the newly developed kerosene sub-mechanism is robust enough to replicate kerosene combustion under diesel engine conditions because the simulated FLOLs are similar to that of experiments. Moreover, it is observed that the fine half-cylindrical mesh is the best candidate for both constant volume spray and combustion simulations.
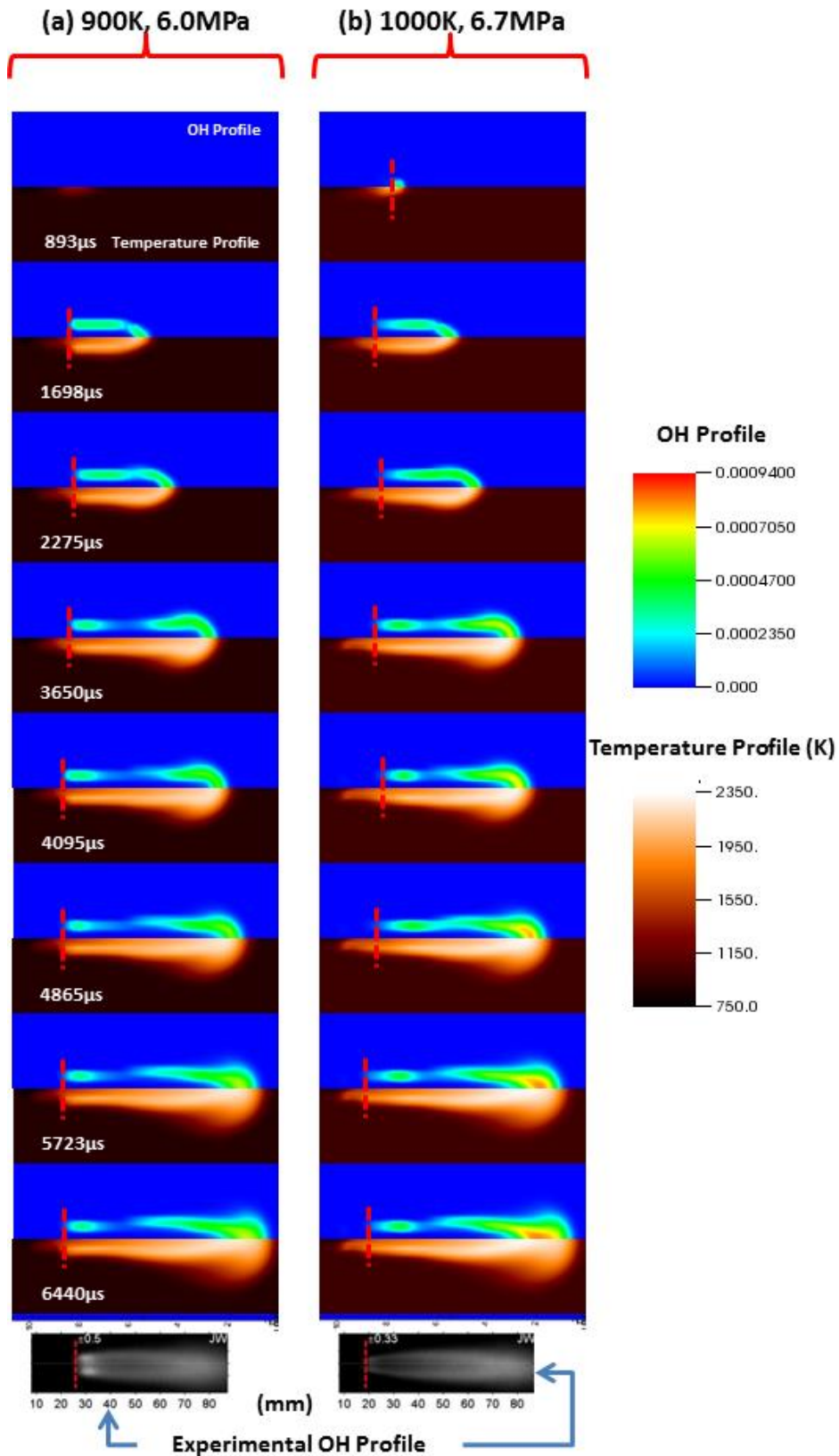
Figure 5-7 Comparison of OH profiles between experiments [93] and simulations for conditions of 1000K/6.7bar and 900K/6.0bar in a CVCC. Time frames chosen are similar to those used in [92]. It should be noted that the length scales for both experimental and simulation results are calibrated and aligned to each other.
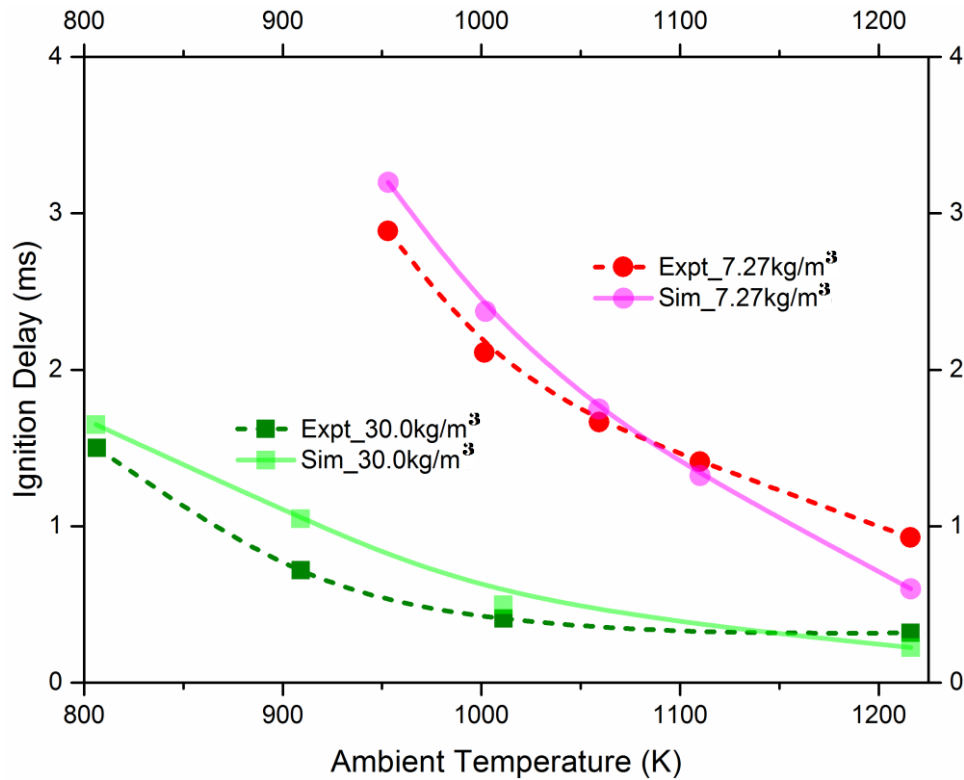
Figure 5-8 Constant volume ignition delay simulation and JP-8 experimental results from [86], under 21% ambient oxygen. Refer to [86] for more details.

Although the kerosene sub-mechanism was validated primarily with Jet-A data, further constant volume ignition delay comparisons are made with JP-8 experiments from [86]. This is a reasonable comparison because JP-8 is extremely similar to Jet-A in terms of its chemical properties and physical characteristics [89]. Figure 5-8 shows the ignition delay times of the simulated results and JP-8 experiments in a CVCC. It should be noted that for the simulations, Jet-A thermo-physical properties from the KIVA4 fuel library [39] was used and the injection duration was assumed from [215] to be 4ms. Furthermore, Equations (4.8) and (4.9) from Chapter 4 are used to do the necessary calculations needed for the simulations. For more experimental details, refer to [86]. It can be observed from Figure 5-8 that under both high

and low ambient densities, for a wide range of temperatures, the ignition delay times for both simulation and experimental results are rather similar. This comparison proves that the developed kerosene sub-mechanism in this work is reasonably well suited to be used for diesel engine simulations.

5.5 Summary

In summary, a highly compact and reliable kerosene-diesel reaction mechanism containing only 48 species and 152 reactions was developed using a PSD approach for diesel engine simulations. This new kerosene-diesel reaction mechanism underwent a series of vigorous validations. Firstly, the ignition delay times of the kerosene sub-mechanism were extensively validated with that of shock tube experiments. Overall, the ignition delay times of the sub-mechanism were reasonably validated under a wide range of conditions. Secondly, the kerosene sub-mechanism was used for CVCC validations. Through the CVCC validations, it is observed that the simulated AHRRs, FLOLs and ignition delay times are comparable to that of experiments, which means that the chemistry of the new kerosene sub-mechanism is suitable to describe kerosene combustion under diesel engine conditions. In essence, it can be concluded that this new kerosene-diesel mechanism is robust and compact enough to be used for diesel engine simulations and it will be useful for the research community.

Chapter 6 Effects of injection rate-shapes and bowl geometries on the combustion characteristics and emissions formation of a kerosene-diesel fueled diesel engine

6.1 Introduction

Researchers have been devising various methods to reduce engine emissions. One way is via exhaust aftertreatment devices such as diesel particulate filter (DPF) [228] and selective catalytic reduction (SCR) [229] to reduce soot and oxides of nitrogen (NO_x) emissions respectively. Another alternative method is by using environmentally friendly fuels such as biodiesels [230] and alcohols [231-235], which are carbon-neutral, renewable and sustainable energy sources. The third method is by controlling the combustion process to curb emissions. It is well-known that high local in-cylinder temperature produces large amounts of NO_x while high equivalence ratios will result in more carbon monoxide (CO) and soot emissions [236]. From the literature review done in Chapter 2, it can be seen that kerosene fueled diesel engines operating under high load conditions generate higher amounts of NO_x emissions as compared to diesel fueled diesel engines. However, one promising method to achieve lower NO_x emissions without having to make too much

modifications to existing conventional diesel engines is by using injection rate-shaping [44, 237]. This is possible because by injecting less fuel during the initial part of the injection period, it will result in lower peak heat-release during the premixed combustion phase. To the best of the author's knowledge and from [44], injection rate-shaping in kerosene fueled diesel engines is unexplored. This may be due to the fact that highly defined injection rate-shapes are made possible only with advancements in diesel injector technology in recent years as seen from [238]. In the past, attempts had been made for mechanical injectors to achieve different rate-shapes by altering the cam contour [44]. However, this meant that effective rate-shaping can only be achieved at certain engine operating conditions. The current generation diesel injectors are solenoid-driven [239] and are controlled by onboard vehicle electronics. This type of injectors allows for more flexibility during fuel injection such as permitting multiple injections. Injection rate-shaping using a solenoid injector is made possible by positioning injection signals close to one another such that two or more individual injections merge to give different rate-shapes [239]. This, however, does not give the desired rate-shapes. In recent years, the latest generation diesel injectors are piezoelectric injectors whereby the needle lift is controlled by a piezo-stack [240]. This latest innovation has allowed needle response time to be extremely fast [241]. This means that highly defined injection rate-shapes can be practically achieved in diesel engines with much

ease.

Some work done over the recent years have shown the results of injection rate-shaping on engine combustion. Juneja et al. [213] from the University of Wisconsin-Madison had shown through numerical simulations that injection rate-shaping significantly affected both liquid and vapor penetrations, which in turn affected the subsequent combustion process and emissions formation. From their work concerning triangular rate-shapes, it was seen that higher initial injection velocity caused good atomization and air entrainment of fuel spray, and this caused the location of the first ignition to be furthest from the injector nozzle, and hence the subsequent flame lift-off length (FLOL) was the longest as compared to the case with lower initial injection velocity. Consequently, with high injection velocity, soot formation was low and NO_x formation was increased. Apart from studying the effects of triangular injection rate-shapes, Desantes et al. [242, 243] investigated the effects of boot-type rate-shapes on engine performance and emissions. From their two-part study, they concluded that long boot length and low boot pressure decreased NO_x emissions but increased brake specific fuel consumption (BSFC) and soot emissions. Moreover, they discovered that boot-type rate-shapes caused substantial change to the diffusion combustion regime as compared to the premixed combustion regime. In addition to just using pure injection rate-shape strategies, Ghaffarpour et al. [244] had shown that NO_x reduction could be as

high as 50% under certain engine operating conditions, when an intercooler was used in conjunction with injection rate-shape strategies. Furthermore, Shuai et al. [237] investigated via numerical simulations the effects of both injection timing and rate-shaping on the performance and emissions in a CI engine. They found that CO, unburnt hydrocarbon (UHC) and soot emissions could be effectively cut down by employing rectangular-type and boot-type rate-shapes compared to other types of rate-shapes. Also, from a recent review paper by Mohan et al. [44], it was generally seen that injection rate-shaping was able to lessen NO_x emissions with the compromise of BSFC and soot emissions. Recently, a notable work by Macian et al. [240] had proven that piezoelectric injectors were capable of producing highly defined injection rate-shapes such as boot-type and ramp-type injection profiles. They highlighted from their experiment that rate-shaping was able to control the amount of fuel burnt during the premixed combustion phase, which in turn affected NO_x production and engine noise. Moreover, it was noticed from their work that rate-shaping affected the location of ignition from the injector nozzle and this agreed with the findings of Juneja et al. [213]. Furthermore, through numerical simulations, Mohan et al. [245] established that high boot pressure and long boot length were capable of bringing about soot and NO_x trade-off for a biodiesel fueled direct injection CI engine. Lately, d'Ambrosio and Ferrari [239] experimentally examined the consequences of injection rate-shaping using solenoid injectors.

By placing two injection signals very close to one another, a crude injection rate-shape was achieved. From their experiment, they concluded that injection rate-shaping was able to reduce engine noise with a compromise of both BSFC and soot emissions.

6.2 Chapter objective

From the aforementioned works, it can be seen that injection rate-shaping is practically viable due to the introduction of piezo-stack in injectors. By employing injection rate-shaping strategies in DICI engines, there is a possibility of reducing NO_x emissions for kerosene fueled diesel engines running at high loads. To the best of the author's knowledge, no investigation has been done on the effects of injection rate-shaping on a kerosene fueled DICI engine. Injection rate-shaping investigations in diesel engines were only carried out using higher viscosity and higher Cetane number (CN) fuels such as diesel and biodiesel [44, 245]. Therefore, due to the aforementioned reasons, it is of great interest in this chapter to investigate in detail the combustion and emissions behavior of a DICI engine subjected to a combination of injection rate-shaping and the use of lower viscosity and lower CN kerosene fuel. One should note that kerosene has a lower CN and is comparatively less viscous as compared to diesel as seen from Table 2-1.

This chapter will be divided into two major sections, namely Part A and

Part B, each with their respective specific objectives. The respective objectives of Part A and Part B are elaborated below.

- ❖ **Part A)** The combined effects of different ramp injection rate-shapes together with different piston bowl geometries on the combustion characteristics in a DICI engine has never been done before. Furthermore, from literature [246-256], most parametric investigations done regarding piston bowl geometries were primarily focused on optimizing the piston bowl geometry together with the use of different swirl ratios. Therefore, the objective of this work is to investigate the combustion characteristics of kerosene-diesel blends using different bowl geometries together with varying ramp injection rate-shapes in a DICI engine. In this work, three different combustion bowl geometries together with different ramp injection rate-shapes will be employed.

- ❖ **Part B)** No detailed analysis was done regarding the effects of boot injection rate-shapes on the trends of engine in-cylinder soot particle dynamics such as soot mass density, soot particle size and number distribution. Hence, the objective of this work is to improve on the kerosene-diesel reaction mechanism developed in Chapter 5 to include soot formation/oxidation in order to investigate through numerical simulations the effects of boot injection rate-shapes on the combustion process and emissions formation of a DICI engine fueled with lower

viscosity and lower CN kerosene and its blends with diesel. The trends of engine in-cylinder soot particle dynamics will be looked into in this work.

The overall objectives of Part A and Part B are to have a deeper understanding of kerosene combustion and emissions behaviour when it is used in conjunction with injection rate-shapes, to investigate the potential of kerosene in reducing emissions when used together with injection rate-shapes in a DICI engine and to proof the robustness of the kerosene-diesel reaction mechanism developed previously.

6.3 Part A: Investigation methodology

In order to study the combined effects of different piston bowl geometries with different ramp injection rate-shapes, a total of three combustion bowl geometries will be used together with six different ramp injection rate-shapes. The base case piston bowl geometry used is the omega combustion chamber (OCC) from [180, 252], while two other additional piston bowl geometries that will be used are the shallow-depth combustion chamber (SCC) from [252] and the shallow-depth re-entrant combustion chamber (SRCC). It should be noted that this particular SRCC geometry is newly proposed in this work and the SRCC mesh is constructed using the KIVA3V pre-processor [184].
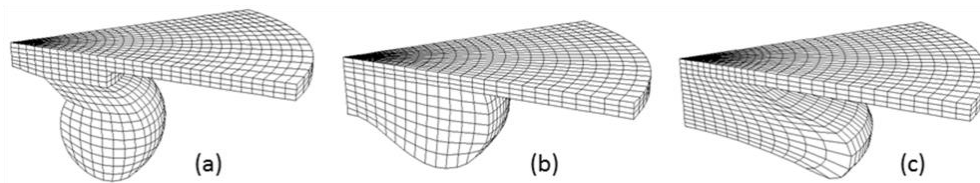
Figure 6-1 The three combustion chambers are the (a) omega combustion chamber (OCC) from [180, 252], the (b) shallow-depth combustion chamber (SCC) from [252] and the (c) shallow-depth re-entrant combustion chamber (SRCC) are shown in this manner for ease of comparison.

Figure 6-1 shows all three combustion chambers for ease of comparison. The six different ramp injection rate-shapes are shown in Figure 6-2b. For ease of subsequent explanations, Figure 6-2a shows the definition of a ramp-shaped injection used in this work.
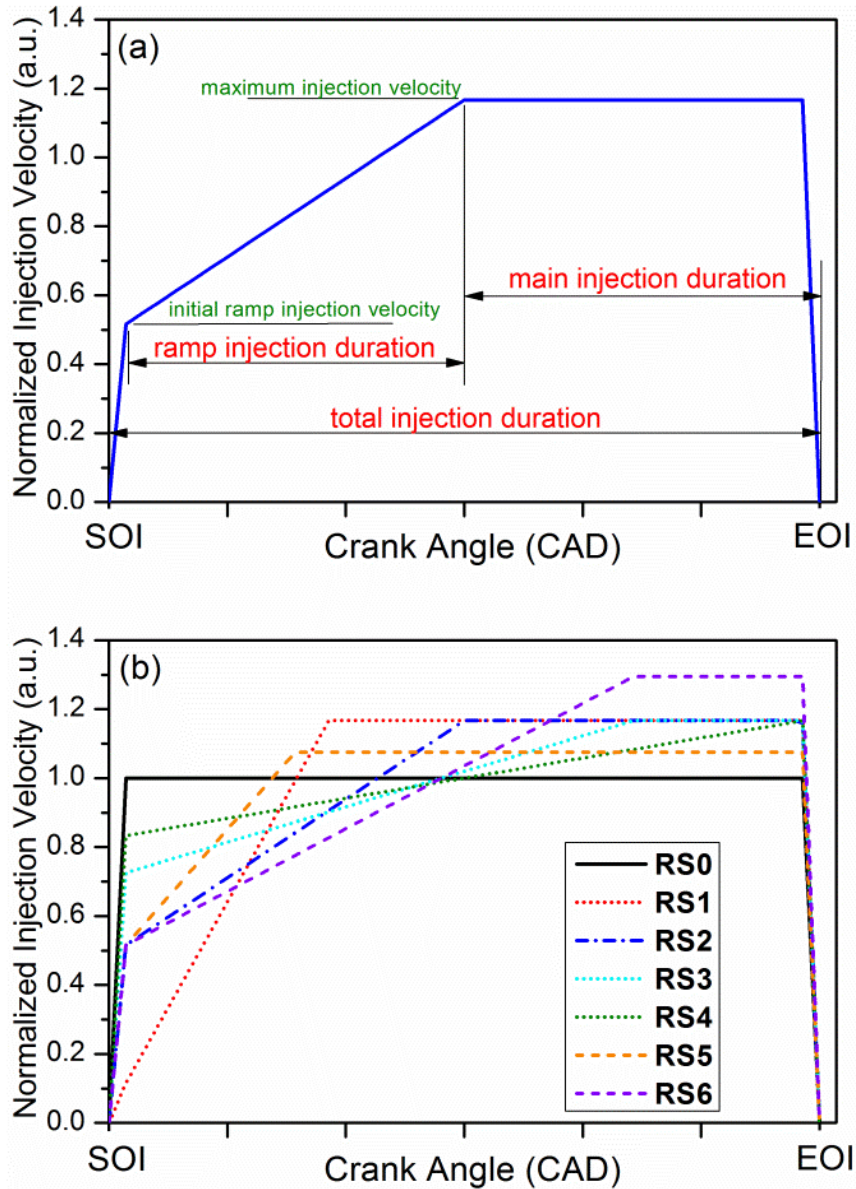
Figure 6-2 (a) The definition of a ramp-shaped injection used in this work and (b) the six different ramp injection rate-shapes.

The six different ramp injection rate-shapes are labelled from RS1 through to RS6, with RS0 being the base case injection profile. Table 6-1 gives a more detailed description of RS0 to RS6. It should be noted that the area under the graphs of RS0 to RS6 are kept the same like in [213]. Furthermore for this work, three blends of fuels which are pure diesel, kerosene-diesel and pure kerosene will be used.

Table 6-1 Detailed description of RS0 to RS6.

Injection profile*	Description
RS0	Constant injection rate (base case).
RS1, RS2, RS3, RS4	These four rate-shapes have the same maximum injection velocity with varying durations of main injection. Their initial ramp injection velocities are different in order to keep the area under the graphs the same.
RS5, RS2, RS6	These three rate-shapes have the same initial ramp injection velocity with different maximum injection velocities. The area under their graphs is kept the same.

*Note: It should be noted that the area under the graphs of RS0 to RS6 are kept the same like in [213].

Table 6-2 Details of the simulation cases in this study together with the annotations used in this work.

Combustion chamber geometries	Kerosene to diesel mass fractions used in simulations*	Injection rate-shapes used in simulations
Omega (OCC), Shallow-depth (SCC), Shallow-depth re-entrant (SRCC)	Pure kerosene (0), 50% kerosene/50% diesel (50), Pure diesel (100)	RS0, RS1, RS2, RS3, RS4, RS5, RS6

*Note: In subsequent figures in this work, "0" represents pure kerosene while "50" and "100" represent 50% kerosene/50% diesel and pure diesel respectively.

Table 6-2 shows the details of the simulation cases in this study together with the annotations used in this work. It should be noted that the energy input of the injected fuel, the initial in-cylinder pressure and temperature, the start of injection (SOI), the engine speed and the duration of injection (DOI) are kept constant for all simulations. More importantly, the compression ratios for all three piston bowl geometries are kept the same like in [257]. The respective thermo-physical properties of kerosene (represented by Jet-A properties) and diesel (represented by $C_{14}H_{28}$ properties) from the KIVA4 fuel library [39] are used. For ease of explanation in the subsequent sections, Table 2-1 shows the

thermo-physical properties of kerosene and diesel. It should also be noted that the base case engine simulation parameters are kept the same as those of the experiment such as the injection duration and quantity.

6.4 Part A: Base case engine validation

It is important that the KIVA4-CHEMKIN [39, 40] code predicts the combustion process well in an engine. For ease of subsequent explanations, Figure 6-3 shows the comparisons between simulated and experimental in-cylinder pressures, heat-release rates and emissions for the pure diesel base case. Refer to Chapter 3 for more details on the engine testbed.
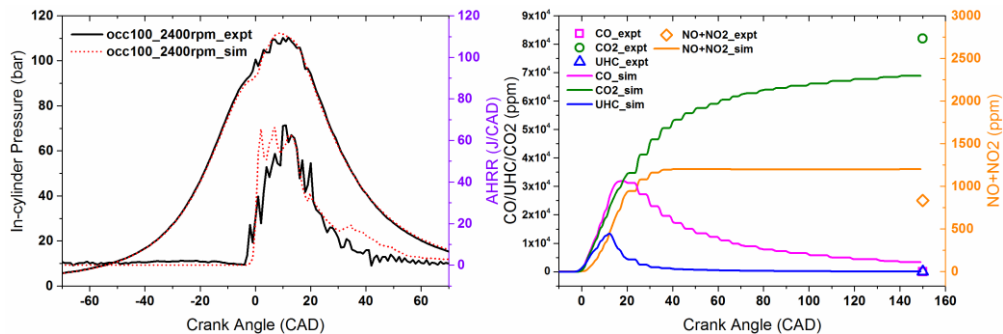
Figure 6-3 This figure shows the comparisons between simulated and experimental in-cylinder pressures, heat-release rates and emissions for the pure diesel base case.

It should be noted that the pure diesel base case experiment was carried out at 2400rpm under 100% load conditions, with the SOI at -3.5 ° after top dead center (ATDC). From the comparison between the simulated and experimental results, it can be seen that the combustion phenomenon is reasonably predicted by the KIVA4-CHEMKIN [39, 40] code. The simulated and experimental in-cylinder pressures and apparent heat-release rates (AHRRs) are rather

similar. Moreover, the simulated emissions are also reasonably matching with that of experimental results.

6.5 Part A: Results and discussion

6.5.1 Velocity vector and turbulence kinetic energy analysis

Prior to analyzing the engine performance and emissions related to the use of different combustion bowl geometries with varying ramp injection rate-shapes, it is needful to first have a closer look at the respective velocity vector fields as well as the turbulence kinetic energies (TKEs) for all the bowl geometries. Figure 6-4 shows the TKEs and the velocity vector fields for the OCC, SCC and SRCC geometries under an engine speed of 2400rpm at top dead center (TDC). It should be noted that the throat length [257], as shown in Figure 6-4, affects the magnitude of velocity vectors within the combustion bowl.
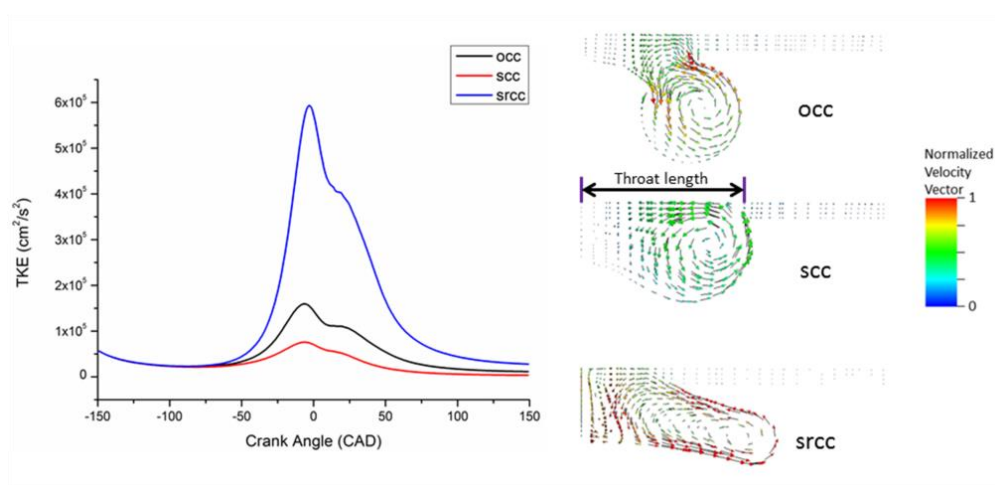
Figure 6-4 The TKEs and the velocity vector fields for the OCC, SCC and SRCC geometries under an engine speed of 2400rpm at TDC.

The TKE of the SRCC geometry is the greatest while that of SCC is the lowest even though the compression ratios are the same for all bowl geometries. With the shortest throat length as in the case of SRCC, the magnitude of velocity vectors is the highest due to the conservation of momentum [255] whereby the air within the cylinder is squeezed through a narrow channel into the combustion bowl. This generates a lot of turbulence. Conversely, the SCC geometry which has the longest throat length gives the lowest TKE as can be inferred from its velocity vectors. Furthermore, the shape of the bowl dictates the location of greatest turbulence. The SRCC geometry gave the strongest TKE near the center of the bowl as well as along the perimeter of the bowl itself. On the other hand, for the OCC geometry, the TKE is the strongest at the narrowest entrance of the bowl. For the case of the SCC geometry, the velocity vectors are distributed more on the outer radii of the combustion bowl.

6.5.2 Engine in-cylinder pressures and apparent heat-release rates

Due to the complexity of this parametric study, the effects of bowl geometry, injection rate-shape and fuel used will be systematically discussed. For the ease of subsequent explanations, it should be noted that conventional diesel combustion consists of four main phases which are the ignition delay period, premixed combustion phase, mixing-controlled combustion phase and the late combustion phase as defined by Heywood [16]. Figure 6-5 shows the

in-cylinder pressures and apparent heat-release rates (AHRRs) for the OCC, SCC and SRCC geometries with pure diesel, kerosene-diesel and pure kerosene fuels, using an injection rate-shape of RS0.
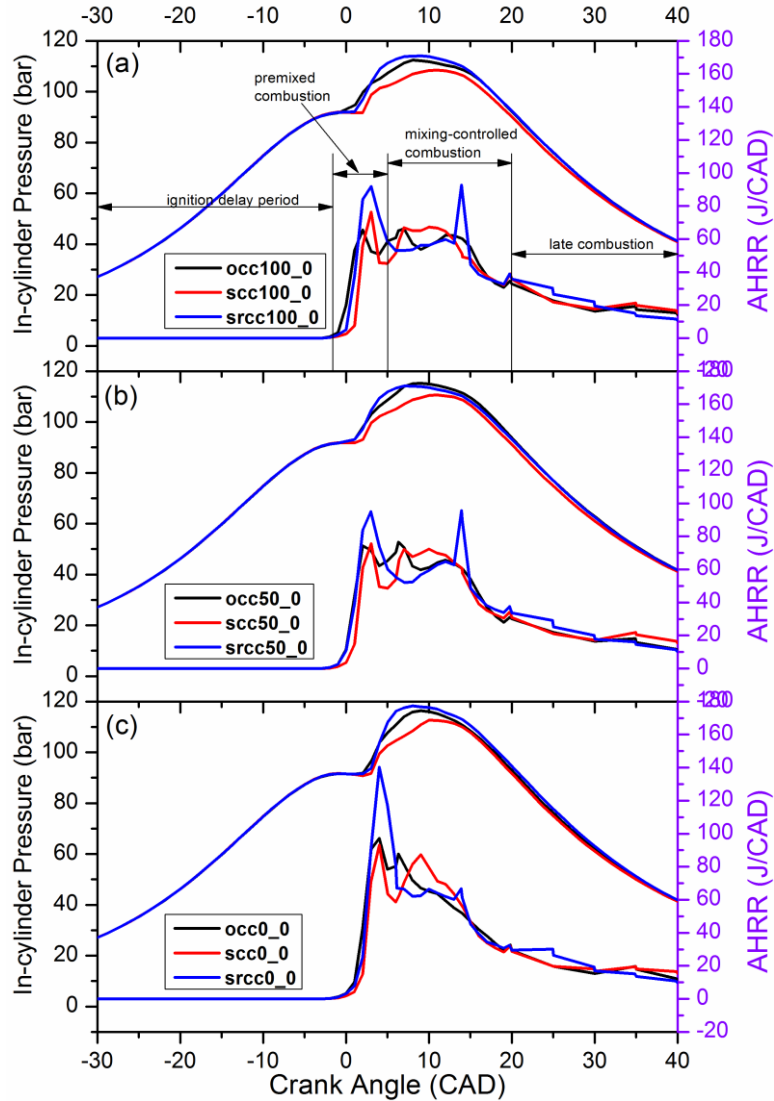
Figure 6-5 In-cylinder pressures and AHRRs for the OCC, SCC and SRCC geometries with pure diesel, kerosene-diesel and pure kerosene fuels, using an injection rate-shape of RS0.

It can be observed that the SCC geometry generally gives the longest ignition delay period, with the lowest peak in-cylinder pressure, of all the geometries due to the fact that the SCC geometry generates the weakest TKE as

compared to its counterparts. When a weak TKE is generated by the piston bowl, the mixing of air and fuel will be poor and hence delays the start of combustion (SOC) and lowers the peak in-cylinder pressure. However, with a low TKE generated, the phases of combustion for the SCC geometry are rather distinct, specifically between the premixed combustion and the mixing-controlled combustion phases. This is due to the fact that combustion is predominantly controlled by the injected fuel spray itself for the SCC geometry when less turbulence is generated by the bowl to interfere with the spray breakup and atomization process. This clear distinction between the combustion phases is not obvious for the OCC and SRCC geometries due to the higher TKEs that are generated. It is interesting to note that there are two peak heat-releases observed for the SRCC geometry, with a primary peak heat-release during the premixed combustion phase and a secondary peak heat-release during the mixing-controlled combustion phase. The secondary peak heat-release is likely due to the very high TKE that is generated by the SRCC geometry, such that the fuel that is injected later during the injection period gets rapidly mixed with air to form a well-mixed charge that combusts swiftly, giving a "second premixed combustion". Moreover, since the TKE generated by the SRCC geometry is substantially higher than the other two geometries, the heat-release during the premixed combustion phase for the SRCC geometry is the highest of all, regardless of the fuel used, due to enhanced air and fuel mixing. In addition, as

129

the injected fuel is changed from pure diesel to pure kerosene, combustion phasing generally occurs for all bowl geometries whereby the heat-release during the premixed combustion phase increases and diminishes during the mixing-controlled and late combustion phases. This is due to the fact that kerosene has a lower CN number as compared to diesel, which causes a longer ignition delay period during which more kerosene premixes with air. Coupled with the fact that kerosene is less viscous as compared to diesel, kerosene is able to better atomize and premix with air during the ignition delay period. Hence, heat-release during the premixed combustion phase increases with kerosene usage. The same trend is observed from the experimental work of Lee et al. [37]. It should be noted that combustion phasing, which is caused by changing diesel to kerosene, is the most prominent for the SRCC geometry and lest prominent for the SCC geometry. This is due to the lower viscosity of kerosene as well as the extremely high TKE generated by the SRCC geometry which causes superior fuel and air mixing as compared to the SCC geometry. It is worth noting that when pure kerosene is used together with the SRCC geometry, the secondary heat-release is significantly diminished due to combustion phasing.

Having discussed about the combined effects of bowl geometries together with the different fuels used, it is now appropriate to look into the combined effects of different injection rate-shapes and bowl geometries on the combustion characteristics. Figure 6-6 shows the in-cylinder pressures and

AHRRs for the OCC, SCC and SRCC geometries for different ramp injection rate-shapes of RS0 to RS6, using the kerosene-diesel blend fuel.
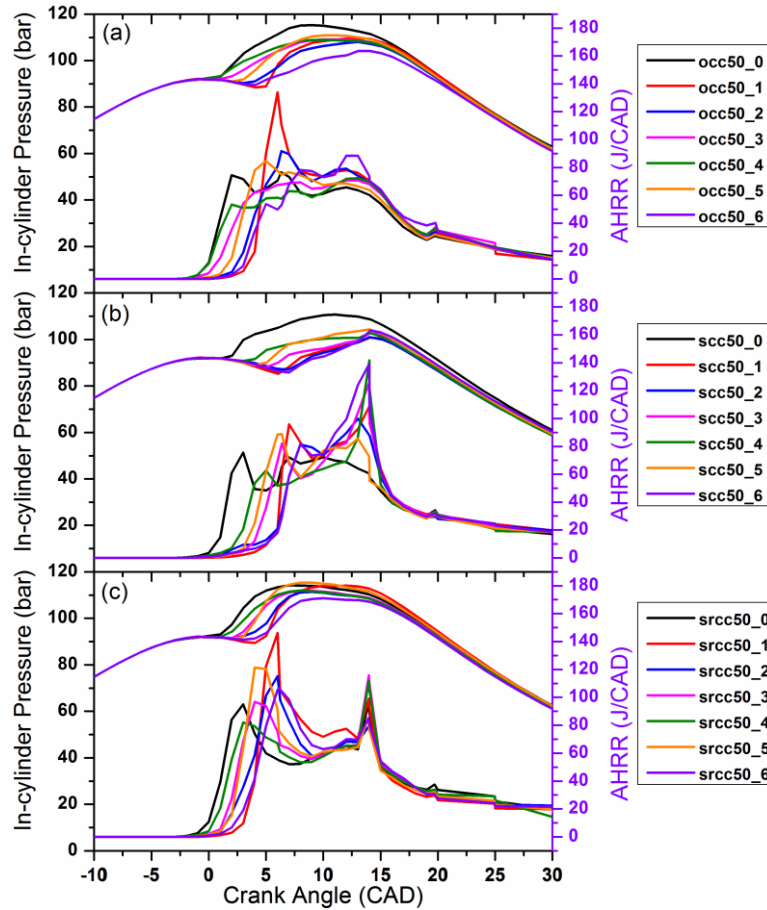
Figure 6-6 In-cylinder pressures and AHRRs for the OCC, SCC and SRCC geometries for different ramp injection rate-shapes of RS0 to RS6, using the kerosene-diesel blend fuel.

It is observed that combustion phasing occurs with injection rate-shaping. Using different ramp injection rate-shapes, the ignition delay period lengthens with decreasing initial injection velocities regardless of the bowl geometry used. This is because of poorer fuel spray breakup and atomization when the injection velocity is low, causing a delayed SOC. It is interesting to note that the magnitude and crank timing of the initial heat-release slope is different with the use of different bowl geometries even though the same injection rate-shape is

used. For the SRCC geometry, the spread of initial heat-release slopes is smaller but higher in magnitude compared to those of the SCC geometry due to the extremely high TKE generated by the SRCC geometry. The high TKE strongly enhances fuel breakup and atomization and affects the heat-release rate to a great extent. Moreover, as explained previously, combustion is predominantly controlled by the injected fuel spray itself for the SCC geometry, and so the effect of injection rate-shaping on the heat-release rate is more obvious for bowl geometries that generate less TKE. This is corroborated by the trend of heat-release for the SCC geometry when ramp injection rate-shapes of RS1 to RS6 are used. It can be generally seen that the heat-release during the premixed combustion phase decreases and that more heat is released during the mixing-controlled combustion phase when initial injection velocities decrease. However, this trend is not so obvious when the SRCC and OCC geometries are used because the majority of the heat is released during the premixed combustion phase with minimal increment of heat-release during the mixing-controlled combustion phase regardless of the rate-shape used.

6.5.3 Combustion characteristics and emissions

6.5.3.1 Combustion characteristics

Figure 6-7 shows the crank angle at which 50% of the total heat is released (CA50), the ignition delay (ID) and the duration of combustion (DOC) for the

OCC, SCC and SRCC geometries for different ramp injection rate-shapes of

RS0 to RS6, using the kerosene-diesel blend fuel. It should be noted that in this

work, the ID is defined as the crank angle duration from SOI to 5% of the total

heat-release, while DOC is defined as the crank angle duration from 5% to 90%

of the total heat-release like in [258].
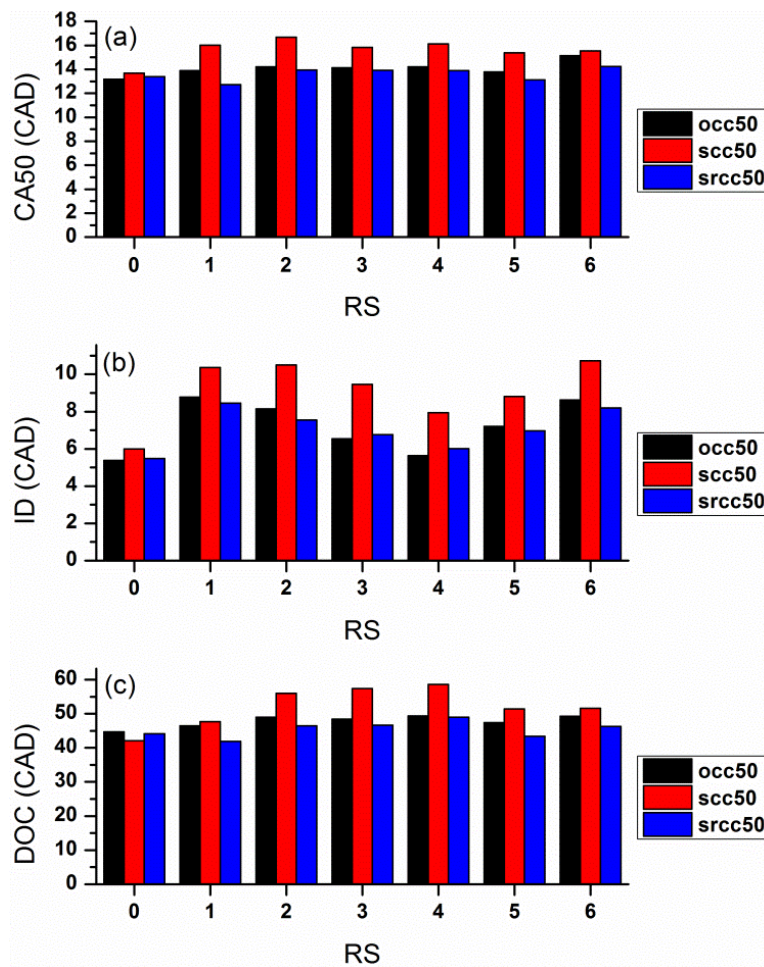
Figure 6-7 The graphs of (a) CA50, (b) ID and (c) DOC for the OCC, SCC and SRCC
geometries for different ramp injection rate-shapes of RS0 to RS6 using the
kerosene-diesel blend fuel.

It can be observed that the IDs for the same injection rate-shape are

different when different bowl geometries are used. In general, the SCC bowl

geometry gives the longest ID regardless of the rate-shapes used, while the

SRCC and OCC geometries give comparably shorter IDs. This is due to the higher TKEs that are produced by the SRCC and OCC geometries which enhance air and fuel mixing that result in earlier SOC. As explained earlier, ID decreases with increasing initial injection velocities. Hence, the ID decreases as the initial ramp injection velocities increase when the rate-shape changes from RS1 to RS4. Similarly, when the rate-shape changes from RS6 to RS2 and then to RS5, the ID decreases due to an increase in injection rate during the early part of the injection period. Furthermore, the DOCs of the SCC geometry are generally longer than those of the SRCC and OCC geometries regardless of the injection rate-shapes used. This is because the SRCC and OCC geometries generate higher TKEs which enhance the mixing of air and fuel, resulting in a more homogeneous charge and a more rapid combustion. Hence, it can be concluded that the higher the TKE, the shorter will be the DOC. Moreover, the effect of injection rate-shaping on DOC is the greatest with the SCC geometry as compared to the other two geometries. This, as explained earlier, is due to the fact that combustion is predominantly controlled by the injected fuel spray itself for the SCC geometry. Not surprisingly, as the DOC for the SCC geometry is the longest of all, its CA50 is also the highest compared to those of the SRCC and OCC geometries.

6.5.3.2 Emissions

Figure 6-8a and b shows the normalized carbon monoxide (CO) and

nitrogen oxide (NO) emissions with respect to the different rate-shapes, while

Figure 6-8c shows the normalized NO against normalized CO emissions for the

OCC, SCC and SRCC geometries using pure diesel, kerosene-diesel and pure
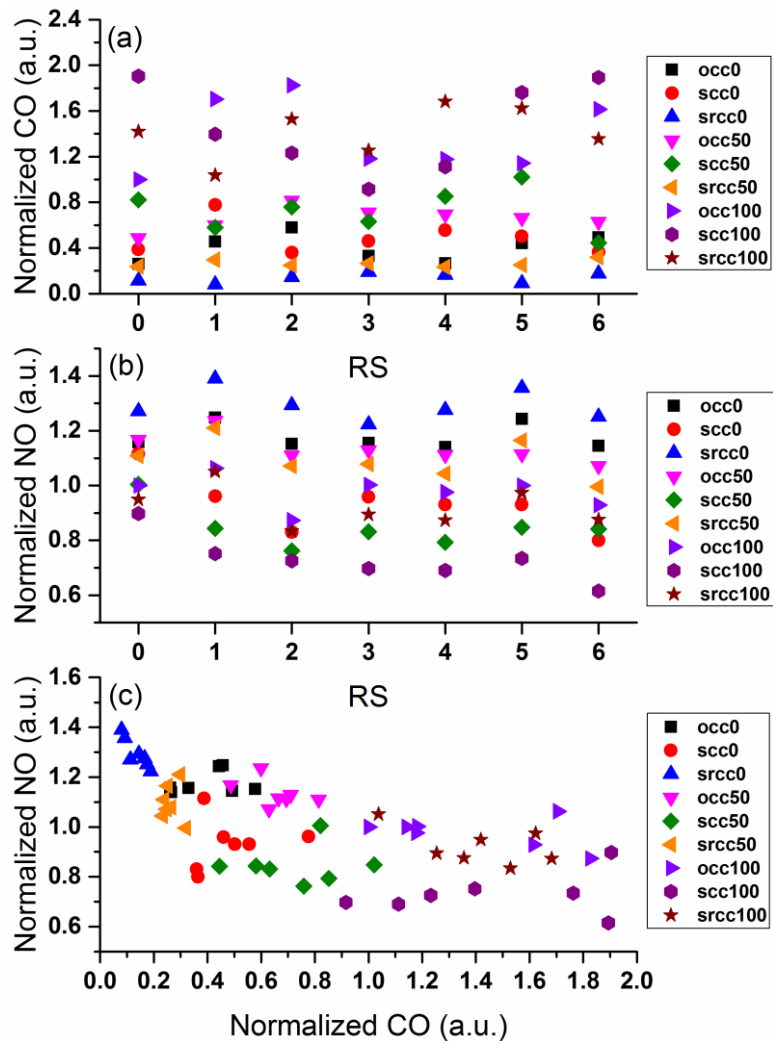
kerosene fuels.

Figure 6-8 The normalized (a) CO and (b) NO emissions with respect to the different rate-shapes as well as (c) the normalized NO against normalized CO emissions for the OCC, SCC and SRCC geometries using pure diesel, kerosene-diesel and pure kerosene fuels.

It can be generally seen that for the bowl geometries that generate higher

TKEs, the level of CO emissions is lower. This is because with a higher TKE,

air and fuel mixing is better and gives rise to improved and more complete

combustion. Moreover, as the injected fuel changes from pure diesel to kerosene-diesel and then to pure kerosene, CO emissions are generally seen to decrease due to the better atomization of lower viscosity kerosene [126] that results in better combustion. However, it should be noted that the aforementioned CO trends are general and that some injection rate-shapes do cause the CO trends to deviate from the norm. Not surprisingly, NO emissions generally increase for bowl geometries that generate high TKEs and for higher fractions of kerosene injection like in [37]. Again, it should be noted that the aforementioned NO trends are general and that some injection rate-shapes do cause the NO trends to stray from the norm. The deviation of both the CO and NO trends for certain cases may be due to fuel-on-wall impingement [259, 260] or the formation of extra lean air-fuel mixture [37], both of which hinder combustion. Figure 6-9 shows the CO and NO emissions at 17 °ATDC for the SCC and SRCC geometries using the RS1 rate-shape together with pure diesel and pure kerosene fuels. From this figure, by comparing the CO and NO emissions for the SCC geometry, the use of kerosene in place of diesel gives lower CO emissions and higher NO emissions. In addition, with the use of the same fuel, it can be seen that the SRCC geometry gives much lower CO emissions but higher NO emissions when compared to the SCC geometry. From Figure 6-8c, it is interesting to note that with careful selection of bowl geometry, fuel type and injection rate-shape for a particular engine condition, it is possible

to achieve lower NO as well as CO emissions simultaneously. For instance, by using the SCC geometry with pure kerosene or kerosene-diesel fuel together with the appropriate injection rate-shape, it is possible to achieve low NO and CO emissions simultaneously, although a slight decrease in power is inevitable.
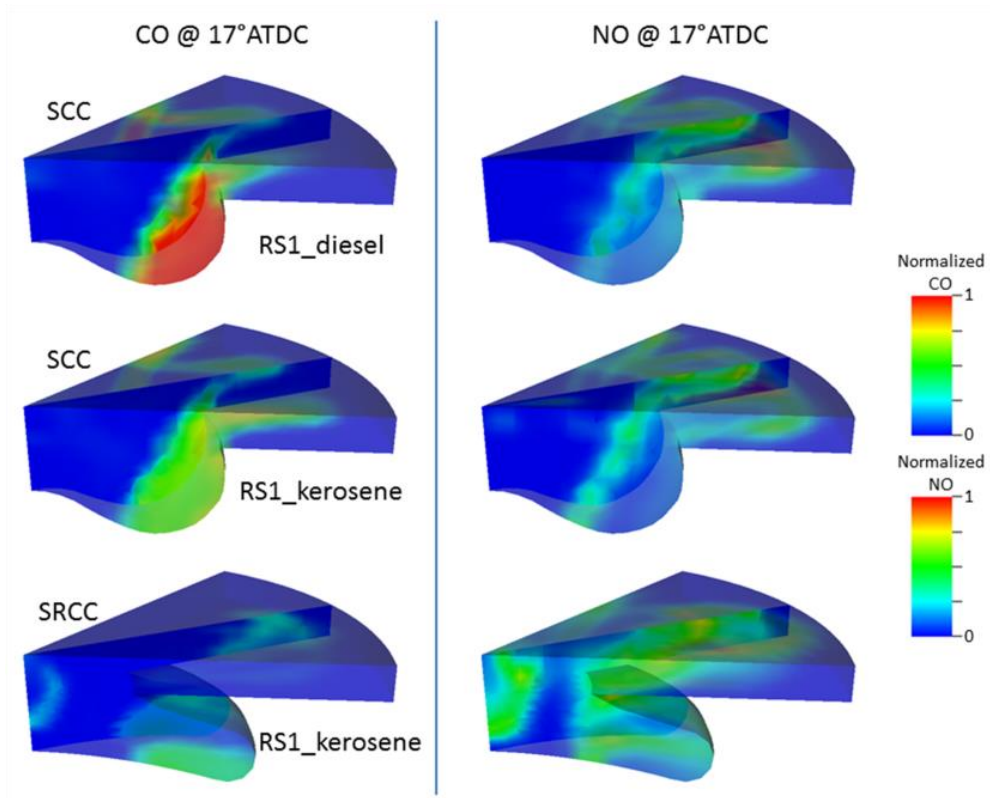
Figure 6-9 The CO and NO emissions at 17 °ATDC for the SCC and SRCC geometries using the RS1 rate-shape together with pure diesel and pure kerosene fuels.

6.6 Part A: Summary

In this work, the performance and emissions of a DICI engine fueled with kerosene-diesel blends, using different piston bowl geometries together with varying injection rate-shapes were investigated. A total of three combustion bowl geometries (OCC, SCC and SRCC) were used together with six different

ramp injection rate-shapes (RS1 to RS6) and different fuels (pure diesel, kerosene-diesel and pure kerosene). The findings are as follows:

a) The SRCC geometry which has the shortest throat length gives the highest TKE while the SCC geometry which has the longest throat length gives the lowest TKE.

b) The SCC geometry gives the longest ID due to its low TKE which retards SOC.

c) The SCC geometry gives rather distinct premixed combustion and mixing-controlled combustion phases due to the fact that combustion is predominantly controlled by the injected fuel spray itself because of the low turbulence generated.

d) Two peak heat-releases are observed for the SRCC geometry, with a primary peak heat-release during the premixed combustion phase and a secondary peak heat-release during the mixing-controlled combustion phase. This is because of the very high TKE that is generated by the SRCC geometry.

e) When kerosene is used in place of diesel, the heat-release during the premixed combustion phase increases and diminishes during the mixing-controlled and late combustion phases.

f) ID period lengthens with decreasing initial injection velocities for ramp injection rate-shapes.

g) The effect of injection rate-shaping on the heat-release rate is more obvious for bowl geometries that generate lower TKEs.

h) The DOCs of the SCC geometry are generally longer than those of the SRCC and OCC geometries because the SRCC and OCC geometries generate higher TKEs which enhance the mixing of air and fuel for quicker combustion.

i) Bowl geometries that generate higher TKEs as well as lower viscosity fuels such as kerosene generally give lower CO emissions and higher NO emissions.

From this work, it can be seen that it is possible to achieve low NO and CO emissions simultaneously by using the appropriate bowl geometry, rate-shape and fuel, although a slight decrease in power is inevitable. Furthermore, many of the findings from this work regarding kerosene combustion and emissions concur with that of literature as seen from Chapter 2. This implies that the kerosene-diesel reaction mechanism developed in Chapter 5 is reliable and robust enough for DICI engine simulations.

6.7 Part B: Investigation Methodology

6.7.1 Chemical reaction mechanism

Numerical simulations will be done to investigate the effects of injection rate-shapes on the combustion characteristics of a DICI engine fueled with kerosene and diesel. Due to the fact that soot particle dynamics trends such as soot mass density, soot particle size and number distribution are to be investigated in this work, a phenomenological soot model [181] is included for the engine simulations. More details about this model can be found in the following section. This soot model uses acetylene (C_2H_2) as the soot precursor specie and for soot surface growth. From diesel engine and CVCC experiments in literature as seen from Chapter 2, it can be clearly seen that diesel fuel generates more soot as compared to kerosene fuel under the same set of engine operating conditions [93, 99]. This is due to the fact that diesel has a higher aromatic content than kerosene [99] and more importantly diesel's higher viscosity [60, 86] contribute to poorer fuel-air mixing in DICI engines resulting in more soot generation. For ease of comparison and subsequent explanations, refer to Table 2-1 for kerosene and diesel properties.

As the original kerosene sub-mechanism from Chapter 5 predicted more C_2H_2 than expected, the magnitude of soot production for kerosene during combustion was initially similar to that of diesel. Therefore, the reaction rate for one of the major kerosene reaction pathways is adjusted for an improved

and lower C_2H_2 yield during combustion. The adjusted kerosene reaction pathway together with the respective original and adjusted [203] (bold) reaction rates are as shown below.

KERO ⇔ KERO- + H   7.00E+17   0.0   0.0   **1.00E+14   0.0   0.0**   (6.1)
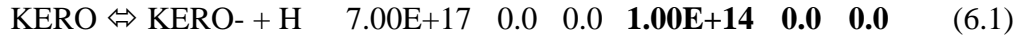
The adjustment of the reaction rate of this kerosene reaction pathway allows the C_2H_2 yield to be altered without compromising the performance of the kerosene sub-mechanism. The performance of the adjusted and enhanced kerosene sub-mechanism is compared to that of the original in terms of its shock tube ignition delay times, constant volume combustion heat-releases and ignition delays. Figure 6-10 shows the comparisons between the adjusted and original kerosene sub-mechanisms' combustion performance and it can be concluded that the adjusted and enhanced kerosene sub-mechanism gives almost identical combustion characteristics as those of the original while giving a lower C_2H_2 yield. As the decoupling methodology [202] was used to construct the reaction mechanism, altering one of the kerosene reactions does not affect the diesel component of the mechanism. It should be noted that the aim of this work is to predict the correct soot trends for kerosene with respect to diesel and not the exact soot yield for kerosene due to lack of suitable kerosene experimental data. For completeness, the adjusted and enhanced kerosene-diesel reaction mechanism is given in Appendix B.
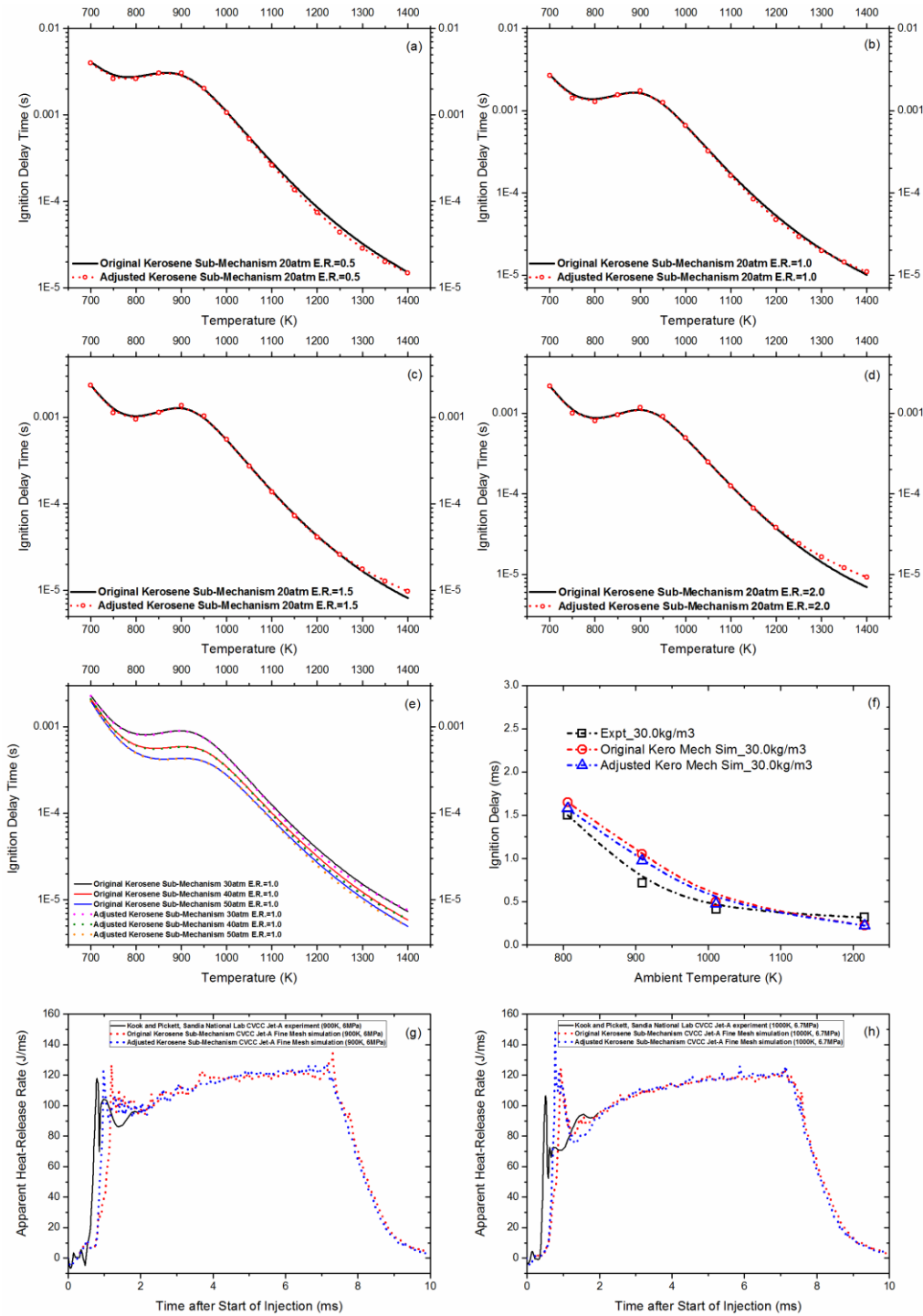
Figure 6-10 Comparisons between the adjusted and original kerosene sub-mechanisms for ignition delay times under different initial shock tube conditions of (a) 20atm/0.5 equivalence ratio, (b) 20atm/1.0 equivalence ratio, (c) 20atm/1.5 equivalence ratio, (d) 20atm/2.0 equivalence ratio and (e) 1.0 equivalence ratio at 30/40/50atm. Comparisons are also made between the adjusted and original kerosene sub-mechanisms together with that of experiments [86, 93] for constant volume combustion (f) ignition delays and (g,h) heat-releases under different ambient temperatures and pressures.

The differences between the experimental and the simulated peaks of heat-release as seen in Figure 5-6 and Figure 6-10g and h may be due to the shock tube validation of the kerosene sub-mechanism up to an equivalence ratio of only 2.0. The differences between the experimental and simulated peaks can be reduced through further shock tube validations with higher equivalence ratios of up to 4.0 [42, 43] (subject to availability of experimental data). This is because for diesel spray combustion, the local equivalence ratios within a spray can be rather high [42, 43]. However, it should be noted that the differences between experiments and simulations are acceptable. As seen from Figure 5-8 and Figure 6-10f, the simulated and experimental ignition delays show reasonable agreements under a wide range of conditions.

6.7.2 Phenomenological soot model

For this work, the KIVA4-CHEMKIN code [39, 40] is used for the engine simulations. The phenomenological soot model, which is incorporated into the KIVA4 [39] code for this work, was previously developed by the author's group [181] and proven to be fit for CI engine simulations. Briefly, this phenomenological soot model consists of a number of sub-models from literature that accounts for soot particle inception, soot coagulation, soot surface growth via the hydrogen-abstraction-carbon-addition (HACA) mechanism and soot surface oxidation by oxygen (O_2) and hydroxyl radical

(OH). In this model, C_2H_2 is taken to be the soot precursor specie from which soot particle inception occurs [261] depending on factors like precursor concentration and cell temperature. After the inception of soot particles, soot coagulation [262] may occur and it is the fusion of soot particles which will cause a decrease in soot particle number and an increase in soot particle size. On the other hand, soot surface growth may also occur. The well-known HACA sub-model is used to describe soot surface growth [263, 264] in this work. Basically, it is supposed that soot (C_S) is activated by hydrogen abstraction to give soot radical ($C_S\bullet$) with an active site for carbon addition in the form of C_2H_2. The addition of C_2H_2 to $C_S\bullet$ forms $C_SCH\dot{C}H$ which enables soot particles to grow in size. In addition to soot surface growth, soot surface oxidation occurs via O_2 (Nagle-Strickland and Constable model [265]) and OH [266]. A higher O_2 partial pressure or increased OH levels will cause the oxidation of more soot. This will result in lower soot mass and soot particle size. It is interesting to note from the work of Tao et al. [261] that in-cylinder soot distribution is much dictated by the distribution of OH radicals especially for spray diffusion combustion. In this work, the formation and oxidation of the soot precursor C_2H_2 is governed by the reaction mechanism itself. One should note that species vital to the phenomenological soot model such as C_2H_2, O_2, OH and H originate from the CHEMKIN chemistry solver [40] which deals with the reaction mechanism used in this work. To keep this

144

chapter concise, refer to [181] for more information on the phenomenological soot model. As the reaction mechanism used in this work for diesel combustion is different from that used in [181], reaction R_4 in the HACA soot surface growth mechanism is adjusted to give a better prediction of soot yield for pure diesel combustion in a diesel engine. Table 6-3 shows the original [264] and the adjusted reaction rates of the HACA soot surface growth mechanism.

Table 6-3 Original [264] and adjusted reaction rates of the HACA soot surface growth mechanism.

Reaction Number	Reactions	Original A [264] (m, kg mol, s)	**Adjusted A** (m, kg mol, s)	E [264] (kJ kg⁻¹ mol⁻¹)
R_1	C_S—H + H → C_S• + H_2	2.5E+11	-	50200
R_{-1}	C_S• + H_2 → C_S—H + H	4.0E+08	-	29300
R_2	C_S• + H → C_S—H	2.2E+11	-	-
R_{-2}	C_S—H → C_S• + H	2.0E+17	-	456000
R_3	C_S• → C_2H_2 + *product*	3.0E+14	-	259000
R_4	C_S• + C_2H_2 → C_SCH$\dot{C}$H	2.0E+09	**3.25E+09**	16700
R_{-4}	C_SCH$\dot{C}$H → C_S• + C_2H_2	5.0E+13	-	159000
R_5	C_SCH$\dot{C}$H → C_S—H + H	5.0E+10	-	-

Reaction R_4 is adjusted based upon engine in-cylinder soot evolution data from an optical diesel engine experiment [104, 262] from literature. Figure 6-11 shows the comparisons between the simulated and the experimental [104, 262] optical diesel engine in-cylinder pressure, AHRR and soot evolution. Reasonable agreements can be seen between the simulated and the experimental in-cylinder pressure, AHRR and soot evolution.
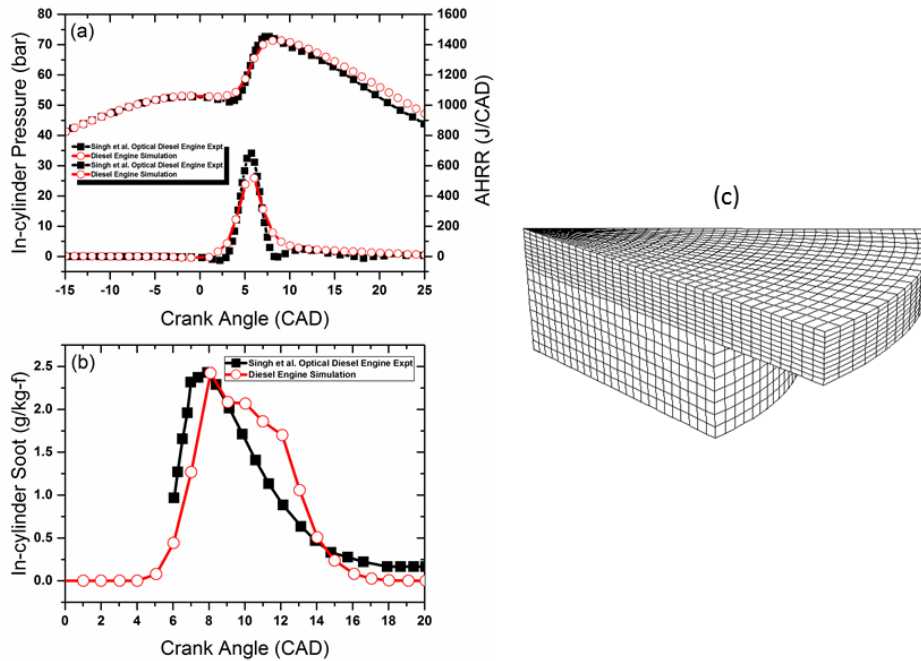
Figure 6-11 Comparisons between the simulated and the experimental [104, 262] optical diesel engine (a) in-cylinder pressure, AHRR and (b) soot evolution. (c) Sector mesh drawn using the KIVA3V pre-processor [184].

It can be observed from Figure 6-11b that the predicted in-cylinder soot evolution between 9-14CAD is slightly more than that of experiment. This is due to two main reasons. Firstly, the soot precursor is simply taken to be C_2H_2 due to the lack of other more complex soot precursor species such as alkynes (e.g. C_4H_2) and PAHs (e.g. A_4) [199, 204, 262] in the reaction mechanism. Secondly, the C_2-C_3 reactions used [202] in the reaction mechanism is not a detailed one. If detailed C_2-C_3 reactions are included in the mechanism, the prediction of C_2H_2 and soot may be more accurate. Nonetheless, the difference between the simulated and experimental soot evolutions is acceptable taking into consideration the compact size of the mechanism.

6.7.3 Parametric cases

In this work, the effects of boot injection rate-shapes on combustion and emissions will be studied together with different kerosene-diesel blends. Figure 6-12 shows the definition of a typical boot injection rate-shape [44, 242], the different boot rate-shapes that will be used for this work as well as the details of the parametric cases in this work. Refer to Figure 6-12 for more details. It should be noted that apart from the injection rate-shapes and fuel type, all other engine parameters such as the energy input, injection timing, injection duration, initial temperature and initial pressure are kept unchanged. Moreover, the area under each injection rate-shape graph is kept the same as in [213]. Finally, the respective thermo-physical properties for diesel and kerosene from the KIVA4 fuel library [39] are used in the simulations. It should also be noted that the base case engine simulation parameters are kept the same as those of the experiment such as the injection duration and quantity.
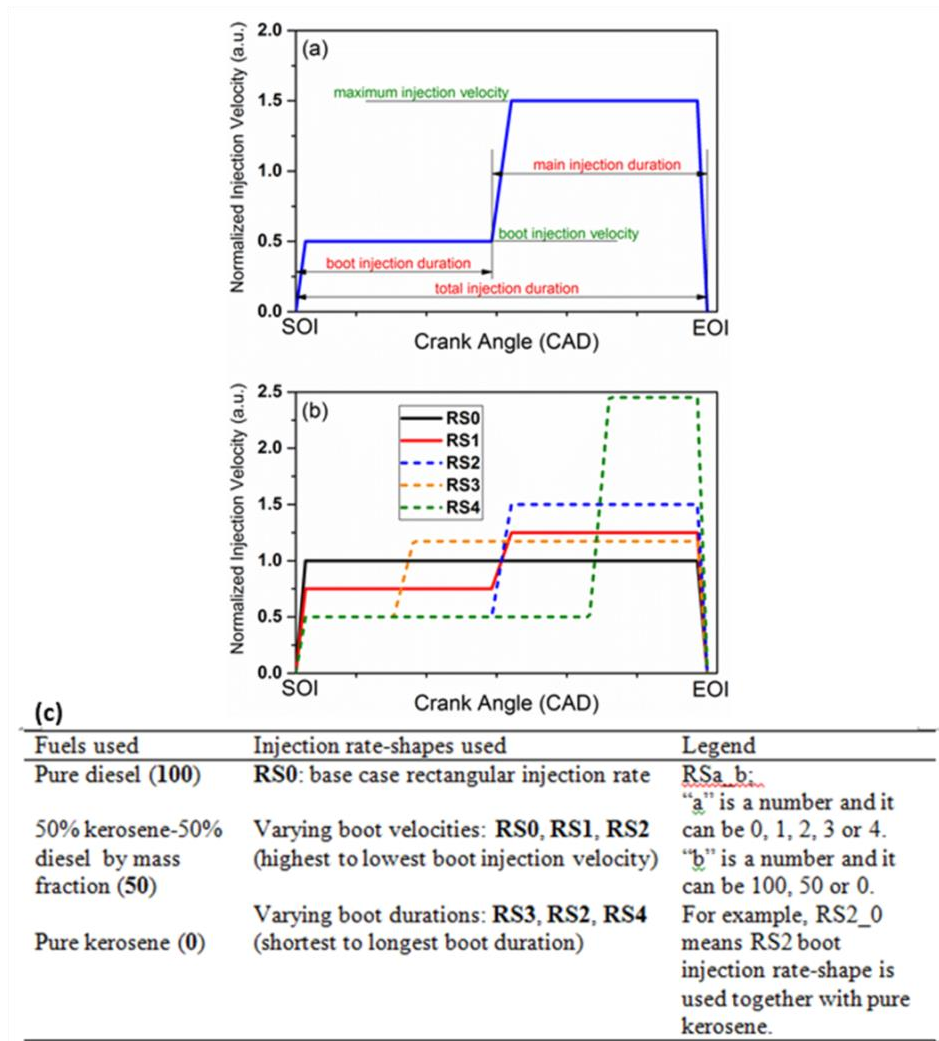
Figure 6-12 (a) Definition of a typical boot injection rate-shape [44, 242], (b) the different boot rate-shapes that will be used for this work and (c) the details of the parametric cases in this work.

6.8 Part B: Base case engine validation

Prior to running engine simulations, engine in-cylinder validation is done for a pure diesel base case at full load at 2400rpm with a conventional rectangular injection rate (RS0). Figure 6-13 shows the engine mesh from [267] used in this work, the experimental and simulated in-cylinder pressures, AHRRs and the CO, CO_2, NO_x and UHC emissions. Reasonable agreements

can be seen between the simulated and experimental results. Refer to Chapter

3 for more details of the engine testbed.
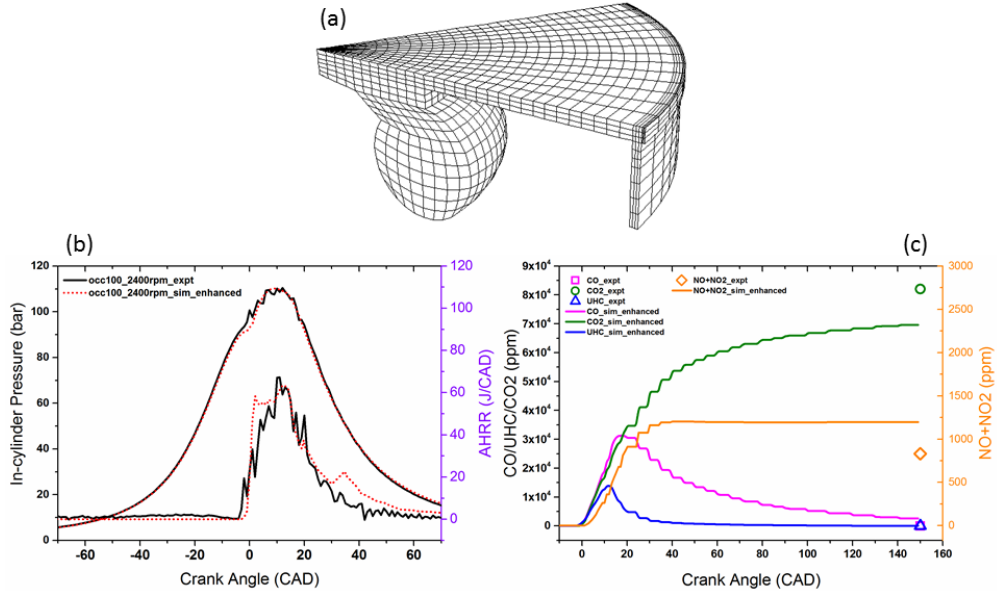
Figure 6-13 (a) Engine mesh from [267] used in this work, the experimental and simulated (b) in-cylinder pressures, AHRRs and (c) the CO, CO_2, NO_x and UHC emissions.

6.9 Part B: Results and discussion

6.9.1 In-cylinder pressures, AHRRs and combustion characteristics
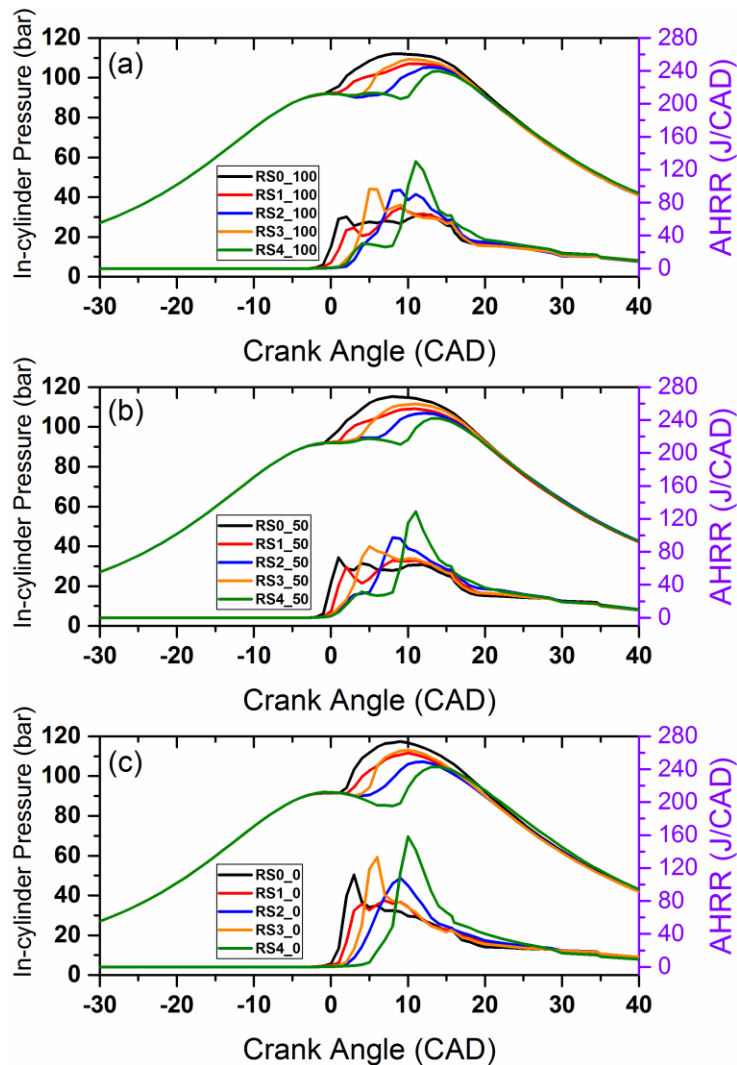
Figure 6-14 The in-cylinder pressures and the respective AHRRs for the different injection rate-shapes (RS0, RS1, RS2, RS3, RS4) used together with (a) pure diesel, (b) kerosene-diesel and (c) pure kerosene fuels.

Figure 6-14 shows the in-cylinder pressures and the respective AHRRs for the different injection rate-shapes (RS0, RS1, RS2, RS3, RS4) used together with pure diesel, kerosene-diesel and pure kerosene fuels. Since fuel is directly injected into the combustion chamber for all the cases, it should be noted that

the combustion process and the subsequent emissions are very much controlled by the fuel spray. Heywood [16] highlighted that conventional combustion in DICI engines consists of four main phases which are the ignition delay period, the premixed combustion phase, the mixing-controlled combustion phase and the late combustion phase. It is observed from Figure 6-14 that as boot injection rate-shapes are employed, combustion phasing occurs. As the boot injection velocity decreases (RS0 to RS1 to RS2) and as the boot injection duration increases (RS3 to RS2 to RS4), the ignition delay period increases. In addition, heat-release during the premixed combustion phase diminishes and increases during the mixing-controlled and late combustion phases. This is because with a lower boot injection velocity and longer boot injection duration, the initial fuel quantity injected into the cylinder is lesser and atomization is also poorer. This results in a longer ignition delay as well as less fuel accumulation for combustion during the premixed combustion phase. As more fuel is injected subsequently, combustion intensifies during the later stages and the peak heat-release is seen to shift with the different boot injection rate-shapes. A larger drop in peak in-cylinder pressure is the consequence of employing boot injection rate-shapes with a lower boot injection velocity and longer boot injection duration. Furthermore, as the fuel is changed from pure diesel to pure kerosene, ignition delay period increases and the intensity of heat-release also

increases. This is due to the thermo-physical properties of the fuels used. As kerosene has a lower Cetane number (CN) as compared to diesel as seen from Table 2-1, ignition delay period lengthens when kerosene is used. This consequential increase in ignition delay period allows for more kerosene to be better premixed with air before combustion starts. Hence, with more kerosene forming a combustible mixture prior to combustion, subsequent kerosene combustion intensity is much higher than that of diesel and less distinction is seen between the premixed and the mixing-controlled combustion phases for kerosene combustion.
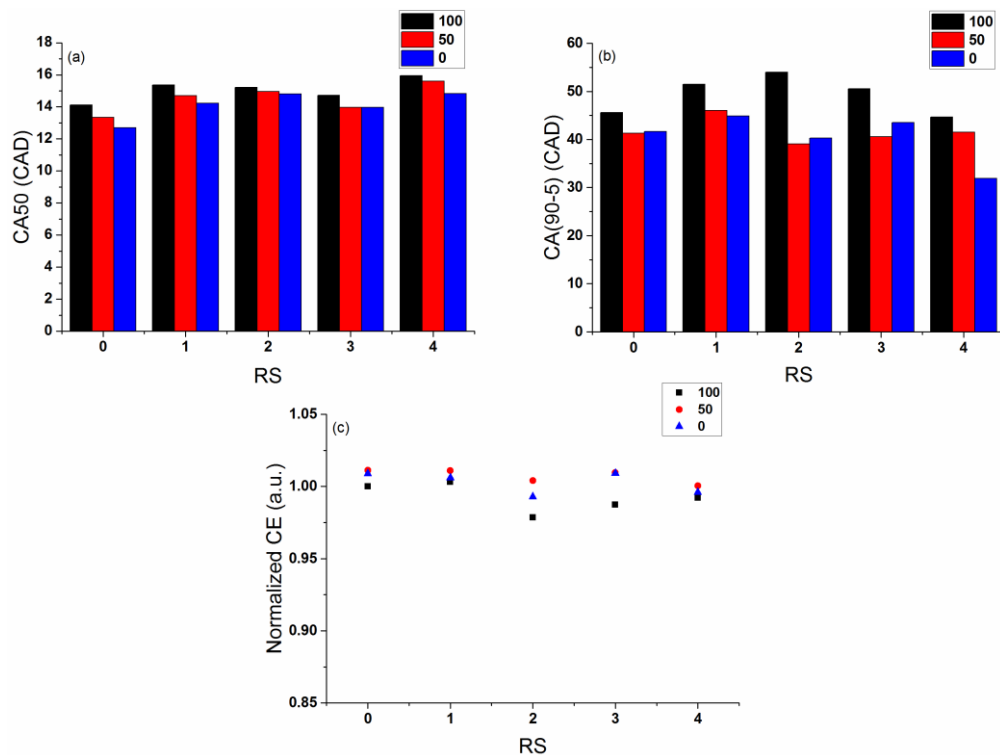
Figure 6-15 (a) The CA50, (b) the DOC and (c) the normalized CE for all simulated cases.

Figure 6-15 shows the crank angle at which 50% of the total heat is released (CA50), the duration of combustion (DOC) and the normalized

combustion efficiency (CE) for all simulated cases. It should be noted that DOC is defined as the total number of crank angle degrees from 5% to 90% of the total heat-release. With the use of pure kerosene or kerosene-diesel blend, the DOCs are seen to be shorter than those of pure diesel regardless of the rate-shapes used. This is because kerosene has a lower viscosity as compared to diesel which enables it to be better atomized to form a more homogeneous combustible mixture that burns better with higher intensity. Due to the shorter DOCs for kerosene and kerosene diesel blend, their CA50s are higher than those of diesel. Next, the CEs for pure kerosene and kerosene-diesel blend are higher than those of pure diesel irrespective of the injection rate-shapes. This is because of the lower viscosity of kerosene which allows for better fuel atomization and oxidation as compared to diesel. It is interesting to note that the CEs for pure diesel combustion are the most sensitive to the injection rate-shapes used. This is probably due to the high viscosity of diesel which depends very much on the spray injection velocity for its good atomization.

6.9.2 Soot particle dynamics, carbon monoxide and nitrogen oxide emissions

Figure 6-16 shows the normalized CO and NO emissions for all the injection rate-shapes and fuels used as well as the graph of normalized NO against normalized CO. Figure 6-16 also includes the in-cylinder temperature and NO evolutions for the RS0_0 and RS2_0 cases.
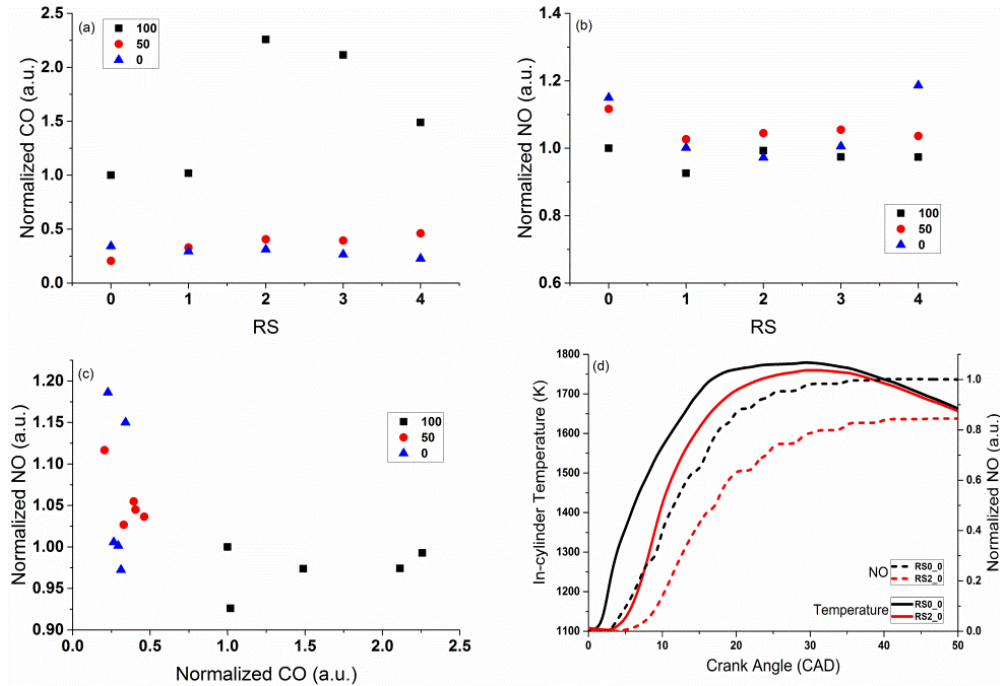
Figure 6-16 Normalized (a) CO and (b) NO emissions for all injection rate-shapes and fuels used. (c) Graph of normalized NO against normalized CO for all injection rates and fuels used. (d) The in-cylinder temperature and NO evolutions for the RS0_0 and RS2_0 cases.

It can be seen that the combustion of pure diesel fuel generates the most CO as compared to pure kerosene and kerosene-diesel blend fuels regardless of the injection rate-shapes used. This is due to the higher viscosity of diesel as compared to kerosene which gives inferior atomization and a more inhomogeneous fuel-air mixture that result in poorer combustion and more CO production. Moreover, RS2, RS3 and RS4 rate-shapes give relatively higher CO emissions due to more high viscosity diesel injected towards the end of the injection duration period. For these cases, more residence time is required for a more complete oxidation of CO. Next, NO emissions are generally seen to decrease when boot injection rate-shapes are used in place of the conventional rectangular injection rate, RS0. Firstly, this may be because combustion starts

slightly later during the expansion stroke for the boot rate-shape cases which causes the in-cylinder temperature to be lower and possibly results in less NO formation. From Figure 6-16d, the RS2 case shows an overall lower in-cylinder temperature than the RS0 case which may imply that there are fewer locally high temperature regions during the combustion of the RS2 case as compared to the RS0 case. Secondly, another reason may be because boot injection rate-shapes cause ignition delay to lengthen which allow more time for a leaner fuel-air mixture to be formed and this reduces the number of locally high temperature zones [42, 43] in the cylinder during combustion. Furthermore, pure diesel combustion generally gives the lowest NO emissions due to poorer combustion as explained previously. With poorer combustion, there are probably fewer locally high temperature zones in the cylinder and so thermal NO production is less. From Figure 6-16c, it is interesting to note that NO-CO trade-off is possible via using the appropriate injection rate-shape and fuel. It can be seen here that using pure kerosene together with a rate-shape of RS2, low CO and NO emissions can be achieved with only a slight decrease in efficiency as compared to the pure diesel base case.
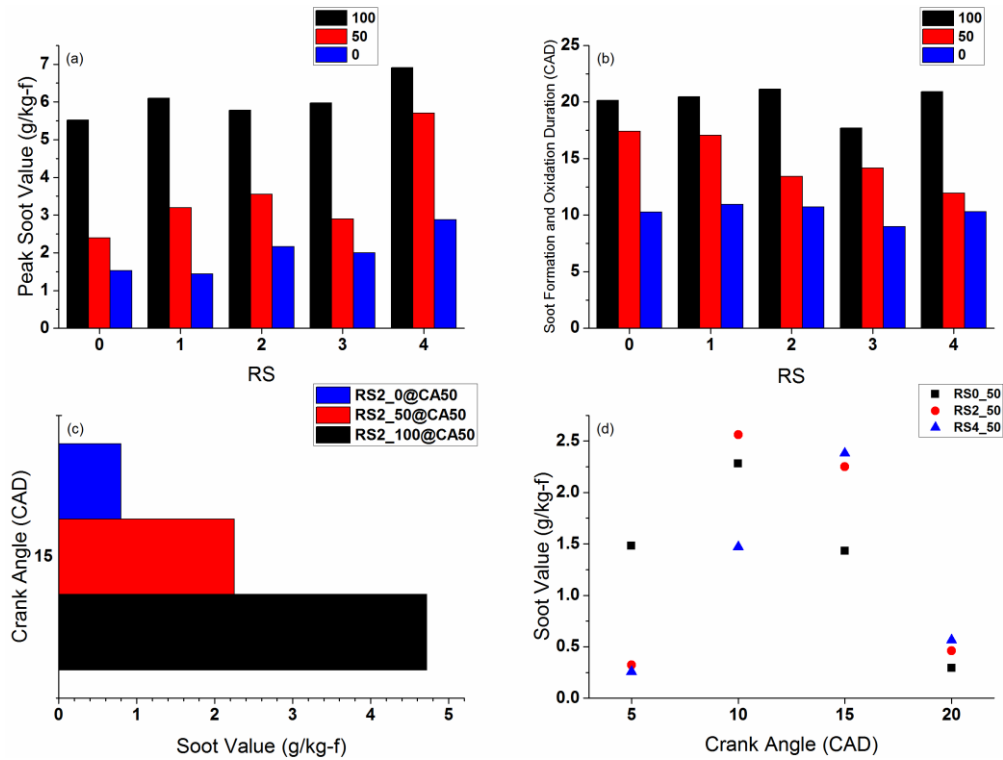
Figure 6-17 (a) The peak soot values and (b) the SFODs for all injection rate-shapes and fuels used. (c) The soot values for the RS2 cases for pure diesel, kerosene-diesel and pure kerosene at CA50 (about 15 °ATDC). (d) Graph of soot value against crank angle for the kerosene-diesel fuel for RS0, RS2 and RS4 cases.

Figure 6-17 shows the peak soot values as well as the soot formation and oxidation durations (SFODs) for all injection rate-shapes and fuels used. It also shows the soot values for the RS2 cases for pure diesel, kerosene-diesel and pure kerosene at CA50, which happens to be at about 15 ° after top dead center (ATDC) for all three cases. Finally, the graph of soot value against crank angle is shown for kerosene-diesel fuel for RS0, RS2 and RS4 cases. It should be noted that in this work SFOD is defined as the total number of crank angles for soot formation and oxidation with the starting and ending soot values taken to be at 0.5g/kg-f. It can be seen from Figure 6-17a that pure diesel combustion gives the highest quantity of soot followed by

kerosene-diesel and pure kerosene regardless of the injection rate-shapes. This trend is also seen in the work of Yu et al. [99]. Firstly, this is due to the fact that kerosene has got lesser aromatic content compared to diesel [99] which causes it to have a lower sooting tendency. Secondly, kerosene has a lower CN, a lower viscosity and a lower surface tension as compared to diesel [60, 86]. For a DICI engine, using a lower viscosity fuel enhances fuel atomization and causes the fuel-air mixture to be more homogeneous. In addition, a lower CN fuel lengthens the FLOL [93] and this allows better air entrainment of the fuel spray before combustion starts. With better air entrainment of fuel spray and a more homogeneous fuel-air mixture, the combustion intensity of kerosene will be higher than that of diesel and it can be seen from Figure 6-14. As a result, a more rapid oxidation of soot particles and soot precursors occurs during kerosene combustion as compared to diesel combustion and results in less soot generation. This explanation agrees with the findings of Kook and Pickett [93]. Next, from Figure 6-17b, it is observed that the SFODs for pure diesel are the highest followed by kerosene-diesel and pure kerosene regardless of the injection rate-shapes. The reasons for this trend are the same as those for Figure 6-17a. Firstly, as kerosene has a lower sooting tendency, less time is required to oxidize the soot particles and soot precursors produced during kerosene combustion as compared to that of diesel. Secondly, as the combustion intensity for kerosene is higher than diesel as can be seen from

157

Figure 6-14, kerosene soot particles and precursors get oxidized at a much higher rate during kerosene combustion as compared to that of diesel combustion. Figure 6-17c substantiates Figure 6-17a and b. From Figure 6-17c, it is seen that at about 15 °ATDC (CA50) for all three RS2 cases with pure diesel, kerosene-diesel and pure kerosene, pure diesel combustion gives the highest soot quantity and pure kerosene combustion gives the lowest soot. Furthermore, from Figure 6-17d, the soot evolution is seen to change with different injection rate-shapes with more soot generated at 20 °ATDC as the boot injection velocity decreases and as the boot injection duration increases.

Figure 6-18 shows the compound graphs of particle number and mass fraction of soot against soot particle size for the RS2 cases at CA50 (about 15 °ATDC) for pure diesel, kerosene-diesel and pure kerosene fuels. It should be noted that the soot mass quantity, soot particle number and soot particle size are the highest for pure diesel combustion followed by that of kerosene-diesel and pure kerosene. This observed trend agrees with the KL factor trend found in [5, 37] for kerosene and diesel combustion, where K is the soot absorption coefficient (cm^{-1}) and L is the line of sight path length through flame (cm). This is due to the lower sooting tendency, the lower CN, and the lower viscosity of kerosene as compared to those of diesel as seen in Table 2-1.
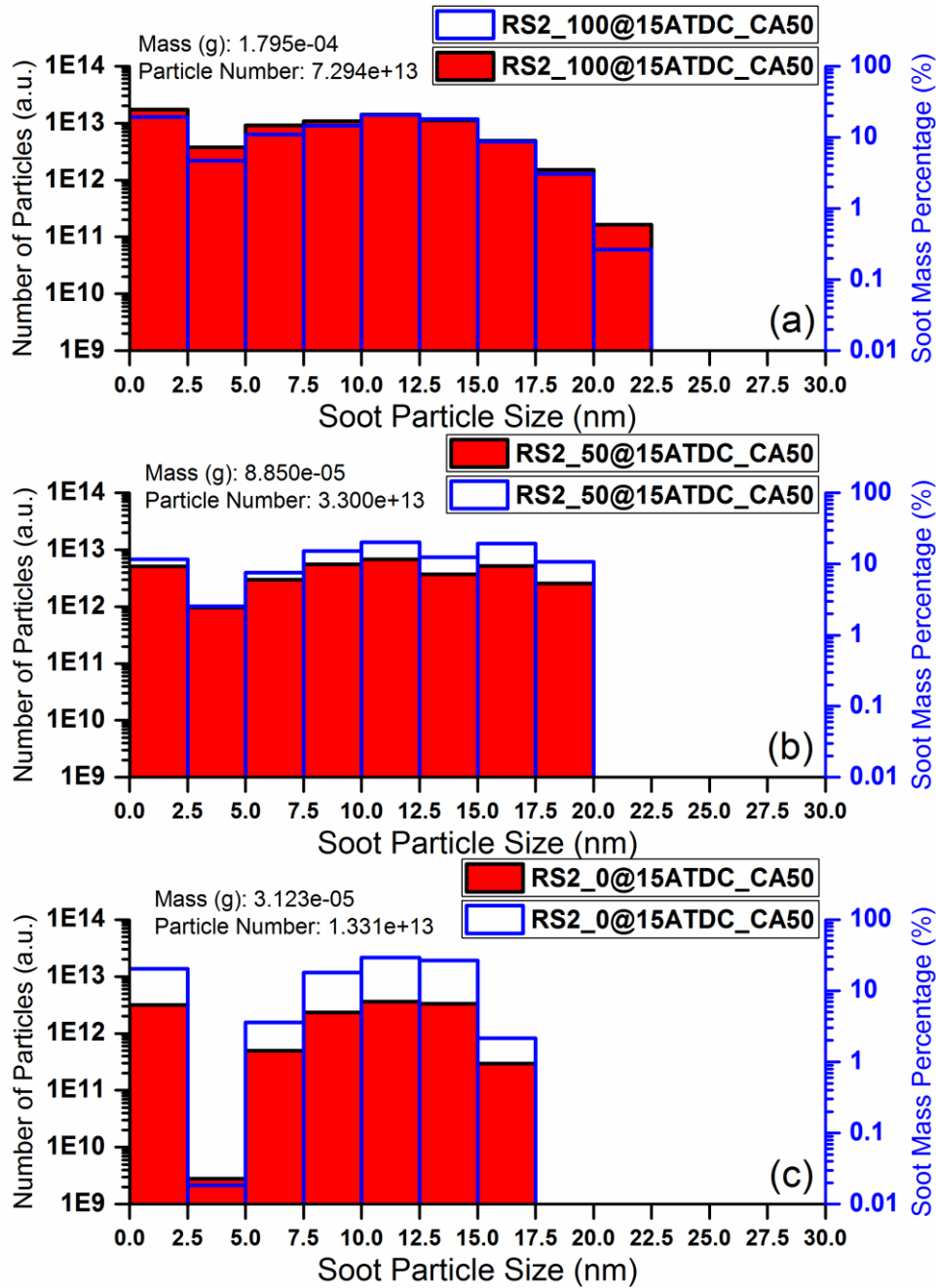
Figure 6-18 Compound graphs of particle number and mass fraction of soot against soot particle size for the RS2 cases at CA50 (about 15 °ATDC) for (a) pure diesel, (b) kerosene-diesel and (c) pure kerosene fuels.

Due to the aforementioned factors, soot precursors (C_2H_2) that are generated during the initial combustion phase are oxidized more rapidly during kerosene combustion and this is also seen in [181]. The rapid oxidation of soot precursors impede the inception of soot particles and contribute to the

decrease in soot particle number. In addition, with fewer number of nascent soot particles, growth of soot particle size through coagulation is also impeded. Furthermore, as C_2H_2 is rapidly being oxidized, soot surface growth through the HACA mechanism is also impeded, resulting in lower soot mass quantity and smaller particle sizes. Moreover, as kerosene is able to form a more homogeneous fuel-air mixture and the combustion intensity of kerosene is higher than diesel, soot surface oxidation occurs at a much higher rate during kerosene combustion as the local O_2 partial pressure and the OH radical level are higher. This causes a rapid drop in soot mass quantity, particle size and number. Therefore, the soot mass quantity, soot particle number as well as soot particle size for pure diesel combustion are all higher than those of pure kerosene.

Figure 6-19 shows the soot, OH, temperature, NO and CO profiles for the RS2 cases at CA50 (about 15°ATDC) for pure diesel, kerosene-diesel and pure kerosene fuels. It can be clearly seen that pure diesel combustion gives the most soot and CO. Moreover, it is interesting to note that OH distribution affects soot distribution for DICI combustion [261]. Also, locally high in-cylinder OH zones result in locally high temperature zones which cause locally high NO emissions in those regions.
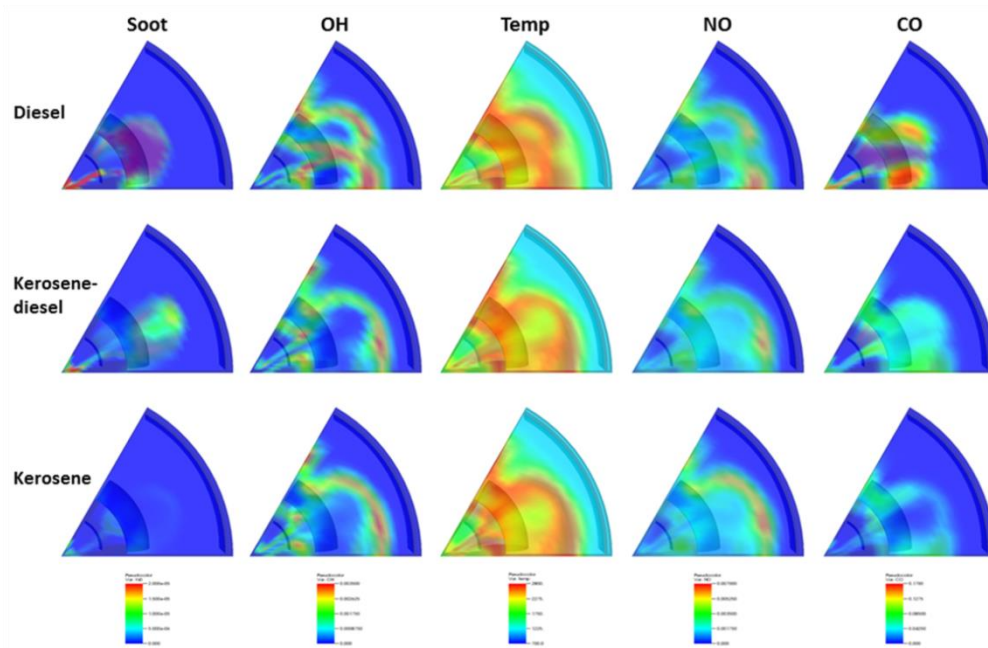
Figure 6-19 Soot, OH, temperature, NO and CO profiles for the RS2 cases at CA50 (about 15 °ATDC) for pure diesel, kerosene-diesel and pure kerosene fuels.
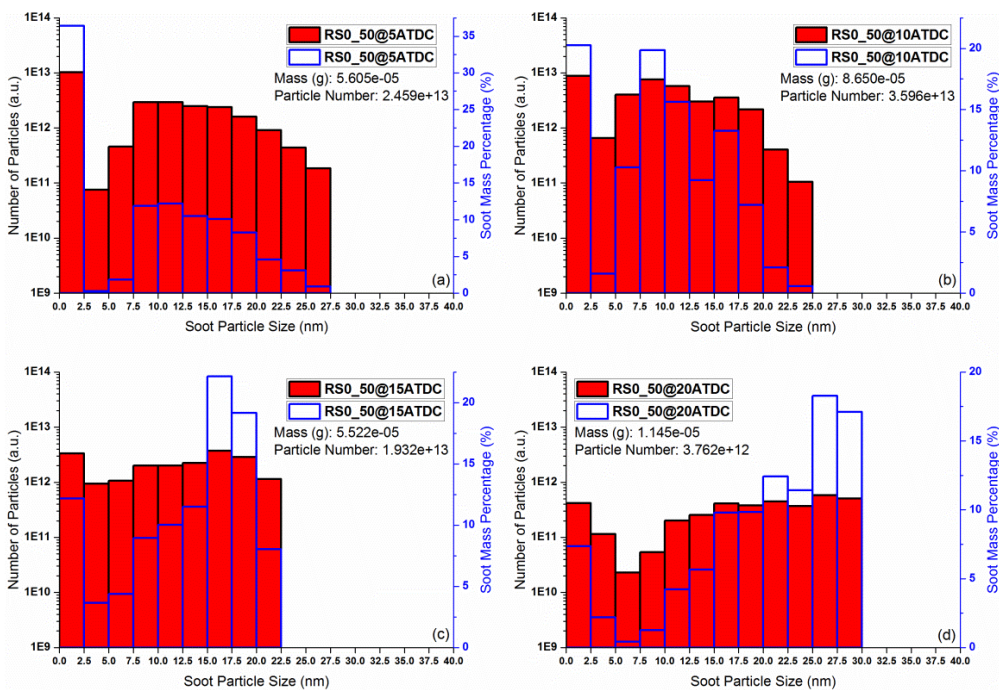
Figure 6-20 Compound graphs of particle number and mass fraction of soot against soot particle size at 5 °, 10 °, 15 ° and 20 °ATDC for the kerosene-diesel blend case of RS0.
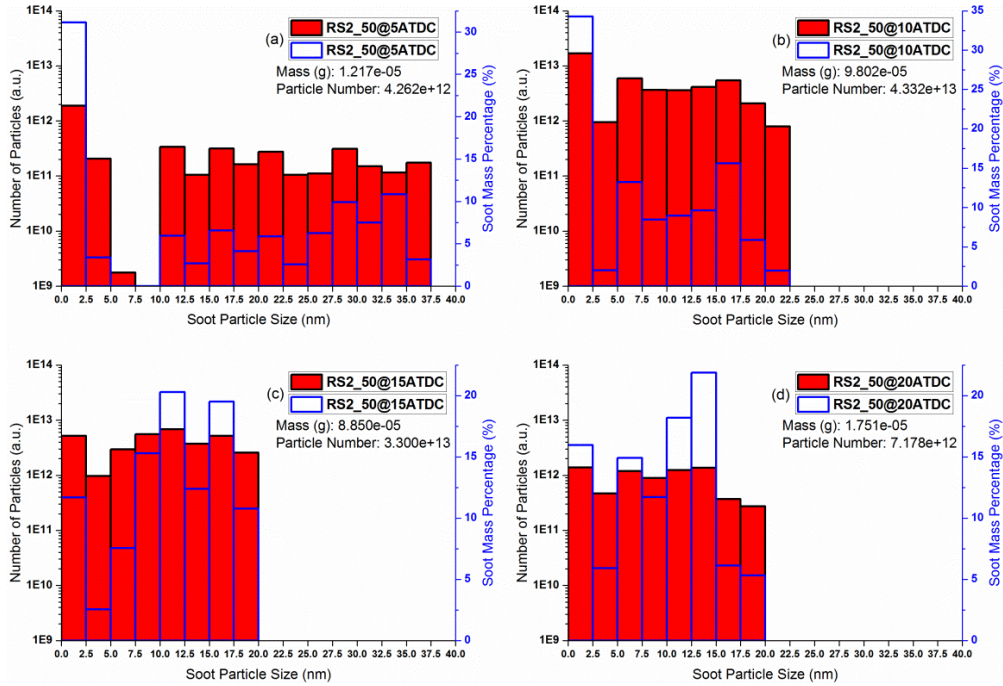
Figure 6-21 Compound graphs of particle number and mass fraction of soot against soot particle size at 5 °, 10 °, 15 ° and 20 °ATDC for the kerosene-diesel blend case of RS2.
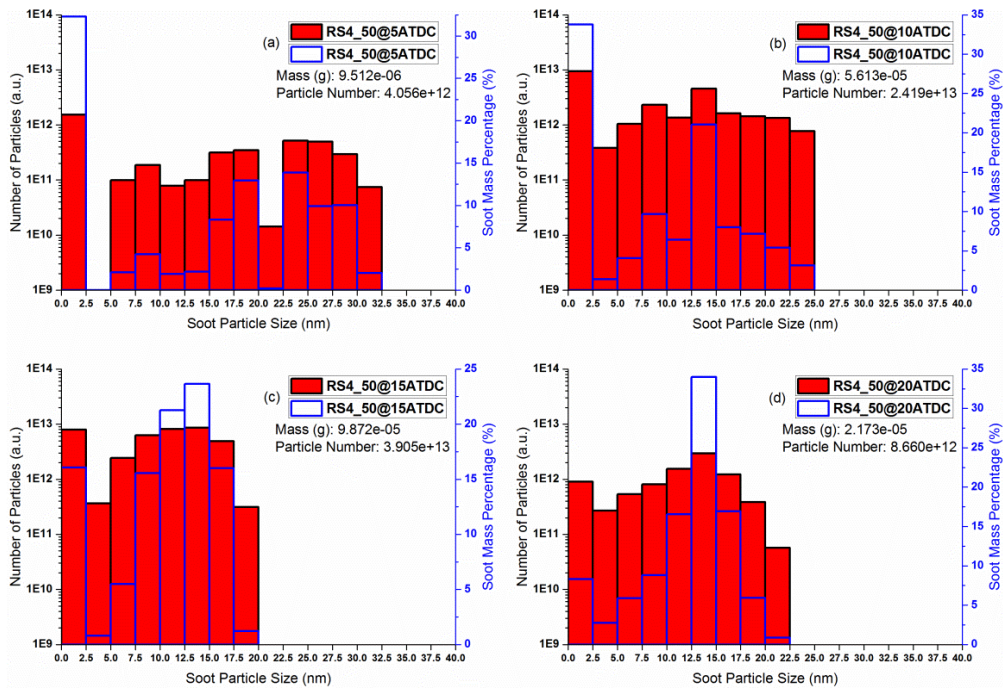
Figure 6-22 Compound graphs of particle number and mass fraction of soot against soot particle size at 5 °, 10 °, 15 ° and 20 °ATDC for the kerosene-diesel blend case of RS4.

Figure 6-20, Figure 6-21 and Figure 6-22 show the compound graphs of particle number and mass fraction of soot against soot particle size at 5 °, 10 °,

15 ° and 20 °ATDC for the kerosene-diesel blend cases of RS0, RS2 and RS4 respectively. From Figure 6-20, Figure 6-21 and Figure 6-22, it is observed that regardless of the injection rate-shapes used, there is an increase followed by a decrease both in soot mass quantity and soot particle number. This is due to the formation of soot precursors as a result of fuel pyrolysis [261], causing soot particle inception and an increase in soot mass and particle number simultaneously. Following which, soot surface growth occurs via the HACA mechanism and causes further increase in soot mass. At the same time, as soon as nascent soot particles form, soot particle coagulation occurs. This is partially responsible for the drop in soot particle number. Subsequently, soot surface oxidation occurs via O_2 and OH and causes a drop in both soot mass and particle number. Interestingly, by analyzing these three figures together with Figure 6-14b, soot particle inception is seen to occur as long as there is heat-release which causes fuel pyrolysis. Similar observation is seen in [181]. From Figure 6-20, during the initial stages of combustion for case RS0, the majority of the total soot mass is dominated by smaller soot particles. As the combustion progresses, the majority of the total soot mass becomes dominated by larger soot particles. This is because soot particle coagulation occurs as time progresses. Next, from Figure 6-21 and Figure 6-22 which are cases employing boot injection rate-shapes, it is observed that larger soot particles are formed at 5 °ATDC as compared to that of RS0. This is due to the lower

boot injection velocity that is used which causes poorer atomization and poorer combustion. As a result, soot particle inception occurs more readily due to more soot precursors available from fuel pyrolysis. This leads to more nascent soot particles participating in soot coagulation and forming larger soot particles. Also, larger soot particles form due to soot surface growth via the HACA mechanism because combustion is poorer. Interestingly, when compared to the RS0 case at 20 °ATDC, the RS2 and RS4 cases give relatively smaller soot particle sizes. This is due to the higher main injection velocity from the boot injection rate-shapes. Having a higher injection velocity and more fuel injected during the latter part of injection will result in higher heat-release during the mixing-controlled and late combustion phases. This in turn causes soot surface oxidation as well as acetylene oxidation to be more rapid during the latter part of combustion. Hence, soot surface growth is impeded and soot particles decrease in size. Finally, when comparing Figure 6-21d and Figure 6-22d, it can be seen that the soot mass distribution for RS4 is much narrower than that of RS2 at 20 °ATDC. This is due to the higher main injection velocity of RS4. This phenomenon is also seen in [262].

Figure 6-23 shows the soot and NO profiles at 5 °, 10 °, 15 ° and 20 °ATDC for kerosene-diesel blend fuel for the RS0 and RS2 cases. From Figure 6-23, it is clearly seen that injection rate-shaping does indeed cause a change in the

evolution of emissions formation. Hence, by changing the injection rate-shapes, one can control the engine-out emissions.
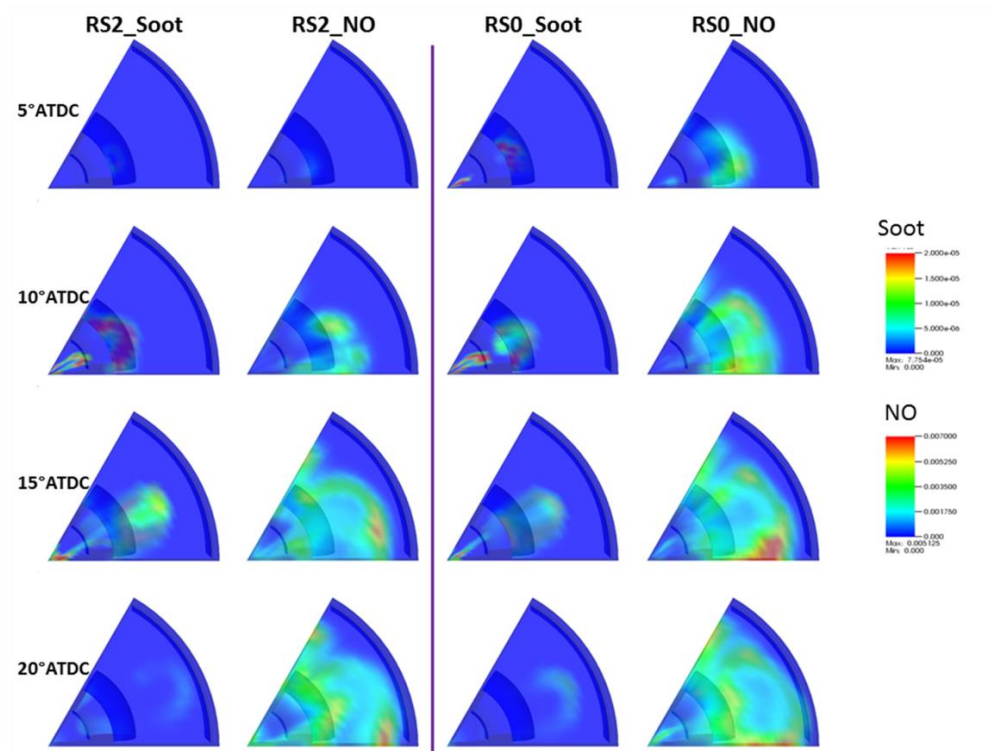
Figure 6-23 Soot and NO profiles at 5 °, 10 °, 15 °and 20 °ATDC for kerosene-diesel blend fuel for the RS0 and RS2 cases.

Finally, from this work, it can be concluded that the adjusted and enhanced kerosene-diesel reaction mechanism is robust enough to predict the performance and emissions trends of kerosene with respect to diesel.

6.10 Part B: Summary

In this work, the effects of boot injection rate-shapes on the combustion process and emissions formation of a DICI engine fueled with kerosene and diesel are investigated. Boot injection rate-shapes with varying boot injection velocity and boot injection duration are used. The KIVA4-CHEMKIN [39, 40]

code is used in conjunction with a phenomenological soot model to study the combustion process and emissions formation. A summary of this work is as follows:

1) The adjusted and enhanced kerosene-diesel reaction mechanism is robust enough to predict the combustion and emissions trends of kerosene with respect to diesel.

2) Combustion phasing occurs when boot injection rate-shapes are used.

3) When diesel is replaced by kerosene, ignition delay period lengthens and the intensity of heat-release increases. This is because of the lower CN of kerosene as compared to diesel. Due to the above reasons, kerosene combustion produces lower CO and higher NO emissions.

4) Due to the lower viscosity of kerosene as compared to diesel, the DOCs for pure kerosene and kerosene-diesel are seen to be shorter than those of pure diesel regardless of the rate-shapes used.

5) NO emissions are generally seen to decrease when boot injection rate-shapes are used in place of the conventional rectangular injection rate.

6) Pure diesel combustion gives the highest quantity of soot mass and SFODs regardless of the injection rate-shapes. This is due to the higher aromatic content of diesel compared to kerosene as well as the higher CN and viscosity of diesel.

7) Soot mass quantity, soot particle number and size are the lowest for pure kerosene combustion.

8) When boot injection rate-shapes are used, it is observed that larger soot particles are formed at 5 °ATDC for the RS2 and RS4 cases as compared to that of RS0 due to the lower boot injection velocity for RS2 and RS4.

9) As compared to the RS0 case at 20 °ATDC, the RS2 and RS4 cases give relatively smaller soot particle sizes due to the higher main injection velocity from the boot injection rate-shapes.

10) The soot mass distribution for RS4 is much narrower than that of RS2 at 20 °ATDC due to the higher main injection velocity of RS4.

In reality, optimized boot injection rate-shapes can be applied to commercial vehicles to limit soot particle size and emissions, especially under high load conditions where there are more soot formation as compared to the low load cases [181]. This injection strategy can be coupled together with exhaust aftertreatment technologies to more effectively reduce soot emissions in order to meet the stringent particulate matter (PM) emissions standards. Moreover, if low viscosity fuels such as kerosene are used in the future in DICI engines, boot injection rate-shapes can also be employed to mitigate NO_x emissions. It can also be seen from this work that the adjusted and enhanced kerosene-diesel reaction mechanism is able to predict the combustion characteristics and emissions formation trends well under DICI engine

conditions. Many of the results obtained in this chapter regarding kerosene and diesel combustion agree with the trends in literature as seen in Chapter 2.

As observed from the parametric study, one can use piezoelectric injectors in conventional diesel engines so that injection rate-shapes can be employed together with kerosene in a DICI engine to reduce NO, CO and soot emissions simultaneously especially under high engine loads. This means that the electronic control unit (ECU) and the injectors of a vehicle must be modified to accommodate this change, which is not difficult to realize.

Chapter 7 Conclusion and recommendations

7.1 Conclusion

From Chapter 1, it can be seen that the use of kerosene in direct injection compression ignition (DICI) engines is fundamentally due to the introduction of the Single Fuel Concept (SFC). Another driving factor behind the use of kerosene in DICI engines is fuel adulteration where kerosene is illegally and unethically mixed with diesel for more profit. As conventional DICI diesel engines are specifically designed to use diesel fuel, the usage of any other alternative fuels with different fuel properties such as kerosene will have adverse effects on engine emissions and combustion characteristics due to the differences between the fuel properties of kerosene and diesel. As a result, in order for kerosene to be properly and efficiently used in diesel engines, it is needful to identify the research gaps regarding the use of kerosene in DICI diesel engines. Therefore, a comprehensive literature review was carried out in Chapter 2. Chapter 2 covers the properties of kerosene, its autoignition and combustion characteristics as well as its emissions formation behavior under diesel engine operating conditions. Moreover, Chapter 2 also reviews the progress made in the development of suitable kerosene surrogates for engine applications as it is a crucial step towards the development of reliable chemical reaction mechanisms for numerical DICI engine simulations.

Through the literature review, it was noted that much experimental work was done for kerosene combustion in DICI engines. Substantial amounts of work were carried out regarding kerosene's ignition delay times in shock tube, ignition quality tester (IQT), fuel ignition tester (FIT), rapid compression machine (RCM), constant volume combustion chamber (CVCC), single-cylinder engine (SCE) and multi-cylinder engine (MCE). Moreover, kerosene's spray, combustion as well as emissions characteristics in CVCC, optical and non-optical engines were also investigated. However, it was observed from the review that reliable and compact chemical reaction mechanisms for kerosene combustion under DICI diesel engine conditions is sorely lacking. As a result, the primary objective of this thesis is to develop suitable kerosene reaction mechanisms which are small and yet robust enough to be used for DICI engine simulations. Moreover, the developed reaction mechanisms should be able to predict the major emissions such as soot, carbon monoxide (CO) and nitrogen oxide (NO). The secondary objective is to investigate the potential of kerosene in reducing emissions through injection rate-shaping. It should be noted that the research methodology is introduced in Chapter 3.

A reasonably validated $C_{12}H_{24}$ kerosene reaction mechanism, containing only 122 species and 585 reactions, with embedded soot chemistry for diesel engine simulations was developed in Chapter 4. Kerosene is simply

represented by $C_{12}H_{24}$ and assumed to be oxidized via a global reaction step. The $C_{12}H_{24}$ kerosene reaction mechanism was validated for its ignition delay times under different initial shock tube conditions of 20atm at equivalence ratios of 0.5, 1.0, 1.5 and 2.0 for temperatures between 700-1400K. Moreover, constant volume combustion validations were carried out under ambient conditions of 900K/6.0MPa and 1000K/6.7MPa and it is seen that the mechanism is able to closely replicate the heat-release rates under these ambient conditions. In addition, constant volume ignition delay validations were done under ambient densities of $14.8kg/m^3$ and $30.0kg/m^3$ for temperatures between 800-1250K. The simulated and experimental constant volume ignition delays are also similar. Furthermore, the reaction mechanism is able to predict the combustion characteristics and soot trends of kerosene reasonably under real engine conditions. In all, this $C_{12}H_{24}$ kerosene reaction mechanism is suitable to be used for diesel engine simulations.

In order to further reduce computational time, a more compact reaction mechanism was developed in Chapter 5. This chapter focuses on the development of a small but reliable kerosene-diesel reaction mechanism, suitable to be used for diesel engine simulations. The new kerosene-diesel reaction mechanism consists only of 48 species and 152 reactions. Furthermore, the kerosene sub-mechanism in this new mechanism is reasonably validated for its ignition delay times under different initial shock

tube conditions of 20atm at equivalence ratios of 0.5, 1.0, 1.5 and 2.0 for temperatures between 700-1400K. Also, the kerosene sub-mechanism has proven to replicate kerosene combustion reasonably in a CVCC. The predicted and experimental heat-release rates as well as flame lift-off lengths (FLOLs) under ambient conditions of 900K/6.0MPa and 1000K/6.7MPa are similar. Moreover, constant volume ignition delay times predicted by the kerosene sub-mechanism are close to those of experiments. Overall, this new kerosene-diesel reaction mechanism is proven to be robust and practical for diesel engine simulations.

In Chapter 6, parametric studies were carried out using the mechanism developed in Chapter 5. Chapter 6 Part A investigates the combustion characteristics of a DICI engine fueled with kerosene-diesel blends, using different piston bowl geometries together with varying injection rate-shapes were investigated. A total of three combustion bowl geometries, namely the omega combustion chamber (OCC), the shallow-depth combustion chamber (SCC) and the shallow-depth re-entrant combustion chamber (SRCC), were used together with six different ramp injection rate-shapes and pure diesel, kerosene-diesel and pure kerosene fuels. It is seen that the SRCC geometry, which has the shortest throat length, gives the highest turbulence kinetic energy (TKE) and this resulted in two peak heat-releases, with a primary peak heat-release during the premixed combustion phase and a secondary peak

heat-release during the mixing-controlled combustion phase. In addition, the SCC geometry gives rather distinct premixed combustion and mixing-controlled combustion phases due to the fact that combustion is predominantly controlled by the injected fuel spray itself because of less turbulence. Also, when kerosene is used in place of diesel, the heat-release during the premixed combustion phase increases and diminishes during the mixing-controlled and late combustion phases. It is interesting to note that the effect of injection rate-shaping on the heat-release rate is more obvious for bowl geometries that generate less TKE. Moreover, bowl geometries that generate higher TKEs as well as fuels with lower viscosities generally give lower CO emissions and higher NO emissions. More importantly, it is possible to achieve low NO and CO emissions simultaneously by using the appropriate bowl geometry, injection rate-shape and fuel, although a slight decrease in power is inevitable. On the other hand, Chapter 6 Part B investigates the effects of boot injection rate-shapes on the combustion process and emissions formation of a direct injection compression ignition engine fueled with kerosene and diesel. Boot injection rate-shapes with varying boot injection velocity and boot injection duration are used. The KIVA4-CHEMKIN code is used in conjunction with a phenomenological soot model and the adjusted and enhanced kerosene-diesel reaction mechanism to study the combustion process and emissions formation. The phenomenological soot model consists of a

number of sub-models from literature that accounts for soot particle inception, soot coagulation, soot surface growth via the hydrogen-abstraction-carbon-addition (HACA) mechanism and soot surface oxidation by oxygen (O_2) and hydroxyl radical (OH). It should be noted that the adjusted and enhanced kerosene-diesel reaction mechanism is robust enough to predict the combustion and emissions trends of kerosene with respect to diesel. From this study, boot injection rate-shapes are seen to cause combustion phasing and produce lower NO emissions in general. Furthermore, it is observed that when kerosene replaces diesel, engine efficiency and NO emissions increase while CO and soot emissions decrease. Soot mass quantity, soot particle number and soot particle size are the lowest for pure kerosene combustion. Finally, detailed analyses of the effects of boot injection rate-shapes on soot particle dynamics are also presented. From Chapter 6, it can be observed that the kerosene-diesel reaction mechanism and its enhanced version are capable of correctly predicting many of the combustion and emissions characteristics as described in Chapter 2's literature review. Moreover, it can be seen from this chapter that by using kerosene together with the appropriate injection rate-shape, one is able to reduce DICI diesel engine emissions relative to diesel fuel combustion.

7.2 Recommendations for future work

This section gives further recommendations for kerosene combustion in CI engines.

a) A substantial amount of fundamental studies on kerosene autoignition had been done thus far as seen from Table 2-2. However, more work can still be done to obtain the needed data for the modelling of kerosene combustion, especially under DICI engine conditions. Most autoignition studies done in the past were for the purpose of modelling the combustion of kerosene in gas turbines and rocket engines which have a narrower range of operating conditions as compared to DICI engines. Future fundamental shock tube and RCM studies can be done with higher equivalence ratios (φ>3) and under higher pressures (P>40atm) as DICI engines operate with high in-cylinder pressures and local in-cylinder equivalence ratios can be rather high. Moreover, as exhaust gas recirculation (EGR) is often used in diesel engines, shock tube, RCM, CVCC and engine experiments can all be carried out using different levels of oxygen content as most works listed in Table 2-2 only used 21% oxygen by volume. Furthermore, CVCC and engine experiments can be extended to cover a wider range of temperatures to simulate kerosene combustion in both hot and cold environments. In this manner, researchers and engineers will then be able to more accurately

model kerosene autoignition under a wider range of engine operating conditions.

b) It can be clearly seen from Chapter 2 that the differences in kerosene's and diesel's fuel properties do affect spray behavior and combustion characteristics. Previous works done in a CVCC regarding kerosene spray and combustion only involved variations in ambient conditions and injection pressures. Moreover, only Song et al. [97] investigated kerosene sprays together with oxygenated fuel in their study. Hence, future spray studies can include oxygenated fuels with kerosene in order to study their effects on spray behavior, combustion characteristics as well as soot evolution. Furthermore, with the advancement of injector technology, especially the development of piezo-electric injectors [238, 268-270], future works can investigate the effects of kerosene injection rate-shapes in a CVCC due to negligible work done in this area [44].

c) From Chapter 2, it was observed that most investigations for kerosene combustion were carried out in conventional DICI diesel engines with relatively fewer works focusing on advanced combustion modes such as reactivity controlled compression ignition (RCCI) [271, 272] and homogeneous charge compression ignition (HCCI) [273] combustion. More investigations regarding kerosene combustion can be done in the aforementioned areas for both engine experiments and simulations as

engine manufacturers aim to improve engine efficiency and reduce

emissions. The research can be focused on both fundamental and

applied studies for the different combustion modes and conditions.

This page was intentionally left blank.

Bibliography

[1] Xing F, Kumar A, Huang Y, Chan S, Ruan C, Gu S, et al. Flameless combustion with liquid fuel: A review focusing on fundamentals and gas turbine application. Applied Energy. 2017;193:28-51.

[2] Şöhret Y, Ekici S, Altuntaş Ö, Hepbasli A, Karakoç TH. Exergy as a useful tool for the performance assessment of aircraft gas turbine engines: A key review. Progress in Aerospace Sciences. 2016;83:57-69.

[3] Li S, Ge Y, Wei X, Li T. Mixing and combustion modeling of hydrogen peroxide/kerosene shear-coaxial jet flame in lab-scale rocket engine. Aerospace Science and Technology. 2016;56:148-54.

[4] Kim S-K, Choi H-S, Kim Y. Thermodynamic modeling based on a generalized cubic equation of state for kerosene/LOx rocket combustion. Combustion and Flame. 2012;159:1351-65.

[5] Lee J, Bae C. Application of JP-8 in a heavy duty diesel engine. Fuel. 2011;90:1762-70.

[6] Lee J, Lee J, Chu S, Choi H, Min K. Emission reduction potential in a light-duty diesel engine fueled by JP-8. Energy. 2015;89:92-9.

[7] Bowden J, Westbrook S, LePera M. Jet kerosene fuels for military diesel application. SAE 892070.

[8] Owens E, LePera M, Lestz S. Use of aviation turbine fuel JP-8 as the single fuel on the battlefield. SAE 892071.

[9] Garrett RK. Is a Single Fuel on the Battlefield Still a Viable Option? : DTIC Document; 1993.

[10] Stucker JP, Schank JF, Dombey-Moore B. Assessment of DoD Fuel Standardization Policies. DTIC Document; 1994.

[11] Montemayor AF, Stavinoha LL, Lestz SJ, LePera ME. Potential Benefits From the Use of JP-8 Fuel in Military Ground Equipment. DTIC Document; 1989.

[12] Ale B. Fuel adulteration and tailpipe emissions. Journal of the Institute of Engineering. 2003;3:12-6.

[13] Kalligeros S, Zannikos F, Stournas S, Lois E. Fuel adulteration issues in Greece. Energy. 2003;28:15-26.

[14] Cunha DA, Montes LF, Castro EV, Barbosa LL. NMR in the time domain: A new methodology to detect adulteration of diesel oil with kerosene. Fuel. 2016;166:79-85.

[15] Shenoy BV. Lessons learned from attempts to reform India's kerosene subsidy. 2010.

[16] Heywood JB. Internal combustion engine fundamentals: Mcgraw-hill New York; 1988.

[17] Muzyka V, Veimer S, Schmidt N. On the carcinogenic risk evaluation of diesel exhaust: Benzene in airborne particles and alterations of heme

metabolism in lymphocytes as markers of exposure. Science of the total environment. 1998;217:103-11.

[18] Oberdörster G, Yu C-P. The carcinogenic potential of inhaled diesel exhaust: a particle effect? Journal of Aerosol Science. 1990;21:S397-S401.

[19] Manzetti S, Andersen O. Biochemical and physiological effects from exhaust emissions. A review of the relevant literature. Pathophysiology. 2016;23:285-93.

[20] Courter LA, Luch A, Musafia-Jeknic T, Arlt VM, Fischer K, Bildfell R, et al. The influence of diesel exhaust on polycyclic aromatic hydrocarbon-induced DNA damage, gene expression, and tumor initiation in Sencar mice in vivo. Cancer letters. 2008;265:135-47.

[21] Clifford RL, Jones MJ, MacIsaac JL, McEwen LM, Goodman SJ, Mostafavi S, et al. Inhalation of diesel exhaust and allergen alters human bronchial epithelium DNA methylation. Journal of Allergy and Clinical Immunology. 2017;139:112-21.

[22] Wang H, Fu L, Zhou Y, Du X, Ge W. Trends in vehicular emissions in China's mega cities from 1995 to 2005. Environmental Pollution. 2010;158:394-400.

[23] Yang L, Zhang S, Wu Y, Chen Q, Niu T, Huang X, et al. Evaluating real-world CO2 and NOX emissions for public transit buses using a remote wireless on-board diagnostic (OBD) approach. Environmental Pollution. 2016;218:453-62.

[24] Bell J, Honour S, Power S. Effects of vehicle exhaust emissions on urban wild plant species. Environmental Pollution. 2011;159:1984-90.

[25] Lawrence S, Sokhi R, Ravindra K. Quantification of vehicle fleet PM10 particulate matter emission factors from exhaust and non-exhaust sources using tunnel measurement techniques. Environmental Pollution. 2016;210:419-28.

[26] Degraeuwe B, Weiss M. Does the New European Driving Cycle (NEDC) really fail to capture the NOX emissions of diesel cars in Europe? Environmental Pollution. 2016.

[27] Font A, Fuller GW. Did policies to abate atmospheric emissions from traffic have a positive effect in London? Environmental pollution. 2016;218:463-74.

[28] Crippa M, Janssens-Maenhout G, Guizzardi D, Galmarini S. EU effect: Exporting emission standards for vehicles through the global market economy. Journal of Environmental Management. 2016;183:959-71.

[29] Heinrichs H, Jochem P, Fichtner W. Including road transport in the EU ETS (European Emissions Trading System): A model-based analysis of the German electricity and transport sector. Energy. 2014;69:708-20.

[30] Hao H, Geng Y, Sarkis J. Carbon footprint of global passenger cars: scenarios through 2050. Energy. 2016;101:121-31.

[31] Rajagopal D, Plevin R, Hochman G, Zilberman D. Multi-objective

regulations on transportation fuels: Comparing renewable fuel mandates and emission standards. Energy Economics. 2015;49:359-69.

[32] Rodriguez-Fernandez J, Tsolakis A, Ahmadinejad M, Sitshebo S. Investigation of the Deactivation of a NOx-Reducing Hydrocarbon-Selective Catalytic Reduction (HC-SCR) Catalyst by Thermogravimetric Analysis: Effect of the Fuel and Prototype Catalyst. Energy & Fuels. 2009;24:992-1000.

[33] Geng P, Cao E, Tan Q, Wei L. Effects of alternative fuels on the combustion characteristics and emission products from diesel engines: A review. Renewable and Sustainable Energy Reviews. 2016.

[34] Sharma A, Murugan S. Durability analysis of a single cylinder DI diesel engine operating with a non-petroleum fuel. Fuel. 2017;191:393-402.

[35] Karonis D, Anastopoulos G. Tribological Evaluation of the Aviation Kerosene for Use in CI Engines. SAE Technical Paper; 2009.

[36] Pandey AK, Nandgaonkar M. Performance, emission and pump wear analysis of JP-8 fuel for military use on a 558 kW, CIDI diesel engine. SAE 2010-01-1518.

[37] Lee J, Oh H, Bae C. Combustion process of JP-8 and fossil Diesel fuel in a heavy duty diesel engine using two-color thermometry. Fuel. 2012;102:264-73.

[38] Dagaut P, Cathonnet M. The ignition, oxidation, and combustion of kerosene: A review of experimental and kinetic modeling. Progress in Energy and Combustion Science. 2006;32:48-92.

[39] Torres DJ, Trujillo MF. KIVA-4: An unstructured ALE code for compressible gas flow with sprays. Journal of Computational Physics. 2006;219:943-75.

[40] Kee RJ, Rupley FM, Miller JA. Chemkin-II: A Fortran chemical kinetics package for the analysis of gas-phase chemical kinetics. Sandia National Labs, Livermore, CA (USA); 1989.

[41] Dec JE. A conceptual model of DI diesel combustion based on laser-sheet imaging. SAE 970873.

[42] Dec JE. Advanced compression-ignition engines—understanding the in-cylinder processes. Proceedings of the combustion institute. 2009;32:2727-42.

[43] Musculus MP, Miles PC, Pickett LM. Conceptual models for partially premixed low-temperature diesel combustion. Progress in Energy and Combustion Science. 2013;39:246-83.

[44] Mohan B, Yang W, kiang Chou S. Fuel injection strategies for performance improvement and emissions reduction in compression ignition engines—A review. Renewable and Sustainable Energy Reviews. 2013;28:664-76.

[45] Kamimoto T, Bae M-h. High combustion temperature for the reduction of particulate in diesel engines. SAE 880423.

[46] Yao M, Zheng Z, Liu H. Progress and recent trends in homogeneous charge compression ignition (HCCI) engines. Progress in Energy and Combustion

Science. 2009;35:398-437.

[47] Kalghatgi GT. The outlook for fuels for internal combustion engines. International Journal of Engine Research. 2014;15:383-98.

[48] No S-Y. Application of biobutanol in advanced CI engines–A review. Fuel. 2016;183:641-58.

[49] Bae C, Kim J. Alternative fuels for internal combustion engines. Proceedings of the Combustion Institute. 2016.

[50] Yu W, Yang W, Tay K, Mohan B, Zhao F, Zhang Y. Macroscopic spray characteristics of kerosene and diesel based on two different piezoelectric and solenoid injectors. Experimental Thermal and Fluid Science. 2016;76:12-23.

[51] Čaika V, Kammerdiener T, Dörr N. Operation of piezoelectric common rail injector with diesel and FT-kerosene. SAE 2007-24-0070.

[52] Edwards T, Stricker J, Harrison III W. Coordinating Support of Fuels and Lubricant Research and Development (R&D) 2. Handbook of Aviation Fuel Properties, 3rd Edition, SAE. 2004.

[53] Wang H, Oehlschlaeger MA. Autoignition studies of conventional and Fischer–Tropsch jet fuels. Fuel. 2012;98:249-58.

[54] Kook S, Pickett LM. Liquid length and vapor penetration of conventional, Fischer–Tropsch, coal-derived, and surrogate fuel sprays at high-temperature and high-pressure ambient conditions. Fuel. 2012;93:539-48.

[55] Wei L, Yao C, Han G, Pan W. Effects of methanol to diesel ratio and diesel injection timing on combustion, performance and emissions of a methanol port premixed diesel engine. Energy. 2016;95:223-32.

[56] Dooley S, Won SH, Heyne J, Farouk TI, Ju Y, Dryer FL, et al. The experimental evaluation of a methodology for surrogate fuel formulation to emulate gas phase combustion kinetic phenomena. Combustion and Flame. 2012;159:1444-66.

[57] Lemaire R, Faccinetto A, Therssen E, Ziskind M, Focsa C, Desgroux P. Experimental comparison of soot formation in turbulent flames of diesel and surrogate diesel fuels. Proceedings of the Combustion Institute. 2009;32:737-44.

[58] Park Y, Bae C, Mounaïm-Rousselle C, Foucher F. Application of jet propellant-8 to premixed charge ignition combustion in a single-cylinder diesel engine. International Journal of Engine Research. 2015;16:92-103.

[59] Fernandes G, Fuschetto J, Filipi Z, Assanis D, McKee H. Impact of military JP-8 fuel on heavy-duty diesel engine performance and emissions. Proceedings of the Institution of Mechanical Engineers, Part D: Journal of Automobile Engineering. 2007;221:957-70.

[60] Shoba T, Crua C, Heikal M, Gold M. Optical characterisation of diesel, RME and kerosene sprays by microscopic imaging. ILASS. 2011.

[61] Shrestha A, Zheng Z, Badawy T, Henein N, Schihl P. Development of JP-8 surrogates and their validation using ignition quality tester. SAE International

Journal of Fuels and Lubricants: SAE 2014-01-9077.

[62] Park SH, Youn IM, Lim Y, Lee CS. Influence of the mixture of gasoline and diesel fuels on droplet atomization, combustion, and exhaust emission characteristics in a compression ignition engine. Fuel processing technology. 2013;106:392-401.

[63] Suh HK, Lee CS. A review on atomization and exhaust emissions of a biodiesel-fueled compression ignition engine. Renewable and Sustainable Energy Reviews. 2016;58:1601-20.

[64] de Menezes EW, da Silva R, Cataluna R, Ortega RJ. Effect of ethers and ether/ethanol additives on the physicochemical properties of diesel fuel and on engine tests. Fuel. 2006;85:815-22.

[65] Yang Y, Boehman AL, Santoro RJ. A study of jet fuel sooting tendency using the threshold sooting index (TSI) model. Combustion and Flame. 2007;149:191-205.

[66] Mensch A, Santoro RJ, Litzinger TA, Lee S-Y. Sooting characteristics of surrogates for jet fuels. Combustion and Flame. 2010;157:1097-105.

[67] Anastopoulos G, Lois E, Zannikos F, Kalligeros S, Teas C. HFRR lubricity response of an additized aviation kerosene for use in CI engines. Tribology International. 2002;35:599-604.

[68] Repetto S, Costello JF, Parmenter D. Current and potential aviation additives for higher biofuel blends in Jet A-1. Biofuels for Aviation: Feedstocks, Technology and Implementation. 2016:261.

[69] Schihl P, Decker-Hoogterp L, Pence K, Leonard K. On the Premixed Phase Combustion Behavior of JP-8 in a Military Relevant Single Cylinder Diesel Engine. SAE 2011-01-0123.

[70] Hui X, Kumar K, Sung C-J, Edwards T, Gardner D. Experimental studies on the combustion characteristics of alternative jet fuels. Fuel. 2012;98:176-82.

[71] Kang D, Kalaskar V, Kim D, Martz J, Violi A, Boehman A. Experimental study of autoignition characteristics of Jet-A surrogates and their validation in a motored engine and a constant-volume combustion chamber. Fuel. 2016;184:565-80.

[72] Valco D, Gentz G, Allen C, Colket M, Edwards T, Gowdagiri S, et al. Autoignition behavior of synthetic alternative jet fuels: An examination of chemical composition effects on ignition delays at low to intermediate temperatures. Proceedings of the Combustion Institute. 2015;35:2983-91.

[73] Zhang C, Li B, Rao F, Li P, Li X. A shock tube study of the autoignition characteristics of RP-3 jet fuel. Proceedings of the Combustion Institute. 2015;35:3151-8.

[74] Zhu Y, Li S, Davidson DF, Hanson RK. Ignition delay times of conventional and alternative fuels behind reflected shock waves. Proceedings of the Combustion Institute. 2015;35:241-8.

[75] Dean A, Penyazkov O, Sevruk K, Varatharajan B. Autoignition of

surrogate fuels at elevated temperatures and pressures. Proceedings of the Combustion Institute. 2007;31:2481-8.

[76] Vasu SS, Davidson DF, Hanson RK. Jet fuel ignition delay times: Shock tube experiments over wide conditions and surrogate model predictions. Combustion and Flame. 2008;152:125-43.

[77] Dooley S, Won SH, Chaos M, Heyne J, Ju Y, Dryer FL, et al. A jet fuel surrogate formulated by real fuel properties. Combustion and Flame. 2010;157:2333-9.

[78] Balagurunathan J. Investigation of ignition delay times of conventional (JP-8) and synthetic (S-8) jet fuels: A shock tube study: Citeseer; 2011.

[79] Mzé-Ahmed A, Dagaut P, Hadj-Ali K, Dayma G, Kick T, Herbst J, et al. Oxidation of a Coal-to-Liquid Synthetic Jet Fuel: Experimental and Chemical Kinetic Modeling Study. Energy & Fuels. 2012;26:6070-9.

[80] Zhukov VP, Sechenov VA, Starikovskiy AY. Autoignition of kerosene (Jet-A)/air mixtures behind reflected shock waves. Fuel. 2014;126:169-76.

[81] De Toni A, Werler M, Hartmann R, Cancino L, Schieβl R, Fikri M, et al. Ignition delay times of Jet A-1 fuel: Measurements in a high-pressure shock tube and a rapid compression machine. Proceedings of the Combustion Institute. 2016.

[82] Davidson D, Zhu Y, Shao J, Hanson R. Ignition delay time correlations for distillate fuels. Fuel. 2017;187:26-32.

[83] Kumar K, Sung C-J. An experimental study of the autoignition characteristics of conventional jet fuel/oxidizer mixtures: Jet-A and JP-8. Combustion and Flame. 2010;157:676-85.

[84] Allen C, Toulson E, Edwards T, Lee T. Application of a novel charge preparation approach to testing the autoignition characteristics of JP-8 and camelina hydroprocessed renewable jet fuel in a rapid compression machine. Combustion and Flame. 2012;159:2780-8.

[85] Allen C, Valco D, Toulson E, Edwards T, Lee T. Ignition behavior and surrogate modeling of JP-8 and of camelina and tallow hydrotreated renewable jet fuels at low temperatures. Combustion and Flame. 2013;160:232-9.

[86] Pickett LM, Hoogterp L. Fundamental spray and combustion measurements of JP-8 at diesel conditions. SAE 2008-01-1083.

[87] Zheng Z, Lee P-I, Shrestha A, Badawy T, Lai M-C, Henein N, et al. Role of volatility in the development of JP-8 surrogates for diesel engine application. SAE 2014-01-1389.

[88] Schihl P, Hoogterp-Decker L. On the ignition behavior of JP-8 in military relevant diesel engines.   SAE Int J Engines: SAE 2011-01-0119.

[89] Rothamer DA, Murphy L. Systematic study of ignition delay for jet fuels and diesel fuel in a heavy-duty diesel engine. Proceedings of the combustion institute. 2013;34:3021-9.

[90] Kim D, Martz J, Violi A. A surrogate for emulating the physical and

chemical properties of conventional jet fuel. Combustion and Flame. 2014;161:1489-98.

[91] Yanowitz J, Ratcliff MA, McCormick RL, Taylor JD, Murphy MJ. Compendium of experimental cetane numbers. Technical Repot National Renewable Energy Laboratory. 2014.

[92] Kook S, Pickett LM. Soot volume fraction and morphology of conventional and surrogate jet fuel sprays at 1000-K and 6.7-MPa ambient conditions. Proceedings of the Combustion Institute. 2011;33:2911-8.

[93] Kook S, Pickett LM. Soot volume fraction and morphology of conventional, fischer-tropsch, coal-derived, and surrogate fuel at diesel conditions. SAE 2012-01-0678.

[94] Jing W, Roberts WL, Fang T. Spray combustion of Jet-A and diesel fuels in a constant volume combustion chamber. Energy Conversion and Management. 2015;89:525-40.

[95] Yu W, Yang W, Mohan B, Tay K, Zhao F, Zhang Y, et al. Numerical and Experimental Study on Internal Nozzle Flow and Macroscopic Spray Characteristics of a Kind of Wide Distillation Fuel (WDF)-Kerosene. SAE 2016-01-0839.

[96] Yu W, Yang W, Zhao F. Investigation of internal nozzle flow, spray and combustion characteristics fueled with diesel, gasoline and wide distillation fuel (WDF) based on a piezoelectric injector and a direct injection compression ignition engine. Applied Thermal Engineering. 2017;114:905-20.

[97] Song L, Liu T, Fu W, Lin Q. Experimental study on spray characteristics of ethanol-aviation kerosene blended fuel with a high-pressure common rail injection system. Journal of the Energy Institute. 2016.

[98] Zha K, Yu X, Jansons M. Simultaneous High-Speed Two-Color Thermometry and Laser-Induced Incandescence Soot Measurement in a Small-Bore Optical Engine Fueled With JP-8. ASME 2012 Internal Combustion Engine Division Fall Technical Conference: American Society of Mechanical Engineers; 2012. p. 313-26.

[99] Yu X, Zha K, Florea R, Jansons M. Comparison of in-cylinder soot evolution in an optically accessible engine fueled with JP-8 and ULSD. SAE 2012-01-1315.

[100] Jansons M, Florea R, Zha K, Gingrich E. The effect of HCHO addition on combustion in an optically accessible diesel engine fueled with JP-8. SAE 2010-01-2136.

[101] Jansons M, Florea R, Zha K, Florea E. The combined effect of HCHO and C2H4 addition on combustion in an optically accessible diesel engine fueled with JP-8. SAE 2011-01-1392.

[102] Zha K, Yu X, Lai M-C, Jansons M. Investigation of Low-Temperature Combustion in an Optical Engine Fueled with Low Cetane Sasol JP-8 Fuel Using OH-PLIF and HCHO Chemiluminescence Imaging. SAE 2013-01-0898.

[103] Lee H. Biodiesel, HSD, and JP-8 combustion process and emission characteristics in a dual-stage fuel injection condition. International Journal of Energy and Power Engineering. 2014;3:209-16.

[104] Singh S, Reitz RD, Musculus MP. Comparison of the characteristic time (CTC), representative interactive flamelet (RIF), and direct integration with detailed chemistry combustion models against optical diagnostic data for multi-mode combustion in a heavy-duty DI diesel engine. SAE 2006-01-0055.

[105] Lutz T, Modiyani R. Brake thermal efficiency improvements of a commercially based diesel engine modified for operation on JP 8 fuel. SAE 2011-01-0120.

[106] Vance E, Giordano DD, Rogers J, Stewart JA. Demonstration of Power Improvements on a Diesel Engine Operating on Multiple Fuels. SAE 2010-01-1318.

[107] Mosburger M, Fuschetto J, Assanis D, Filipi Z, McKee H. Impact of high sulfur military JP-8 fuel on heavy duty diesel engine EGR cooler condensate. SAE 2008-01-1081.

[108] Smith M, Filipi Z, Schihl P, Assanis D. Effect of High Sulfur Military JP-8 Fuel on Heavy Duty Diesel Engine Emissions and EGR Cooler Condensate. ASME Internal Combustion Engine Division Fall Technical Conference. 2010:99-110.

[109] Yost DM, Montalvo DA, Frame EA. US Army investigation of diesel exhaust emissions using JP-8 fuels with varying sulfur content. SAE 961981.

[110] Yassine M, Tagomori M, Henein N, Bryzik W. White smoke emissions under cold starting of diesel engines. SAE 960249.

[111] Teoh Y, Masjuki H, Kalam M, Amalina M, How H. Impact of Premixed Kerosene Fuel on Performance, Emission and Combustion Characteristics in Partial HCCI Engine. Energy Procedia. 2014;61:1830-4.

[112] Pischinger S, Rajamani VK, Jeihouni Y. Impact of Fuel Properties on the Performance of a Direct Injection Diesel Engine under Part Homogeneous Operating Conditions. SAE 2011-01-1358.

[113] Muether M, Lamping M, Kolbeck A, Cracknell RF, Rickeard DJ, Ariztegui J, et al. Advanced combustion for low emissions and high efficiency Part 1: impact of engine hardware on HCCI combustion. SAE 2008-01-2405.

[114] Cracknell RF, Rickeard DJ, Ariztegui J, Rose KD, Muether M, Lamping M, et al. Advanced combustion for low emissions and high efficiency Part 2: impact of fuel properties on HCCI combustion. SAE 2008-01-2404.

[115] Wu Y-Y, Tsai H-C, Liu T-C. Investigation of running HCCI with dual-fuel in a small scale engine. ASME Internal Combustion Engine Division Fall Technical Conference. 2010:341-9.

[116] Risberg P, Kalghatgi G, Ångstrom H-E, Wåhlin F. Auto-ignition quality of diesel-like fuels in HCCI engines. SAE 2005-01-2127.

[117] Soloiu V, Covington A, Lewis J, Duggan M, LoBue J, Jansons M.

Performance of JP-8 Unified Fuel in a Small Bore Indirect Injection Diesel Engine for APU Applications. SAE 2012-01-1199.

[118] Soloiu V, Covington A, Lewis J, Welch J. JP-8 Combustion Characteristics in a Small Diesel Auxiliary Power Unit. ASME Internal Combustion Engine Division Fall Technical Conference. 2011:151-8.

[119] Chiatti G, Chiavola O. Performance Characteristics of a Diesel Engine Fueled With Avio-Kerosene. ASME Internal Combustion Engine Division Spring Technical Conference. 2003:45-51.

[120] Kotsiopoulos P, Yfantis E, Lois E, Hountalas D. Diesel and JP-8 fuel performance on a Petter AV1 diesel engine. AIAA 2001-0500.

[121] Andrews G, Abdelhalim S, Williams P. Characterization of diesel particulate emissions of two IDI diesel engines using diesel and kerosene fuels. SAE 961231.

[122] Andrews G, Abdelhalim S, Williams P. Pyrosynthesis of PAH in a modern IDI diesel engine. SAE 961230.

[123] Arkoudeas P, Kalligeros S, Zannikos F, Anastopoulos G, Karonis D, Korres D, et al. Study of using JP-8 aviation fuel and biodiesel in CI engines. Energy Conversion and Management. 2003;44:1013-25.

[124] Patil K, Thipse S. Characteristics of performance and emissions in a direct-injection diesel engine fuelled with kerosene/diesel blends. International Journal of Automotive and Mechanical Engineering. 2014;10:2102.

[125] Nargunde J, Jayakumar C, Sinha A, Henein NA, Bryzik W, Sattler E. Effect of Swirl and Injection Pressure on Performance and Emissions of JP-8 Fueled High Speed Single Cylinder Diesel Engine. ASME Internal Combustion Engine Division Fall Technical Conference. 2010:163-73.

[126] Nargunde J, Jayakumar C, Sinha A, Acharya K, Bryzik W, Henein N. Comparison between Combustion, Performance and Emission Characteristics of JP-8 and Ultra Low Sulfur Diesel Fuel in a Single Cylinder Diesel Engine. SAE 2010-01-1123.

[127] Chen G, Gamble JN, McAndrew DW, McGowan J, Lynch JR. Analytical and Experimental Investigation of Medium-Speed Diesel Engine Using a Kerosene Fuel. ASME Internal Combustion Engine Division Spring Technical Conference. 2006:437-42.

[128] Morita A, Sugiyama G. Influence of density and viscosity of diesel fuel on exhaust emissions. SAE 2003-01-1869.

[129] Labeckas G, Slavinskas S, Vilutienė V. Combustion, performance and emission characteristics of diesel engine operating on jet fuel treated with the cetane improver. Proceedings of 12th International Scientific Conference "Engineering for Rural Development", Latvia, Jelgava, LUA. 2013:23-4.

[130] Soloiu V, Ochieng H, Weaver J, Duggan M, Harp S, Vlcek B, et al. Combustion and Emissions Characteristics of JP-8 Blends and ULSD# 2 with Similar CN in a Direct Injection Naturally Aspirated Compression Engine. SAE

2013-01-1682.

[131] Jayakumar C, Zheng Z, Joshi U, Bryzik W, Henein N, Sattler E. Effect of Intake Pressure and Temperature on the Auto-ignition of Fuels with different Cetane Number and Volatility. SAE 2012-01-1317.

[132] Murphy L, Rothamer D. Effects of Cetane Number on Jet Fuel Combustion in a Heavy-Duty Compression Ignition Engine at High Load. SAE 2011-01-0335.

[133] Jayakumar C, Zheng Z, Joshi UM, Bryzik W, Henein NA, Sattler E. Effect of inlet air temperature on auto-ignition of fuels with different Cetane number and volatility. ASME Internal Combustion Engine Division Fall Technical Conference. 2011:261-72.

[134] Wadumesthrige K, Johnson N, Winston-Galant M, Sattler E, Bezaire N, Zeng S, et al. Performance, Durability, and Stability of a Power Generator Fueled with ULSD, S-8, JP-8, and Biodiesel. SAE 2010-01-0636.

[135] Kotsiopoulos P, Papagiannakis R, Tsakalou P, Gazinou I, Yfantis E. Experimental investigation concerning the effect of the use of Biodiesel and F-34 (JP-8) aviation fuel on performance and emissions of a DI Diesel engine. SAE 2007-01-1450.

[136] Jayakumar C, Nargunde J, Sinha A, Bryzik W, Henein NA, Sattler E. Effect of Biodiesel, Jet Propellant (JP-8) and Ultra Low Sulfur Diesel Fuel on Auto-Ignition, Combustion, Performance and Emissions in a Single Cylinder Diesel Engine. Journal of Engineering for Gas Turbines and Power. 2012;134:022801.

[137] Mahmudul H, Hagos F, Mamat R, Adam AA, Ishak W, Alenezi R. Production, characterization and performance of biodiesel as an alternative fuel in diesel engines–A review. Renewable and Sustainable Energy Reviews. 2017;72:497-509.

[138] Roy MM, Wang W, Alawi M. Performance and emissions of a diesel engine fueled by biodiesel–diesel, biodiesel–diesel-additive and kerosene–biodiesel blends. Energy Conversion and Management. 2014;84:164-73.

[139] Patil K, Thipse S. Experimental investigation of CI engine combustion, performance and emissions in DEE–kerosene–diesel blends of high DEE concentration. Energy Conversion and Management. 2015;89:396-408.

[140] Labeckas G, Slavinskas S. Combustion phenomenon, performance and emissions of a diesel engine with aviation turbine JP-8 fuel and rapeseed biodiesel blends. Energy Conversion and Management. 2015;105:216-29.

[141] Aydın H. Scrutinizing the combustion, performance and emissions of safflower biodiesel–kerosene fueled diesel engine used as power source for a generator. Energy Conversion and Management. 2016;117:400-9.

[142] Uyumaz A, Solmaz H, Yılmaz E, Yamık H, Polat S. Experimental examination of the effects of military aviation fuel JP-8 and biodiesel fuel blends on the engine performance, exhaust emissions and combustion in a

direct injection engine. Fuel Processing Technology. 2014;128:158-65.

[143] Bayındır H, Işık MZ, Aydın H. Evaluation of combustion, performance and emission indicators of canola oil-kerosene blends in a power generator diesel engine. Applied Thermal Engineering. 2017;114:234-44.

[144] Uddin SA, Azad AK, Alam M, Ahamed J. Performance of a diesel engine run with mustard-kerosene blends. Procedia Engineering. 2015;105:698-704.

[145] Yamik H. An investigation of effect of biodiesel and aviation fuel jeta-1 mixtures performance and emissions on diesel engine. Thermal Science. 2014;18:239-47.

[146] Venkanna B, Reddy CV. Performance, emission and combustion characteristics of DI diesel engine running on blends of honne oil/diesel fuel/kerosene/DMC. International Journal of Agricultural and Biological Engineering. 2011;4:48-57.

[147] Korres D, Painesaki A, Karonis D, Lois E, Kalligeros S. Use of ethanol along with biodiesel in diesel and jet fuels on a stationary diesel engine. SAE 2005-01-3676.

[148] Korres DM, Lois E, Karonis D. Use of JP-8 aviation fuel and biodiesel on a diesel engine. SAE 2004-01-3033.

[149] Bayindir H. The Effects of Cottonseed Oil–Kerosene Blends on a Diesel Engine Performance and Exhaust Emissions. Energy Sources, Part A: Recovery, Utilization, and Environmental Effects. 2010;32:901-8.

[150] Malewicki T, Gudiyella S, Brezinsky K. Experimental and modeling study on the oxidation of Jet A and the n-dodecane/iso-octane/n-propylbenzene/1, 3, 5-trimethylbenzene surrogate fuel. Combustion and Flame. 2013;160:17-30.

[151] Vandersickel A, Wright Y, Boulouchos K. Global reaction mechanism for the auto-ignition of full boiling range gasoline and kerosene fuels. Combustion Theory and Modelling. 2013;17:1020-52.

[152] Yu X, Luo X, Jansons M, Kim D, Martz J, Violi A. A Fuel Surrogate Validation Approach Using a JP-8 Fueled Optically Accessible Compression Ignition Engine. SAE International Journal of Fuels and Lubricants: SAE 2015-01-0906.

[153] Dagaut P, Karsenty F, Dayma G, Diévart P, Hadj-Ali K, Mzé-Ahmed A, et al. Experimental and detailed kinetic model for the oxidation of a Gas to Liquid (GtL) jet fuel. Combustion and Flame. 2014;161:835-47.

[154] Honnet S, Seshadri K, Niemann U, Peters N. A surrogate fuel for kerosene. Proceedings of the Combustion Institute. 2009;32:485-92.

[155] Dagaut P, Gaïl S. Chemical kinetic study of the effect of a biofuel additive on Jet-A1 combustion. The Journal of Physical Chemistry A. 2007;111:3992-4000.

[156] Violi A, Yan S, Eddings E, Sarofim A, Granata S, Faravelli T, et al. Experimental formulation and kinetic model for JP-8 surrogate mixtures.

Combustion Science and Technology. 2002;174:399-417.

[157] Mawid M, Sekar B. Detailed Chemical Kinetic Modeling of JP-8/Jet-A Fuels Ignition in High Pressure Shock Tube. AIAA Paper. 2006;5102:9-12.

[158] Lindstedt R, Maurice L. Detailed chemical-kinetic model for aviation fuels. Journal of Propulsion and Power. 2000;16:187-95.

[159] Zhang HR, Eddings EG, Sarofim AF. Criteria for selection of components for surrogates of natural gas and transportation fuels. Proceedings of the Combustion Institute. 2007;31:401-9.

[160] Chen X, Khani E, Chen C. A unified jet fuel surrogate for droplet evaporation and ignition. Fuel. 2016;182:284-91.

[161] Shrestha A, Joshi U, Zheng Z, Badawy T, Henein N, Sattler E, et al. Experimental Validation and Combustion Modeling of a JP-8 Surrogate in a Single Cylinder Diesel Engine. SAE 2014-01-1376.

[162] Roquemore W, Litzinger T, Colket M, Katta V, McNesby K, Sidhu S, et al. Combustion science to reduce PM emissions for military platforms. DTIC Document; 2012.

[163] Denman BM, Munzar JD, Bergthorson JM. An Experimental and Numerical Study of the Laminar Flame Speed of Jet Fuel Surrogate Blends. ASME Turbo Expo 2012: Turbine Technical Conference and Exposition: American Society of Mechanical Engineers; 2012. p. 1417-26.

[164] Gokulakrishnan P, Gaines G, Currano J, Klassen M, Roby R. Experimental and kinetic modeling of kerosene-type fuels at gas turbine operating conditions. Journal of Engineering for Gas Turbines and Power. 2007;129:655-63.

[165] Strelkova M, Kirillov I, Potapkin B, Safonov A, Sukhanov L, Umanskiy SY, et al. Detailed and reduced mechanisms of Jet A combustion at high temperatures. Combustion Science and Technology. 2008;180:1788-802.

[166] Cooke JA, Bellucci M, Smooke MD, Gomez A, Violi A, Faravelli T, et al. Computational and experimental study of JP-8, a surrogate, and its components in counterflow diffusion flames. Proceedings of the Combustion Institute. 2005;30:439-46.

[167] Mawid M, Park T, Sekar B, Arana C. Development of detailed chemical kinetic mechanisms for ignition/oxidation of JP-8/Jet-A/JP-7 fuels. ASME Turbo Expo 2003, collocated with the 2003 International Joint Power Generation Conference. 2003:613-24.

[168] Montgomery C, Cannon S, Mawid M, Sekar B. Reduced chemical kinetic mechanisms for JP-8 combustion. 40th AIAA Aerospace Sciences Meeting & Exhibit. 2002.

[169] Agosta A. Development of a chemical surrogate for JP-8 aviation fuel using a pressurized flow reactor: Drexel University; 2002.

[170] Guéret C, Cathonnet M, Boettner J-C, Gaillard F. Experimental study and modeling of kerosene oxidation in a jet-stirred flow reactor. Symposium

(International) on Combustion. 1991;23:211-6.

[171] Vovelle C, Delfau J-L, Reuillon M. Formation of aromatic hydrocarbons in decane and kerosene flames at reduced pressure. Soot formation in combustion: Springer; 1994. p. 50-65.

[172] Dagaut P. On the kinetics of hydrocarbons oxidation from natural gas to kerosene and diesel fuel. Physical Chemistry Chemical Physics. 2002;4:2079-94.

[173] Dagaut P, El Bakali A, Ristori A. The combustion of kerosene: Experimental results and kinetic modelling using 1-to 3-component surrogate model fuels. Fuel. 2006;85:944-56.

[174] Dagaut P. Kinetics of jet fuel combustion over extended conditions: Experimental and modeling. Journal of Engineering for Gas Turbines and Power. 2007;129:394-403.

[175] Zaev IA, Strelkova MI, Kirillov IA, Okun MV, Potapkin BV, Tangirala VE, et al. Validation of a Short Kinetic Mechanism for Jet A-Air Detonations. 43rd AIAA Joint Propulsion Conference & Exhibit2007.

[176] Wang T-S. Thermophysics characterization of kerosene combustion. Journal of Thermophysics and Heat Transfer. 2001;15:140-7.

[177] Cung K, Bhagat M, Zhang A, Lee S-Y. Numerical Study on Emission Characteristics of High-Pressure Dimethyl Ether (DME) under Different Engine Ambient Conditions. SAE 2013-01-0319.

[178] Agosta A, Cernansky N, Miller D, Faravelli T, Ranzi E. Reference components of jet fuels: kinetic modeling and experimental results. Experimental Thermal and Fluid Science. 2004;28:701-8.

[179] Eddings EG, Yan S, Ciro W, Sarofim AF. Formulation of a surrogate for the simulation of jet fuel pool fires. Combust Sci and Tech. 2005;177:715-39.

[180] An H, Yang W, Maghbouli A, Li J, Chou S, Chua K. A numerical study on a hydrogen assisted diesel engine. International Journal of Hydrogen Energy. 2013;38:2919-28.

[181] Zhao F, Yang W, Zhou D, Yu W, Li J, Tay KL. Numerical modelling of soot formation and oxidation using phenomenological soot modelling approach in a dual-fueled compression ignition engine. Fuel. 2017;188:382-9.

[182] An H, Yang W, Maghbouli A, Li J, Chua K. A skeletal mechanism for biodiesel blend surrogates combustion. Energy Conversion and Management. 2014;81:51-9.

[183] Kavuri C, Singh S, Krishnan SR, Srinivasan KK, Ciatti S. Computational Analysis of Combustion of High and Low Cetane Fuels in a Compression Ignition Engine. Journal of Engineering for Gas Turbines and Power. 2014;136:121506.

[184] Amsden AA. KIVA-3V, release 2, improvements to KIVA-3V. Los Alamos National Laboratory, Los Alamos, NM, Report No LA-UR-99-915. 1999.

[185] Amsden AA. KIVA-3: A KIVA program with block-structured mesh for complex geometries. Los Alamos National Lab., NM (United States); 1993.

[186] Amsden AA, O'rourke P, Butler T. KIVA-II: A computer program for chemically reactive flows with sprays. Los Alamos National Lab., NM (USA); 1989.

[187] Maghbouli A, Yang W, An H, Li J, Chou SK, Chua KJ. An advanced combustion model coupled with detailed chemical reaction mechanism for DI diesel engine simulation. Applied energy. 2013;111:758-70.

[188] Inc. A. ICEM CFD v14.0. 2012.

[189] Wulf A, Akdag V. Tuned grid generation with ICEM CFD. 1995.

[190] Torres DJ, O'Rourke PJ, Amsden AA. Efficient multicomponent fuel algorithm. Combust Theor Model. 2003;7:66-86.

[191] Faeth GM. Mixing, transport and combustion in sprays. Prog Energ Combust. 1987;13:293-345.

[192] Beale JC, Reitz RD. Modeling spray atomization with the Kelvin-Helmholtz/Rayleigh-Taylor hybrid model. Atomization and Sprays. 1999;9.

[193] Mohan B, Yang W, kiang Chou S. Development of an accurate cavitation coupled spray model for diesel engine simulation. Energy Conversion and Management. 2014;77:269-77.

[194] O'Rourke PJ, Amsden AA. The TAB method for numerical calculation of spray droplet breakup. 1987.

[195] O'Rourke PJ. Collective drop effects on vaporizing liquid sprays. 1981.

[196] Han Z, Reitz RD. Turbulence modeling of internal combustion engines using RNG κ-ε models. Combustion Science and Technology. 1995;106:267-95.

[197] Reitz R, Corcione F, Valentino G. Interpretation of k-ε computed turbulence length-scale predictions for engine flows. Symposium (International) on Combustion: Elsevier; 1996. p. 2717-23.

[198] Lutz AE, Kee RJ, Miller JA. SENKIN: A FORTRAN program for predicting homogeneous gas phase chemical kinetics with sensitivity analysis. 1988.

[199] Chen W, Shuai S, Wang J. A soot formation embedded reduced reaction mechanism for diesel surrogate fuel. Fuel. 2009;88:1927-36.

[200] Wang H, Yao M, Yue Z, Jia M, Reitz RD. A reduced toluene reference fuel chemical kinetic mechanism for combustion and polycyclic-aromatic hydrocarbon predictions. Combustion and Flame. 2015;162:2390-404.

[201] Wang H, Reitz RD, Yao M, Yang B, Jiao Q, Qiu L. Development of an n-heptane-n-butanol-PAH mechanism and its application for combustion and soot prediction. Combustion and Flame. 2013;160:504-19.

[202] Chang Y, Jia M, Liu Y, Li Y, Xie M. Development of a new skeletal mechanism for n-decane oxidation under engine-relevant conditions based on a

decoupling methodology. Combustion and Flame. 2013;160:1315-32.

[203] Westbrook CK, Pitz WJ, Herbinet O, Curran HJ, Silke EJ. A comprehensive detailed chemical kinetic reaction mechanism for combustion of n-alkane hydrocarbons from n-octane to n-hexadecane. Combustion and Flame. 2009;156:181-99.

[204] Golovichev V. Diesel oil surrogate mechanism. 2007.http://www.tfd.chalmers.se/~valeri/MECH/chem.inp_diesel.

[205] Golovitchev VI, Nordin N, Jarnicki R, Chomiak J. 3-D diesel spray simulations using a new detailed chemistry turbulent combustion model. SAE 2000-01-1891.

[206] Vishwanathan G, Reitz RD. Development of a practical soot modeling approach and its application to low-temperature diesel combustion. Combustion Science and Technology. 2010;182:1050-82.

[207] LLC CPCC. Safe Handling of Storage of AlphaPlus® 1-Decene and AlphaPlus® 1-Dodecene. 2013.http://www.cpchem.com/bl/nao/en-us/shglibrary/1-Decene%201-Dodecene%202013%20Final.pdf.

[208] Niemeyer KE, Sung C-J. On the importance of graph search algorithms for DRGEP-based mechanism reduction methods. Combustion and Flame. 2011;158:1439-43.

[209] Niemeyer KE, Sung C-J. Mechanism reduction for multicomponent surrogates: a case study using toluene reference fuels. Combustion and Flame. 2014;161:2752-64.

[210] Niemeyer KE, Sung C-J, Raju MP. Skeletal mechanism generation for surrogate fuels using directed relation graph with error propagation and sensitivity analysis. Combustion and flame. 2010;157:1760-70.

[211] Davidson D, Hanson R. Fundamental kinetics database utilizing shock tube measurements. 2014.http://hanson.stanford.edu/researchReports/kinetics/Fundamental_Kinetics_Database_Volume_4.pdf.

[212] Zhang K, Liang Z, Wang J, Wang Z. Diesel diffusion flame simulation using reduced n-heptane oxidation mechanism. Applied Energy. 2013;105:223-8.

[213] Juneja H, Ra Y, Reitz RD. Optimization of injection rate shape using active control of fuel injection. SAE 2004-01-0530.

[214] Pickett L. Injector Characterization. 2014.http://www.sandia.gov/ecn/cvdata/sandiaCV/injectorCharacterization.php.

[215] Sandia NL. DATA SEARCHING UTILITY. 2014.http://www.sandia.gov/ecn/cvdata/dsearch/frameset.php.

[216] Team V. VISIT: Software the Delivers Parallel Interactive Visualization. 2003.http://www.llnl.gov/visit.

[217] Rasband WS. ImageJ. 1997-2014.http://imagej.nih.gov/ij/.

[218] Tay KL, Yang W, Mohan B, An H, Zhou D, Yu W. Development of a robust and compact kerosene-diesel reaction mechanism for diesel engines. Energy Conversion and Management. 2016;108:446-58.

[219] Zeuch T, Moréac G, Ahmed SS, Mauss F. A comprehensive skeletal mechanism for the oxidation of n-heptane generated by chemistry-guided reduction. Combustion and Flame. 2008;155:651-74.

[220] Curran HJ, Gaffuri P, Pitz WJ, Westbrook CK. A comprehensive modeling study of n-heptane oxidation. Combustion and Flame. 1998;114:149-77.

[221] Shen H-PS, Steinberg J, Vanderover J, Oehlschlaeger MA. A shock tube study of the ignition of n-heptane, n-decane, n-dodecane, and n-tetradecane at elevated pressures. Energy & Fuels. 2009;23:2482-9.

[222] Maroteaux F, Noel L. Development of a reduced n-heptane oxidation mechanism for HCCI combustion modeling. Combustion and Flame. 2006;146:246-67.

[223] Demirel Y. Energy: production, conversion, storage, conservation, and coupling: Springer Science & Business Media; 2012.

[224] Sharma S, Raman S, Green WH. Intramolecular hydrogen migration in alkylperoxy and hydroperoxyalkylperoxy radicals: accurate treatment of hindered rotors. The Journal of Physical Chemistry A. 2010;114:5689-701.

[225] Chang Y, Jia M, Li Y, Zhang Y, Xie M, Wang H, et al. Development of a skeletal oxidation mechanism for biodiesel surrogate. Proceedings of the Combustion Institute. 2015;35:3037-44.

[226] Pickett LM, Siebers DL, Idicheria CA. Relationship between ignition processes and the lift-off length of diesel fuel jets. SAE 2005-01-3843.

[227] Donkerbroek A, Boot M, Luijten C, Dam N, Ter Meulen J. Flame lift-off length and soot production of oxygenated fuels in relation with ignition delay in a DI heavy-duty diesel engine. Combustion and Flame. 2011;158:525-38.

[228] Guan B, Zhan R, Lin H, Huang Z. Review of the state-of-the-art of exhaust particulate filter technology in internal combustion engines. Journal of environmental management. 2015;154:225-58.

[229] Samojeden B, Motak M, Grzybek T. The influence of the modification of carbonaceous materials on their catalytic properties in SCR-NH 3. A short review. Comptes Rendus Chimie. 2015;18:1049-73.

[230] Ghazali WNMW, Mamat R, Masjuki H, Najafi G. Effects of biodiesel from different feedstocks on engine performance and emissions: A review. Renewable and Sustainable Energy Reviews. 2015;51:585-602.

[231] Kumar BR, Saravanan S. Use of higher alcohol biofuels in diesel engines: A review. Renewable and Sustainable Energy Reviews. 2016;60:84-115.

[232] Yang P-M, Lin KC, Lin Y-C, Jhang S-R, Chen S-C. Emission evaluation of a diesel engine generator operating with a proportion of isobutanol as a fuel

additive in biodiesel blends. Applied Thermal Engineering. 2016;100:628-35.

[233] Datta A, Mandal BK. Impact of alcohol addition to diesel on the performance combustion and emissions of a compression ignition engine. Applied Thermal Engineering. 2016;98:670-82.

[234] Ibrahim A. Performance and combustion characteristics of a diesel engine fuelled by butanol–biodiesel–diesel blends. Applied Thermal Engineering. 2016;103:651-9.

[235] Prashant G, Lata D, Joshi P. Investigations on the effect of methanol blend on the combustion parameters of dual fuel diesel engine. Applied Thermal Engineering. 2016;103:187-94.

[236] Imtenan S, Varman M, Masjuki H, Kalam M, Sajjad H, Arbab M, et al. Impact of low temperature combustion attaining strategies on diesel engine emissions for diesel and biodiesels: a review. Energy Conversion and Management. 2014;80:329-56.

[237] Shuai S, Abani N, Yoshikawa T, Reitz RD, Park SW. Evaluation of the effects of injection timing and rate-shape on diesel low temperature combustion using advanced CFD modeling. Fuel. 2009;88:1235-44.

[238] Payri R, Gimeno J, Viera JP, Plazas AH. Needle lift profile influence on the vapor phase penetration for a prototype diesel direct acting piezoelectric injector. Fuel. 2013;113:257-65.

[239] d'Ambrosio S, Ferrari A. Effects of pilot injection parameters on low temperature combustion diesel engines equipped with solenoid injectors featuring conventional and rate-shaped main injection. Energy Conversion and Management. 2016;110:457-68.

[240] Macian V, Payri R, Ruiz S, Bardi M, Plazas AH. Experimental study of the relationship between injection rate shape and Diesel ignition using a novel piezo-actuated direct-acting injector. Applied Energy. 2014;118:100-13.

[241] Plamondon E, Seers P. Development of a simplified dynamic model for a piezoelectric injector using multiple injection strategies with biodiesel/diesel-fuel blends. Applied Energy. 2014;131:411-24.

[242] Desantes J, Benajes J, Molina S, Gonzalez C. The modification of the fuel injection rate in heavy-duty diesel engines. Part 1: Effects on engine performance and emissions. Applied Thermal Engineering. 2004;24:2701-14.

[243] Desantes J, Benajes J, Molina S, Gonzàlez C. The modification of the fuel injection rate in heavy-duty diesel engines: part 2: effects on combustion. Applied thermal engineering. 2004;24:2715-26.

[244] Ghaffarpour M, Azarfam M, Noorpoor A. Emission reduction in diesel engines using new fuel injection system. JSME International Journal Series B. 2006;49:1298-306.

[245] Mohan B, Yang W, Yu W, Tay KL, Chou SK. Numerical investigation on the effects of injection rate shaping on combustion and emission characteristics of biodiesel fueled CI engine. Applied Energy. 2015;160:737-45.

[246] Shi Y, Reitz RD. Optimization study of the effects of bowl geometry, spray targeting, and swirl ratio for a heavy-duty diesel engine operated at low and high load. International Journal of Engine Research. 2008;9:325-46.

[247] Prasad B, Sharma C, Anand T, Ravikrishna R. High swirl-inducing piston bowls in small diesel engines for emission reduction. Applied Energy. 2011;88:2355-67.

[248] Jaichandar S, Annamalai K. Effects of open combustion chamber geometries on the performance of pongamia biodiesel in a DI diesel engine. Fuel. 2012;98:272-9.

[249] Jaichandar S, Annamalai K. Influences of re-entrant combustion chamber geometry on the performance of Pongamia biodiesel in a DI diesel engine. Energy. 2012;44:633-40.

[250] Jaichandar S, Kumar PS, Annamalai K. Combined effect of injection timing and combustion chamber geometry on the performance of a biodiesel fueled diesel engine. Energy. 2012;47:388-94.

[251] Jaichandar S, Annamalai K. Combined impact of injection pressure and combustion chamber geometry on the performance of a biodiesel fueled diesel engine. Energy. 2013;55:330-9.

[252] Li J, Yang W, An H, Maghbouli A, Chou S. Effects of piston bowl geometry on combustion and emission characteristics of biodiesel fueled diesel engines. Fuel. 2014;120:66-73.

[253] Taghavifar H, Khalilarya S, Jafarmadar S. Engine structure modifications effect on the flow behavior, combustion, and performance characteristics of DI diesel engine. Energy Conversion and Management. 2014;85:20-32.

[254] Vedharaj S, Vallinayagam R, Yang W, Saravanan C, Lee P. Optimization of combustion bowl geometry for the operation of kapok biodiesel–diesel blends in a stationary diesel engine. Fuel. 2015;139:561-7.

[255] Gafoor CA, Gupta R. Numerical investigation of piston bowl geometry and swirl ratio on emission from diesel engines. Energy Conversion and Management. 2015;101:541-51.

[256] Bapu BR, Saravanakumar L, Prasad BD. Effects of combustion chamber geometry on combustion characteristics of a DI diesel engine fueled with calophyllum inophyllum methyl ester. Journal of the Energy Institute. 2015.

[257] Li J, Yang W, Zhou D. Modeling study on the effect of piston bowl geometries in a gasoline/biodiesel fueled RCCI engine at high speed. Energy Conversion and Management. 2016;112:359-68.

[258] Li J, Yang W, An H, Zhao D. Effects of fuel ratio and injection timing on gasoline/biodiesel fueled RCCI engine: A modeling study. Applied Energy. 2015;155:59-67.

[259] Lahane S, Subramanian K. Impact of nozzle holes configuration on fuel spray, wall impingement and NO x emission of a diesel engine for biodiesel–diesel blend (B20). Applied Thermal Engineering. 2014;64:307-14.

[260] Kiplimo R, Tomita E, Kawahara N, Yokobe S. Effects of spray impingement, injection parameters, and EGR on the combustion and emission characteristics of a PCCI diesel engine. Applied Thermal Engineering. 2012;37:165-75.

[261] Tao F, Reitz RD, Foster DE, Liu Y. Nine-step phenomenological diesel soot model validated over a wide range of engine conditions. International Journal of Thermal Sciences. 2009;48:1223-34.

[262] Vishwanathan G, Reitz RD. Application of a semi-detailed soot modeling approach for conventional and low temperature diesel combustion–Part I: Model performance. Fuel. 2015;139:757-70.

[263] Frenklach M, Wang H. Detailed modeling of soot particle nucleation and growth. Symposium (International) on Combustion: Elsevier; 1991. p. 1559-66.

[264] Kim C, El-Leathy A, Xu F, Faeth G. Soot surface growth and oxidation in laminar diffusion flames at pressures of 0.1–1.0 atm. Combustion and flame. 2004;136:191-207.

[265] Nagle J, Strickland-Constable R. Oxidation of Carbon between 1000-2000 C. Proceedings of the fifth carbon conference: Pergamon Oxford; 1962. p. 154.

[266] Fenimore CP, Jones GW. Oxidation of soot by hydroxyl radicals. The Journal of Physical Chemistry. 1967;71:593-7.

[267] Jiaqiang E, Liu T, Yang W, Li J, Gong J, Deng Y. Effects of fatty acid methyl esters proportion on combustion and emission characteristics of a biodiesel fueled diesel engine. Energy Conversion and Management. 2016;117:410-9.

[268] Ferrari A, Mittica A. FEM modeling of the piezoelectric driving system in the design of direct-acting diesel injectors. Applied Energy. 2012;99:471-83.

[269] Le D, Pietrzak BW, Shaver GM. Dynamic surface control of a piezoelectric fuel injector during rate shaping. Control Engineering Practice. 2014;30:12-26.

[270] Viera JP, Payri R, Swantek AB, Duke DJ, Sovis N, Kastengren AL, et al. Linking instantaneous rate of injection to X-ray needle lift measurements for a direct-acting piezoelectric injector. Energy Conversion and Management. 2016;112:350-8.

[271] Reitz RD, Duraisamy G. Review of high efficiency and clean reactivity controlled compression ignition (RCCI) combustion in internal combustion engines. Progress in Energy and Combustion Science. 2015;46:12-71.

[272] Li J, Yang W, Zhou D. Review on the management of RCCI engines. Renewable and Sustainable Energy Reviews. 2017;69:65-79.

[273] Khandal S, Banapurmath N, Gaitonde V, Hiremath S. Paradigm shift from mechanical direct injection diesel engines to advanced injection strategies of diesel homogeneous charge compression ignition (HCCI) engines-A

comprehensive review. Renewable and Sustainable Energy Reviews. 2017;70:369-84.

Appendix A: $C_{12}H_{24}$ kerosene reaction mechanism

ELEMENTS					
H	C	O	N		

SPECIES					
C12H24	CH3	NC3H7	IC4H7	OC6H4O	A2-
NC7H16	CH4	C4H8	IC4H7O	C6H5OH	A1C2H-
IC8H18	C2H2	PC4H9	IC4H6OH	C6H5CH2OO	A1C2H
C7H8	C2H3	C5H10	IC3H7CHO	C6H5CH2O	A1C2H3
O2	C2H4	NC3H7CHO	IC3H7CO	C6H5CHO	A2R5
N2	C2H5	NC3H7CO	IC3H7	C6H5CO	A3-
CO2	HCCO	C7H15-2	IC3H5CHO	C2H3CO	A1
H2O	CH2CO	C7H15O2-2	IC3H5CO	NC3H7COC2H3	A2
CO	CH3CO	C7H14OOH2-4	CH2CCH2OH	N2O	A3
H2	CH3CHO	C7H14OOH2-4O2	TC3H6CHO	NO	A4
OH	CH2CHO	NC7KET24	TC3H6O2CHO	NO2	C(S)
H2O2	CH3O2	AC8H17	TC3H6O2HCO	C2H	NC9H20
HO2	CH3OH	AC8H17O2	CH3COCH3	C3H2	C9H19-4
H	CH2OH	AC8H16OOH-B	CH3COCH2	C4H2	C9H19O2-4
O	CH3O2H	IC8ETERAB	CH3COCH2O2	C4H3	C9OOH4-5
CH3O	C2H6	AC8H16OOH-BO2	C3KET21	C4H4	NC4H9CO
CH2O	C3H3	IC8KETAB	C6H5CH2	IC4H5	C9OOH4-5O2
HCO	C3H4	IC4H9	C6H4CH3	C5H5	C9KET4-5
CH	C3H5	TC4H9	OC6H4CH3	C6H5O	NC3H7CHCO
CH2	C3H6	IC4H8	HOC6H4CH3	NC4H9CHO	C9O4-5

200

	REACTIONS	A	b	E
1	7C12H24+O2=>3C7H8+7NC9H20+2H2O	1.00E+51	0	10500
2	C9H19-4+H=NC9H20	1.00E+14	0	0
3	NC9H20+H=C9H19-4+H2	2.60E+06	2.4	4471
	Reverse Arrhenius coefficients:	3.93E+03	2.7	11260
4	NC9H20+O=C9H19-4+OH	9.54E+04	2.7	2106
	Reverse Arrhenius coefficients:	6.33E+01	3	6798
5	NC9H20+OH=C9H19-4+H2O	1.50E+08	1.6	-35
	Reverse Arrhenius coefficients:	6.15E+05	1.9	21910
6	NC9H20+HO2=C9H19-4+H2O2	1.12E+13	0	17690
	Reverse Arrhenius coefficients:	4.35E+11	0	8165
7	NC9H20+O2=C9H19-4+HO2	8.00E+15	0	50150
	Reverse Arrhenius coefficients:	1.10E+09	0.7	-541
8	C5H10+PC4H9=C9H19-4	1.00E+11	0	8200
9	C9H19O2-4=C9H19-4+O2	1.36E+23	-2.4	37670
	Reverse Arrhenius coefficients:	7.54E+12	0	0
10	C9H19O2-4=C9OOH4-5	1.50E+12	0	26850
	Reverse Arrhenius coefficients:	2.26E+10	-0.1	14270
11	C9OOH4-5O2=C9OOH4-5+O2	4.37E+23	-2.4	37640
	Reverse Arrhenius coefficients:	7.54E+12	0	0
12	C9OOH4-5O2=C9KET4-5+OH	1.00E+11	0	23850
	Reverse Arrhenius coefficients:	1.18E+04	1.4	47350

13	C9KET4-5=OH+NC3H7CO+NC4H9CHO	1.05E+17	0	41600
	Reverse Arrhenius coefficients:	0.00E+00	0	0
14	C9OOH4-5=C9O4-5+OH	6.00E+11	0	22000
	Reverse Arrhenius coefficients:	0.00E+00	0	0
15	C9OOH4-5=NC3H7COC2H3+NC3H7+H2O	6.00E+11	0	22000
	Reverse Arrhenius coefficients:	0.00E+00	0	0
16	C9O4-5+OH=NC3H7COC2H3+NC3H7+H2O	2.50E+12	0	0
	Reverse Arrhenius coefficients:	0.00E+00	0	0
17	C9O4-5+OH=NC3H7CHCO+PC4H9+H2O	2.50E+12	0	0
	Reverse Arrhenius coefficients:	0.00E+00	0	0
18	NC4H9CHO+O2=NC4H9CO+HO2	2.00E+13	0.5	42200
	Reverse Arrhenius coefficients:	1.00E+07	0	40000
19	NC4H9CHO+OH=NC4H9CO+H2O	2.69E+10	0.8	-340
	Reverse Arrhenius coefficients:	2.14E+10	0.7	31240
20	NC4H9CHO+H=NC4H9CO+H2	4.00E+13	0	4200
	Reverse Arrhenius coefficients:	1.80E+13	0	24000
21	NC4H9CHO+O=NC4H9CO+OH	5.00E+12	0	1790
	Reverse Arrhenius coefficients:	1.00E+12	0	19000
22	NC4H9CHO+HO2=NC4H9CO+H2O2	2.80E+12	0	13600
	Reverse Arrhenius coefficients:	1.00E+12	0	10000
23	NC4H9CHO+CH3=NC4H9CO+CH4	1.70E+12	0	8440
	Reverse Arrhenius coefficients:	1.50E+13	0	28000
24	NC4H9CHO+CH3O=NC4H9CO+CH3OH	1.15E+11	0	1280

	Reverse Arrhenius coefficients:	3.00E+11	0	18000
25	NC4H9CHO+CH3O2=NC4H9CO+CH3O2H	1.00E+12	0	9500
	Reverse Arrhenius coefficients:	2.50E+10	0	10000
26	NC4H9CO=PC4H9+CO	1.00E+11	0	9600
	Reverse Arrhenius coefficients:	1.00E+11	0	0
27	NC3H7COC2H3+H=H2+C3H6+C2H3CO	3.00E+12	0	0
	Reverse Arrhenius coefficients:	0.00E+00	0	0
28	NC3H7COC2H3+OH=H2O+C3H6+C2H3CO	3.00E+12	0	0
	Reverse Arrhenius coefficients:	0.00E+00	0	0
29	NC3H7COC2H3+O=OH+C3H6+C2H3CO	3.00E+12	0	0
	Reverse Arrhenius coefficients:	0.00E+00	0	0
30	NC3H7COC2H3+HO2=H2O2+C3H6+C2H3CO	5.00E+12	0	15000
	Reverse Arrhenius coefficients:	0.00E+00	0	0
31	NC3H7CHCO+H=H2+C3H6+HCCO	3.00E+12	0	0
	Reverse Arrhenius coefficients:	0.00E+00	0	0
32	NC3H7CHCO+O=OH+C3H6+HCCO	3.00E+12	0	0
	Reverse Arrhenius coefficients:	0.00E+00	0	0
33	NC3H7CHCO+OH=H2O+C3H6+HCCO	3.00E+12	0	0
	Reverse Arrhenius coefficients:	0.00E+00	0	0
34	NC3H7CHCO+HO2=H2O2+C3H6+HCCO	5.00E+12	0	15000
	Reverse Arrhenius coefficients:	0.00E+00	0	0
35	NC3H7CHCO+H=PC4H9+CO	3.00E+12	0	0
	Reverse Arrhenius coefficients:	0.00E+00	0	0

36	NC3H7CHCO+O=C4H8+CO2	3.00E+12	0	0
	Reverse Arrhenius coefficients:	0.00E+00	0	0
37	NC3H7CHCO+OH=PC4H9+CO2	3.00E+12	0	0
	Reverse Arrhenius coefficients:	0.00E+00	0	0
38	NC7H16<=>H+C7H15-2	1.30E+88	-21	139500
	Reverse Arrhenius coefficients:	2.26E+83	-20.3	40830
39	NC7H16+H<=>C7H15-2+H2	2.60E+06	2.4	4471
	Reverse Arrhenius coefficients:	1.81E+01	3.4	9318
40	NC7H16+O<=>C7H15-2+OH	9.54E+04	2.7	2106
	Reverse Arrhenius coefficients:	3.48E-01	3.7	5541
41	NC7H16+OH<=>C7H15-2+H2O	1.90E+06	2	-596
	Reverse Arrhenius coefficients:	3.62E+02	2.9	19140
42	NC7H16+HO2<=>C7H15-2+H2O2	4.00E+03	3.4	13720
	Reverse Arrhenius coefficients:	4.98E-01	3.7	2562
43	NC7H16+O2<=>C7H15-2+HO2	2.80E+13	0	50150
	Reverse Arrhenius coefficients:	1.00E+09	0.6	309
44	C7H15-2<=>PC4H9+C3H6	3.25E+19	-1.8	31360
	Reverse Arrhenius coefficients:	1.00E+11	0	8200
45	C7H15O2-2<=>C7H15-2+O2	1.36E+23	-2.4	37670
	Reverse Arrhenius coefficients:	2.34E+12	0	0
46	C7H15O2-2<=>C7H14OOH2-4	6.00E+10	0	20450
47	C7H14OOH2-4O2<=>C7H14OOH2-4+O2	1.39E+23	-2.4	37600
	Reverse Arrhenius coefficients:	7.54E+12	0	0

48	C7H14OOH2-4O2<=>NC7KET24+OH	1.25E+10	0	17450
49	NC7KET24<=>NC3H7CHO+CH3COCH2+OH	5.00E+16	0	39000
	Reverse Arrhenius coefficients:	0.00E+00	0	0
50	C7H14OOH2-4<=>OH+CH3CHO+C5H10	1.55E+12	0.6	30090
	Reverse Arrhenius coefficients:	0.00E+00	0	0
51	IC8H18=TC4H9+IC4H9	1.50E+30	-3.9	84150
	Reverse Arrhenius coefficients:	3.59E+14	-0.8	0
52	IC8H18+H=AC8H17+H2	7.34E+05	2.8	8147
	Reverse Arrhenius coefficients:	5.10E+01	3.4	10480
53	IC8H18+OH=AC8H17+H2O	7.50E+06	1.8	1431
54	IC8H18+HO2=AC8H17+H2O2	2.00E+03	3.6	17160
55	IC8H18+O2=AC8H17+HO2	6.30E+13	0	50760
	Reverse Arrhenius coefficients:	2.30E+10	0.3	-1592
56	IC8H18+O=AC8H17+OH	8.55E+03	3	3123
	Reverse Arrhenius coefficients:	3.12E-01	3.7	4048
57	IC8H18=AC8H17+H	5.75E+17	-0.4	101200
	Reverse Arrhenius coefficients:	1.00E+14	0	0
58	IC4H8+IC4H9=AC8H17	6.09E+02	2.5	8520
	Reverse Arrhenius coefficients:	1.00E+14	-0.1	26780
59	AC8H17O2=AC8H17+O2	3.46E+20	-1.7	35720
	Reverse Arrhenius coefficients:	4.52E+12	0	0
60	AC8H17O2=AC8H16OOH-B	2.50E+10	0	20450
61	AC8H16OOH-B=>IC8ETERAB+OH	3.00E+11	0	14250

62	AC8H16OOH-BO2=AC8H16OOH-B+O2	1.36E+23	-2.4	37280
	Reverse Arrhenius coefficients:	7.54E+12	0	0
63	AC8H16OOH-BO2=IC8KETAB+OH	2.50E+10	0	21000
64	IC8ETERAB+OH=>IC4H8+IC3H7CO+H2O	1.25E+12	0	0
65	IC8ETERAB+HO2=>IC4H8+IC3H7CO+H2O2	2.50E+12	0	17700
66	IC8KETAB=>IC3H7CHO+TC3H6CHO+OH	1.00E+16	0	39000
67	IC8H18+C7H15-2=NC7H16+AC8H17	1.50E+11	0	14500
68	C7H15-2+C7H8=NC7H16+C6H5CH2	7.00E+12	0	8900
69	AC8H17+C7H8=IC8H18+C6H5CH2	7.00E+12	0	7900
70	C7H8+OH=C6H5CH2+H2O	1.77E+04	2.4	-602
71	C7H8+HO2=C6H5CH2+H2O2	7.00E+04	3	12000
72	C7H8+O2=C6H5CH2+HO2	2.18E+07	2.5	46000
73	C7H8+HO2=C6H4CH3+H2O2	9.20E+12	0	28800
74	C7H8+OH=C6H4CH3+H2O	2.34E+02	2.7	730
75	C7H8+O=OC6H4CH3+H	2.48E+14	-0.3	4670
76	C6H5CH2+HO2=C6H5CH2O+OH	5.50E+12	0	0
77	C7H8+H=C6H4CH3+H2	1.90E+07	2	9696
78	C7H8+O=C6H4CH3+OH	2.00E+13	0	14700
79	C7H8+CH3=C6H4CH3+CH4	1.70E+00	3.7	9500
80	C6H4CH3+H=C7H8	1.00E+14	0	0
81	C7H8=A1-+CH3	2.66E+16	0	97830.4
82	C7H8=C6H5CH2+H	1.09E+15	0	87463.4
83	C7H8+H=A1+CH3	5.78E+13	0	8088

84	C6H5OH+CH3=C7H8+OH	4.00E+11	0	7700
85	C7H8+H=C6H5CH2+H2	6.47E+00	4	3384
86	C7H8+O=C6H5CH2+OH	6.00E+10	0.7	7632
87	C6H5O+C7H8=C6H5OH+C6H5CH2	1.60E+12	0	15100
88	C6H5CH2O+C6H5CH2=C6H5CHO+C7H8	1.00E+13	0	0
89	C6H5CHO+C6H5CH2=C6H5CO+C7H8	1.60E+12	0	13100
90	C6H5CH2+O=C6H5CHO+H	1.51E+13	0	0
91	C6H5CH2+O=A1-+CH2O	2.00E+14	0	0
92	C6H5CH2+CH3O2=C6H5CH2O+CH3O	5.00E+12	0	0
93	C6H4CH3+H=C6H5CH2+H	1.00E+13	0	0
94	C3H4+C4H3=C6H5CH2	1.00E+14	0	0
95	C6H5CH2+O2=C6H5CH2OO	1.38E+41	-9.4	9020
96	C6H5CH2OO=C6H5CHO+OH	4.00E+76	-20	64725
97	C6H5CH2OO=C6H5O+CH2O	1.70E+76	-20	64725
98	C6H5CH2OO+HO2=>C6H5CH2O+OH+O2	6.30E+10	0	-720
99	C6H5CH2OO+CH3O2=>C6H5CH2O+CH3O+O2	6.30E+10	0	-720
100	2C6H5CH2OO=>2C6H5CH2O+O2	6.30E+10	0	-720
101	C6H5CH2O+O2=HO2+C6H5CHO	6.60E+10	0	2200
102	C6H5CH2O=C6H5CHO+H	1.00E+14	0	29100
103	C6H5CH2O=A1-+CH2O	1.46E+20	-2	35090
104	C6H5CH2O+H=C6H5CHO+H2	4.00E+13	0	0
105	C6H5CH2O+OH=C6H5CHO+H2O	2.00E+13	0	0
106	C6H5CH2O+HO2=C6H5CHO+H2O2	2.00E+13	0	0

107	C6H5CH2O+CH3=C6H5CHO+CH4	2.00E+13	0	0
108	A1-+HCO=C6H5CHO	5.00E+12	0	0
109	C6H5CHO+OH=H2O+C6H5CO	3.44E+09	1.2	-447
110	C6H5CHO+H=H2+C6H5CO	7.47E+00	4	1384
111	C6H5CHO=C6H5CO+H	4.00E+15	0	83700
112	C6H5CHO+O=C6H5CO+OH	6.00E+12	0	1800
113	C6H5CHO+O2=C6H5CO+HO2	7.00E+11	0	39500
114	C6H5CHO+HO2=C6H5CO+H2O2	7.00E+02	3	10000
115	C6H5CHO+CH3=C6H5CO+CH4	2.00E-06	5.6	1500
116	C6H5CHO+A1-=C6H5CO+A1	2.00E+01	3.5	3743
117	C6H5CO=A1-+CO	1.37E+21	-2.2	39410
118	C6H5CO+HO2=A1-+CO2+OH	1.00E+13	0	0
119	C6H4CH3+O2=OC6H4CH3+O	7.27E+29	-4.7	15600
120	C6H4CH3+O=OC6H4CH3	1.00E+14	0	0
121	C6H4CH3+OH=HOC6H4CH3	3.00E+13	0	0
122	C6H4CH3+HO2=OC6H4CH3+OH	5.00E+12	0	0
123	OC6H4CH3+H=HOC6H4CH3	2.50E+14	0	0
124	HOC6H4CH3+O2=OC6H4CH3+HO2	1.00E+13	0	38900
125	HOC6H4CH3+H=C6H5OH+CH3	5.80E+12	0	8100
126	HOC6H4CH3+H=OC6H4CH3+H2	1.20E+14	0	12400
127	HOC6H4CH3+O=OC6H4CH3+OH	1.30E+13	0	2900
128	HOC6H4CH3+OH=OC6H4CH3+H2O	1.40E+08	1.4	-960
129	HOC6H4CH3+HO2=OC6H4CH3+H2O2	1.00E+12	0	10000

130	HOC6H4CH3+A1-=OC6H4CH3+A1	4.90E+12	0	4400
131	OC6H4CH3=H+A1+CO	7.60E+10	0	43800
132	C6H5OH+O2=C6H5O+HO2	3.00E+10	0	37000
133	C6H5OH+H=C6H5O+H2	1.20E+14	0	12400
134	C6H5OH+O=C6H5O+OH	1.30E+13	0	5000
135	C6H5OH+OH=C6H5O+H2O	3.00E+06	2	-1310
136	C6H5OH+HO2=C6H5O+H2O2	1.00E+12	0	8000
137	C6H5OH+CH3=C6H5O+CH4	1.81E+11	0	9010
138	C6H5OH+A1-=C6H5O+A1	4.90E+12	0	4400
139	C6H5O+H=C6H5OH	1.50E+14	0	0
140	A1+O=C6H5OH	5.10E+13	-0.3	4674
141	A1+OH=C6H5OH+H	8.00E+01	3.2	5590
142	A1-+OH=C6H5OH	3.00E+13	0	0
143	A1+HO2=A1-+H2O2	7.50E+03	2.5	27619
144	A1+CH3=A1-+CH4	1.70E+00	3.7	9500
145	C6H5O+O=OC6H4O+H	2.00E+14	0	0
146	A1-+O2=C6H5O+O	8.21E+41	-7.7	27770
147	A1-+HO2=C6H5O+OH	3.00E+13	0	0
148	C6H5O<=>C5H5+CO	5.40E+10	0	43910
149	A1-+O2=OC6H4O+H	3.00E+13	0	9000
150	OC6H4O+H=>CO+C2H3CO+C2H2	2.50E+13	0	4700
151	OC6H4O+O=>CO+HCCO+C2H3CO	2.48E+14	-0.3	4674
	Declared duplicate reaction...			

152	OC6H4O+O=>CO+HCCO+C2H3CO	1.40E+13	0	14700
	Declared duplicate reaction...			
153	OC6H4O+OH=>HCO+C2H3CO+HCCO	2.00E+06	2	4000
154	C2H3CO=C2H3+CO	1.37E+21	-2.2	39410
	Reverse Arrhenius coefficients:	1.51E+11	0	4810
155	C4H4+O=HCCO+C2H3	1.00E+13	0	0
156	C4H4+OH=CH2CO+C2H3	3.00E+13	0	0
157	C2H3+C4H4=A1+H	1.39E+16	-1	8900
158	A1=A1-+H	5.50E+38	-6.2	132000
159	A1+O2=A1-+HO2	6.31E+13	0	60832
160	C4H4+C2H2=A1	4.47E+11	0	30000
161	A1+O=A1-+OH	1.62E+07	2	8782
162	A1+O=C6H5O+H	2.48E+14	-0.3	4674
163	A1+H=A1-+H2	6.00E+13	0	12000
164	A1+OH=A1-+H2O	2.34E+04	2.7	730
165	C5H10=C2H5+C3H5	9.17E+20	-1.6	73990
	Reverse Arrhenius coefficients:	4.00E+12	0	-596
166	C5H10+O=PC4H9+HCO	1.00E+11	0	0
167	C5H10+OH=PC4H9+CH2O	1.00E+12	0	0
168	PC4H9+O2=C4H8+HO2	1.60E+24	-3.9	7600
169	PC4H9=C2H5+C2H4	7.50E+17	-1.4	29580
	Reverse Arrhenius coefficients:	3.30E+11	0	7200
170	PC4H9=C4H8+H	1.16E+17	-1.2	38160

	Reverse Arrhenius coefficients:	1.00E+13	0	2900
171	C4H8+H=C2H4+C2H5	1.60E+22	-2.4	11180
172	C4H8+H=C3H6+CH3	3.20E+22	-2.4	11180
173	C4H8=C3H5+CH3	5.00E+15	0	71000
	Reverse Arrhenius coefficients:	5.00E+12	0	0
174	C4H8=C2H3+C2H5	1.00E+19	-1	96770
	Reverse Arrhenius coefficients:	9.00E+12	0	0
175	C4H8+OH=NC3H7+CH2O	1.00E+12	0	0
	Reverse Arrhenius coefficients:	1.62E+12	0	13230
176	C4H8+O=C3H6+CH2O	7.23E+05	2.3	-1050
	Reverse Arrhenius coefficients:	2.00E+05	2.3	80280
177	NC3H7CHO+O2=NC3H7CO+HO2	2.00E+13	0.5	42200
	Reverse Arrhenius coefficients:	1.00E+07	0.5	4000
178	NC3H7CHO+OH=NC3H7CO+H2O	2.69E+10	0.8	-340
	Reverse Arrhenius coefficients:	1.85E+10	0.8	31220
179	NC3H7CHO+HO2=NC3H7CO+H2O2	2.80E+12	0	13600
	Reverse Arrhenius coefficients:	1.00E+12	0	10000
180	NC3H7CO=NC3H7+CO	5.32E+15	-0.9	13400
	Reverse Arrhenius coefficients:	1.50E+11	0	4800
181	NC3H7+H=C2H5+CH3	3.70E+24	-2.9	12500
182	NC3H7+OH=C3H6+H2O	2.40E+13	0	0
183	NC3H7+O2=C3H6+HO2	1.71E+42	-9.2	19790
184	NC3H7=CH3+C2H4	2.28E+14	-0.6	28400

	Reverse Arrhenius coefficients:	4.10E+11	0	7204
185	NC3H7=H+C3H6	2.67E+15	-0.6	36820
	Reverse Arrhenius coefficients:	1.00E+13	0	2500
186	TC4H9=H+IC4H8	4.65E+46	-9.8	55080
	Reverse Arrhenius coefficients:	5.89E+44	-9.4	16980
187	TC4H9+O2=IC4H8+HO2	7.00E+24	-3.9	6600
188	IC4H9+O2=IC4H8+HO2	1.60E+24	-3.9	7600
189	IC4H9=C3H6+CH3	1.64E+37	-7.4	38670
	Reverse Arrhenius coefficients:	1.59E+34	-7.1	18030
190	IC4H9=IC4H8+H	4.98E+32	-6.2	40070
	Reverse Arrhenius coefficients:	1.61E+29	-5.2	6265
191	IC4H8+OH=IC4H7+H2O	5.20E+06	2	-298
	Reverse Arrhenius coefficients:	4.56E+08	1.4	32470
192	IC4H8+HO2=IC4H7+H2O2	1.93E+04	2.6	13910
	Reverse Arrhenius coefficients:	1.00E+07	1.7	15210
193	IC4H8=IC4H7+H	3.07E+55	-11.5	114300
	Reverse Arrhenius coefficients:	3.30E+52	-11.1	24460
194	IC4H8+O2=IC4H7+HO2	6.00E+12	0	39900
	Reverse Arrhenius coefficients:	2.21E+12	-0.3	30
195	TC3H6O2CHO=TC3H6CHO+O2	2.79E+25	-4.1	28450
	Reverse Arrhenius coefficients:	1.99E+17	-2.1	0
196	TC3H6CHO+HO2=IC3H7CHO+O2	3.68E+12	0	1310
	Reverse Arrhenius coefficients:	1.24E+14	-0.2	43350

197	TC3H6O2CHO=TC3H6O2HCO	1.00E+11	0	25750
	Reverse Arrhenius coefficients:	8.26E+11	-0.5	22800
198	TC3H6O2HCO=CH3COCH3+CO+OH	4.24E+18	-1.4	4800
199	TC3H6CHO=IC3H5CHO+H	2.88E+16	-0.6	41280
	Reverse Arrhenius coefficients:	1.30E+13	0	1200
200	IC3H7CHO+OH=IC3H7CO+H2O	2.69E+10	0.8	-340
	Reverse Arrhenius coefficients:	1.16E+10	0.8	31200
201	IC3H7CHO+OH=TC3H6CHO+H2O	1.68E+12	0	-781
	Reverse Arrhenius coefficients:	1.19E+13	-0.1	29810
202	IC3H7CO=IC3H7+CO	1.43E+13	0	10950
	Reverse Arrhenius coefficients:	1.50E+11	0	4810
203	IC3H7CHO+HO2=IC3H7CO+H2O2	3.00E+12	0	11920
	Reverse Arrhenius coefficients:	7.71E+12	-0.3	11990
204	IC4H7+HO2=IC4H7O+OH	7.00E+12	0	-1000
	Reverse Arrhenius coefficients:	2.18E+13	-0.2	12050
205	CH3O2+IC4H7=CH3O+IC4H7O	7.00E+12	0	-1000
	Reverse Arrhenius coefficients:	2.13E+15	-0.8	16810
206	IC4H7+O2=C3H4+CH2O+OH	7.29E+29	-5.7	21450
207	IC4H7=C3H4+CH3	1.23E+47	-9.7	74260
	Reverse Arrhenius coefficients:	3.02E+41	-8.7	26620
208	IC4H7+O2=IC3H5CHO+OH	2.47E+13	-0.5	23020
	Reverse Arrhenius coefficients:	1.62E+14	-0.8	73390
209	IC4H7+O2=CH3COCH2+CH2O	7.14E+15	-1.2	21050

	Reverse Arrhenius coefficients:	1.23E+15	-1.2	90190
210	IC4H7O=IC4H6OH	1.39E+11	0	15600
	Reverse Arrhenius coefficients:	4.23E+11	-0.2	31670
211	IC4H7O+O2=IC3H5CHO+HO2	3.00E+10	0	1649
	Reverse Arrhenius coefficients:	6.31E+10	-0.1	38980
212	IC4H7O=IC3H5CHO+H	5.00E+13	0	29100
	Reverse Arrhenius coefficients:	3.07E+11	0.5	16470
213	IC4H6OH+HO2=CH2CCH2OH+CH2O+OH	1.45E+13	0	0
214	CH2CCH2OH+O2=CH2OH+CO+CH2O	4.34E+12	0	0
215	IC3H5CHO+OH=IC3H5CO+H2O	2.69E+10	0.8	-340
	Reverse Arrhenius coefficients:	4.40E+10	0.8	36080
216	IC3H5CHO+HO2=IC3H5CO+H2O2	1.00E+12	0	11920
	Reverse Arrhenius coefficients:	9.71E+12	-0.3	16880
217	IC3H5CO=C3H5+CO	1.28E+20	-1.9	34460
	Reverse Arrhenius coefficients:	1.51E+11	0	4809
218	IC3H7+O2=C3H6+HO2	3.90E+48	-11	21250
219	IC3H7=H+C3H6	8.57E+18	-1.6	40340
	Reverse Arrhenius coefficients:	1.30E+13	0	1560
220	IC3H7+H=C2H5+CH3	2.00E+13	0	0
	Reverse Arrhenius coefficients:	4.82E+09	0.7	12090
221	IC3H7+OH=C3H6+H2O	2.41E+13	0	0
	Reverse Arrhenius coefficients:	2.98E+12	0.6	83820
222	IC3H7+O=CH3COCH3+H	4.82E+13	0	0

	Reverse Arrhenius coefficients:		1.29E+16	-0.2	79380
223	IC3H7+H=C3H6+H2		3.20E+12	0	0
224	CH3COCH3=CH3CO+CH3		5.11E+30	-4.2	89780
225	CH3COCH3+OH=CH3COCH2+H2O		1.25E+05	2.5	445
226	CH3COCH3+O2=CH3COCH2+HO2		6.03E+13	0	48500
227	CH3COCH3+HO2=CH3COCH2+H2O2		1.70E+13	0	20460
228	CH2CO+CH3=CH3COCH2		1.76E+04	2.5	6130
229	CH3COCH2+O2=CH3COCH2O2		1.20E+11	0	-1100
230	CH2O+CH3COCH2O2=HCO+C3KET21		1.29E+11	0	9000
231	HO2+CH3COCH2O2=C3KET21+O2		1.00E+12	0	0
232	C3KET21=>CH2O+CH3CO+OH		1.00E+16	0	43000
233	C3H6+O=C2H5+HCO		3.50E+07	1.6	-972.8
234	C3H6+OH=C3H5+H2O		3.10E+06	2	-298.3
235	C3H6+O=CH2CO+CH3+H		1.20E+08	1.6	327.4
236	C3H6+H=C3H5+H2		1.70E+05	2.5	2492.8
237	C3H6+H=C2H4+CH3		1.60E+22	-2.4	11185.5
238	C3H5+H=C3H4+H2		1.80E+13	0	0
239	C3H5+O2=C3H4+HO2		4.99E+15	-1.4	22428.1
240	C3H5+CH3=C3H4+CH4		3.00E+12	-0.3	-131
241	C2H2+CH3(+M)=C3H5(+M)		6.00E+08	0	0
	Low pressure limit:				
	0.20000E+10 0	0.1 E+01	0.00000E	0	
	TROE centering:	0.1 E+31	0.00000E	0	

```
            0.50000E+00   0
242   C3H5+OH=C3H4+H2O                                           6.00E+12        0        0
243   C3H5+H(+M)=C3H6(+M)                                        2.00E+14        0        0
            CH4            Enhanced by      2.000E+00
            CO             Enhanced by      1.500E+00
            CO2            Enhanced by      2.000E+00
            C2H6           Enhanced by      3.000E+00
            H2O            Enhanced by      6.000E+00
            H2             Enhanced by      2.000E+00
       Low pressure limit:  0.13300E+61 -0.12000E+02  0.59680E+04
       TROE centering:       0.20000E-01  0.10970E+04  0.10970E+04  0.68600E+04
244   C3H5+HO2=C3H6+O2                                           2.66E+12        0        0
245   C3H5+HO2=OH+C2H3+CH2O                                      3.00E+12        0        0
246   CH3+C2H3=C3H5+H                                            1.50E+24     -2.8   18618.5
247   C3H4+O=C2H4+CO                                             2.00E+07      1.8     1000
248   C3H4+O=HCCO+CH3                                            7.30E+12        0     2250
249   C3H4+OH=C3H3+H2O                                           5.30E+06        2     2000
250   C3H4+H(+M)=C3H5(+M)                                        4.00E+13        0        0
       Low pressure limit:  0.30000E+25 -0.20000E+01  0.00000E+00
       TROE centering:       0.80000E+00  0.10000E+31  0.00000E+00
251   C3H4+O2=CH3+HCO+CO                                         4.00E+14        0    41826
252   C3H3+H(+M)=C3H4(+M)                                        3.00E+13        0        0
       Low pressure limit:  0.90000E+16  0.10000E+01  0.00000E+00
```

253	C3H3+HO2=C3H4+O2	2.50E+12	0	0
254	C3H3+O2=CH2CO+HCO	3.00E+10	0	2868.1
255	C3H3+HCO=C3H4+CO	2.50E+13	0	0
256	C3H3+HO2=OH+CO+C2H3	8.00E+11	0	0
257	2CH3(+M)=C2H6(+M)	2.28E+15	-0.7	174.9

      H2O   Enhanced by   5.000E+00
      CO   Enhanced by   2.000E+00
      CO2   Enhanced by   3.000E+00
    Low pressure limit: 0.80540E+32 -0.37500E+01 0.98160E+03
    TROE centering: 0.00000E+00 0.57000E+03 0.10000E+31 0.10000E+31

258	C2H5+H(+M)=C2H6(+M)	5.21E+17	-1	1580

      H2   Enhanced by   2.000E+00
      H2O   Enhanced by   6.000E+00
      CO   Enhanced by   1.500E+00
      CO2   Enhanced by   2.000E+00
      CH4   Enhanced by   2.000E+00
    Low pressure limit: 0.19900E+42 -0.70800E+01 0.66850E+04
    TROE centering: 0.84200E+00 0.12500E+03 0.22190E+04 0.68820E+04

259	C2H6+H=C2H5+H2	1.15E+08	1.9	7530
260	C2H6+O=C2H5+OH	3.55E+06	2.4	5830
261	C2H6+OH=C2H5+H2O	1.48E+07	1.9	950
262	C2H6+O2=C2H5+HO2	6.03E+13	0	51870

263	C2H6+CH3=C2H5+CH4	5.48E-01	4	8280
264	C2H6+HO2=C2H5+H2O2	3.46E+01	3.6	16920
265	C2H6+CH3O2=C2H5+CH3O2H	1.94E+01	3.6	17100
266	C2H6+CH3O=C2H5+CH3OH	2.41E+11	0	7090
267	C2H4+H(+M)=C2H5(+M)	9.57E+08	1.5	1355

	H2	Enhanced by	2.000E+00
	H2O	Enhanced by	6.000E+00
	CO	Enhanced by	1.500E+00
	CO2	Enhanced by	2.000E+00
	CH4	Enhanced by	2.000E+00

Low pressure limit: 0.14190E+40 -0.66420E+01 0.57690E+04

TROE centering: -0.56900E+00 0.29900E+03 -0.91470E+04 0.15240E+03

268	2C2H4=C2H5+C2H3	4.82E+14	0	71530
269	CH3+C2H5=CH4+C2H4	1.18E+04	2.5	-2921
270	2CH3=H+C2H5	2.11E+05	2.3	12150
271	C2H5+H=C2H4+H2	2.00E+12	0	0
272	C2H5+O2=C2H4+HO2	7.56E+14	-1	4749
	Declared duplicate reaction...			
273	C2H5+O2=C2H4+HO2	6.61E+00	3.5	14160
	Declared duplicate reaction...			
274	CH2CO+CH3=C2H5+CO	4.77E+04	2.3	9468
275	C2H5+O=CH3CHO+H	1.10E+14	0	0
276	C2H5+O2=CH3CHO+OH	8.26E+02	2.4	5285

277	C2H3+H(+M)=C2H4(+M)			6.08E+12	0.3	280
	H2	Enhanced by	2.000E+00			
	H2O	Enhanced by	6.000E+00			
	CO	Enhanced by	1.500E+00			
	CO2	Enhanced by	2.000E+00			
	CH4	Enhanced by	2.000E+00			
	Low pressure limit:	0.14000E+31 -0.38600E+01 0.33200E+04				
	TROE centering:	0.78200E+00 0.20750E+03 0.26630E+04 0.60950E+04				
278	C2H4+H=C2H3+H2			5.07E+07	1.9	12950
279	C2H4+O=CH3+HCO			7.45E+06	1.9	183
280	C2H4+O=CH2CHO+H			6.10E+06	1.9	183
281	C2H4+OH=C2H3+H2O			2.23E+04	2.7	2216
282	C2H4+OH=CH2O+CH3			8.00E+12	0	960
283	C2H4+CH3=C2H3+CH4			6.62E+00	3.7	9500
284	C2H4+O2=C2H3+HO2			4.22E+13	0	57620
285	C2H4+CH3O=C2H3+CH3OH			1.20E+11	0	6750
286	C2H4+CH3O2=C2H3+CH3O2H			8.59E+00	3.8	27130
287	2C2H3=C2H2+C2H4			9.60E+11	0	0
288	C2H4+OH=CH3CHO+H			2.94E+09	0.9	12530
289	C2H2+H(+M)=C2H3(+M)			1.71E+10	1.3	2709
	H2	Enhanced by	2.000E+00			
	H2O	Enhanced by	6.000E+00			
	CO	Enhanced by	1.500E+00			

| | CO2 | Enhanced by | 2.000E+00 |
| | CH4 | Enhanced by | 2.000E+00 |

Low pressure limit: 0.63460E+32 -0.46640E+01 0.37800E+04

TROE centering: 0.78800E+00 -0.10200E+05 0.10000E-29

#	Reaction	A	n	E
290	C2H3+O2=CH2O+HCO	1.70E+29	-5.3	6503
291	C2H3+O2=CH2CHO+O	7.00E+14	-0.6	5262
292	C2H3+O2=>H+CO+CH2O	5.19E+15	-1.3	3313
293	C2H3+H=C2H2+H2	9.00E+13	0	0
294	C2H3+OH=C2H2+H2O	3.01E+13	0	0
295	C2H2+HCO=C2H3+CO	1.00E+07	2	6000
296	CH+HCCO=CO+C2H2	5.00E+13	0	0
297	C2H2+O=CH2+CO	7.40E+08	1.3	2472
298	C2H2+O=HCCO+H	2.96E+09	1.3	2472
299	C2H2+OH=CH2CO+H	1.50E+05	2.1	4048
300	C2H2+OH=CH3+CO	1.00E+07	1.4	4315
301	CH2O+CH3O=CH3OH+HCO	6.62E+11	0	2294
302	CH3+CH3OH=CH4+CH3O	1.44E+01	3.1	6935
303	CH2OH+CH3O=CH2O+CH3OH	2.40E+13	0	0
304	CH3OH+HCO=CH2OH+CH2O	9.63E+03	2.9	13110
305	2CH2OH=CH2O+CH3OH	3.00E+12	0	0
306	CH3OH(+M)=CH3+OH(+M)	2.08E+18	-0.6	92540

Low pressure limit: 0.15000E+44 -0.69950E+01 0.97990E+05

TROE centering: -0.47480E+00 0.35580E+05 0.11160E+04 0.90230E+04

307	CH3OH(+M)=CH2OH+H(+M)	7.90E-03	5	84470

Low pressure limit: 0.33900E+43 -0.72440E+01 0.10520E+06

TROE centering: -0.73910E+02 0.37050E+05 0.41500E+05 0.52200E+04

308	CH3OH+H=CH2OH+H2	3.07E+05	2.5	5440
309	CH3OH+H=CH3O+H2	1.99E+05	2.6	10300
310	CH3OH+O=CH2OH+OH	3.88E+05	2.5	3080
311	CH3OH+OH=CH2OH+H2O	3.08E+04	2.6	-806.7
312	CH3OH+OH=CH3O+H2O	1.50E+02	3	-763
313	CH3OH+O2=CH2OH+HO2	2.05E+13	0	44900
314	CH3OH+HO2=CH2OH+H2O2	1.08E+04	2.5	10530
315	CH3OH+CH3=CH2OH+CH4	3.19E+01	3.2	7172
316	CH3O+CH3OH=CH2OH+CH3OH	3.00E+11	0	4074
317	2CH3O=CH3OH+CH2O	6.03E+13	0	0
318	CH3OH+CH3O2=CH2OH+CH3O2H	1.81E+12	0	13710
319	2CH3O2=>CH2O+CH3OH+O2	3.11E+14	-1.6	-1051
320	CH3O2+OH=CH3OH+O2	6.00E+13	0	0
321	CH2O+H(+M)=CH2OH(+M)	5.40E+11	0.5	3600

H2   Enhanced by   2.000E+00

H2O   Enhanced by   6.000E+00

CO   Enhanced by   1.500E+00

CO2   Enhanced by   2.000E+00

CH4   Enhanced by   2.000E+00

Low pressure limit: 0.12700E+33 -0.48200E+01 0.65300E+04

	TROE centering:	0.71870E+00 0.10300E+03 0.12910E+04 0.41600E+04		
322	CH2OH+O2=CH2O+HO2	1.51E+15	-1	0
	Declared duplicate reaction...			
323	CH2OH+O2=CH2O+HO2	2.41E+14	0	5017
	Declared duplicate reaction...			
324	CH2OH+H=CH2O+H2	6.00E+12	0	0
325	CH2OH+HO2=CH2O+H2O2	1.20E+13	0	0
326	CH2OH+HCO=2CH2O	1.80E+14	0	0
327	OH+CH2OH=H2O+CH2O	2.40E+13	0	0
328	O+CH2OH=OH+CH2O	4.20E+13	0	0
329	CH3+OH=CH2OH+H	1.02E+14	-0.1	7423
330	CH2CO+OH=CH2OH+CO	2.00E+12	0	-1010
331	CH3CHO(+M)=CH3+HCO(+M)	2.45E+22	-1.7	86360
	Low pressure limit: 0.10300E+60 -0.11300E+02 0.95910E+05			
	TROE centering:	0.24900E-02 0.71810E+03 0.60890E+01 0.37800E+04		
332	CH3CHO+H=CH3CO+H2	1.31E+05	2.6	1220
333	CH3CHO+H=CH2CHO+H2	2.72E+03	3.1	5210
334	CH3CHO+O=CH3CO+OH	5.94E+12	0	1868
335	CH3CHO+OH=CH3CO+H2O	3.37E+12	0	-619
336	CH3CHO+O2=CH3CO+HO2	3.01E+13	0	39150
337	CH3CHO+HO2=CH3CO+H2O2	3.01E+12	0	11920
338	CH3O2+CH3CHO=CH3O2H+CH3CO	3.01E+12	0	11920
339	CH3CHO+OH=CH2CHO+H2O	1.72E+05	2.4	815

340	CH2CHO(+M)=CH2CO+H(+M)	1.43E+15	-0.1	45600

Low pressure limit: 0.60000E+30 -0.38000E+01 0.43420E+05
TROE centering: 0.98500E+00 0.39300E+03 0.98000E+10 0.50000E+10

341	CH2CHO(+M)=CH3+CO(+M)	2.93E+12	0.3	40300

Low pressure limit: 0.95200E+34 -0.50700E+01 0.41300E+05
TROE centering: 0.71300E-16 0.11500E+04 0.49900E+10 0.17900E+10

342	CH2CHO+O2=CH2CO+HO2	7.05E+07	1.6	25290
343	CH2CHO+O2=>CH2O+CO+OH	8.95E+13	-0.6	10120
344	CH3CO(+M)=CH3+CO(+M)	1.07E+12	0.6	16900

Low pressure limit: 0.56500E+19 -0.97000E+00 0.14600E+05
TROE centering: 0.62900E+00 0.87300E+10 0.55200E+01 0.76000E+08

345	CH3CO+H=CH2CO+H2	2.00E+13	0	0
346	CH3CO+O=CH2CO+OH	2.00E+13	0	0
347	CH3CO(+M)=CH2CO+H(+M)	9.41E+07	1.9	44990

Low pressure limit: 0.15160E+52 -0.10270E+02 0.55390E+05
TROE centering: 0.60090E+00 0.81030E+10 0.66770E+03 0.50000E+10

348	CH2+CO(+M)=CH2CO(+M)	8.10E+11	0	0

H2   Enhanced by   2.000E+00
H2O   Enhanced by   6.000E+00
CO   Enhanced by   1.500E+00
CO2   Enhanced by   2.000E+00
CH4   Enhanced by   2.000E+00
Low pressure limit: 0.26900E+34 -0.51100E+01 0.70950E+04

	TROE centering:	0.59070E+00	0.27500E+03	0.12260E+04	0.51850E+04		
349	CH2CO+H=HCCO+H2				1.40E+15	-0.2	8783
350	CH2CO+H=CH3+CO				7.70E+13	-0.2	4183
351	CH2CO+O=CH2+CO2				1.75E+12	0	1350
352	CH2CO+O=HCCO+OH				1.00E+13	0	8000
353	CH2CO+OH=HCCO+H2O				1.00E+13	0	2000
354	CH+CH2O=H+CH2CO				9.46E+13	0	-515
355	CH2O+CH3=HCO+CH4				3.83E+01	3.4	4312
356	HCO+CH3=CH4+CO				2.65E+13	0	0
357	CH3O+CH3=CH2O+CH4				1.20E+13	0	0
358	CH3+H(+M)=CH4(+M)				1.27E+16	-0.6	383

        H2   Enhanced by   2.000E+00

        H2O   Enhanced by   6.000E+00

        CO   Enhanced by   1.500E+00

        CO2   Enhanced by   2.000E+00

        CH4   Enhanced by   2.000E+00

    Low pressure limit: 0.24770E+34 -0.47600E+01 0.24400E+04

	TROE centering:	0.78300E+00	0.74000E+02	0.29410E+04	0.69640E+04		
359	CH4+H=CH3+H2				6.14E+05	2.5	9587
360	CH4+OH=CH3+H2O				5.83E+04	2.6	2190
361	CH4+O=CH3+OH				1.02E+09	1.5	8600
362	CH4+HO2=CH3+H2O2				1.69E+01	3.7	21010
363	CH3+HO2=CH4+O2				1.16E+05	2.2	-3022

364	CH3CHO(+M)=CH4+CO(+M)	2.72E+21	-1.7	86360

Low pressure limit: 0.11440E+59 -0.11300E+02 0.95910E+05

TROE centering: 0.24900E-02 0.71810E+03 0.60890E+01 0.37800E+04

365	CH3CHO+CH3=CH3CO+CH4	7.08E-04	4.6	1966
366	CH4+CH3O2=CH3+CH3O2H	9.60E-01	3.8	17810
367	CH3CO+CH3=CH2CO+CH4	5.00E+13	0	0
368	CH3O(+M)=CH2O+H(+M)	6.80E+13	0	26170

H2   Enhanced by   2.000E+00

H2O   Enhanced by   6.000E+00

CO   Enhanced by   1.500E+00

CO2   Enhanced by   2.000E+00

CH4   Enhanced by   2.000E+00

Low pressure limit: 0.18670E+26 -0.30000E+01 0.24310E+05

TROE centering: 0.90000E+00 0.25000E+04 0.13000E+04 0.10000+100

369	CH3O+O2=CH2O+HO2	4.38E-19	9.5	-5501
370	CH3O+H=CH2O+H2	2.00E+13	0	0
371	CH3O+HO2=CH2O+H2O2	3.01E+11	0	0
372	CH3+OH=CH2O+H2	1.98E+15	-1.2	5993
373	CH3+OH=H+CH3O	1.37E+10	0.7	12670
374	CH3+HO2=CH3O+OH	1.00E+12	0.3	-687.5
375	CH3+O=CH2O+H	5.54E+13	0.1	-136
376	CH3+O2=CH3O+O	7.55E+12	0	28320
377	CH3+O2=CH2O+OH	2.64E+00	3.3	8105

378	CH3+O2(+M)=CH3O2(+M)	7.81E+09	0.9	0

Low pressure limit: 0.68500E+25 -0.30000E+01 0.00000E+00

TROE centering: 0.60000E+00 0.10000E+04 0.70000E+02 0.17000E+04

379	CH3O2+CH2O=CH3O2H+HCO	1.99E+12	0	11660
380	CH3O2+CH3=2CH3O	5.08E+12	0	-1411
381	CH3O2+HO2=CH3O2H+O2	2.47E+11	0	-1570
382	2CH3O2=>O2+2CH3O	1.40E+16	-1.6	1860
383	CH3O2+H=CH3O+OH	9.60E+13	0	0
384	CH3O2+O=CH3O+O2	3.60E+13	0	0
385	CH3O2H=CH3O+OH	6.31E+14	0	42300
386	H2+CH3O2=H+CH3O2H	1.50E+14	0	26030
387	H+O2=O+OH	1.04E+14	0	15290
388	O+H2=H+OH	5.08E+04	2.7	6292
389	OH+H2=H+H2O	4.38E+13	0	6990
390	O+H2O=2OH	2.97E+06	2	13400
391	H2+M=2H+M	4.58E+19	-1.4	104400

H2   Enhanced by   2.500E+00

H2O   Enhanced by   1.200E+01

CO   Enhanced by   1.900E+00

CO2   Enhanced by   3.800E+00

CH4   Enhanced by   2.000E+00

392	2O+M=O2+M	6.16E+15	-0.5	0

H2   Enhanced by   2.500E+00

	H2O	Enhanced by	1.200E+01		
	CO	Enhanced by	1.900E+00		
	CO2	Enhanced by	3.800E+00		
	CH4	Enhanced by	2.000E+00		
393	O+H+M=OH+M			4.71E+18	-1	0
	H2	Enhanced by	2.500E+00		
	H2O	Enhanced by	1.200E+01		
	CO	Enhanced by	1.500E+00		
	CO2	Enhanced by	2.000E+00		
	CH4	Enhanced by	2.000E+00		
394	H+OH+M=H2O+M			3.50E+22	-2	0
	H2	Enhanced by	7.300E-01		
	H2O	Enhanced by	3.650E+00		
	CH4	Enhanced by	2.000E+00		
	C2H6	Enhanced by	3.000E+00		
395	H+O2(+M)=HO2(+M)			4.65E+12	0.4	0
	H2	Enhanced by	1.300E+00		
	H2O	Enhanced by	1.000E+01		
	CO	Enhanced by	1.900E+00		
	CO2	Enhanced by	3.800E+00		
	CH4	Enhanced by	2.000E+00		

Low pressure limit: 0.17370E+20 -0.12300E+01 0.00000E+00

TROE centering: 0.67000E+00 0.10000E-29 0.10000E+31 0.10000E+31

396	HO2+H=2OH				7.08E+13	0	295
397	H2+O2=H+HO2				5.18E+05	2.4	53500
398	HO2+O=OH+O2				3.25E+13	0	0
399	HO2+OH=H2O+O2				2.46E+13	0	-497
400	2HO2=H2O2+O2				1.30E+11	0	-1630
	Declared duplicate reaction...						
401	2HO2=H2O2+O2				3.66E+14	0	12000
	Declared duplicate reaction...						
402	H2O2(+M)=2OH(+M)				2.00E+12	0.9	48750
	H2	Enhanced by	3.700E+00				
	O2	Enhanced by	1.200E+00				
	H2O	Enhanced by	0.000E+00				
	N2	Enhanced by	1.500E+00				
	H2O2	Enhanced by	7.700E+00				
	Low pressure limit: 0.24900E+25 -0.23000E+01 0.48750E+05						
	TROE centering: 0.43000E+00 0.10000E-29 0.10000E+31						
403	H2O2+H=H2O+OH				2.41E+13	0	3970
404	H2O2+H=H2+HO2				2.15E+10	1	6000
405	H2O2+O=OH+HO2				9.55E+06	2	3970
406	H2O2+OH=H2O+HO2				1.74E+12	0	318
	Declared duplicate reaction...						
407	H2O2+OH=H2O+HO2				7.59E+13	0	7269
	Declared duplicate reaction...						

408	CO+O(+M)=CO2(+M)			1.36E+10	0	2384

408   CO+O(+M)=CO2(+M)   1.36E+10   0   2384

No.	Reaction	A	n	E
408	CO+O(+M)=CO2(+M)	1.36E+10	0	2384

H2   Enhanced by   2.000E+00
H2O   Enhanced by   1.200E+01
CO   Enhanced by   1.750E+00
CO2   Enhanced by   3.600E+00
Low pressure limit: 0.11730E+25 -0.27900E+01   0.41910E+04

| 409 | CO+O2=CO2+O | 1.12E+12 | 0 | 47700 |
| 410 | CO+OH=CO2+H | 7.02E+04 | 2.1 | -355.7 |

Declared duplicate reaction...

| 411 | CO+OH=CO2+H | 5.76E+12 | -0.7 | 331.8 |

Declared duplicate reaction...

412	CO+HO2=CO2+OH	1.57E+05	2.2	17940
413	HCCO+OH=>H2+2CO	1.00E+14	0	0
414	HCCO+O=>H+2CO	8.00E+13	0	0
415	HCCO+O2=>OH+2CO	1.91E+11	0	1020
416	HCCO+O2=>CO2+CO+H	4.78E+12	-0.1	1150
417	CH+CO+M=HCCO+M	7.57E+22	-1.9	0
418	HCO+M=H+CO+M	5.70E+11	0.7	14870

H2   Enhanced by   2.000E+00
H2O   Enhanced by   1.200E+01
CO   Enhanced by   1.500E+00
CO2   Enhanced by   2.000E+00
CH4   Enhanced by   2.000E+00

419	HCO+O2=CO+HO2	7.58E+12	0	410
420	HCO+H=CO+H2	7.34E+13	0	0
421	HCO+O=CO+OH	3.02E+13	0	0
422	HCO+O=CO2+H	3.00E+13	0	0
423	HCO+OH=CO+H2O	1.02E+14	0	0
424	HCO+HO2=>CO2+H+OH	3.00E+13	0	0
425	2HCO=>H2+2CO	3.00E+12	0	0
426	CH2O+O2=HCO+HO2	8.07E+15	0	53420
427	2HCO=CH2O+CO	1.80E+13	0	0
428	HCO+H(+M)=CH2O(+M)	1.09E+12	0.5	-260

    H2   Enhanced by   2.000E+00
    H2O   Enhanced by   6.000E+00
    CO   Enhanced by   1.500E+00
    CO2   Enhanced by   2.000E+00
    CH4   Enhanced by   2.000E+00
   Low pressure limit: 0.13500E+25 -0.25700E+01 0.14250E+04
    TROE centering: 0.78240E+00 0.27100E+03 0.27550E+04 0.65700E+04

429	CH2O+OH=HCO+H2O	7.82E+07	1.6	-1055
430	CH2O+H=HCO+H2	5.74E+07	1.9	2740
431	CH2O+O=HCO+OH	6.26E+09	1.1	2260
432	CH2O+HO2=HCO+H2O2	1.88E+04	2.7	11520
433	CH2+O2=HCO+OH	1.06E+13	0	1500
434	CH2+O2=>CO2+2H	2.64E+12	0	1500

435	CH2+O=>CO+2H			5.00E+13	0	0
436	CH2+H=CH+H2			1.00E+18	-1.6	0
	Declared duplicate reaction...					
437	CH2+OH=CH+H2O			1.13E+07	2	3000
438	CH+O2=HCO+O			3.30E+13	0	0
439	CH+O=CO+H			5.70E+13	0	0
440	CH+OH=HCO+H			3.00E+13	0	0
441	CH2+H=CH+H2			2.70E+11	0.7	25700
	Declared duplicate reaction...					
442	CH+H2O=H+CH2O			1.71E+13	0	-755
443	CH+CO2=HCO+CO			1.70E+12	0	685
444	CO+H2(+M)=CH2O(+M)			4.30E+07	1.5	79600
	H2	Enhanced by	2.000E+00			
	H2O	Enhanced by	6.000E+00			
	CO	Enhanced by	1.500E+00			
	CO2	Enhanced by	2.000E+00			
	CH4	Enhanced by	2.000E+00			
	Low pressure limit:	0.50700E+28 -0.34200E+01 0.84350E+05				
	TROE centering:	0.93200E+00 0.19700E+03 0.15400E+04 0.10300E+05				
445	CH2+H(+M)=CH3(+M)			2.50E+16	-0.8	0
	H2	Enhanced by	2.000E+00			
	H2O	Enhanced by	6.000E+00			
	CO	Enhanced by	1.500E+00			

| | | CO2 | Enhanced by | 2.000E+00 | | |
| | | CH4 | Enhanced by | 2.000E+00 | | |

Low pressure limit: 0.32000E+28 -0.31400E+01 0.12300E+04

TROE centering: 0.68000E+00 0.78000E+02 0.19950E+04 0.55900E+04

446	N+NO<=>N2+O	3.50E+13	0	330
447	N+O2<=>NO+O	2.65E+12	0	6400
448	N+OH<=>NO+H	7.33E+13	0	1120
449	N2O+O<=>N2+O2	1.40E+12	0	10810
450	N2O+O<=>2NO	2.90E+13	0	23150
451	N2O+H<=>N2+OH	4.40E+14	0	18880
452	N2O+OH<=>N2+HO2	2.00E+12	0	21060
453	N2O(+M)<=>N2+O(+M)	1.30E+11	0	59620

Low pressure limit: 0.62000E+15 0.00000E+00 0.56100E+05

	H2	Enhanced by	2.000E+00
	H2O	Enhanced by	6.000E+00
	CH4	Enhanced by	2.000E+00
	CO	Enhanced by	1.500E+00
	CO2	Enhanced by	2.000E+00

| 454 | HO2+NO<=>NO2+OH | 2.11E+12 | 0 | -480 |
| 455 | NO+O+M<=>NO2+M | 1.06E+20 | -1.4 | 0 |

	H2	Enhanced by	2.000E+00
	H2O	Enhanced by	6.000E+00
	CH4	Enhanced by	2.000E+00

	CO	Enhanced by	1.500E+00	
	CO2	Enhanced by	2.000E+00	

456	NO2+O<=>NO+O2	3.90E+12	0	-240
457	NO2+H<=>NO+OH	1.32E+14	0	360
458	C2H3+O2<=>C2H2+HO2	1.12E+14	-0.8	2541
459	CH2CHO+CH3<=>C2H5+HCO	5.00E+13	0	0
460	C2H3+CH2O<=>C2H4+HCO	5.42E+03	2.8	5824
461	C2H3+H2O2<=>C2H4+HO2	1.21E+10	0	-590.1
462	H2+C2H<=>C2H2+H	1.08E+13	0	2165
463	C2H2+C2H<=>C4H2+H	9.03E+13	0	0
464	C2H2+OH<=>C2H+H2O	6.00E+13	0	12920
465	C2H2+M<=>C2H+H+M	1.14E+17	0	106800

	O2	Enhanced by	4.000E-01	
	H2O	Enhanced by	6.500E+00	
	CO	Enhanced by	7.500E-01	

466	C2H+C2H3<=>2C2H2	1.90E+13	0	0
467	C2H+OH<=>CH2+CO	1.81E+13	0	0
468	C2H4+C2H<=>C4H4+H	1.20E+13	0	0
469	C3H2+O<=>C2H+H+CO	6.80E+13	0	0
470	C3H3+O<=>CH2O+C2H	1.40E+14	0	0
471	2C2H2<=>C4H3+H	2.00E+09	0	57840
472	C2H2+C2H<=>C4H3	4.17E+36	-7.3	8723
473	C4H3+O<=>CH2CO+C2H	2.00E+13	0	0

474	C4H4+C2H<=>C4H2+C2H3	1.00E+13	0	0
475	C4H4+C2H<=>C4H3+C2H2	4.00E+13	0	0
476	2C2H3<=>IC4H5+H	4.00E+13	0	0
477	IC4H5+C2H<=>2C3H3	4.00E+12	0	0
478	C4H2+O<=>C3H2+CO	7.89E+12	0	1348
479	C4H2+OH<=>C3H2+HCO	6.68E+12	0	-408.7
480	C3H3+OH<=>C3H2+H2O	2.00E+13	0	0
481	C3H2+OH<=>C2H2+CO+H	5.00E+13	0	0
482	C3H3+H<=>C3H2+H2	5.00E+12	0	0
483	C3H2+CH2<=>C4H3+H	3.00E+13	0	0
484	C3H3+O<=>C2H2+CO+H	1.39E+14	0	0
485	C2H2+CH2<=>C3H3+H	1.20E+13	0	6577
486	C3H3+OH<=>HCO+C2H3	4.00E+13	0	0
487	C4H3+C2H3<=>2C3H3	4.00E+12	0	0
488	C4H4+O<=>HCO+C3H3	3.20E+08	1.4	549.4
489	C3H3+CH2<=>H+C4H4	4.00E+13	0	0
490	C3H3+C2H3<=>C5H5+H	9.60E+40	-7.8	28630
491	C3H3+C2H2<=>C5H5	2.40E+11	0	9995
492	C4H3+M<=>C4H2+H+M	1.12E+16	0	46510

	O2	Enhanced by	4.000E-01
	H2O	Enhanced by	6.500E+00
	CO	Enhanced by	7.500E-01

493	2C2H2<=>C4H2+H2	1.51E+14	0	42420

494	C4H2+H<=>C4H3	1.10E+30	-4.9	10730
495	C4H2+H2<=>C4H4	4.00E+14	0	53250
496	C4H3+H<=>C4H2+H2	5.00E+13	0	0
497	C4H3+OH<=>C4H2+H2O	3.00E+13	0	0
498	C4H3+H2<=>C2H2+C2H3	5.01E+10	0	19870
499	C4H4+M<=>C4H3+H+M	1.10E+20	0	98630
500	C4H4+H<=>C4H3+H2	5.01E+06	2	5961
501	C4H4+OH<=>C4H3+H2O	7.50E+06	2	5019
502	C4H4+C2H3<=>C4H3+C2H4	5.00E+11	0	16190
503	C4H4<=>2C2H2	3.40E+13	0	76640
504	C2H3+C2H2<=>H+C4H4	2.00E+11	0	4968
505	IC4H5(+M)<=>C4H4+H(+M)	1.00E+14	0	49680
	Low pressure limit: 0.20000E+16 0.00000E+00 0.41730E+05			
506	IC4H5+O2<=>C4H4+HO2	1.00E+12	0	2980
507	IC4H5+H<=>C4H4+H2	1.00E+14	0	0
508	IC4H5+OH<=>C4H4+H2O	2.00E+07	2	999.1
509	IC4H5<=>C2H3+C2H2	1.00E+14	0	43610
510	C5H5+O<=>IC4H5+CO	1.00E+13	0	0
511	C5H5+OH<=>CH2O+2C2H2	2.00E+12	0	0
512	2C3H3<=>A1	1.00E+36	-7.2	8413
513	2C3H3<=>A1-+H	3.00E+35	-7.2	8413
514	C4H3+C2H3<=>A1	3.00E+13	0	0
515	C4H3+C2H3<=>A1-+H	6.00E+12	0	0

516	C4H3+C2H2<=>A1-	5.00E+13	0	14800
517	C4H4+C2H2<=>A1-+H	1.00E+09	0	29800
518	IC4H5+C2H2<=>A1+H	1.60E+15	-1.3	5365
519	IC4H5+C2H3<=>A1+H2	1.80E-13	7.1	-3577
520	IC4H5+C2H<=>A1	1.00E+13	0	0
521	IC4H5+C2H<=>A1-+H	6.00E+12	0	0
522	A1+C2H<=>A1-+C2H2	2.00E+13	0	0
523	A1-+O<=>C5H5+CO	1.00E+14	0	0
524	A1-+OH<=>C6H5O+H	5.00E+13	0	0
525	IC4H5+C4H2<=>A1C2H+H	3.16E+11	0	1788
526	A1C2H-+H(+M)<=>A1C2H(+M)	1.00E+14	0	0

       Low pressure limit: 0.66000E+76 -0.16300E+02 0.13910E+05

       TROE centering: 0.10000E+01 0.10000E+00 0.58490E+03 0.61130E+04

           H2   Enhanced by   2.000E+00

           H2O   Enhanced by   6.000E+00

           CO   Enhanced by   1.500E+00

527	C4H3+C4H2<=>A1C2H-	9.60E+70	-17.8	31120
528	A1-+C4H2<=>A1C2H+C2H	2.00E+13	0	21860
529	A1-+C2H3<=>A1C2H+H2	7.90E+12	0	6358
530	A1-+C4H4<=>A1C2H+C2H3	3.20E+11	0	1352
531	A1+C2H<=>A1C2H+H	1.00E+12	0	0
532	A1-+C2H<=>A1C2H	5.24E+14	-0.5	596.1
533	A1C2H+O<=>A1C2H-+OH	1.10E+13	0	8147

534	A1C2H+O<=>C6H5O+C2H	2.20E+13	0	4491
535	A1C2H+H<=>A1C2H-+H2	2.70E+13	0	9701
536	A1C2H+H<=>A1-+C2H2	2.00E+14	0	9701
537	A1C2H+OH<=>A1C2H-+H2O	2.10E+13	0	4570
538	A1C2H+OH<=>A1-+CH2CO	2.18E-04	4.5	-993.5
539	A1C2H+C2H<=>A1C2H-+C2H2	2.00E+13	0	0
540	2C4H4<=>A1C2H3	1.80E+20	-1.9	40200
541	IC4H5+C4H4<=>A1C2H3+H	3.16E+11	0	596.1
542	A1+C2H3<=>A1C2H3+H	7.90E+11	0	6358
543	A1-+C2H3<=>A1C2H3	1.06E+26	-4	5266
544	A1-+C2H4<=>A1C2H3+H	2.51E+12	0	6150
545	A1C2H3+O<=>A1-+CH2CHO	3.00E+08	1.4	894.2
546	A1C2H3+O<=>A1-+CH3+CO	1.92E+07	1.8	218.6
547	IC4H5+A1=>A2+H2+H	5.00E+11	0	2987
548	2C5H5<=>A2+2H	4.30E+13	0	9713
549	2C5H5<=>A2+H2	4.30E+36	-6.3	45370
550	A1-+C4H3<=>A2	3.18E+23	-3.2	4232
551	A1-+C4H3<=>A2-+H	2.00E-10	7.1	1562
552	A1-+C4H4<=>A2+H	3.30E+33	-5.7	25330
553	A1C2H-+C2H2<=>A2-	4.00E+13	0	10130
554	A2+O<=>CH2CO+A1C2H	2.20E+13	0	4501
555	A2+O<=>A2-+OH	2.00E+13	0	14700
556	A2+H<=>A2-+H2	2.50E+14	0	15900

557	A2+OH<=>A2-+H2O	2.10E+13	0	4570
558	A2+OH=>A1C2H+CH2CO+H	1.30E+13	0	10530
559	A2-+H<=>A2	7.80E+13	0	0
560	A1C2H-+C4H4<=>A2R5+H	1.60E+16	-1.3	6557
561	A2-+C2H2<=>A2R5+H	1.90E+31	-5.3	20860
562	A2R5<=>A1C2H+C4H2	2.00E+17	0	115200
563	A2R5+OH<=>A2-+CH2CO	1.00E+11	0	9935
564	C4H2+A2R5=>A4	2.41E+02	2.2	-1131
565	A1C2H+A1C2H-<=>A4+H	1.10E+24	-2.9	15920
566	A2+A1-<=>A4+H+H2	1.00E+11	0	4968
567	A2-+A1<=>A4+H+H2	1.00E+12	0	4968
568	A2-+A1-=>A4+H2	4.30E+37	-6.3	44770
569	A1C2H+A1-<=>A3+H	1.10E+23	-2.9	15920
570	A1C2H-+A1<=>A3+H	1.10E+23	-2.9	15920
571	A2-+C4H4<=>A3+H	3.30E+33	-5.7	25330
572	A2-+C4H2<=>A3-	3.30E+33	-5.7	25330
573	A2R5+C2H2=>A3	2.76E+04	2.5	29080
574	A2+C4H2=>A3	2.76E+04	2.5	29080
575	A3+O<=>A3-+OH	2.00E+13	0	14700
576	A3+H<=>A3-+H2	2.50E+14	0	15900
577	A3-+O2=>CO+HCO+A2R5	2.00E+12	0	7352
578	A3-+H<=>A3	1.00E+14	0	0
579	A3-+C2H2<=>A4+H	6.60E+24	-3.4	17680

580	A4+OH<=>A3-+CH2CO	2.00E+13	0	41730
581	C4H2=4C(S)+H2	1.00E+04	0	0
582	C(S)+O2=O+CO	1.69E+09	0	12800
583	C(S)+H2O=CO+H2	4.00E+10	0	42800
584	C(S)+OH=CO+H	3.00E+10	0	36800
585	A4=16C(S)+5H2	2.00E+03	0	0

This page was intentionally left blank.

Appendix B: Adjusted and enhanced kerosene-diesel reaction mechanism

ELEMENTS					
C	AR	H	O	N	HE

SPECIES				
C10H22	O	C2H3	CH2CO	C10#OOH
KERO	H	C2H4	HCCO	N2O
O2	H2	C2H5	C5H11CO	KERO-
CO	H2O2	C3H4	C10-	KERO-OO
CO2	HO2	C3H5	C10-OO	KERO#OOH
OH	CH4	C3H6	N	KERO#
H2O	CH3O	C3H7	C10#	OOKERO#OOH
NO	CH2O	CH2OH	HE	KERO#KET
NO2	HCO	CH3OH	C10KET	
N2	CH3	C2H2	OOC10#OOH	

	REACTIONS	A	b	E
1	KERO+O2<=>KERO-+HO2	2.90E+12	0.00E+00	27800
	Reverse Arrhenius coefficients:	1.00E+12	0.00E+00	0
2	KERO+OH<=>KERO-+H2O	7.70E+06	1.90E+00	58.5
	Reverse Arrhenius coefficients:	6.15E+08	1.90E+00	21910
3	KERO+H=>KERO-+H2	1.00E+11	2.00E+00	2500
4	KERO-+O2<=>KERO-OO	4.30E+12	0.00E+00	0
	Reverse Arrhenius coefficients:	2.51E+13	0.00E+00	27400
5	KERO-OO<=>KERO#OOH	1.51E+11	0.00E+00	19000
	Reverse Arrhenius coefficients:	1.00E+11	0.00E+00	11000

6	KERO#OOH+O2<=>OOKERO#OOH	7.56E+12	0.00E+00	0
	Reverse Arrhenius coefficients:	2.51E+13	0.00E+00	27400
7	OOKERO#OOH<=>KERO#KET+OH	7.31E+08	0.00E+00	17000
8	KERO#KET=>CH2O+C5H11CO+OH+C3H6	9.98E+16	0.00E+00	43000
9	KERO-+O2=KERO#+HO2	2.16E+12	0.00E+00	6000
	Reverse Arrhenius coefficients:	3.16E+11	0.00E+00	19500
10	KERO#+O2=>2C3H6+C2H5+CH2O+HCO	5.16E+11	0.00E+00	10000
11	KERO-+H=KERO	1.00E+14	0.00E+00	0
12	C10H22+O2<=>C10-+HO2	7.00E+12	0.00E+00	27800
	Reverse Arrhenius coefficients:	1.00E+12	0.00E+00	0
13	C10H22+OH<=>C10-+H2O	5.00E+07	1.90E+00	58.5
	Reverse Arrhenius coefficients:	6.15E+08	1.90E+00	21910
14	C10H22+H=>C10-+H2	1.00E+08	2.00E+00	2500
15	C10-+O2<=>C10-OO	3.00E+12	0.00E+00	0
	Reverse Arrhenius coefficients:	2.51E+13	0.00E+00	27400
16	C10-OO<=>C10#OOH	1.51E+11	0.00E+00	19000
	Reverse Arrhenius coefficients:	1.00E+11	0.00E+00	11000
17	C10#OOH+O2<=>OOC10#OOH	5.56E+10	0.00E+00	0
	Reverse Arrhenius coefficients:	2.51E+13	0.00E+00	27400
18	OOC10#OOH<=>C10KET+OH	8.91E+10	0.00E+00	17000
19	C10KET=>CH2O+C5H11CO+OH+C3H6	3.98E+15	0.00E+00	43000
20	C5H11CO+O2=>C3H7+C2H3+CO+HO2	3.16E+13	0.00E+00	10000
21	C10-+O2=C10#+HO2	3.16E+11	0.00E+00	6000

	Reverse Arrhenius coefficients:	3.16E+11	0.00E+00	19500
22	C10#+O2=>2C3H6+C2H5+CH2O+HCO	3.16E+13	0.00E+00	10000
23	C10-=>2C3H6+C2H5+C2H4	3.50E+12	0.00E+00	28810
24	C3H7=C2H4+CH3	9.60E+13	0.00E+00	30950
25	C3H7=C3H6+H	1.25E+14	0.00E+00	36900
26	C3H6=C2H3+CH3	3.15E+15	0.00E+00	85500
27	C3H6+CH3=C3H5+CH4	9.00E+12	0.00E+00	8480
28	C3H5+O2=C3H4+HO2	6.00E+11	0.00E+00	10000
29	C3H4+OH=C2H3+CH2O	1.00E+12	0.00E+00	0
30	C3H4+OH=C2H4+HCO	1.00E+12	0.00E+00	0
31	C2H5+O2=C2H4+HO2	2.00E+10	0.00E+00	-2200
32	C2H4+OH=CH2O+CH3	6.00E+13	0.00E+00	960
33	C2H4+OH=C2H3+H2O	8.02E+13	0.00E+00	5955
34	C2H3+O2=CH2O+HCO	4.00E+12	0.00E+00	-250
35	C2H3+HCO=C2H4+CO	6.03E+13	0.00E+00	0
36	H+C2H4(+M)=C2H5(+M)	1.08E+12	0.5	1822

Low pressure limit: 0.11120E+35 -0.50000E+01   0.44480E+04

TROE centering: 0.10000E+01   0.10000E-14   0.95000E+02   0.20000E+03

H2	Enhanced by	2.000E+00	
H2O	Enhanced by	5.000E+00	
CO	Enhanced by	2.000E+00	
CO2	Enhanced by	3.000E+00	

37	C3H5=C2H2+CH3	2.40E+48	-9.9	82080

	Reverse Arrhenius coefficients:	2.61E+46	-9.8	36950
38	C2H4(+M)=C2H2+H2(+M)	1.80E+13	0	76000

Low pressure limit: 0.15000E+16 0.00000E+00 0.55440E+05

39	C2H3+O2=C2H2+HO2	2.12E-06	6	9484
	Reverse Arrhenius coefficients:	1.11E-07	6.3	17570
40	C2H3+H=C2H2+H2	2.00E+13	0	2500
	Reverse Arrhenius coefficients:	1.33E+13	0	68080
41	C2H2+H(+M)=C2H3(+M)	3.11E+11	0.6	2589

Low pressure limit: 0.22540E+41 -0.72690E+01 0.65770E+04

TROE centering: 0.10000E+01 0.10000E-14 0.67500E+03 0.10000E+16

H2	Enhanced by	2.000E+00
H2O	Enhanced by	5.000E+00
CO	Enhanced by	2.000E+00
CO2	Enhanced by	3.000E+00

42	C2H2+O2=HCCO+OH	2.00E+08	1.5	30100
	Reverse Arrhenius coefficients:	2.23E+05	1.5	25400
43	C2H2+O=HCCO+H	1.43E+07	2	1900
	Reverse Arrhenius coefficients:	2.02E+05	2	13310
44	C2H2+OH=CH2CO+H	2.19E-04	4.5	-1000
	Reverse Arrhenius coefficients:	2.16E-03	4.5	19660
45	CH2CO+H=CH3+CO	1.10E+13	0	3400
	Reverse Arrhenius coefficients:	2.40E+12	0	40200
46	CH2CO+O=HCCO+OH	1.00E+13	0	8000

	Reverse Arrhenius coefficients:			1.43E+10	0	-1255
47	CH2CO+OH=HCCO+H2O			1.00E+13	0	2000
	Reverse Arrhenius coefficients:			1.41E+11	0	9995
48	CH2CO+H=HCCO+H2			2.00E+14	0	8000
	Reverse Arrhenius coefficients:			6.52E+11	0	840
49	HCCO+OH=HCO+HCO			1.00E+13	0	0
	Reverse Arrhenius coefficients:			2.41E+14	0	40360
50	HCCO+O=H+CO+CO			8.00E+13	0	0
	Reverse Arrhenius coefficients:			0.00E+00	0	0
51	HCCO+O2=CO2+HCO			2.40E+11	0	-854
	Reverse Arrhenius coefficients:			1.47E+14	0	133600
52	H+O2=O+OH			3.55E+15	-0.4	16599
53	O+H2=H+OH			5.08E+04	2.7	6290
54	H2+OH=H2O+H			2.16E+08	1.5	3430
55	O+H2O=OH+OH			2.97E+06	2	13400
56	H2+M=H+H+M			4.58E+19	-1.4	104380
	H2	Enhanced by	2.500E+00			
	H2O	Enhanced by	1.200E+01			
	CO	Enhanced by	1.900E+00			
	CO2	Enhanced by	3.800E+00			
	HE	Enhanced by	0.000E+00			
57	O+O+M=O2+M			6.17E+15	-0.5	0
	H2	Enhanced by	2.500E+00			

	H2O	Enhanced by	1.200E+01	
	HE	Enhanced by	0.000E+00	
	CO	Enhanced by	1.900E+00	
	CO2	Enhanced by	3.800E+00	

58 O+H+M=OH+M 4.71E+18 -1 0

H2	Enhanced by	2.500E+00	
H2O	Enhanced by	1.200E+01	
HE	Enhanced by	7.500E-01	
CO	Enhanced by	1.900E+00	
CO2	Enhanced by	3.800E+00	

59 H+OH+M=H2O+M 3.80E+22 -2 0

H2	Enhanced by	2.500E+00	
H2O	Enhanced by	1.200E+01	
HE	Enhanced by	3.800E-01	
CO	Enhanced by	1.900E+00	
CO2	Enhanced by	3.800E+00	

60 H+O2(+M)=HO2(+M) 1.48E+12 0.6 0

Low pressure limit: 0.63660E+21 -0.17200E+01 0.52480E+03
TROE centering: 0.80000E+00 0.10000E-29 0.10000E+31

H2	Enhanced by	2.000E+00	
H2O	Enhanced by	1.100E+01	
O2	Enhanced by	7.800E-01	
CO	Enhanced by	1.900E+00	

		CO2	Enhanced by	3.800E+00			
61	HO2+H=H2+O2				1.66E+13	0	823
62	HO2+H=OH+OH				7.08E+13	0	295
63	HO2+O=O2+OH				3.25E+13	0	0
64	HO2+OH=H2O+O2				2.89E+13	0	-497
65	HO2+HO2=H2O2+O2				4.20E+14	0	11982

Declared duplicate reaction…

| 66 | HO2+HO2=H2O2+O2 | 1.30E+11 | 0 | -1629.3 |

Declared duplicate reaction…

| 67 | H2O2(+M)=OH+OH(+M) | 2.95E+14 | 0 | 48430 |

Low pressure limit: 0.12020E+18 0.00000E+00 0.45500E+05

TROE centering: 0.50000E+00 0.10000E-29 0.10000E+31

	H2	Enhanced by	2.500E+00
	H2O	Enhanced by	1.200E+01
	CO	Enhanced by	1.900E+00
	CO2	Enhanced by	3.800E+00
	HE	Enhanced by	6.400E-01

68	H2O2+H=H2O+OH	2.41E+13	0	3970
69	H2O2+H=HO2+H2	4.82E+13	0	7950
70	H2O2+O=OH+HO2	9.55E+06	2	3970
71	H2O2+OH=HO2+H2O	1.00E+12	0	0

Declared duplicate reaction…

| 72 | H2O2+OH=HO2+H2O | 5.80E+14 | 0 | 9557 |

Declared duplicate reaction…

#	Reaction				A	n	Ea
73	CO+O(+M)=CO2(+M)				1.80E+10	0	2384
	Low pressure limit:	0.15500E+25	-0.27900E+01	0.41910E+04			
	H2	Enhanced by	2.500E+00				
	H2O	Enhanced by	1.200E+01				
	CO	Enhanced by	1.900E+00				
	CO2	Enhanced by	3.800E+00				
74	CO+O2=CO2+O				2.53E+12	0.00E+00	47700
75	CO+HO2=CO2+OH				3.01E+13	0.00E+00	23000
76	CO+OH=CO2+H				2.23E+05	1.90E+00	-1158.7
77	HCO+M=H+CO+M				4.75E+11	0.7	14874
	H2	Enhanced by	2.500E+00				
	H2O	Enhanced by	6.000E+00				
	CO	Enhanced by	1.900E+00				
	CO2	Enhanced by	3.800E+00				
78	HCO+O2=CO+HO2				7.58E+12	0.00E+00	410
79	HCO+H=CO+H2				7.23E+13	0.00E+00	0
80	HCO+O=CO+OH				3.02E+13	0.00E+00	0
81	HCO+OH=CO+H2O				3.02E+13	0.00E+00	0
82	HCO+O=CO2+H				3.00E+13	0.00E+00	0
83	HCO+HO2=CO2+OH+H				3.00E+13	0.00E+00	0
84	HCO+CH3=CO+CH4				1.20E+14	0.00E+00	0
85	HCO+HCO=H2+CO+CO				3.00E+12	0.00E+00	0

86	HCO+HCO=CH2O+CO			3.00E+13	0.00E+00	0
87	CH2O+M=HCO+H+M			3.30E+39	-6.3	99900
	H2	Enhanced by	2.500E+00			
	H2O	Enhanced by	1.200E+01			
	CO	Enhanced by	1.900E+00			
	CO2	Enhanced by	3.800E+00			
88	CH2O+M=CO+H2+M			3.10E+45	-8	97510
	H2	Enhanced by	2.500E+00			
	H2O	Enhanced by	1.200E+01			
	CO	Enhanced by	1.900E+00			
	CO2	Enhanced by	3.800E+00			
89	CH2O+H=HCO+H2			5.74E+07	1.90E+00	2748.6
90	CH2O+O=HCO+OH			1.81E+13	0.00E+00	3080
91	CH2O+OH=HCO+H2O			3.43E+09	1.20E+00	-447
92	CH2O+O2=HCO+HO2			1.23E+06	3.00E+00	52000
93	CH2O+HO2=HCO+H2O2			4.11E+04	2.50E+00	10210
94	CH2O+CH3=HCO+CH4			3.64E-06	5.40E+00	998
95	CH3+O=CH2O+H			8.43E+13	0.00E+00	0
96	CH3+O2=CH3O+O			1.99E+18	-1.60E+00	29230
97	CH3+O2=CH2O+OH			3.74E+11	0.00E+00	14640
98	CH3+HO2=CH3O+OH			2.41E+10	8.00E-01	-2325
99	CH3+H(+M)=CH4(+M)			1.27E+16	-0.6	383

Low pressure limit: 0.24770E+34 -0.47600E+01 0.24400E+04

	TROE centering:	0.78300E+00	0.74000E+02	0.29410E+04	0.69640E+04	
	H2	Enhanced by	2.000E+00			
	H2O	Enhanced by	6.000E+00			
	CH4	Enhanced by	2.000E+00			
	CO	Enhanced by	1.500E+00			
	CO2	Enhanced by	2.000E+00			
100	CH4+H=CH3+H2			5.47E+07	2	11210
101	CH4+O=CH3+OH			3.15E+12	0.5	10290
102	CH4+OH=CH3+H2O			5.72E+06	2	2639
103	CH3+HO2=CH4+O2			3.16E+12	0	0
104	CH4+HO2=CH3+H2O2			1.81E+11	0	18580
105	CH2OH+M=CH2O+H+M			1.00E+14	0	25100
106	CH2OH+H=CH2O+H2			6.00E+12	0	0
107	CH2OH+H=CH3+OH			9.64E+13	0	0
108	CH2OH+O=CH2O+OH			4.20E+13	0	0
109	CH2OH+OH=CH2O+H2O			2.40E+13	0	0
110	CH2OH+O2=CH2O+HO2			2.41E+14	0	5017
	Declared duplicate reaction…					
111	CH2OH+O2=CH2O+HO2			1.51E+15	-1	0
	Declared duplicate reaction…					
112	CH2OH+HO2=CH2O+H2O2			1.20E+13	0	0
113	CH2OH+HCO=CH3OH+CO			1.00E+13	0	0
114	CH2OH+HCO=CH2O+CH2O			1.50E+13	0	0

115	2CH2OH=CH3OH+CH2O	3.00E+12	0	0
116	CH2OH+CH3O=CH3OH+CH2O	2.40E+13	0	0
117	CH3O+M=CH2O+H+M	8.30E+17	-1.2	15500
118	CH3O+H=CH3+OH	3.20E+13	0	0
119	CH3O+O=CH2O+OH	6.00E+12	0	0
120	CH3O+OH=CH2O+H2O	1.80E+13	0	0
121	CH3O+O2=CH2O+HO2	9.03E+13	0	11980
	Declared duplicate reaction…			
122	CH3O+O2=CH2O+HO2	2.20E+10	0	1748
	Declared duplicate reaction…			
123	CH3O+HO2=CH2O+H2O2	3.00E+11	0	0
124	CH3O+CO=CH3+CO2	1.60E+13	0	11800
125	CH3O+HCO=CH3OH+CO	9.00E+13	0	0
126	2CH3O=CH3OH+CH2O	6.00E+13	0	0
127	OH+CH3(+M)<=>CH3OH (+M)	2.79E+18	-1.4	1330

Low pressure limit: 0.40000E+37 -0.59200E+01 0.31400E+04

TROE centering: 0.41200E+00 0.19500E+03 0.59000E+04 0.63940E+04

H2	Enhanced by	2.000E+00
H2O	Enhanced by	6.000E+00
CH4	Enhanced by	2.000E+00
CO	Enhanced by	1.500E+00
CO2	Enhanced by	2.000E+00

128	H+CH2OH(+M)<=>CH3OH(+M)	1.06E+12	0.5	86

Low pressure limit: 0.43600E+32 -0.46500E+01 0.50800E+04

TROE centering: 0.60000E+00 0.10000E+03 0.90000E+05 0.10000E+05

H2	Enhanced by	2.000E+00
H2O	Enhanced by	6.000E+00
CH4	Enhanced by	2.000E+00
CO	Enhanced by	1.500E+00
CO2	Enhanced by	2.000E+00

129	H+CH3O(+M)<=>CH3OH(+M)		2.43E+12	0.5	50

Low pressure limit: 0.46600E+42 -0.74400E+01 0.14080E+05

TROE centering: 0.70000E+00 0.10000E+03 0.90000E+05 0.10000E+05

H2	Enhanced by	2.000E+00
H2O	Enhanced by	6.000E+00
CH4	Enhanced by	2.000E+00
CO	Enhanced by	1.500E+00
CO2	Enhanced by	2.000E+00

130	CH3OH+H=CH2OH+H2	3.20E+13	0.00E+00	6095
131	CH3OH+H=CH3O+H2	8.00E+12	0.00E+00	6095
132	CH3OH+O=CH2OH+OH	3.88E+05	2.50E+00	3080
133	CH3OH+OH=CH3O+H2O	1.00E+06	2.10E+00	496.7
134	CH3OH+OH=CH2OH+H2O	7.10E+06	1.80E+00	-596
135	CH3OH+O2=CH2OH+HO2	2.05E+13	0.00E+00	44900
136	CH3OH+HCO=CH2OH+CH2O	9.64E+03	2.90E+00	13110
137	CH3OH+HO2=CH2OH+H2O2	3.98E+13	0.00E+00	19400

138	CH3OH+CH3=CH2OH+CH4	3.19E+01	3.20E+00	7172
139	CH3O+CH3OH=CH3OH+CH2OH	3.00E+11	0.00E+00	4060
140	N+NO=N2+O	3.50E+13	0.00E+00	330
141	N+O2=NO+O	2.65E+12	0.00E+00	6400
142	N+OH=NO+H	7.33E+13	0.00E+00	1120
143	N+CO2=NO+CO	1.90E+11	0.00E+00	3400
144	N2O+O=N2+O2	1.40E+12	0.00E+00	10810
145	N2O+O=NO+NO	2.90E+13	0.00E+00	23150
146	N2O+H=N2+OH	4.40E+14	0.00E+00	18880
147	N2O+OH=N2+HO2	2.00E+12	0.00E+00	21060
148	N2O+M=N2+O+M	1.30E+11	0.00E+00	59620
149	NO+HO2=NO2+OH	2.11E+12	0.00E+00	-480
150	NO2+O=NO+O2	3.90E+12	0.00E+00	-240
151	NO2+H=NO+OH	1.32E+14	0.00E+00	360
152	NO+O+M=NO2+M	1.06E+20	-1.4	0